Chapter One

INTRODUCTION

This chapter presents an introduction into the field of micromechanics. A summary is presented of transduction principles that are applied in microactuators. The important class of electrostatic microactuators is described and a survey of micromechanical fabrication techniques is given. Finally the scope and the outline of this thesis are summarised.

1.0 MICROMECHANICS

The advances made by silicon IC technology have led to the application of microelectronic devices and components in a wide range of new areas. The trends for microelectronic systems are characterised by increasing miniaturisation, decreasing costs with respect to function, and increasing complexity and performance. Various transducers such as sensors and actuators are required to enable electronic systems to interface with their environment. Untill now transducers have mainly been fabricated using conventional fine mechanics. This is a limiting factor for further system integration with respect to miniaturisation, performance and price. Therefore an increasing demand for new transducers based on IC fabrication and other thin film technologies can be observed.

Micromachining techniques use silicon as a mechanical material due to its good mechanical properties and exploit the highly developed technology of integrated circuits for the fabrication of mechanical structures with very small dimensions. The use of silicon as a base material allows the monolithic integration of mechanical structures with electronic circuitry on the same chip. This enables the fabrication of sophisticated microsystems with totally new types of applications and performance.

Due to fundamental scaling properties, the microworld is dominated by surface forces such as surface tension and friction. Bulk forces like inertia and weight tend to become insignificant in the small domain. In the presentations

"There's plenty of room at the bottom" [1.1] and "Infinitesimal machinery" [1.2], dating from respectively 1967 and 1982, R.P. Feynman described the coming technology of making small things and small scale information. He already anticipated the sacrificial layer method of making silicon micromotors, the use of electrostatic actuation and the importance of friction and stiction [1.3].

Systems with small dimensions have advantages that include speed, accuracy and sensitivity. Improvements with respect to reproducibility and reliability of micromechanical devices are also a direct consequence of the batch processing technique employed in the usual silicon IC manufacturing process. Furthermore, a small system can be built from very expensive materials with desirable properties as the cost of materials scales at the third power with characteristic dimensions. Except for thin film processes, it is quite difficult to determine alternative means of building the structures used in microfabricated actuators that involve well characterised and controlled processes.

Micromechanical devices are used for a wide range of applications covering the field of sensors, actuators and constructive elements. Sensors are normally used for transferring information between the electronic and non-electronic world. Micromechanical sensors are mainly used for the detection of mechanical properties such as pressure, acceleration, force, position or flow. Beyond this, micromechanical structures are used for applications where small size and/or small heat capacity increases the performance of the device with respect to sensitivity, response time, power consumption, etc. Typical examples are chemical sensors, temperature sensors and sensors for the detection of radiation. Up to now, pressure and acceleration sensors are the most advanced micromechanical devices.

Even though miniaturisation of mechanical systems is often compared to the miniaturisation of electronics, one should not assume that all mechanical systems will benefit from miniaturisation. For many mechanical systems such as those in the automotive industry, miniaturisation is not practical. However, even in these cases micromechanical devices for sensing and actuation can often improve the overall performance of the system and are attractive because of the batch processing nature of the technology, which produces devices with a low unit cost. However, it should be noted that the overall costs of a final device are also determined by costs such as application specific packaging, bonding and testing. An implicit advantage of the technology is the ability to make a large number of micromechanical devices on the same substrate. Many applications can benefit from the collective operation of a large number of

devices. For example a silicon optical display using a large array of individually addressable torsional mirrors.

The world market for these micromechanical devices is expected to grow to about 10,000 million ECU in the year 2000 [1.4]. Sensors are dominating the markets, but within this decade actuators will gain importance and are expected to hold about 40% of the market in the year 2000. Micromechanical devices are governing the competitiveness of larger instruments or systems, with a market value of about two orders of magnitude larger, demonstrating the role of micromechanics as a key technology of this decade. During the past decade the need for microactuator technology has been increasingly emphasised, and recent advances in microactuators are transforming the field of solid state tranducers into the field of *Micro Electro Mechanical Systems* (MEMS).

1.1 MICROACTUATORS

In contrast to microsensors, research on microfabricated actuators (microactuators) has been largely neglected. The realisation of micromechanical actuators is generally handicapped by the fact that silicon does not exhibit a direct electromechanical actuation mechanism of itself. Electromechanical signal conversion has to be achieved, therefore, via secondary materials and/or system properties.

Actuators are used for the transformation of non-mechanical input energy into mechanical output energy. Microactuators can be divided into two classes: mechanisms and deformable microstructures. Mechanism-type actuators such as micromotors provide displacement and force through rigid-body motion whereas deformable microstructures such as beams and diaphragms provide displacement and force through mechanical deformations. An important issue, especially related to mechanism type of actuators, is microtribology.

An important step in the progress of microactuator technology is the development of actuation forms that can be implemented with the materials and processing technologies of silicon microelectronics. In addition, the actuation should be powered and controlled electrically in order to be compatible with microelectronics. Despite these stringent requirements, a variety of physical phenomena for microactuator applications have been demonstrated [1.5-1.15].

Microactuators employing electrostatic [1.16-1.90], piezoelectric [1.91-1.103], and magnetic [1.104-1.119] effects have been realised. Also microactuators based on thermal effects such as thermal expansion and bi-metal effects [120-131], thermopneumatic and phase change actuators [1.132-1.141] as well as Shape Memory Alloy actuators [1.142-1.146] have been fabricated. Beside these methods other mechanisms like fluid actuated devices [1.147-1.152], giant magnetostrictive alloy actuators [1.153-1.155], electrochemical actuators [1.156] and mechanochemical actuators [1.157] have also been used. The most commonly used microactuation mechanisms are electromagnetic or thermal. The most notable thermal microactuation methods are bi-metallic, thermopneumatics and SMA and the most important electromagnetic microactuation methods are electrostatic, piezoelectric and magnetic.

The force or torque produced by a specific actuator is equal to its spatial rate of energy conversion. Assuming that equivalent spatial rates can be obtained by the different actuation mechanisms, a comparison of available stored energy provides a reasonable metric for comparison of force and torque. Other factors such as down scaling, speed, power consumption, material issues, fabrication technology, size, integration and application must also be considered when comparing different microactuation methods. Each actuation principle has its own advantages and disadvantages. The choice and the optimisation should be made according to the requirements and applications. Some general considerations will be discussed here which are restricted to thermal and electromagnetic actuators.

Although heating and cooling rates increase with decreasing dimensions, in generally thermal microactuators have a slow response time and a higher power consumption compared to electromagnetic microactuators. Thermal actuation methods are generally more suited for deformable types of microactuators and have been shown to be useful in large deflection and large force actuator applications.

As previously mentioned, important electromagnetic microactuation methods are electrostatic, piezoelectric and magnetic actuation. Magnetic and electrostatic actuation are often employed in microactuators and have been compared by many authors [1.158-1.162]. Although with superconducting magnets very high magnetic fields are feasible, magnetic induction is normally limited to about 1.5 T because of magnetic saturation. The electric breakdown limit in air increases drastically from 3.10^6 V/m for macroscopic air gaps to 10^8 for air gaps on the order of a micrometer. As a result the stored energy densities of magnetic and electrostatic actuation are comparable at micron

scales and are of the order of 10^5 to 10^6 J/m^3.

Efficiency considerations favour electrostatic microactuators over magnetic microactuators. Static excitation of magnetic actuators requires static currents through its windings, leading to persistent conduction losses. However static excitation of electrostatic actuators requires static voltages across gaps which can be essentially lossless. This argument holds as the speed of the actuator increases until reactive power dominates the electrical excitation of the actuator. This should occur at comparable speeds in both types of actuators. Most magnetic actuators contain magnetisable material that will exhibit increasing eddy-current and hysteresis losses as the speed increases.

Typical piezoelectric materials and thin films used in microactuator technology are quartz, zinc oxide (ZnO), lead zirconate titanate (PZT), and polyvinylidene fluoride (PVDF). High energy densities are feasible with PZT. Piezoelectric actuation has been used for deformable types of structures. But piezoelectric motors have also been fabricated that are based on travelling wave ultrasonics, impact drive mechanisms and stick-slip or walking mechanisms where fast vibratory motions are transformed into a slower macroscopic motion.

Generally, the most important factors that have to be considered are the choice of materials and microfabrication techniques. For electrostatic actuators, conductors and insulators are easily available in IC technology, while magnetic or piezoelectric materials are not readily obtainable in integrated circuit processing. Furthermore, piezoelectric materials and soft magnetic materials, hard magnetic materials and magnetic circuit components such as coils are more difficult to implement in micromachining processes. As a result, many electrostatically driven actuators have been developed and realised, and only little actuators have been fabricated employing magnetic or piezoelectric actuation.

Research on microactuators is developing fast and much progress has been made in recent years. One is at the point where micromechanisms are starting to walk [1.50, 1.79, 1.163], swim [1.164] and fly [1.115, 1.165, 1.166].

1.2 ELECTROSTATIC MICROACTUATORS

Electrostatic actuators have a long history dating back to the 18th century when several types of electrostatic motors were built [1.167]. In macroscopic devices electrostatic forces are relatively small and high driving voltages are

needed. For this reason, electrostatic actuation is rarely used in macroscopic devices. In contrast, electrostatic actuation is attractive for microactuators as explained earlier [1.158-1.162]. One of the first applications of electrostatic forces in silicon micromechanism was to bend or tilt micro beams for use in mechanical filters, light modulator arrays and electromechanical switches [1.168].

Electrostatic actuation is based upon attractive or repulsive forces between positive and negative charges. In fig. 1 two conducting parallel plates are shown with equal but opposite charges. The vectors indicate the electric forces acting between the upper and the lower plate. These attractive forces tend to align and pull the plates together. A mechanically unrestrained conducting body with net charge, in an electric field created by stationary external conductors each with fixed total charge, can never be in stable equilibrium. Therefore, a mechanically restraining structure is necessary, like a spring or bearing, in order to obtain a stable electrostatic actuator.

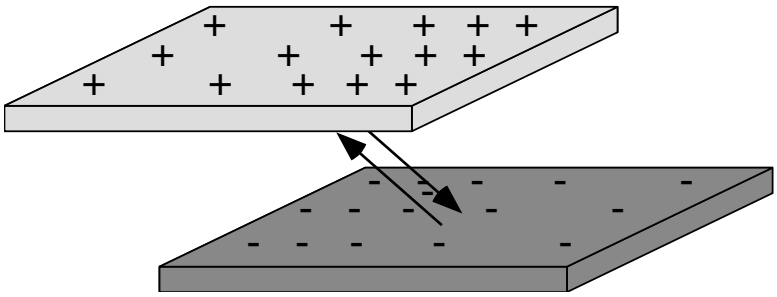

Fig. 1.1 *Electric forces induced by offset charge distributions.*

Several types of electrostatic actuators can be distinguished by the manner in which the rotor charge distribution is defined. For example: a permanent electret motor has a fixed charge embedded in the rotor. An electric hysteresis motor uses hysteresis in the polarisability of the rotor to maintain the proper phase difference between the rotor and stator charge distributions. An electric induction motor is designed in such a way that the charge distribution is induced in a resistive rotor by the stator charge distribution with the proper spatial phase difference maintained by charge relaxation. The rotor charge distribution can also be induced by the stator charge distribution, but its definition and offset can be obtained by geometrical variations in the stator to rotor gap like, for example, saliencies in the highly conductive rotor. Motors based on this principle are called variable capacitance motors.

Electrostatic actuators can be charge or voltage driven. The driving condition is not irrespective with regard to the actuator behaviour. The voltage is in

many cases the most suitable choice for the independent variable because the electrodes define equipotential surfaces making the voltage independent of position. Constant charge conditions can only be guaranteed at terminal level, i.e. global and not local. Constant voltage conditions at terminal level on the other hand also imply constant voltage conditions locally. The electrostatic force or torque acting on a charged body can be calculated from the spatial derivative of the electrostatic energy at constant charge or from the spatial derivative of the electrostatic co-energy at constant voltage.

A variety of electrostatic microactuators employing arrangements such as parallel plate capacitors, interdigitated finger or comb structures and rotor/stator designs have been fabricated.

1.3 FABRICATION TECHNOLOGIES

The processing technology of IC's generally consists of a sequence of planar processes modifying the properties of the semiconductor material and the surface topology within a few micron's depth. The fabrication of most micromechanical devices relies on a three dimensional structuring of the substrate material and or secondary layers deposited on top of the original plane.

Probably the oldest micromachining technique is called bulk micromachining [1.168-1.170]. For bulk micromachining, anisotropic dry and wet etching processes are applied to structure the monocrystalline bulk material. Several silicon etchants, like KOH, EDP and NH_4OH, exhibit a dependency of the etch rate on the crystallographic orientation of single crystal silicon. Using silicondioxide, silicon nitride or metals like e.g. Cr, Au, Ag and Pt as a mask well defined grooves, cavities and mesas bounded by slower etching (111) planes can be etched. Furthermore silicon dopants and electric potential can be used to create etch stop layers. Together with wafer-to-wafer bonding techniques, like anodic bonding and direct bonding, several wafers can be stacked together which results in an increased versatility of the devices that can be fabricated [1.171, 1.172].

In addition to bulk micromachining, surface micromachining techniques have been developed [1.173-1.179]. In surface micromachining structural parts are embedded in layers of a sacrificial material during the fabrication process. The sacrificial material is then etched or dissolved in a chemical etchant that does not attack the structural parts. Polysilicon surface micromachining using

doped or undoped polysilicon as the structural material and silicon dioxide or PSG as the sacrificial layer is the most widely used surface micromachining technique.

Another important fabrication method is LIGA [1.180-1.183]. LIGA techniques are based on X-ray exposure and development of thick resist layers, and subsequent electroplating of metal layers to form the micromechanical structures. After stripping of the resist either a final metal structure or a metal mould insert for subsequent replication processes like injection moulding is obtained. With LIGA techniques very high aspect ratio structures can be obtained with thicknesses ranging up to about one mm and lateral dimensions down to the submicron range.

Besides LIGA other moulding techniques based on UV exposure emerged which are characterised by a lower aspect ratio of around 10, a structural thickness of up to about 100 µm and less dimensional control [1.184-1.189].

Dry fabrication techniques like SCREAM [1.190, 1.191], SIMPLE [1.192] and BSM [1.194] have also been used to fabricate micromechanical structures. These are based upon patterning of the silicon wafer by deep anisotropic etching of silicon, subsequent sidewall passivation and release of the structures by dry isotropic underetching of the silicon wafer.

Combinations of previous techniques are also possible. For example sacrificial layers are also employed in the LIGA technique and recently 3D surface micromachining techniques (HEXSIL) have also been demonstrated. Here small and deep etching grooves in the silicon wafer are used as a mold for the sacrificial layer and are subsequently filled with the structural material [1.194]. After removal of the sacrificial layer 3D structures are obtained and the silicon mold can be recycled for further use. Other examples are a combination of bonding and deep dry etching techniques [1.195, 1.196], the dissolved wafer process where dry anisotropic etching, highly boron doped etch stop techniques, bonding, and wet etching are employed [1.197, 1.198] and DEEMO where deep dry etching of silicon is employed to fabricate a mould for multiple replications [1.199].

1.4 OUTLINE OF THIS THESIS

Conventional microstructures, such as cantilever beams, bridges and diaphragms, are able to move only a limited amout of micrometers perpendicular to the plane of the substrate. This restrained travel in one degree

of freedom has restricted existing microactuators to small motion applications. A flexible microactuator technology requires structures that have unrestrained motion in at least one degree of freedom. Surface micromachining techniques provide this possibility. At the onset of this work only bulk micromachining was used at the MESA Research Institute. A surface micromachining technology needed to be developed and implemented within the existing cleanroom facilities. Polysilicon surface micromachining is the best documented surface micromachining technique to date and has been used in this work. Two central issues in surface micromachining are: the understanding and control of the mechanical properties of microstructural films and the release of the microstructure, for example by wet etching, followed by the drying and surface passivation of the microstructure. Another important fabrication aspect is dimensional control of fabricated structures. The fabrication of electrostatic actuators demands small gaps and compliant or high aspect ratio polysilicon microstructures. This requires anisotropic etching techniques of polysilicon. It was therefore necessary to develop a dry anisotropic etching process based on fluorine chemistry. The resulting surface micromachining technology has been used to fabricate a variety of electrostatically driven actuators.

Current microactuation techniques provide either large motion or high force and torque. For many practical applications both characteristics are needed. In order to extend the possibilities of electrostatic actuators emphasis was given to the design and development of electrostatic actuators that provide relatively large forces and displacements.

In this first chapter a general introduction to micromachining technology and microactuators has been given. Chapters 2-4 deal with technological aspects and in chapters 5-9 emphasis is given to device design and performance of different electrostatic actuators. General conclusions are drawn in chapter 10. Chapter 2 presents an overview of surface micromachining technology with emphasis on polysilicon surface micromachining. The basic fabrication steps are described and material requirements are discussed. Methods to determine the mechanical properties of thin films are summarised. The control of polysilicon mechanical properties, etch characteristics of silicon dioxide in hydrofluoric acid and techniques to prevent stiction of surface micromachined structures are described. Examples of basic surface micromachining processes and some special techniques are given.

In chapter 3 the mechanisms causing stiction of polysilicon structures fabricated by surface micromachining techniques are investigated. A simplified

model is used to show that capillary forces are responsible for bringing micromechanical structures into contact with the underlying substrate. Experimental results obtained from drying experiments are given and compared with the theory. Measured adhesion energies of sticking microbridges after drying are compared with various adhesion mechanisms in order to reveal the origin of the forces.

Chapter 4 describes a study of reactive ion etching of silicon, using $SF_6/O_2/CHF_3$, plasmas in an RF parallel plate system. Surface response methodology is used to examine etch rate, selectivity, anisotropy and self-bias voltage as a function of SF_6 flow, O_2 flow, CHF_3 flow, pressure and the RF power. The effects of the variables on the measured responses are discussed. Examples of anisotropic etching of high aspect ratio structures with smooth etch surfaces are given.

In chapter 5 the design and performance of a curved electrode actuator is presented. Its operation is based on the deformation of a movable micromechanical structure which is deflected by electrostatic forces along a fixed curved electrode. The behaviour of this type of actuator is studied by using cantilever beam structures. A theoretical description of the static behaviour of a deformable cantilever beam that is forced into contact with a rigid structure by means of electrostatic forces is given. Modelling of the static behaviour is done by a simplified model based on energy methods and by 3D coupled electromechanical simulations using CoSolve-EM. Experiments are performed in order to verify theoretical results.

Chapter 6 presents the design, fabrication and experimental results of lateral comb-drive actuators for large displacements at low driving voltages. Several suspension designs are compared with respect to large deflection behaviour. The electromechanical behaviour of comb-drive actuators is considered with respect to large deflection behaviour. Static and dynamic properties are determined experimentally and are compared with theory.

Chapter 7 presents the design, modelling, fabrication and first performance characteristics of electrostatically driven axial-gap polysilicon wobble motors. Aspects like the gear ratio, torque generation, excitation schemes and torque coverage, normal forces, friction, rotor kinetics and dynamical behaviour are addressed. The motor performance is characterised by gear ratio measurements and measuring starting and stopping voltages.

In chapter 8 a surface micromachining process is presented that has been used for the fabrication of electrostatic microactuators which are connected with eachother and linked to other movable microstructures by integrated gear

linkages. The gear linkages consist of rotational and linear gear structures and the electrostatic microactuators include curved electrode actuators, comb drive actuators and axial gap wobble motors. It is a first step towards mechanical power transmission in micromechanical systems.

In chapter 9 basic design issues and a fabrication process based on surface micromachining techniques for electrostatically driven vacuum encapsulated polysilicon resonators are presented. Experimental results, including an admittance plot of the one-port resonator and a plot indicating the dependence of the *Q*-factor on the resonator geometry and ambient pressure are presented.

Finally in chapter 10 general conclusions are drawn and suggestions for further research are given.

REFERENCES

[1.1] R.P. Feynman, There's plenty of room at the bottom, Journal of microelectromechanical systems, Vol. 1, 1992, pp. 60-66.

[1.2] R.P. Feynman, Infitesimal machinery, Journal of microelectromechanical systems, Vol. 2, 1993, pp. 4-14.

[1.3] S.D. Senturia, Feynman revisited, Proc. IEEE Micro Electro Mechanical Systems, Oiso, Japan, Jan. 25-28, 1994, pp. 309-312.

[1.4] G. Tschulena, Micromechanics business opportunities, Proc. 3rd Int. Conf. on micro electro, opto, mechanic systems and components, Berlin, October 21-23, 1992, pp. 51-57.

[1.5] R.S. Muller, From IC's to microstructures: materials and technologies, Proc. IEEE Micro Robots and Teleoperators Workshop, Hyannis, MA, U.S.A., Nov. 9-11, 1987. , pp. 1-5.

[1.6] W.S.N. Trimmer, Microrobots and Micromechanical systems, Sensors and Actuators, 19, 1989, pp. 267-287.

[1.7] W. Benecke, Silicon micromachining for microsensors and microactuators, Microelectronic Engineering, Vol. 11, 1990, pp. 73-82.

[1.8] R. S. Muller, Microdynamics, Sensors and Actuators, A21-A23, 1990, pp. 1-8.

[1.9] K.D. Wise, Integrated microelectromechanical systems: A perspective on MEMS in the 90s, Proc. IEEE Micro Electro Mechanical Systems, Nara, Japan, Jan. 30-Feb. 2, 1991, pp. 33-38.

[1.10] H. Fujita and K.Gabriel, New opportunities for micro actuators, Proc. 6th Int. Conf. Solid-State Sensors and Actuators (Transducers '91), San Fransisco, CA, USA, June 24-27, pp. 14-20.

[1.11] W. Benecke, Silicon microactuators: activation mechanisms and scaling problems, Proc. 6th Int. Conf. Solid-State Sensors and Actuators (Transducers '91), San Fransisco, CA, USA, June 24-27, pp. 46-50.

[1.12] P. Dario, R. Valleggi, M.C. Carrozza, M.C. Montesi and M. Cocco, Microactuators for microrobots: a critical survey, J. Micromech. Microeng. , Vol. 2, 1992, pp. 141-157.

[1.13] M. Mehregany, Microelectromechanical Systems, IEEE Circuits and Devices Magazine, Vol. 9, 1993, pp. 14-22.

[1.14] T. Hayashi, Micromechanism and their characteristics, Proc. IEEE Micro Electro Mechanical Systems, Oiso, Japan, Jan. 25-28, 1994, pp. 39-44.

[1.15] H. Fujita, Recent progress of microactuators and micromotors, Microsystem Technologies, Vol. 1, 1995, pp. 93-97.

[1.16] H. C. Nathanson, W. E. Newell, R. A. Wickstrom and J.R. Davis jr., The resonant gate transistor, IEEE Trans. on El. Dev., ED-14 (1967), pp. 117-133.

[1.17] H.Fujita and A. Omodaka, The fabrication of an electrostatic linear actuator by silicon micromachining, IEEE Trans. on El. Devices, Vol. 35, 1988, pp. 731-734.

[1.18] Electrostatic-comb drive of lateral polysilicon resonators, W.C. Tang, T.C.H. Nguyen, M.W. Judy and R.T. Howe, Proc. 5th Int. Conf. Solid-State Sensors and Actuators (Transducers '89), Montreux, Switzerland, June 25-30, 1989, pp. 328-331.

[1.19] Y.C. Tai, L.S. Fan and R.S. Muller, IC-processed micro-motors: design, technology and testing, Proc. IEEE Micro Electro Mechanical Systems, Salt Lake City, Utah, U.S.A., Feb. 20-22, 1989, pp. 1-6.

[1.20] R. Jebens, W. Trimmer and J. Walker, Microactuators for aligning optical fibers, Sensors and Actuators, 20, 1989, pp. 65-73.

[1.21] M. Mehregany, S.F. Bart, L.S. Tavrow, J.H. Lang, S.D. Senturia and M.F. Schlecht, A study of three microfabricated variable-capacitance motors, Proc. 5th Int. Conf. Solid-State Sensors and Actuators (Transducers '89), Montreux, Switzerland, June 25-30, 1989, pp. 173-179.

[1.22] L.S. Tavrow, S.F. Bart, J.H. Lang and M.F. Schlecht, A LOCOS process for an electrostatic microfabricated motor, Proc. 5th Int. Conf. Solid-State Sensors and Actuators (Transducers '89), Montreux, Switzerland, June 25-30, 1989, pp. 893-898.

[1.23] R. Mahadevan, K.J. Gabriel and Mehregany, Application of electric microactuators to silicon micromechanics, Proc. 5th Int. Conf. Solid-State Sensors and Actuators (Transducers '89), Montreux, Switzerland, June 25-30, 1989, pp. 219-225.

[1.24] R.A. Brennen, M.G. Lim, A.P. Pisano and A.T. Chou, Large displacement linear actuator, Proc. IEEE Solid-State Sensors and Actuators Workshop, Hilton Head Island, SC, U.S.A. June 4-7, 1990, pp. 135-139.

[1.25] S. Egawa and T. Higuchi, Multi-layered electrostatic film actuator, Proc. IEEE Micro Electro Mechanical Systems, Napa Valley, CA, U.S.A., Feb. 11-14, 1990, pp. 166-171.

[1.26] K.S.J. Pister, R.S. Fearing and R.S. Howe, A planar air levitated electrostatic actuator system, Proc. IEEE Micro Electro Mechanical Systems, Napa Valley, CA, U.S.A., Feb. 11-14, 1990, pp. 67-71.

[1.27] W.C. Tang, M.G. Lim and R.T. Howe, Electrostatically balanced comb drive for controlled levitation, Proc. IEEE Solid-State Sensors and Actuators Workshop, Hilton Head Island, SC, U.S.A. June 4-7, 1990, pp. 23-27.

[1.28] R.A. Brennen, A.P. Pisano and W.C. Tang, Multiple mode micromechanical resonators, Proc. IEEE Micro Electro Mechanical Systems, Napa Valley, CA, U.S.A., Feb. 11-14, 1990, pp. 9-14.

[1.29] S. Nakagawa, S. Shoji and M. Esashi, Micromachined silicon microvalve, Proc. IEEE Micro Electro Mechanical Systems, Napa Valley, CA, U.S.A., Feb. 11-14, 1990, pp. 95-98.

[1.30] P.L. Bergstrom, T. Tamagawa and D.L. Polla, Design and fabrication of micromechanical logic elements, Proc. IEEE Micro Electro Mechanical Systems, Napa Valley, CA, U.S.A., Feb. 11-14, 1990, pp. 15-20.

[1.31] M. Mehregany, P. Nagarkar, S.D. Senturia and J.H. Lang, Operation of microfabricated harmonic and ordinary side-drive motors, Proc. IEEE Micro Electro Mechanical Systems, Napa Valley, CA, U.S.A., Feb. 11-14, 1990, pp. 1-8.

[1.32] M. Mehregany, S.M. Philips, E.T. Hsu and J.H. Lang, Operation of harmonic side-drive micromotors studied through gear ratio measurements, Proc. 6th Int. Conf. Solid-State Sensors and Actuators (Transducers '91), San Fransisco, CA, USA, June 24-27, pp. 59-62.

[1.33] L.S. Tavrow, S.F Bart and J.H. Lang, Operational characteristics of microfabricated electric motors, Proc. 6th Int. Conf. Solid-State Sensors and Actuators (Transducers '91), San Fransisco, CA, USA, June 24-27, pp. 877-881.

[1.34] N. Takeshima, K. J. Gabriel, M. Ozaki, J. Takahasji, H. Horiguchi and H. Fujita, Electrostatic parallelogram actuators, Proc. 6th Int. Conf. Solid-State Sensors and Actuators (Transducers '91), San Fransisco, CA, USA, June 24-27, 1991, pp. 63-66.

[1.35] P. Gunther, SiO_2 electrets for electric-field generation in sensors and actuators, Sensors and Actuators, Vol. A32, 1992, pp. 357-360.

[1.36] K.J. Gabriel, O. Tabata, K. Shimaoka, S. Sugiyama and H. Fujita, Surface-normal electrostatic / pneumatic actuator, Proc. IEEE Micro Electro Mechanical Systems, Travemünde, Germany, Feb. 4-7, 1992, pp. 128-132.

[1.37] U. Breng, T. Gessner, C. Kaufmann, R. Kienscherf and J. Markert, Electrostatic micromechanic actuators, Journal of Micromechanics and Microengineering, Vol. 2, 1992, pp. 256-262.

[1.38] V.P. Jaecklin, C. Linder, N.F. de Rooy and J.M. Moret, Micromechanical comb actuators with low driving voltage, J. Micromech. Microeng., Vol. 2, 1992, pp. 250-255.

[1.39] T. Hirano, T. Furuhata, K.J. Gabriel and H. Fujita, Design, fabrication and operation of sub-micron gap electrostatic comb-drive actuators, Journal of Microelectromechanical Systems, Vol. 1, No. 1, March 1992, pp. 52-59.

[1.40] K. Sato and M. Shikida, Electrostatic film actuator with large vertical displacement, Proc. IEEE Micro Electro Mechanical Systems, Travemunde, Germany, February 4-7, 1992, pp. 1-5.

[1.41] C.J. Kim, A.P. Pisano and R.S. Muller, Overhung electrostatic micro gripper, Journal of Microelectromechanical Systems, Vol. 1, No. 1, March 1992, pp. 31-36.

[1.42] J. Branebjerg and P. Gravesen, A new electrostatic actuator providing improved stroke length and force, Proc. IEEE Micro Electro Mechanical Systems, Travemunde, Germany, February 4-7, 1992, pp. 6-11.

[1.43] A.P. Lee and A.P. Pisano, Polysilicon angular microvibromotors, Journal of Microelectromechanical Systems, Vol. 1, No. 2, June 1992, pp. 70-76.

[1.44] W.C. Tang, M.G. Lim and R.T. Howe, Electrostatic comb drive levitation and control method, Journal of Microelectromechanical Systems, Vol. 1, No. 4, Dec. 1992, pp. 170-178.

[1.45] U. Breng, C. Kaufmann, R. Kiehnscherf, J. Markert and M. Rauch, Electrostatic micromechanic actuators, 3rd Int Conf. on New Actuators (Actuator '92), Bremen, Germany, 24-26 June, 1992, pp. 177-182.

[1.46] V.P. Jaecklin, C. Linder, N.F. de Rooij, J.M. Moret, R. Bischot and F. Rudolf, Novel polysilicon comb actuators for xy-stages, Proc. IEEE Micro Electro Mechanical Systems, Travemünde, Germany, Feb. 4-7, 1992, pp. 147-149.

[1.47] N. Tirole, D. Hauden, P. Blind, M. Froelicher and L. Gaudriot, 3D silicon electrostatic microactuator, Journal of Micromechanics and Microengineering, Vol. 3, 1993, pp. 155-157.

[1.48] M. Yamaguchi, S. Kawamura, K Minami and M Esashi, Distributed electrostatic micro actuator, Proc. IEEE Micro Electro Mechanical Systems, Fort Lauderdale, Florida, U.S.A., February 7-10, 1993, pp. 18-23.

[1.49] V.P. Jaecklin, C. Linder, N.F. de Rooij, Comb actuators for xy-microstages, Sensors and Actuators, Vol. A 39, 1993, pp. 83-89.

[1.50] T. Akiyama and K. Shono, Controlled stepwise motion in polysilicon microstructures, Journal of Microelectromechanical Systems, Vol. 2, No. 3, Sept. 1993, pp. 106-110.

[1.51] T. Niino, S. Egawa and T. Higuchi, High-power and high-efficiency electrostatic actuator, Proc. IEEE Micro Electro Mechanical Sytems, Fort Lauderdale, Fl, U.S.A., February 7-10, 1993, pp. 236-241.

[1.52] T. Hirano, T. Furuhata and H. Fujita, Dry released Nickel micromotors and their friction characteristics, Proc. 7th Int. Conf. Solid-State Sensors and Actuators (Transducers '93), Yokohama, Japan, June 7-10, pp. 80-83.

[1.53] L.Y. Chen, E.J.P. Santos and N.C. MacDonald, Serial-parallel isolated capacitive microactuators, Proc. 7th Int. Conf. Solid-State Sensors and Actuators (Transducers '93), Yokohama, Japan, June 7-10, pp. 84-87.

[1.54] G. Fuhr and B. Wagner, Surface-charge induction micromotors with two aluminium rotors isolated by SiO_2, Proc. 7th Int. Conf. Solid-State Sensors and Actuators (Transducers '93), Yokohama, Japan, June 7-10, pp. 88-92.

[1.55] A.P. Lee, A.P. Pisano and D.J. Nikkel, Polysilicon linear microvibromotors, Proc. 7th Int. Conf. Solid-State Sensors and Actuators (Transducers '93), Yokohama, Japan, June 7-10, pp. 46-49.

[1.56] T. Matsubara, M. Yamaguchi, K. Minami and M. Esashi, Stepping electrostatic microactuator, Proc. 7th Int. Conf. Solid-State Sensors and Actuators (Transducers '93), Yokohama, Japan, June 7-10, pp. 50-53.

[1.57] V.P. Jaecklin, C. Linder, N.F. deRooij, J.M. Moret and R. Vuilleumier, Optical microshutters and torsional micromirrors for ligth modulator arrays, Proc. IEEE Micro Electro Mechanical Systems, Ford Lauderdale, Florida, U.S.A., Feb. 7-10, 1993, pp. 124-127.

[1.58] V.P. Jaecklin, C. Linder, J. Brugger and N.F. deRooij, Mechanical and optical properties of surface micromachined torsional mirrors in silicon, polysilicon and aluminum, Proc. 7th Int. Conf. Solid-State Sensors and Actuators (Transducers '93), Yokohama, Japan, June 7-10, pp. 958-961.

[1.59] K. Aratani, P.J. French, P.M. Sarro, R.F. Wolffenbuttel and S. Middelhoek, Surface micromachined tunable interferometer array, Proc. 7th Int. Conf. Solid-State Sensors and Actuators (Transducers '93), Yokohama, Japan, June 7-10, pp. 678-681.

[1.60] J.B. Sampsell, The digital micromirror device and its application to projection displays, Proc. 7th Int. Conf. Solid-State Sensors and Actuators (Transducers '93), Yokohama, Japan, June 7-10, pp. 24-27.

[1.61] E. Obermeier, J. Lin and V. Schlichting, Design and Fabrication of an electrostatically driven micro-shutter, Proc. 7th Int. Conf. Solid-State Sensors and Actuators (Transducers '93), Yokohama, Japan, June 7-10, pp. 132-137.

[1.62] O. Tabata, R. Asahi, N. Fujitsuka, M. Kimura and S. Sugiyama, Electrostatic driven optical chopper using SOI, Proc. 7th Int. Conf. Solid-State Sensors and Actuators (Transducers '93), Yokohama, Japan, June 7-10, pp. 124-127.

[1.63] J. Bernstein, A.T. King, A. Kourepenis, P. Maciel and M. Weinberg, A micromachined comb-drive tuning fork rate gyroscope, Proc. IEEE Micro Electro Mechanical Systems, Ford Lauderdale, Florida, U.S.A., Feb. 7-10, 1993, pp. 143-148.

[1.64] J.W. Judy, T. Tamagawa and D.L. Polla, Surface-machined micromechanical membrane pump, Proc. IEEE Micro Electro Mechanical Systems, Ford Lauderdale, Florida, U.S.A., Feb. 7-10, 1993, pp. 182-186.

[1.65] S.M. Bobbio, M.D. Kellam, B.W. Dudley, S. Goodwin-Johansson, S.K. Jones, J.D. Jacobson, F.M. Tranjan and T.D. DuBois, Integrated force arrays, Proc. IEEE Micro Electro Mechanical Systems, Ford Lauderdale, Florida, U.S.A., Feb. 7-10, 1993, pp. 149-154.

[1.66] J. Schimkat, L. Kiesewetter, H.J. Gevatter, F. Arndt, A. Steckenborn and H.F. Schlaak, Moving wedge actuator: An electrostatic actuator for use in microrelay, Proc. 4th Int. Conf. and Exhibition on Micro Electro, Opto, Mechanical Systems and Components (Actuator '94), Berlin, Germany, October 19-21, 1994, pp. 989-996.

[1.67] H. Guckel, T.R. Christenson, T. Earles, K.J. Skrobis and J. Klein, Processing and design considerations for high force output-large throw electrostatic, linear micro actuators, 4th Int Conf. on New Actuators (Actuator '94), Bremen, Germany, 15-17 June, 1994, pp. 105-108.

[1.68] H. Kalb, B. Kowanz, W. Bacher, J. Mohr and R. Ruprecht, Electrostatically driven linear stepping motor in LIGA technique, 4th Int Conf. on New Actuators (Actuator '94), Bremen, Germany, 15-17 June, 1994, pp. 83-85.

[1.69] K. Deng and M. Mehregany, Outer-rotor polysilicon wobble micromotors, Proc. IEEE Micro Electro Mechanical Systems, Oiso, Japan, Jan. 25-28, 1994, pp. 269-272.

[1.70] K. Deng, H. Miyajima, V.H. Dhuler, M. Mehregany, S.W. Smith, F.L. Merit and S. Furukawa, The development of polysilicon micromotors for optical scanner applications, Proc. IEEE Solid-State Sensors and Actuators Workshop, Hilton Head Island, SC, U.S.A., June 13-16, 1994, pp. 234-238.

[1.71] R.B. Apte, F.S.A. Sandejas, W.C. Banyai and D.M. Bloom, Deformable grating ligth valves for high resolution displays, Proc. IEEE Solid-State Sensors and Actuators Workshop, Hilton Head Island, SC, U.S.A., June 13-16, 1994, pp. 1-6.

[1.72] P.Y. Chen and R.S. Muller, Microchopper-modulated IR microlamp, Proc. IEEE Solid-State Sensors and Actuators Workshop, Hilton Head Island, SC, U.S.A., June 13-16, 1994, pp. 239-242.

[1.73] C. W. Stroment, D. A. Borkholder, V. A. Westerlind, J. W. Suh, N. I. Maluf and G. T. A. Kovacs, Dry-released process for aluminum electrostatic actuators, Proc. Solid-State Sensor and Actuator Workshop, Hilton Head Island, SC, U. S. A., June 13-16, 1994, pp. 95-98.

[1.74] M. Fischer, H. Graaf and W. von Münch, Electrostatically deflectable polysilicon torsional mirrors, Sensors and Actuators, Vol. A 44, 1994, pp. 83-89.

[1.75] R. Zengerle, S. Kluge, M. Richter and A. Richter, A bidirectional silicon micropump, Proc. IEEE Micro Electro Mechanical Systems, Amsterdam, The Netherlands, Jan. 29-Feb. 2, 1995, pp. 19-24.

[1.76] A.A. Yasseen, S.W. Smith, M. Mehregany and F.L. Merat, Diffraction grating scanners using polysilicon micromotors, Proc. IEEE Micro Electro Mechanical Systems, Amsterdam, The Netherlands, Jan. 29-Feb. 2, 1995, pp. 175-180.

[1.77] P.F. Indermuhle, V.P. Jaecklin, J. Brugger, C. Linder, N.F. De Rooij and M. Binggeli, AFM imaging with an xy-micropositioner with integrated tip, Sensors and Actuators, A47, 1995, pp. 562-565.

[1.78] A. Selvakumar, K. Najafi. W.H. Juan and S. Pang, Vertical comb array microactuators, Proc. IEEE Micro Electro Mechanical Systems, Amsterdam, The Netherlands, Jan. 29-Feb. 2, 1995, pp. 43-47.

[1.79] T. Akiyama and H. Fujita, A quantitative analysis of scratch drive actuator using buckling motion, Proc. IEEE Micro Electro Mechanical Systems, Amsterdam, The Netherlands, Jan. 29-Feb. 2, 1995, pp. 310-315.

[1.80] P. Rangsten, L. Smith, L. Rosengren and B. Hök, Electrostatically excited diaphragm driven as a loudspeaker, Proc. 8th Int. Conf. Solid-State Sensors and Actuators (Transducers '95), Stockholm, Sweden, June 25-29, 1995, Vol. 1, pp. 430-433.

[1.81] L.S. Fan, S. Woodman, T.C. Reiley, H.H. Zappe and T. Furuhata, Batch fabrication of mechanical platforms for high density data storage, Proc. 8th Int. Conf. Solid-State Sensors and Actuators (Transducers '95), Stockholm, Sweden, June 25-29, 1995, Vol. 1, pp. 434-437.

[1.82] S.G. Adams, F.M. Bertsch, K.A. Shaw, P.G. Hartwell, N.C. MacDonald and F.C. Moon, Capacitance based tunable micromechanical resonators, Proc. 8th Int. Conf. Solid-State Sensors and Actuators (Transducers '95), Stockholm, Sweden, June 25-29, 1995, Vol. 1, pp. 438-441.

[1.83] M.T.A. Saif and N.C. MacDonald, A milli Newton micro loading device, Proc. 8th Int. Conf. Solid-State Sensors and Actuators (Transducers '95), Stockholm, Sweden, June 25-29, 1995, Vol. 2, pp. 60-63.

[1.84] J. Drake, H. Jerman, B. Lutze and M. Stuber, An electrostatically actuated micro-relay, Proc. 8th Int. Conf. Solid-State Sensors and Actuators (Transducers '95), Stockholm, Sweden, June 25-29, 1995, Vol. 2, pp. 380-383.

[1.85] J.J. Yao and M.F. Chang, A surface micromachined miniature switch for telecommunications applications with signal frequencies from DC up to 4 GHz, Proc. 8th Int. Conf. Solid-State Sensors and Actuators (Transducers '95), Stockholm, Sweden, June 25-29, 1995, Vol. 2, pp. 384-387.

[1.86] J.J. Sniegowski and C. Smith, An application of mechanical leverage to microactuation, Proc. 8th Int. Conf. Solid-State Sensors and Actuators (Transducers '95), Stockholm, Sweden, June 25-29, 1995, Vol. 1, pp. 364-367.

[1.87] E.J. Garcia and J.J. Sniegowski, Surface micromachined microengine as the driver for micromechanical gears, Proc. 8th Int. Conf. Solid-State Sensors and Actuators (Transducers '95), Stockholm, Sweden, June 25-29, 1995, Vol. 2, pp. 365-368.

[1.88] R. Legtenberg, E. Berenschot, M. Elwenspoek and J. Fluitman, Electrostatic curved electrode actuators,Proc. IEEE Micro Electro Mechanical Systems, Amsterdam, The Netherlands, Jan. 29-Feb. 2, 1995, pp. 37-42.

[1.89] R. Legtenberg, E. Berenschot, T. Lammerink and M. Elwenspoek, An electrostatic axial gap wobble motor, Proc. 8th Int. Conf. Solid-State Sensors and Actuators (Transducers '95), Stockholm, Sweden, June 25-29, 1995, Vol. 2, pp. 404-407.

[1.90] R. Legtenberg, A.W.Groeneveld and M. Elwenspoek, Towards position control of electrostatic comb drives, Proc. 6th European workshop on micromachining, micromechanics and microsystems (MME '95), Copenhagen, Denmark, Sept. 3-5, 1995, pp. 124-127.

[1.91] H.T.G. van Lintel, F.C.M. van de Pol and S. Bouwstra, A piezoelectric micropump based on micromachining of silicon, Sensors and Actuators, Vol. 15, 1988, pp. 153-167.

[1.92] W.P. Robbins, D.L Polla, T. Tamagawa, D.E. Glumac and J.W. Judy, Linear motion microactuators using piezoelectric thin films, Proc. Int. Conf. on Solid-State Sensors and Actuators, (Transducers '91), San Fransisco, CA, U. S. A., June 24-27, 1991, pp. 55-58.

[1.93] A.M. Flynn, L.S. Tavrow, S.F. Bart, R.A. Brooks, D.J. Ehrlich, K.R. Udayakumar and L.E. Cross, Piezoelectric micromotors for microrobots, Journal of microelectromechanical systems, Vol. 1, 1992, pp. 44-51.

[1.94] D.E. Brei and J. Blechschmidt, Design and static modeling of a semiconductor polymeric piezoelectric microactuator, Journal of Microelectromechanical Systems, Vol. 1, 1992, pp. 106-115.

[1.95] T. Yasuda, I. Shimoyama and H. Miura, Microrobot actuated by a vibrating energy field, Proc. 7th Int. Conf. Solid-State Sensors and Actuators (Transducers '93), Yokohama, Japan, June 7-10, pp. 42-45.

[1.96] G.A. Racine, R. Luthier and N.F. de Rooij, Hybrid ultrasonic micromachined motors, Proc. IEEE Micro Electro Mechanical Systems, Ford Lauderdale, Florida, U.S.A., Feb. 7-10, 1993, pp. 128-132.

[1.97] H. Toshiyoshi, H. Fujita, T. Kawai and T. Ueda, Piezoelectrically operated actuators by quartz micromachining for optical application, Proc. IEEE Micro Electro Mechanical Systems, Ford Lauderdale, Florida, U.S.A., Feb. 7-10, 1993, pp. 133-142.

[1.98] P. Schiller and D.L. Polla, Integrated piezoelectric microactuators based on PZT thin films, Proc. 7th Int. Conf. Solid-State Sensors and Actuators (Transducers '93), Yokohama, Japan, June 7-10, pp. 154-157.

[1.99] P. Dario, M.C. Carrozza, N. Gracew and B. Magnani, A piezoelectric micropump realized by stereolithography, 4th Int Conf. on New Actuators (Actuator '94), Bremen, Germany, 15-17 June, 1994, pp. 42-45.

[1.100] H. Toshiyoshi, D. Kobayashi, H. Fujita and T. Ueda, A piezoelectric pseudo-static actuator for large displacement under ac voltage operation, Proc. 8th Int. Conf. Solid-State Sensors and Actuators (Transducers '95), Stockholm, Sweden, June 25-29, 1995, Vol. 1, pp. 389-392.

[1.101] P. Muralt, A. Kholkin, M. Kohli, T. Maeder, K.G. Brooks, R. Luthier and N. Setter, Fabrication and characterization of PZT films for micromotors, Proc. 8th Int. Conf. Solid-State Sensors and Actuators (Transducers '95), Stockholm, Sweden, June 25-29, 1995, Vol. 1, pp. 397-400.

[1.102] M. Sakata, S. Wakabayashi, H. Totani, M. Ikeda, H. Goto, M. Takeuchi and T. Yada, Basic characteristics of a piezoelectric buckling type of actuator, Proc. 8th Int. Conf. Solid-State Sensors and Actuators (Transducers '95), Stockholm, Sweden, June 25-29, 1995, Vol. 1, pp. 422-425.

[1.103] M. Mescher, T. Abe, B. Brunett, H. Metla, E. Schlesinger and M.L. Reed, Piezoelectric Lead Zirconate Titanate actuator films for microelectromechanical systems applications, Proc. IEEE Micro Electro Mechanical Systems, Amsterdam, The Netherlands, Jan. 29-Feb. 2, 1995, pp. 261-266.

[1.104] K. Yanagisawa, A. Tago, T. Ohkubo and H. Kuwano, Magnetic micro-actuator, Proc. IEEE Micro Electro Mechanical Systems, Nara, Japan, Jan. 30-Feb. 2,1991, pp. 120-124.

[1.105] B. Wagner, M. Kreutzer and W. benecke, Electromagnetic microactuators with multiple degrees of freedom, Proc. 6th Int. Conf. Solid-State Sensors and Actuators (Transducers '91), San Fransisco, CA, USA, June 24-27, pp. 614-617.

[1.106] B. Wagner, W. Benecke, G. Engelmann and J. Simon, Microactuators with moving magnets for linear, torsional or multiaxial motion, Sensors and Actuators, Vol. A32, 1992, pp. 598-603.

[1.107] C.H. Ahn and M.G. Allen, A fully integrated surface micromachined magnetic

microactuator with a multilevel meander magnetic core, Journal of Microelectromechanical Systems, Vol. 2, 1993, pp. 15-22.

[1.108] K. Yanagisawa, H. Kuwano and A Tago, An electromagnetivally driven microvalve, Proc. 7th Int. Conf. Solid-State Sensors and Actuators (Transducers '93), Yokohama, Japan, June 7-10, pp. 102-105.

[1.109] H. Guckel, T.R. Christenson, K.J. Skrobis, T.S. Jung, J. Klein, K.V. Hartojo and I. Widjaja, A first functional current excited planar rotational magnetic micromotor, Proc. IEEE Micro Electro Mechanical Systems, Ford Lauderdale, Florida, U.S.A., Feb. 7-10, 1993, pp. 7-11.

[1.110] C.H. Ahn and M.G.Allen, A planar micromachined spiral inductor for integrated magnetic microactuator applications, Journal of Micromechanics and Microengineering, Vol. 3, 1993, pp. 37-44.

[1.111] D. Bosch, B. Heimhofer, G. Muck, H. Seidel, U. Thumser and W. Welser, A silicon microvalve with combined electromagnetic/electrostatic actuation, Sensors and Actuators, A37-A38, 1993, pp. 684-692.

[1.112] C. Liu, T Tsao, Y.C. Tai and C.M. Ho, Surface micromachined magnetic actuators, Proc. IEEE Micro Electro Mechanical Systems, Oiso, Japan, Jan. 25-28, 1994, pp. 57-62.

[1.113] H. Guckel, T. Christenson, T. Earles, K. Skrobis, D. Zook and T. Ohnstein, Electromagnetic, spring constrained linear actuator with large throw, 4th Int Conf. on New Actuators (Actuator '94), Bremen, Germany, 15-17 June, 1994, pp. 52-55.

[1.114] B. Lochel, A. Maciossek, H.J. Quenzer, B. Wagner and G. Engelmann, Magnetically driven microstructures fabricated with multilayer electroplating, Sensors and Actuators, A46, 1995, pp. 98-104.

[1.115] K.I. Arai, W. Sugawara and T. Honda, Magnetic small flying machines, Proc. 8th Int. Conf. Solid-State Sensors and Actuators (Transducers '95), Stockholm, Sweden, June 25-29, 1995, Vol. 1, pp. 316-319.

[1.116] B. Rogge, J. Schultz, J. Mohr, A. Thommes and W. Menz, Fully batch fabricated magnetic microactuators using a two layer LIGA process, Proc. 8th Int. Conf. Solid-State Sensors and Actuators (Transducers '95), Stockholm, Sweden, June 25-29, 1995, Vol. 1, pp. 320-321.

[1.117] H. Guckel, T. Earles, J. Klein, D. Zook and T. Ohnstein, Electromagnetic linear actuators with inductive position sensing for micro relay, micro valve and precision positioning applications, Proc. 8th Int. Conf. Solid-State Sensors and Actuators (Transducers '95), Stockholm, Sweden, June 25-29, 1995, Vol. 1, pp. 324-327.

[1.118] J.W. Judy and R.S. Muller, Magnetic microactuation of torsional polysilicon structures, Proc. 8th Int. Conf. Solid-State Sensors and Actuators (Transducers '95), Stockholm, Sweden, June 25-29, 1995, Vol. 1, pp. 332-335.

[1.119] C.H. Ahn and M.G.Allen, Fluid micropumps based on rotary magnetic actuators, Proc. IEEE Micro Electro Mechanical Systems, Amsterdam, The Netherlands, Jan. 29-Feb. 2, 1995, pp. 408-412.

[1.120] W. Benecke and W. Riethmuller, Applications of silicon microactuators based on bimorph structures, Proc. IEEE Micro Electro Mechanical Systems, Salt Lake City, Utah, U.S.A., Feb. 20-22, 1989, pp. 116-120.

[1.121] M. Parameswaran, L. Ristic, K. Chau, A.M. Robinson and W. Allegretto, CMOS electrothermal microactuators, Proc. IEEE Micro Electro Mechanical Systems, Napa Valley, CA, U.S.A., Feb. 11-14, 1990, pp. 128-131.

[1.122] Q. Dong, W. Benecke and H. Schliwinski, SiO_n-Au double layer microactuator fabrication, Microelectronic Engineering, Vol. 15, 1991, pp. 415-418.

[1.123] M. Ataka, A. Omodaka, N. Takeshima and H. Fujita, Fabrication and operation of polyimide bimorph actuators for a ciliary motion system, Journal of Microelectromechanical Systems, Vol. 2, 1993, pp. 146-150.

[1.124] B. Rashidian and M.G. Allen, Electrothermal microactuators based on dielectric loss heating, Proc. IEEE Micro Electro Mechanical Systems, Ford Lauderdale, Florida, U.S.A., Feb. 7-10, 1993, pp. 24-29.

[1.125] W.H. Chu, M. Mehregany and R.L. Mullen, Analysis of tip deflection and force of a bimetallic cantilever microactuator, Journal of Micromechanics and Microengineering, Vol. 3, 1993, pp. 4-7.

[1.126] T. Lisec, S. Hoerschelmann, H.J. Quenzer and B. Wagner, A fast switching silicon valve for pneumatic control systems, 4th Int Conf. on New Actuators (Actuator '94), Bremen, Germany, 15-17 June, 1994, pp. 30-33.

[1.127] H. Matoba and T. Ishikawa, A bistable snapping microactuator, Proc. IEEE Micro Electro Mechanical Systems, Oiso, Japan, Jan. 25-28, 1994, pp. 45-50.

[1.128] P.W. Barth, Silicon microvalves for gas flow control, Proc. 8th Int. Conf. Solid-State Sensors and Actuators (Transducers '95), Stockholm, Sweden, June 25-29, 1995, Vol. 2, pp. 276-279.

[1.129] H.J. Quenzer, A. Maciossek, B. Wagner and H. Pott, Surface micromachined metallic microactuator with buckling characteristics, Proc. 8th Int. Conf. Solid-State Sensors and Actuators (Transducers '95), Stockholm, Sweden, June 25-29, 1995, Vol. 1, pp.128-131.

[1.130] J. Franz, H. baumann and H.P. Trah, A silicon microvalve with integrated flow sensor, Proc. 8th Int. Conf. Solid-State Sensors and Actuators (Transducers '95), Stockholm, Sweden, June 25-29, 1995, Vol. 2, pp. 313-316.

[1.131] C.G. Keller and R.T. Howe, Nickel-filled HEXSIL thermally actuated tweezers, Proc. 8th Int. Conf. Solid-State Sensors and Actuators (Transducers '95), Stockholm, Sweden, June 25-29, 1995, Vol. 2, pp. 376-379.

[1.132] F.C.M. van de Pol, H.T.G. van Lintel, M. Elwenspoek and J.H.J. Fluitman, A thermo-pneumatic micropump based on micro-engineering techniques, Sensors and Actuators, Vol. A21-A23, 1990, pp. 198-202.

[1.133] L. Lin, A.P. Pisano and A.P. Lee, Microbubble powered actuator, Proc. 6th Int. Conf. Solid-State Sensors and Actuators (Transducers '91), San Fransisco, CA, USA, June 24-27, pp. 1041-1044.

[1.134] J.J. Sniegowski, A microactuation mechanism based on liquid-vapor surface tension, Proc. 6th Int. Conf. Solid-State Sensors and Actuators (Transducers '91), Abstracts of late news papers, San Fransisco, CA, USA, June 24-27, pp. 1041-1044.

[1.135] T.S.J. Lammerink, M. Elwenspoek and J.H.J. Fluitman, Integrated micro-liquid dosing system, Proc. IEEE Micro Electro Mechanical Systems, Ford Lauderdale, Florida, U.S.A., Feb. 7-10, 1993, pp. 254-259.

[1.136] M.J. Zdeblick, R. Anderson, J. Jankowski, B. Kline-Schoder, L. Cristel, R. Miles and W. Weber, Thermopneumatically actuated microvalves and integrated electro-fluidic circuits, 4th Int Conf. on New Actuators (Actuator '94), Bremen, Germany, 15-17 June, 1994, pp. 56-60.

[1.137] J. Fahrenberg, D. Maas, W. Menz and W.K. Schomburg, Active microvalve system manufactured by the LIGA process, 4th Int Conf. on New Actuators (Actuator '94), Bremen, Germany, 15-17 June, 1994, pp. 71-74.

[1.138] B. Büstgens, W. Bacher, W. Bier, R. Ehnes, D. Maas, R. Ruprecht, W.K. Schomburg and L. Keydel, Micromembrane pump manufactured by molding, 4th Int Conf. on New Actuators (Actuator '94), Bremen, Germany, 15-17 June, 1994, 1994, pp. 86-90.

[1.139] J. Chen and K.D. Wise, A high-resolution silicon monolithic nozzle array for inkjet printing, Proc. 8th Int. Conf. Solid-State Sensors and Actuators (Transducers '95), Stockholm, Sweden, June 25-29, 1995, Vol. 2, pp. 321-324.

[1.140] P. Krause, E. Obermeier and W. Wehl, Backshooter-A new smart micromachined single-chip inkjet print head, Proc. 8th Int. Conf. Solid-State Sensors and Actuators (Transducers '95), Stockholm, Sweden, June 25-29, 1995, Vol. 2, pp. 325-328.

[1.141] P.L. Bergstrom, J. Ji, Y.N. Liu, M. Kaviany and K.D. Wise, Thermally driven phase-change microactuation, Journal of Microelectromechanical Systems, Vol. 4, 1995, pp. 10-17.

[1.142] M. Bergamasco, P. Dario and F. Salsedo, Shape memory alloy microactuators, Sensors and Actuators, Vol. A21, 1990, pp. 253-257.

[1.143] A.D. Johnson, Vacuum-deposited TiNi shape memory film: characterization and applications in microdevices, Journal of Micromechanics and Microengineering, Vol. 1, 1991, pp. 34-41.

[1.144] S. Miyazaki and K. Momura, Development of perfect shape memory effect in sputter-deposited Ti-Ni thin films, Proc. IEEE Micro Electro Mechanical Systems, Oiso, Japan, Jan. 25-28, 1994, pp. 176-181.

[1.145] A.P. Lee, D.R. Ciarlo, P.A. Krulevitch, S. Lehew, J. Trevino and M.A. Northrup, A practical microgripper by fine alignment, eutectic bonding and SMA actuation, Proc. 8th Int. Conf. Solid-State Sensors and Actuators (Transducers '95), Stockholm, Sweden, June 25-29, 1995, Vol. 2, pp. 368-371.

[1.146] A.D. Johnson and E.J. Shahoian, Recent progress in thin film shape memory microactuators, Proc. IEEE Micro Electro Mechanical Systems, Amsterdam, The Netherlands, Jan. 29-Feb. 2, 1995, pp. 216-220.

[1.147] L.A. Field, R. M. White and A.P Pisano, Fluid-powered rotary gears and micro-flow channels, Proc. 6th Int. Conf. Solid-State Sensors and Actuators (Transducers '91), San Fransisco, CA, USA, June 24-27, pp. 1033-1036.

[1.148] Y. Ikei, A. Koga, H. Morkiawa and Y. Okawa, Fluid driven microactuator with feedback mechanism, Proc. IEEE Micro Electro Mechanical Systems, Ford Lauderdale, Florida, U.S.A., Feb. 7-10, 1993, pp. 213-218.

[1.149] S. Konishi and H. Fujita, A conveyance system using air flow based on the concept of distributed micro motion systems, Proc. 7th Int. Conf. Solid-State Sensors and Actuators (Transducers '93), Yokohama, Japan, June 7-10, pp. 28-31.

[1.150] D.Y. Sim, T. Kurabayashi and M. Esashi, Backable silicon pneumatic microvalve, Proc. 8th Int. Conf. Solid-State Sensors and Actuators (Transducers '95), Stockholm, Sweden, June 25-29, 1995, Vol. 2, pp. 280-283.

[1.151] C. Vieider, O. Öhman and H. Elderstig, A pneumatically actuated micro valve with a silicone rubber membrane for integration with fluid handling systems, Proc. 8th Int. Conf. Solid-State Sensors and Actuators (Transducers '95), Stockholm, Sweden, June 25-29, 1995, Vol. 2, pp. 284-286.

[1.152] T.S.J. Lammerink, N.R. Tas, J.W. Berenschot, M.C. Elwenspoek and J.H.J. Fluitman, Micromachined hydraulic astable multivibrator, Proc. IEEE Micro Electro Mechanical Systems, Amsterdam, The Netherlands, Jan. 29-Feb. 2, 1995, pp. 13-18.

[1.153] T. Fukuda, H. Hosokai, H. Ohyama, H. Hashimoto and F. Arai, Giant magnetostrictive alloy (GMA) applications to micro mobile robot as a micro actuator without power supply cables, Proc. IEEE Micro Electro Mechanical Systems, Nara, Japan, Jan. 30-Feb. 2,1991, pp. 210-215.

[1.154] T. Honda, K.I. Arai and M. Yamaguchi, Fabrication of actuators using magnetostrictive thin films, Proc. IEEE Micro Electro Mechanical Systems, Oiso, Japan, Jan. 25-28, 1994, pp. 51-56.

[1.155] E. Quandt and K. Seemann, Fabrication of giant magnetostrictive thin film actuators, Proc. IEEE Micro Electro Mechanical Systems, Amsterdam, The Netherlands, Jan. 29-Feb. 2, 1995, pp. 273-277.

[1.156] M.W. Hamberg, C. Neagu, J.G.E. Gardeniers, D.J. Ijntema and M.C. Elwenspoek, An electrochemical microactuator, Proc. IEEE Micro Electro Mechanical Systems, Amsterdam, The Netherlands, Jan. 29-Feb. 2, 1995, pp. 106-110.

[1.157] T. Nagakura, K. Ishihara, T. Furukawa, K. Masuda and T. Tsuda, Auto-regulated medical pump without energy supply, Proc. 8th Int. Conf. Solid-State Sensors and Actuators (Transducers '95), Stockholm, Sweden, June 25-29, 1995, Vol. 2, pp. 287-290.

[1.158] H. Fujita and A. Omodaka, Electrostatic actuators for micromechatronics, Proc. IEEE Micro Robots and Teleoperators Workshop, Hyannis, MA, U.S.A., Nov. 9-11, 1987.

[1.159] J.H. Lang and S.F. Bart, Towards the design of successful electric micromotors, Proc. IEEE Solid-State Sensors and Actuators Workshop, Hilton Head Island, SC, U.S.A., June 6-9, 1988, pp. 127-130.

[1.160] S.F. Bart, T.A. Lober, R.T. Howe, J.H. Lang and M.F. Schlecht, Design considerations for micromachined electric actuators, Sensors and Actuators, 14, 1988, pp. 269-292.

[1.161] R.H. Price, J.E. Wood and S.C. Jacobsen, Modelling considerations for electrostatic forces in electrostatic microactuators, Sensors and Actuators, 20, 1989, pp. 107-114.

[1.162] I.J. Busch-Vishniac, The case for magnetically driven microactuators, Sensors and Actuators, A33, 1992, pp. 207-220.

[1.163] N.R. Tas, R. Legtenberg, J.W. Berenschot, M.C. Elwenspoek and J.H.J. Fluitman, The electrostatic shuffle motor, Proc. 6th European workshop on micromachining, micromechanics and microsystems (MME '95), Copenhagen, Denmark, Sept. 3-5, 1995, pp. 128-131.

[1.164] T. Fukuda, A. Kawamoto, F. Arai and H. Matsura, Mechanism and swimming experiment of micro mobile robot in water, Proc. IEEE Micro Electro Mechanical Systems, Oiso, Japan, Jan. 25-28, 1994, pp. 273-278.

[1.165] I. Shimoyama, Y. Kubo, T. Kaneda and H. Miura, Simple microflight mechanism on silicon wafer, Proc. IEEE Micro Electro Mechanical Systems, Oiso, Japan, Jan. 25-28, 1994, pp. 148-152.

[1.166] I. Shimoyama, Y. Fulisawa, G.D. Getzan, H. Miura, M. Shimada and Y. Matsumoto, Fluid dynamics of microwing, Proc. IEEE Micro Electro Mechanical Systems, Amsterdam, The Netherlands, Jan. 29-Feb. 2, 1995. pp. 374-379.

[1.167] A.D. Moore, Electrostatics and its applications, John Wiley & Sons, 1973.

[1.168] K. E. Petersen, Silicon as a mechanical material, Proc. IEEE, 70 (198), pp. 420-457.

[1.169] H. Seidel, The mechanism of anisotropic silicon etching and its relevance for micromachining, Proc. Int. Conf. Solid-State Sensors and Actuators (Transducers '87), Tokyo, Japan, 1987, pp. 120-125.

[1.170] B. Hök, Micromechanics and micromachining of semiconductor sensors, Acta Polytechnica Scandinavia El. Eng. Series, E163 (1988), pp. 65-84.

[1.171] P.W. Barth, Silicon fusion bonding for fabrication of sensors, actuators and microstructures, Proc. 5th Int. Conf. Solid-State Sensors and Actuators (Transducers '89), Montreux, Switzerland, June 25-30, 1989, pp. 919-926.

[1.172] Silicon-to-silicon anodic bonding, A. Hanneborg, M. Nese and P. Ohlckers, Proc. 2nd European workshop on micromachining, micromechanics and microsystems (MME '90), Berlin, Germany, Nov. 26-27, 1990, pp. 100-107.

[1.173] H. Guckel and D. W. Burns, A technology for integrated transducers, Proc. Int. Conf. Solid-State Sensors and Actuators (Transducers '85), Philadelphia, PA, U. S. A., June 11-14, 1985, pp. 90-92.

[1.174] R. T. Howe, Surface micromachining for microsensors and microactuators, J. Vac. Sci. Technol., B 6 (6) (1988), pp. 1809-1813.

[1.175] Surface micromachining, C. Linder, L. Paratte, M. A. Gretillat, V. P. Jaecklin and N. F. de Rooij, J. Micromech. Microeng., 2 (1992), pp. 122-132.

[1.176] R.S. Muller, Microdynamics, Proc. 5th Int. Conf. Solid-State Sensors and Actuators (Transducers '89), Montreux, Switzerland, June 25-30, 1989, pp. 1-8.

[1.177] L. S. Fan, Y. C. Tai and R. S. Muller, Integrated movable micromechanical structures for sensors and actuators, IEEE Trans. on El. Dev., 35 (6) (1988), pp. 724-730.

[1.178] M. Mehregany and Y. C. Tai, Surface micromachined mechanisms and micromotors, J. Micromech. Microeng., 1 (1991), pp. 73-85.

[1.179] T.A. Lober and R.T. Howe, Surface-micromachining processes for electrostatic microactuator fabrication, Proc. IEEE Solid-State Sensors and Actuators Workshop, Hilton Head Island, SC, U.S.A., June 6-9, 1988, pp. 59-62.

[1.180] W. Ehrfeld, P. Bley, F. Götz. P Hagmann, A. Maner, J. Mohr, H. O. Moser. D. Münchmeyer, W. Schelb, D. Schmodt and E. W. Becker, Fabrication of microstructures using the LIGA process, IEEE ,1987.

[1.181] H. Guckel, T. Christenson and K. Skrobis, Metal micromechanisms via deep X-ray lithography, electroplating and assembly, J. Micromech. Microeng., 2 (1992), pp. 225-228.

[1.182] A. Rogner, J. Eicher, D. Münchmeyer, R. P. Peters and J. Mohr, The LIGA technique-What are the new opportunities, J. Micromech. Microeng., 2 (1992), pp. 133-140.

[1.183] J. Mohr, P. Bley, M. Strohrmann and U. Wallrabe, Microactuators fabricated by the LIGA process, Journal of Micromechanics and Microengineering, Vol. 2, 1992, pp. 234-241. .

[1.184] B. Löchel, A. Maciossek, M. König, H.J. Quenzer and B. Wagner, Electroplated electromagnetic components for actuators, Proc. 4th Int. Conf. and Exhibition on Micro Electro, Opto, Mechanical Systems and Components (Actuator '94), Berlin, Germany, October 19-21, 1994, pp. 109-113.

[1.185] A.B. Frazier and M.G.Allen, High aspect ratio electroplated microstructures using a photosensotive polyimide process, Proc. IEEE Micro Electro Mechanical Systems, Travemünde, Germany, Feb. 4-7, 1992, pp. 87-92.

[1.186] A.B. Frazier and M.G. Allen, Metallic microstructures fabricated using photosensitive polyimide electroplating molds, Journal of Microelectromechanical Systems, Vol. 2, 1993, pp. 87-94.

[1.187] H. Lorentz, L. Paratte, R. Luthier, N.F. de Rooij and P. Renaud, Low-cost technology for multilayer electroplated parts using laminated dry film resist, Proc. of the 8th Int. Conf. on Solid-State Sensors and Actuators (Transducers '95), Stockholm, Sweden, June 25-29, 1995, Vol. 1, pp. 569-572.

[1.188] S.C. Chang, M.W. Putty and D.B. Hicks, The formation of electroplating molds by reactive ion etching, Proc. 8th Int. Conf. Solid-State Sensors and Actuators (Transducers '95), Stockholm, Sweden, June 25-29, 1995, Vol. 1, pp. 577-580.

[1.189] S. Roy and M. Mehregany, Fabrication of electrostatic Nickel microrelays by Nickel surface micromachining, Proc. IEEE Micro Electro Mechanical Systems, Amsterdam, The Netherlands, Jan. 29-Feb. 2, 1995, pp. 353-357.

[1.190] Z. L. Zhang and N. C. MacDonald, An RIE process for submicron, silicon electromechanical structures, Proc. Int. Conf. on Solid-State Sensors and Actuators, (Transducers '91), San Fransisco, CA, U. S. A., June 24-27, 1991, pp. 520-523.

[1.191] K.A. Shaw, Z.L. Zhang and N.C. MacDonald, Scream I: a single mask, single crystal, silicon process for microelectromechanical structures, Sensors & Actuators, Vol A40, (1994), pp. 63-70.

[1.192] Y.X. Li, P.J. French, P.M. Sarro and R.F. Wolffenbuttel, Fabrication of a single crystalline silicon capactive lateral accelerometer using micromachining based on single step plasma etching, Proc. IEEE Micro Electro Mechanical Systems, Amsterdam, The Netherlands, Jan. 29-Feb. 2, 1995, pp. 398-403.

[1.193] M. de Boer, H. Jansen and M. Elwenspoek, The black silicon method V: A study of the fabrication of movable structures for micro electromechanical systems, Proc. 8th Int. Conf. Solid-State Sensors and Actuators (Transducers '95), Stockholm, Sweden, June 25-29, 1995, Vol. 1, pp. 565-568.

[1.194] C. Keller and M. Ferrari, Milli-scale polysilicon structures, Proc. IEEE Solid-State Sensors and Actuators Workshop, Hilton Head Island, SC, U.S.A., June 13-16, 1994, pp. 132-137.

[1.195] A. Benitez, J. Esteve and J. Bausells, Bulk silicon micro electromechanical devices fabricated from commercial BESOI substrates, Proc. IEEE Micro Electro Mechanical Systems, Amsterdam, The Netherlands, Jan. 29-Feb. 2, 1995, pp. 404-407.

[1.196] E.H. Klaassen, K. Petersen, M. Noworolski, J. Logan, N.I. Maluf, J. Brown, C. Storment, W. McCulley and G.T.A. Kovacs, Silicon fusion bonding and deep reactive ion etching; a new technology for microstructures, Proc. 8th Int. Conf. Solid-State Sensors and Actuators (Transducers '95), Stockholm, Sweden, June 25-29, 1995, Vol. 1, pp. 556-559.

[1.197] Y. Gianchandani and K. Najafi, Micron-sized, high aspect ratio bulk silicon micromechanical devices, Proc. IEEE Micro Electro Mechanical Systems, Travemünde, Germany, Feb. 4-7, 1992, pp. 208-213.

[1.198] W.H. Juan and S.W. Pang, A novel etch-diffusion process for fabricating high aspect ratio Si microstructures, Proc. 8th Int. Conf. Solid-State Sensors and Actuators (Transducers '95), Stockholm, Sweden, June 25-29, 1995, Vol. 1, pp. 560-563.

[1.199] J. Elders, H.V. Jansen, M.C. Elwenspoek and W. Ehrfeld, DEEMO: A new technology for the fabrication of microstructures, Proc. IEEE Micro Electro Mechanical Systems, Amsterdam, The Netherlands, Jan. 29-Feb. 2, 1995, pp. 238-243.

Chapter Two

POLYSILICON SURFACE MICROMACHINING TECHNOLOGY

In this chapter, an overview is presented of surface micromachining technology. Emphasis is given to polysilicon surface micromachining using silicon dioxide as a sacrificial layer that is etched in hydrofluoric acid solutions to free the polysilicon structural parts. The basic fabrication steps are described and material requirements are discussed. Control of polysilicon mechanical properties, etch characteristics of silicon dioxide in hydrofluoric acid and techniques to prevent stiction of surface micromachined structures after drying from rinsing liquids are described. Examples of elementary surface micromachined components are given.

2.0 INTRODUCTION

Nowadays a large variety of micromechanical structures can be fabricated using thin film techniques. The fabrication of these micromechanical structures is mainly based upon three fabrication methods; bulk micromachining, LIGA techniques and surface micromachining. In bulk micromachining, structures are fabricated by etching and bonding techniques of silicon wafers [2.1-2.3]. LIGA techniques are based on X-ray exposure and development of thick resist layers, and subsequent electroplating of metal layers to form the micromechanical structures [2.4-2.6].

In surface micromachining structural parts are embedded in layers of sacrificial material during the fabrication process [2.7-2.9]. These layers are usually deposited onto a silicon substrate. The sacrificial material is then etched or dissolved in a chemical etchant resulting in freely movable structures. This process requires a compatible set of structural materials, sacrificial layers and chemical etchants. Mechanical structures with more than one degree of freedom can be built by surface micromachining using one sided processing without the need for complicated assembling techniques [2.10-2.15].

However, the thin film materials must posses the desired mechanical properties for the application in mind, e.g. a controllable residual stress and stress gradient which are of primary importance. The sacrificial layer and the structural material deposition and processing techniques must be compatible with each other. The etchant should have a high etch selectivity with respect to the structural layer in order to prevent chemical attack during sacrificial layer etching. The etch rate should also be high enough to release the structural layer in reasonable etch times and the etch process should not leave etch residue behind.

In an electromechanical system the structures are used for transduction purposes of different quantities that are generally linked to the electrical domain. In addition to technological and mechanical requirements, this also calls for desired properties in the electrical domain. Based on IC-technology several thin film materials, processes and techniques have been developed in order to fulfil these demands. For example, good conductive properties or a high breakdown voltage and good insulating properties are needed in electrostatic transducers. In this case, polysilicon is often used as a conductive mechanical structure after heavily doping with boron or phosphorus. Silicon dioxide, silicon nitride and air gaps are generally used as insulating layers.

The sacrificial layer etch technique was first demonstrated by Nathanson [2.16] in 1967 with the fabrication of resonant gate transistors that employed free standing gold beams. The fabrication of free standing structures from polycrystalline silicon using a silicon dioxide sacrificial layer that was removed in hydrofluoric acid was introduced by Howe [2.17]. Since then, surface micromachining techniques have been developed, and greatly improved, resulting in a large variety of structural materials and sacrificial layer combinations [2.18-2.36]. However, most of the work has been focused on the polysilicon and silicon dioxide combination using HF solutions to etch the silicon dioxide.

Polysilicon surface micromachining is the best documented surface micromachining technique. It closely meets many of the requirements described above, and the materials and the etchants are IC compatible and can be integrated with IC processes [2.37-2.43]. The emphasis of this chapter will therefore be on polysilicon surface micromachining techniques. The basic fabrication steps are shown in fig. 2.1.

The first step is the deposition and subsequent patterning of the silicon dioxide sacrificial layer. This is followed by the deposition and patterning of the polysilicon structural layer. Next the sacrificial layer is selectively etched in a

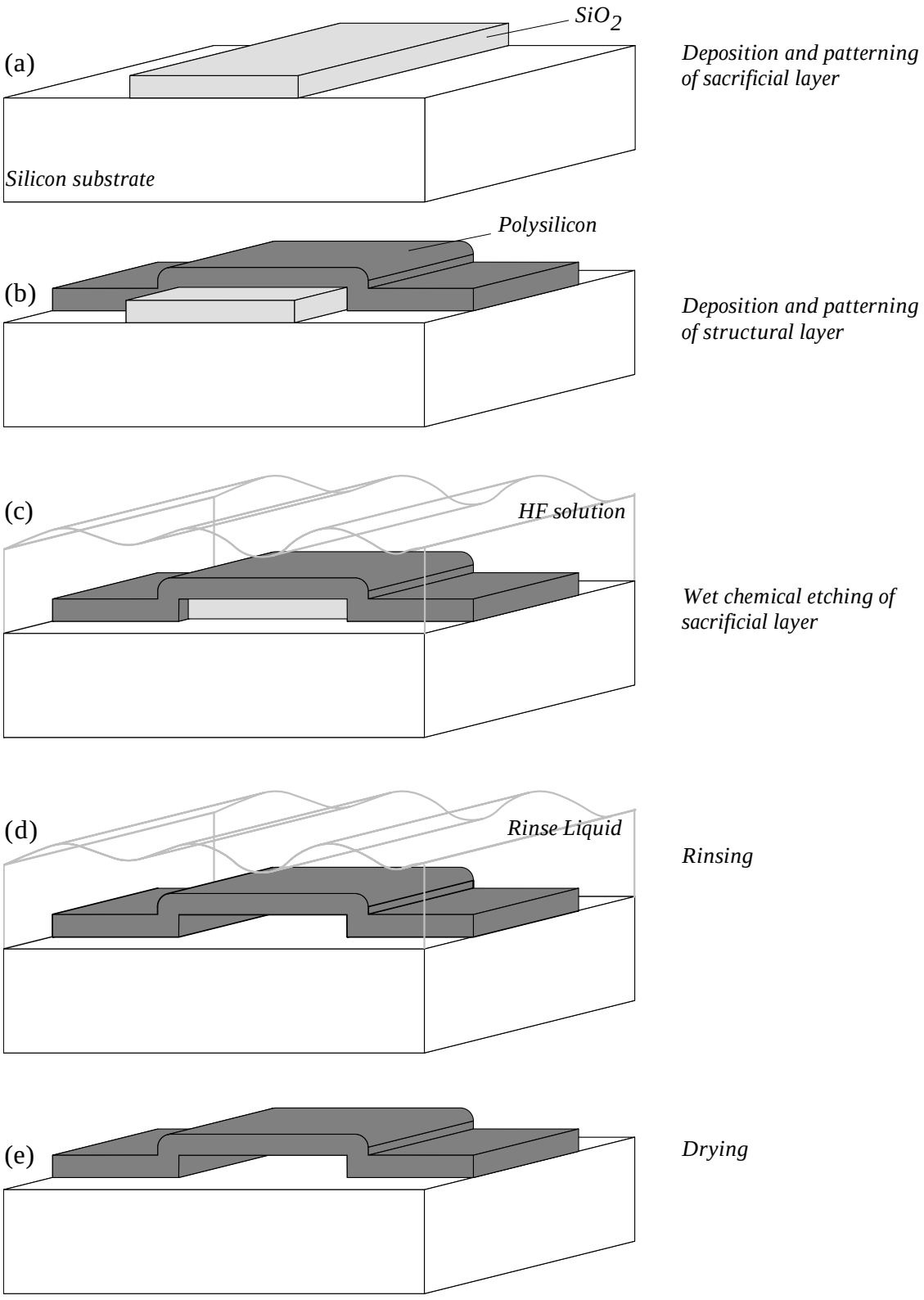

Fig. 2.1 *Basic surface micromachining steps. a) Deposition and patterning of the silicon dioxide sacrificial layer. b) Deposition and patterning of the polysilicon structural layer. c) Sacrificial layer etching in a hydrofluoric acid solution. d) Rinsing steps. e) Drying procedure.*

fluoric acid solution. This is followed by rinsing procedures to remove the fluoric acid and the last step is drying from the rinse liquid.

In the next paragraphs, key steps in polysilicon surface micromachining techniques will be discussed. First, the characterisation of mechanical properties of thin films will be addressed. The next part deals with control of residual strain in polysilicon thin films. Then the sacrificial layer etch process will be described in more detail. This is followed by a discussion of methods to prevent unwanted adhesion problems, stiction, that can occur after drying of the mechanical structures. Finally a number of basic surface micromachining processes will be presented that have been used for successful fabrication of elementary components and some special techniques will be addressed.

2.1 CHARACTERISATION OF POLYSILICON MECHANICAL PROPERTIES

A critical factor in the fabrication of surface micromachined structures is the control and determination of the mechanical properties of the structural material. Design of micromechanical structures requires knowledge of the material properties such as Young's modulus E_y, Poisson's ratio ν, residual stress and tensile strength. Improper mechanical properties, especially residual stress, can lead to warpage, buckling, unwanted deflections, and fracture that result in dimensional limitations, unwanted operation and device failure. Compressive stress can easily cause mechanical microstructures such as bridges and diaphragms to buckle (see fig. 2.2). Free standing and one-sided clamped structures like cantilevers will curl if normal stress gradients relax, when the beam is released after removal of the sacrificial layer (see fig. 2.3). Cracking occurs from excessive internal stresses and blistering and peeling can result from poor adhesion to the substrate.

For isotropic materials under a bi-axial state of stress the average internal strain ε_0 in the plane of the film is related to the in-plane stress $\sigma_0=\sigma_x=\sigma_y$ by the relation:

$$\varepsilon_0 = \frac{\sigma_0 (1-\nu)}{E_y} \qquad (2.1)$$

using Hooke's law and neglecting stresses in the direction of the thickness of the film h, the average stress in the thin film σ_0 is:

$$\sigma_0 = \frac{1}{h} \int_{-\frac{h}{2}}^{\frac{h}{2}} \sigma_{0(z)}\, dz \qquad (2.2)$$

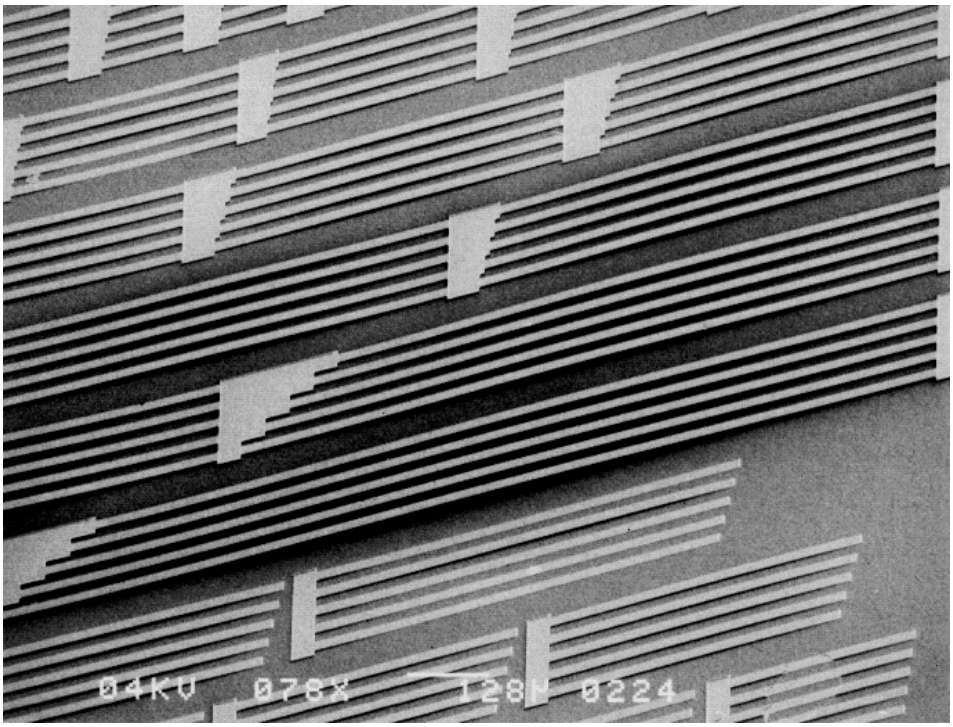

Fig. 2.2 *SEM photograph of free standing microbridges. The long microbridges are buckled because of compressive residual stress. The cantilever beams bend downward because of a negative stress gradient which also results in stiction problems.*

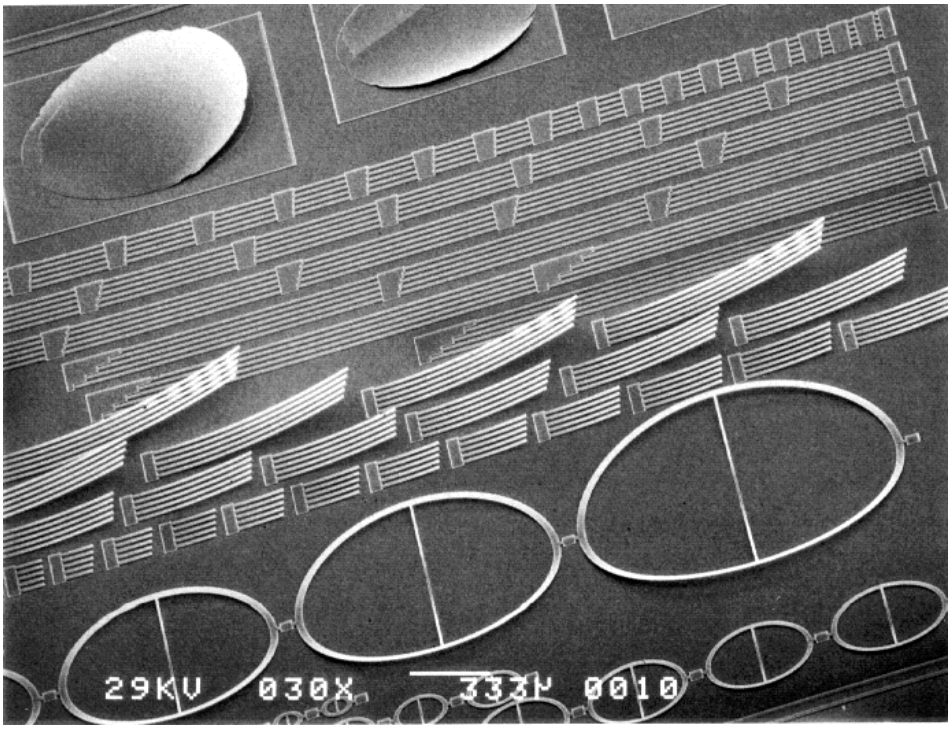

Fig. 2.3 *SEM photograph of free standing beams. The cantilever beams are curved upward by a positive stress gradient across the beam thickness. The microbridges are straight because of an average tensile stress in the polysilicon film whereas the circular membranes even show fracture as a result of excessive tensile stress.*

2.1.1 Measurement techniques

A variety of different load to deflection techniques and approaches have been used in order to determine thin film mechanical properties. Many measurement techniques have been used to determine residual stress, Young's modulus and fracture strength. Experimental determination of other properties, for example shear modulus and Poisson's ratio, are rare.

Tensilometers:

Ideally one would like to measure the stress-strain diagram in order to determine mechanical properties like Young's modulus and yield strength. For thin films microtensilometers have been used to perform this measurement. However the small thickness of thin films makes this approach difficult and accurate measurements can only be made by dedicated instruments [2.44-2.46].

Wafer curvature:

One of the easiest approaches to measure the residual stress is the measurement of the wafer curvature of a silicon wafer covered at one side with a layer of the thin film under investigation [2.47-2.49]. This approach does not require patterning and etching of the film or substrate. The residual bi-axial stress σ_0 can be found from:

$$\sigma_0 = \frac{E_s}{\left(1-\nu_s\right)} \frac{t_s^{\,2}}{6\, t_f\, R} \qquad (2.3)$$

where E_S is the Young's modulus of the substrate material, ν_S is the Poisson's ratio of the substrate material, t_S is the thickness of the substrate, t_f is the thickness of the thin film, and R is the radius of wafer curvature.

Bulge test:

A method to determine Young's modulus, residual stress and fracture strain is the bulge test [2.50-2.56]. This technique is based upon the measurement of the load-deflection characteristic of a membrane by applying a pressure. By least-square fitting of the measured load-deflection characteristic both $E/1\text{-}\nu$ and σ_0 can be determined. The membrane is constructed from the thin film material or consists of a composition of a mechanical carrier and the thin film material under investigation. Circular, square and rectangular membranes have been used for this technique. The load-deflection relationship is given by:

$$P = \frac{C_1 h \sigma_0}{a^2}\delta + \frac{C_2 h}{a^4}\frac{E}{(1-\nu)}\delta^3 \qquad (2.4)$$

where P is the applied pressure, h is the membrane thickness, $2a$ is the length or diameter of the membrane and δ is the deflection at the center of the membrane. The constants C_1 and C_2 are dependent on the membrane shape and have been determined by Pan [2.56] using FEM analysis for circular and square membranes. The values of C_1 and C_2 are respectively 4.0 and 2.67 for circular membranes and 3.41 and 1.37 for square membranes, in case the Poisson's ratio is equal to 0.25.

Surface profiler techniques:

Concentrated load-deflection measurements of micromechanical structures have also been performed. Loading of microfabricated structures by a stylus type surface profiler [2.57], cantilever beam bending experiments using a nanointender [2.58, 2.59] or micromanipulator [2.60] and loading of membranes by a surface profiler [2.61] have been used to extract thin film mechanical properties.

Extraction from resonance data:

Resonant microstructures can be used to determine the residual strain and the Young's modulus by using the resonant frequency data of beams [2.52-2.66]. The expression for the natural frequencies of clamped-clamped beams with rectangular cross sections and a large width b, under plane strain conditions (ε_y=0, b>5h), can be written as:

$$\omega_n = \frac{\alpha_n^2}{\sqrt{12}}\sqrt{\frac{E_y/(1-\nu^2)}{\rho}}\frac{h}{l^2}\sqrt{1+\gamma_n \varepsilon_0 (1-\nu^2)\left(\frac{l}{h}\right)^2} \qquad (2.5)$$

where α_n and γ_n are mode shape constants that are respectively 4.73 and 0.295 for the fundamental mode, ρ is the density of the beam material, h is the beam thickness, l is the beam length and ε_0 is the residual strain.

A linear fit of $(\omega_n l)^2$ versus $(h/l)^2$ gives the Young's modulus from the slope of the straight line, and the residual strain from the zero offset. The residual strain can also be found from the ratio of higher overtones to the fundamental frequency.

Diagnostic test structures:

A number of micromechanical diagnostic test structures have been developed in order to determine thin film mechanical properties. This approach has the advantage that their fabrication is complementary to the fabrication and development of other microstructures and is suited to create standard "drop-in" mechanical test structures, analogous to transistor test structures used for extraction of electrical device parameters.

An array of microbridges can be used to measure compressive strain [2.67]. A doubly clamped beam under plane stress conditions ($\sigma_y=0$)will buckle if its length exceeds a critical length L_{cr}:

$$L_{cr} = \sqrt{\frac{\pi^2 h^2}{3\,\varepsilon_0}} \tag{2.6}$$

Under bi-axial stress conditions a square plate, clamped at all four edges, will buckle if the length exceeds the critical length a_{cr} given by:

$$a_{cr} = \sqrt{\frac{4\,\pi^2 h^2}{9\,(1+\nu)\,\varepsilon_0}} \tag{2.7}$$

The strain is deduced by determining the smallest geometry for which buckling occurs. Buckling can be readily determined using a phase contrast microscope. Using arrays of ring shaped structures [2.68] or diamond-like structures [2.69] that convert tensile residual strain into compressive forces, it is also possible to measure tensile strains.

Cantilever beams and spiral structures [2.70-2.72] can be used to measure strain gradients across the beam thickness. Variation in film stress with thickness results in an internal moment per unit width M_0 equal to:

$$M_0 = \int_{-\frac{h}{2}}^{\frac{h}{2}} \sigma_{x(z)}\, z\, dz \tag{2.8}$$

where z is taken as the distance from the center of the film. After release, the internal stress relaxes and the structural film will curl with a radius of curvature R:

$$R = \frac{E_y h^3}{12\, M_0} \tag{2.9}$$

Passive T-shaped structures with a wide, long center stem and thinner deformable cross [2.73], bridges with an intermediate lateral displacement that rotate a long pointer [2.74-2.76] and strain diagnostics with a bent beam deformation multiplier [2.77] have been used to determine the residual strain.

Furthermore, active micromechanical test structures have been fabricated. Comb drive structures have been used to determine Young's modulus and residual strain [2.78, 2.79]. The pull-in voltage of cantilever beams, microbridges and membranes can be used to determine the residual stress, Poisson's ratio and Young's modulus [2.80, 2.81].

Diagnostic test structures have also been used to determine the fracture strength of thin films. Examples are spiral springs [2.11], bridge-slider structures [2.82] and cantilever beams with an end ring [2.83] which have been externally loaded by mechanical probes until fracture occurred. Surface micromachined cleaving structures [2.84] and test structures consisting of a narrow center beam, loaded by wider beams which are under tensile stress can be used for in-situ fracture stress measurement [2.85, 2.86].

2.1.2 Residual stress in polysilicon

The residual stress in polysilicon can be controlled by varying the deposition variables, by annealing procedures and by doping. Stresses in as-deposited, undoped polysilicon change from several hundred MPa tensile to several hundred MPa compressive over a small deposition temperature range with corresponding changes in thin film microstructure. Consequently as-deposited low stress polysilicon is difficult to obtain without doping or annealing. Annealing at high temperatures or doping and subsequent annealing reduces the magnitude of stresses in polysilicon films to small values, regardless of the initial stress state, film microstructure and substrate. At moderate annealing temperatures, a tensile stress develops in initially amorphous films which decays to low values at high annealing temperatures. Films deposited in a polycrystalline form exhibit an initial compressive stress that also decays to low values with increasing annealing temperature. A more detailed discussion about residual stress will be given in the section on control of polysilicon residual strain.

2.1.3 Young's Modulus of polysilicon

The Young's modulus of polysilicon can be calculated theoretically from well-known mono-crystalline properties by averaging over the grain

orientations in the film [2.87]. For all classes of cubic crystals, Young's modulus E_y can be expressed as a function of orientation:

$$\frac{1}{E_y} = s_{11} - 2\left(s_{11} - s_{12} - \frac{1}{2}s_{44}\right)\left(l_1^2 l_2^2 + l_2^2 l_3^2 + l_3^2 l_1^2\right) \qquad (2.10)$$

where s_{ij} represents elastic compliance, and l_i are the directional cosines of the orientation with respect to the $\langle 100 \rangle$ axes. The shear modulus G is given by:

$$\frac{1}{G} = s_{44} - \left(2\,s_{11} - 2\,s_{12} - s_{44}\right)\left(l_1^2 m_1^2 + l_2^2 m_2^2 + l_3^2 m_3^2\right) \qquad (2.11)$$

where m_i are the directional cosines in the orthogonal direction m under consideration with respect to the $\langle 100 \rangle$ axes. If both the Young's modulus and the shear modulus are known, the Poisson's ratio can be calculated from:

$$\nu = \frac{E_y}{2\,G} - 1 \qquad (2.12)$$

For a {111} oriented film, irrespective for all orthogonal directions l within {111} planes, the value inside the second bracket of eq. (2.10) is constant at 1/4. Therefore, the in-plane Young's modulus and shear modulus are constant for crystallites oriented with {111} planes parallel to the substrate surface.

For silicon, the elastic compliances are s_{11} = 0.768 10^{-11} Pa^{-1}, s_{12} = -0.214 10^{-11} Pa^{-1} and s_{44} = 1.256 10^{-11} Pa^{-1}. Assuming that effects of grain boundaries are negligible this gives: Ey = 169 GPa, G = 67 GPa, and ν = 0.262 for in plane directions of {111} oriented thin polysilicon films [2.88].

Guckel calculated a theoretical Young's modulus for polysilicon with randomly oriented grains and reported a theoretical Young's modulus of 161 GPa, a shear modulus of 65.9 GPa and a Poisson's ratio of 0.226 [2.89].

Another theoretical calculation of the Young's modulus of polysilicon and amorphous silicon thin films, based on the combination of grain and grain boundary effects as well as the dependence of crystalline orientations was presented by Guo [2.90]. They showed that the Young's modulus is a function of grain size and boundary elastic constant and varies between 150 to 170 GPa for films with {110}, {111} and {311} orientations and a grain size of 80 nm.

An overview of experimentally determined Young's moduli is shown in table 2.1. There exists a large variation in measured Young's moduli of polysilicon which ranges from 130 GPa to 190 GPa. This is suggested to result from differences in processing conditions, impurities, annealing processes and

doping that affect thin film properties like grain size, grain boundary, crystal orientations, etc. which in their turn change the Young's modulus. Because of the anisotropic nature of polysilicon, the direction in which the load is applied, i.e. the direction in which the Young's modulus is measured, is also important.

E [GPa]	Ref. #
175±15	[2.42]
160	[2.47]
123	[2.53]
151	[2.61]
174	[2.70]
175±21	[2.75]
190	[2.78]
168±7 (undoped) 130-160 (in-situ P-doped)	[2.79]
149-162 (600-1100˚C ann.)	[2.93]
140	[2.96]
150	[2.157]
170±20 (B doped)	[this thesis]*

Table 2.1 *Overview of measured Young's moduli of polysilicon thin films.*

2.1.4 Fracture strain of polysilicon

The fracture strain of polysilicon has been determined by Fan using a spiral spring resulting in a value of 1.7 % [2.11]. Koskinen *et al* measured the fracture strain of polysilicon fibers using a microtensilometer [2.46]. They found a tensile strength between 2.8 and 3.4 GPa (1.6-1.9 %), depending on grain size and found that all fibers failed in a brittle fashion. Employing a bridge-slider structure the fracture strain of polysilicon was found to be 1.72±0.09 % for unannealed samples and 0.93±0.04 % for samples annealed at 1000 °C for one hour [2.82]. A value of 2.84±0.09 GPa (≈ 1.7 %) was extracted for the fracture stress of undoped polysilicon from in-situ fracture structures [2.86]. Doping with boron, showed no significant effect, doping with arsenic showed minor effect and phosphorus doping lead to a 25 % reduction in the fracture stress. A 17 % decrease of the fracture stress was observed for a 100 % increase in the

* See Section 6.4.1 of Chapter 6, page 144.

etching time and no difference was observed for samples etched in concentrated HF or BHF. Most of the reported fracture strains of polysilicon are close to the fracture strain of single crystal silicon which is measured to be 2.6 % [2.91].

2.2 CONTROL OF POLYSILICON RESIDUAL STRESS

Residual stress results from a mismatch in thermal expansion between the film and the substrate (thermal stress), accentuated by depositions performed at elevated temperatures, and from effects of grain growth and deposition which "freeze" atoms in positions other than at zero-stress lattice points (intrinsic stress). The detailed physical mechanisms behind this intrinsic stress generation are not fully known. The effect of process conditions, annealing and doping on the residual stress of polysilicon will be discussed.

2.2.1 As deposited films

Polysilicon is usually deposited by Low Pressure Chemical Vapour Deposition (LPCVD) from pyrolyses of silane (SiH_4) at temperatures around 600 ˚C and pressures of several hundred mTorr. The residual stress varies significantly with processing conditions, especially with deposition temperature and silane pressure. The general dependency of residual stress, texture and crystal orientation is shown in fig. 2.4 and will be discussed below.

A transition between the deposition of amorphous and polycrystalline silicon generally occurs around 580 ˚C for operating pressures at about 200 mTorr and shifts to higher values with increasing pressure up to 680 ˚C when the deposition takes place at atmospheric pressure [2.92]. Below this temperature little surface diffusion exists and amorphous silicon films are grown that exhibit a large compressive stress [2.93, 2.94].

LPCVD silicon films deposited near the crystallisation temperature transform from the amorphous to the crystalline state during deposition resulting in equi-axed grains. These films generally have crystal orientations with {110}, {111}, {112} and {113} components [2.88, 2.95-2.101]. The transformation from amorphous to crystalline silicon is coupled with a volume contraction inducing large tensile stresses [2.98-2.102]. It has been suggested that the tensile strain is associated with the presence of the {112} and {113} orientations. The magnitude of tension in the film has been found to decrease towards the

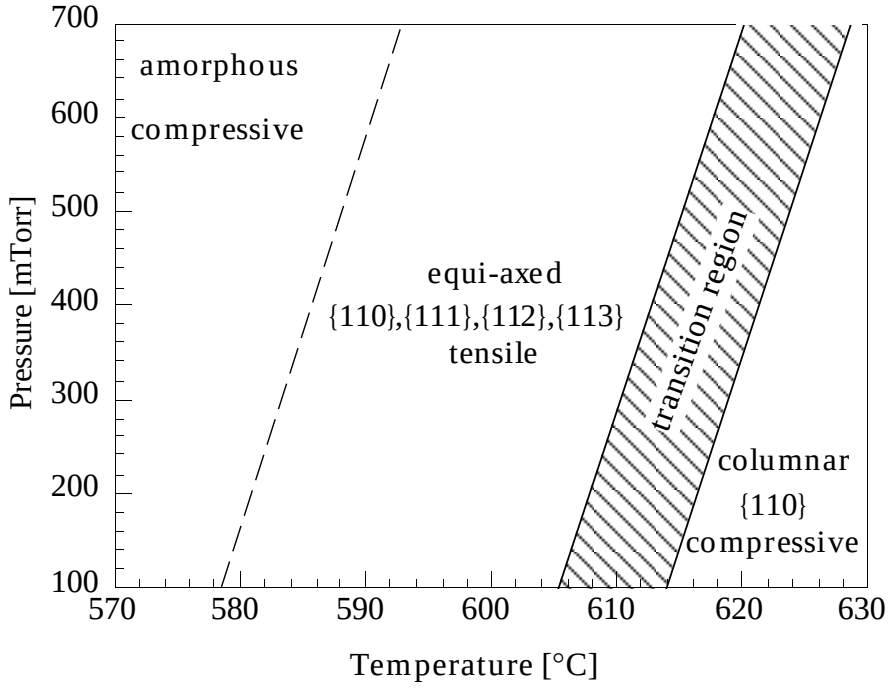

Fig. 2.4 *General found polysilicon structure , orientation, and stress vs. deposition temperature and pressure.*

substrate [2.98, 2.100, 2.101]. Therefore polysilicon structures grown under these conditions will exhibit a positive stress gradient and curl upward after release.

Deposition temperatures above 630 ˚C produce films that nucleate at the substrate surface creating a strong {110} texture, with columnar grains extending through the film thickness and a region with smaller grains at the film/substrate interface [2.97-2.101]. At increasing temperatures up to 700 ˚C, {100} texture becomes dominant with grains that also exhibit a columnar structure [2.95-2.101]. Films deposited in the temperature range from 560 ˚C to 630 ˚C at pressures below 100 mTorr also have been found to show a preferred {110} orientation [2.103].

Because the amorphous to crystalline transition does not occur in these columnar films, the tensile component disappears and films are under compressive stress which decreases with increasing deposition temperature. For films deposited at 650 ˚C the magnitude of compression increases towards the substrate, again resulting in a positive stress gradient [2.98, 2.100, 2.101].
Between the temperature region where tensile films develop and the higher temperature region where compressive films are formed, a region has been found where stress, structure and texture vary with wafer position in the boat, even though temperature is constant [2.97-2.100]. This region, like the

amorphous to crystalline transition temperature, is pressure dependent and lies around a temperature of about 615 ˚C.

It should be avoided because of unpredictable stresses that range from tensile to compressive from the front to the end of the boat. The transition along the boat has been suggested to be due to silane depletion or increased hydrogen partial pressure [2.98, 2.99].

Impurities, like oxygen that is difficult to control in polysilicon, can impede surface migration during the deposition. As a result the structure will be less ordered than in high purity material. Small amounts of carbon can also change the grain size, the film structure, and the amount of stress in the film [2.92]. Polysilicon films have been shown to exhibit a surface layer of approximately 0.1 μm thick that is 50-100 MPa more compressive than adjacent sub-surface layers [2.101]. It is suggested that this compression arises from oxidation and oxygen entrapment that occurs when the wafers are exposed to atmosphere at process temperatures during unloading as well as subsequent annealing steps. Oxidation, which occurs preferentially at grain boundaries, is a recognised source of compression in polysilicon films.

2.2.2 Annealing:

Films deposited at lower temperatures in an amorphous form are unstable and crystallise readily during annealing at moderate temperatures and can crystallise during long heat treatments at temperatures as low as 600 ˚C [2.74, 2.89, 2.92, 2.104]. Initially compressive amorphous films develop equi-axed grain structures after annealing at high temperatures as a result of grain growth and primary recrystallization. Recrystallization refers to nucleation and growth of new grains within an already crystalline film and is usually driven by the reduction of bulk defect energies and results in new grains with low defect densities which grow at the expense of high defect density old grains. It has been found that the elementary process of polysilicon grain growth process is attributed to silicon self-diffusion across the grain boundaries. Films with orientations in the {110}, {111}, {112} and {113} direction have been found after annealing [2.101,2.104]. The accompanying volume contraction changes the direction of the stress from compressive to tensile. The tensile stress is initially higher for moderate annealing temperatures and decays to a low value with increasing annealing temperature [2.94].

Undoped films deposited in a polycrystalline form are more stable on annealing at moderate temperatures and high temperature annealing is needed before changes occur in grain orientations. The as deposited

compressive residual stress generally decreases to low values with increasing annealing temperature [2.103-2.105]. During annealing of initially {110} oriented films, an increasing {331} orientation develops with increasing temperature up to 1000˚C. Above 1100 ˚C the {110} texture decreases significantly and the {311} and {111} orientation increase [2.104]. Rapid thermal annealing at high temperature also produces low residual stress polysilicon films [2.39, 2.106].

2.2.3 Doping:

Doping and subsequent thermal activation of polysilicon films also reduces the residual stress. Diffusion of phosphorus in polysilicon at elevated temperatures produces low stress polysilicon films with negligible stress gradient regardless of the original stress state or microstructure of the thin film [2.70, 2.101, 2.107]. Residual strain of implanted films is dependent on dopant types, implantation dose and subsequent annealing temperature. Phosphorus, arsenic and boron implantation followed by an annealing step has been found to result in stress reversal of initially tensile films resulting in compressive stresses [2.108, 2.109]. For initial compressive films boron and phosphorus implantation and annealing was found to result in low strain films [2.110, 2.111]. Wada and Nishimatsu showed that P-implanted polysilicon films undergo grain growth at temperatures as low as 800 ˚C [2.112]. The rate of grain growth was shown to increase in phosphorus doped films with concentrations above 4.10^{20} cm^{-3} attributed to the enhancement of the silicon self-diffusion in the presence of phosphorus. Grain growth was found to depend strongly on the phosphorous concentration that acts as a catalyst to recrystallization. Mei *et al* confirmed this result for phosphorus-doped films and demonstrated that the rate of grain growth is not a function of boron content in boron doped films [2.113]. It has been observed that stress gradients are related directly to phosphorus doping profile and can be minimised by a flat doping profile [2.72]. The properties of in situ phosphorus doped polysilicon films after annealing show an overall agreement with undoped polysilicon films where an increasing phosphorus content tends to decrease residual stress after annealing because of the increased silicon self diffusitivity [2.114]. Also, in situ doping results in a uniform dopant distribution resulting in excellent control of strain gradients.

In this thesis solid source boron indiffusion has been used to produce boron doped polysilicon layers. The effect of solid source boron indiffusion on residual stress is shown in fig. 2.5 for films deposited initially in amorphous

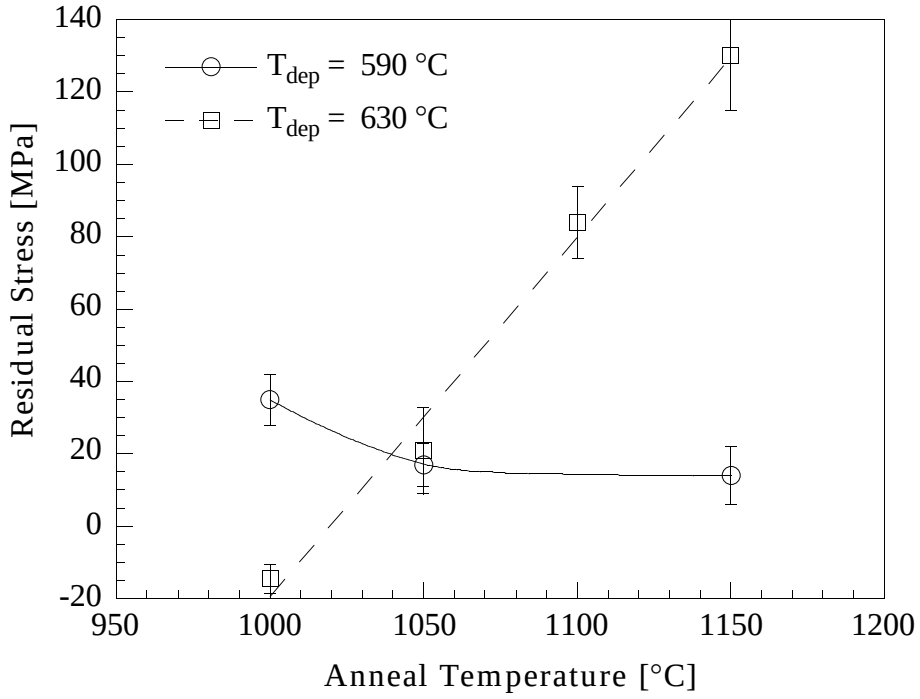

Fig. 2.5 *Residual stress of 2 µm thick polysilicon thin films after solid source boron indiffusion for one hour in N_2 as a function of diffusion temperature for polysilicon films deposited at 250 mTorr, a silane flow of 50 sccm and a temperature of 590 °C and 630 °C.*

(590 °C) and polycrystalline state (630 °C) at a pressure of 250 mTorr and a silane flow of 50 sccm. After boron doping the stress of the initially amorphous films grown at 590 °C decays to small values. For the films grown at 630 °C a stress reversal from compressive to tensile occurs between 1000 and 1050 °C after boron indiffusion. In the strongly {110} oriented films, deposited at 630 °C, an increasing {111} orientation with increasing diffusion temperature is observed by x-ray diffraction. This suggests that this stress reversal is induced by recrystallisation effects and is related to the development of the {111} orientation and not a result of boron doping itself.

2.3 SACRIFICIAL LAYER ETCHING OF SILICON DIOXIDE IN HF SOLUTIONS

Another important process step in surface micromachining is the etching of the sacrificial layer to release the microstructure. For the polysilicon / silicon oxide combination hydrofluoric acid is used for sacrificial layer etching. This takes advantage of the isotropic nature and high selectivity of wet etching to

release overlying structural films. It is important to model and understand this sacrificial layer etching process in order to be able to predict etching times a priori instead of simply extrapolating initial etch rates and using trial and error to fully release microstructures because the etch process is destructive.

2.3.1 Chemical reaction

A heterogeneous reaction model for the etching of sacrificial silicon dioxide layers, as presented by D.J. Monk [2.115,2.116] is shown in fig. 2.6.

The etching can be divided into seven steps: **1** Mass transfer of the reactant by diffusion from the bulk to the external etch opening; **2** Diffusion of the reactant from the etch opening through the etch channels to the immediate vicinity of the internal surface; **3** Adsorption of the reactant; **4** The reaction at the surface; **5** Desorption of the products from the surface; **6** Diffusion of the products from the interior of the etch channels; **7** Subsequent mass transfer of the products from the etch opening to the bulk fluid.

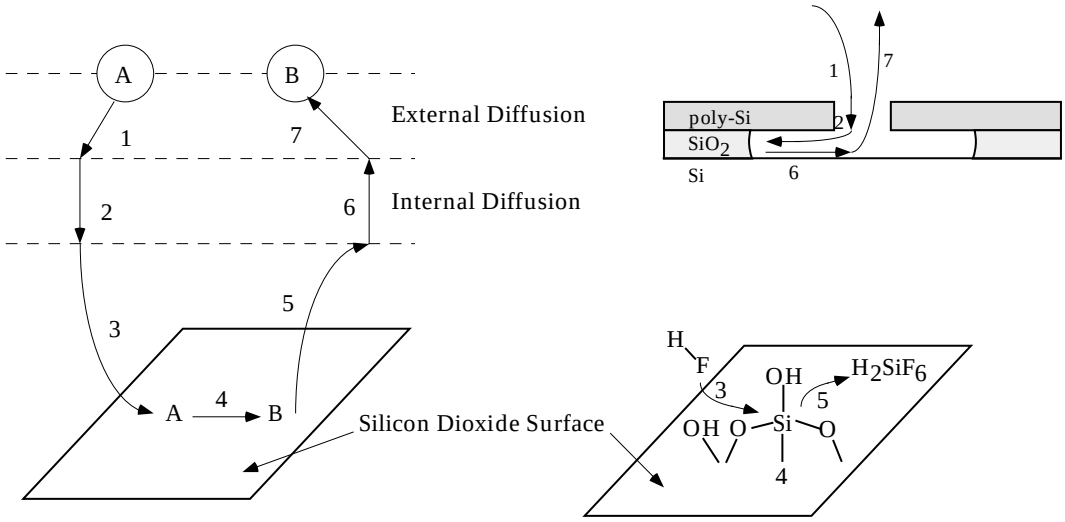

Fig. 2.6 *A model for the etching of sacrificial silicon dioxide layers in micromachining.*

Hydrofluoric acid (HF) is a weak acid, therefore several hydrogen fluoride species are present in the solution. Silicon dioxide (SiO_2) is used in micromachining as an amourphous film which etches isotropically.

Etching is believed to occur in two elementary reactions. First the protons break up the siloxane bonds to form silanol species on the surface. Then the fluorinated species attack the silicon in the silanol nucleophilically to form SiF_4 (g) which is soluble in water and forms H_2SiF_6 (aq). Any fluorinated species in the hydrofluoric acid may supply the fluorine for this reaction.

Silicon dioxide etching is, therefore, much more complicated than the overall reaction that is usually reported:

$$SiO_2 + 6\,HF \Rightarrow H_2SiF_6 + 2\,H_2O \qquad (2.13)$$

2.3.2 Etch rate models

Sacrificial layer etching has been modelled by D.J. Monk by a combination of the diffusion of reactant to the etch surface and the chemical reaction at that surface using respectively Deal-Grove and non-first order models [2.117,2.118], and by J. Liu by using a first and second order combined model [2.119]. In the Deal-Grove (D-G) model, the concentration in the channel is assumed to be linear. If the rate of chemical reaction is assumed to be linearly proportional to the etching front concentration the solution of the D-G model for the first order chemical reaction model is:

$$\delta = -\frac{D}{k} + \sqrt{\left(\frac{D}{k}\right)^2 + \frac{D\,C_b\,MW_{SiO_2}}{3\,\rho_{SiO_2}}\,t} \qquad (2.14)$$

where δ is the etch length, D is the diffusion constant, k is the first-order reaction rate coefficient, C_b is the bulk HF concentration, MW_{SiO2} is the molecular weight of SiO_2, ρ_{SiO2} is the density of SiO_2 and t is the etch time. For specific concentrations this model and non-first-order models fit etching data well. A more universal model which predicts accurately the etching length vs. time over a wide range of HF concentrations has been obtained by using a combined first and second order model which is a specific case of the Freundlich adsorption isotherm reaction-rate model [2.119]. This results in the following first order differential equation for the etch length:

$$\frac{d\delta}{dt} = \frac{MW_{HF}}{4\,\rho_{SiO_2}\,k_2}\left(\frac{D}{\delta}\right)^2\left[1 + b\left(\frac{\delta}{D}\right) - \varphi\right] \qquad (2.15)$$

with

$$b = k_1 + 2\,C_b\,k_2$$
$$\varphi = \sqrt{1 + 2b\left(\frac{\delta}{D}\right) + k_1^{\,2}\left(\frac{\delta}{D}\right)^2} \qquad (2.16)$$

where MW_{HF} is the molecular weight of HF, k_1 is the linear reaction rate constant and k_2 is the quadratic reaction rate constant. This equation can be solved numerically. However instead of searching for solutions of the form $\delta=f(t)$, one can integrate this equation from $\delta=0$ at $t=0$ to δ at time t to find:

$$t = \frac{D\left\{\varphi\,\phi + 2\,k_1^{\,2}\left(\frac{\delta}{D}\right) + b\left(k_1^{\,2}\left(\frac{\delta}{D}\right)^2 - 1\right)\right\}}{8\,a\,C_b\,k_1^{\,2}\,k_2\left(k_1 + C_b\,k_2\right)} - \frac{D}{2\,a\,k_1^{\,3}}\log\frac{\phi + k_1\,\varphi}{2\left(k_1 + C_b\,k_2\right)} \qquad (2.17)$$

where

$$\phi = k_1 + 2\,C_b\,k_2 + k_1^{\,2}\left(\frac{\delta}{D}\right) \qquad (2.18)$$

The coefficients k_1, k_2 and D can be determined by least square fitting of experimental data of the etching process. This has been done for etching of PSG with a phosphorus concentration of 6 wt.% in HF solutions at room temperature. The bulk concentration C_b in the HF solutions was varied from 3.6 to 49 wt.%. The following values have been found; k_1=1.2 x 10^{-4} cm/sec, k_2=6.5 x 10^{-2} cm^4/mole.sec and D=1.6 x 10^{-5} cm^2/sec. The theoretical etch length is shown in fig. 2.7 as a function of the etch time.

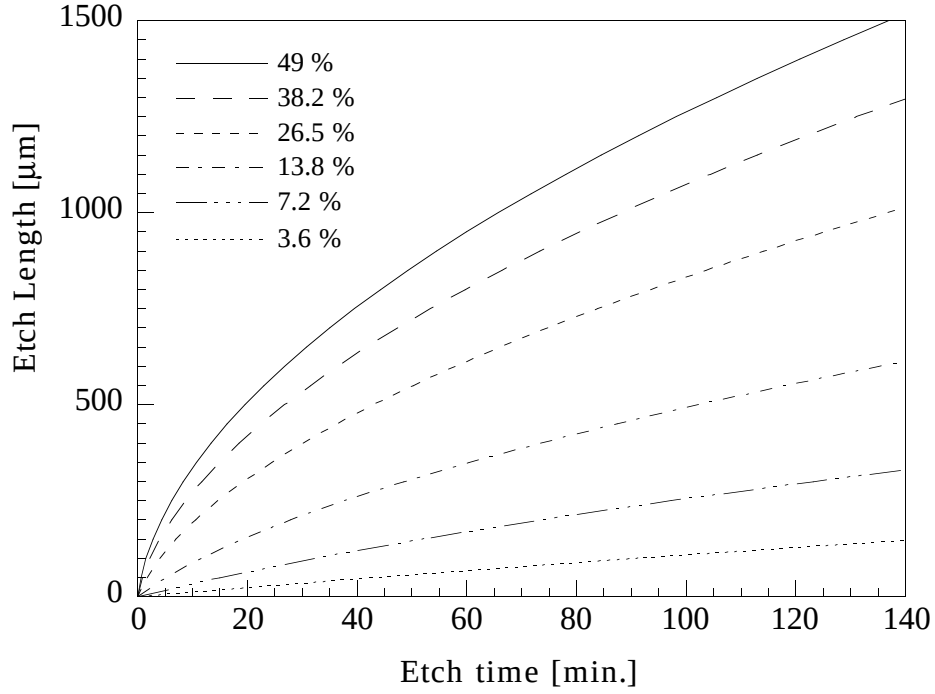

Fig. 2.7 *Modelled sacrificial layer etch length as a function of etch time at different HF concentrations.*

This model was shown to be in excellent agreement with experimental data. At low concentrations, the etching is dominated by a first order chemical reaction. The etching reactions become enhanced in higher concentration hydrofluoric acid solutions. This supports the hypothesis that the etching of silicon dioxide in hydrofluoric acid is a two-step reaction. An overall reaction that consists of two elementary reactions would have a reaction order of two. At low HF concentrations, less of the reactants, H^+ for the first reaction and HF or HF_2^- for the second reaction are present. At high concentrations the etching is dominated by a second order chemical reaction.

Diffusion limitations can be observed after an etch length of approximately 200 µm. This is generally more than the total etch length needed to free micromechanical structures. So, in most cases the total etch time to release a structure can be determined by a linear extrapolation of the etch rate.

Increasing the phosphorus content in the PSG films, increasing the HF concentration, and the addition of HCl to HF solutions increases the initial etch rate of silicon dioxide sacrificial layers [2.120, 2.121]. Buffered HF and surfactant buffered HF did not show to enhance the etching of silicon dioxide sacrificial layers. Etch channel width, structural material choice and stress condition, and applied stress did also not show to affect the sacrificial layer etch rate appreciably. However it was found that thinner sacrificial layers are etched somewhat slower than thicker ones for thicknesses ranging from 0.24 µm to 1.7 µm. Other useful HF solutions are mixtures like HF and glycerol [2.122] or NH_4F and acetic acid [2.123] which etch silicon dioxides without attacking aluminum layers.

Besides undoped oxides and PSG also BPSG as a sacrificial layer has been reported in order to be able to obtain reflow at low temperatures for planarization purposes [2.124].

2.3.3 Attack of polysilicon

Reported values of single crystal silicon etch rates in HF solutions are smaller than 1 Å / min [2.125, 2.126]. Etch selectivity between silicon oxides and silicon is therefore very large. However degradation of thin polysilicon in HF has been reported by Lober, Walker and Monk [2.127-2.129]. As-deposited, tensile, about 0.1 µm thick polysilicon films on PSG crack upon exposure to HF [2.114]. The HF most likely attacks the polysilicon at its grain boundaries, which may undergo sufficient oxidation upon removal from the reactor into the ambient environment. Thin unannealed and annealed polysilicon on LTO

and PSG show blistering at different attack rates. As-deposited compressive films (650 ˚C) do not appear to be affected by HF. Phosphorus has been shown to play a critical role in the susceptibility of polysilicon films to both stress-corrosion cracking and HF penetration. Residual stress and fracture strain were found to decrease, and the Young's modulus was found to increase for undoped polysilicon films exposed for two hours to solutions with increasing HF concentration [2.128].

2.4 METHODS TO PREVENT STICTION

After etching the sacrificial layers in an HF-solution, specific drying procedures are generally required to prevent free structures from sticking to the underlying substrate. Standard drying procedures such as spin drying or air drying produce capillary forces during drying that cause "pull-down" of the thin film structures [2.130-2.133] (see chapter 3). Once physical contact has been made, other forces like van der Waals forces, electrostatic forces, hydrogen bridging, solid bridging and chemical reactions come into play resulting in permanent attachment of the structures to the substrate [2.130-2.139]. Stiction can be prevented or reduced in several ways which can roughly be divided into two groups. First there are methods based upon the prevention of physical contact between the structures and the substrate during the drying process. This can be done by avoiding the attractive meniscus forces that bring the structures in contact with the substrate during the drying process, e.g. by freeze drying [2.140-2.143], critical point drying [2.144], dry etching techniques [2.145-2.149] or by rapid heating of rinse liquids [2.150]. Also temporary increasing the mechanical stiffness of the structures by breakaway supports [2.151], fusible supports [2.152] or stiff membranes that are patterned by dry etching afterwards has been applied [2.153]. Another interesting but barely investigated method for sacrificial layer etching of silicon dioxide without stiction is vapour HF etching [2.127, 2.154]. This technique is commonly used in IC technology for wafer cleaning. The boiling point of HF is 19.54 °C and the temperature of etch samples has to be elevated in order to prevent condensation of HF and water vapour. A general problem resulting from vapour HF etching is the formation of hydrated silica particles as a result of reverse gas phase reactions. Very high yields can be obtained and very large structures have been released without sticking problems [2.154].

All these methods have the disadvantage that stiction can still occur if the structures are brought into contact with the substrate afterward by external forces like large accelerations or static charges [2.143].

Methods that directly reduce the adhesional forces do not have this disadvantage. Adhesional forces can be reduced by minimising the surface energy, for instance by surface treatments [2.134] or by using hydrophobic surfaces [2.155], and by reduction of the real contact area by using stand-off bumps [2.107,2.156] or by increasing the surface roughness [2.157, 2.158]. These methods result in a permanent reduction of the adhesional forces.

Another method that has been presented is to release the structures after stiction has occurred by electromagnetic pulses that lift current carrying structures out of the substrate [2.159].

An elegant way to prevent the in process sticking problem is freeze drying. The freeze drying method has been developed as a drying method for biological specimens by Boyde and Wood in 1969 [2.160]. Guckel [2.140] first implemented this technique for the sacrificial layer etching of surface micromachined structures. In general, during freeze drying a final rinse liquid is frozen by lowering the temperature below its melting point after which the solid is sublimated by lowering the pressure. A P-T diagram showing the freeze drying as well as the super critical drying trajectory is given in fig. 2.8.

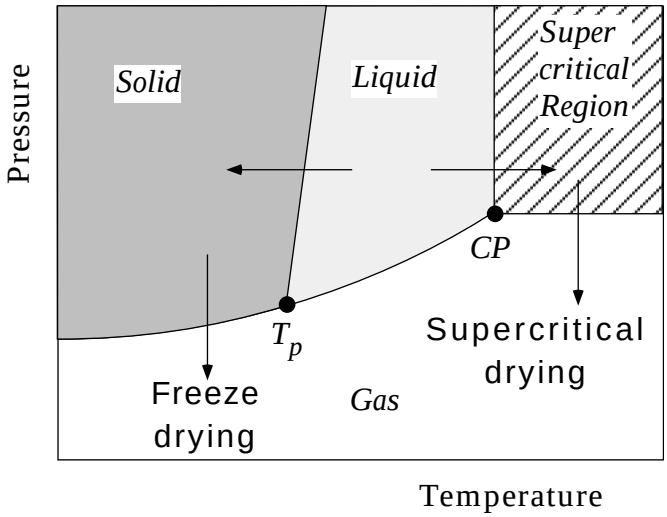

Fig. 2.8 *Sketch of the P-T diagram for a pure substance showing the sublimation process and the triple point T_p, and the supercritical drying process and the critical point CP.*

A fast freeze drying technique that does not require vacuum equipment but can be performed at atmospheric pressures has been used to fabricate the structures that are presented in this thesis. Cyclohexane which freezes at about 6.7˚C is used as the final rinse agent. Freezing and subsequent sublimation is

readily accomplished by placing the substrate under a nitrogen flow on a regulated Peltier element at a temperature below the freezing point as shown in fig. 2.9. The total time for the freeze-sublimation process depends on the geometry of the sample and typically takes a few minutes.

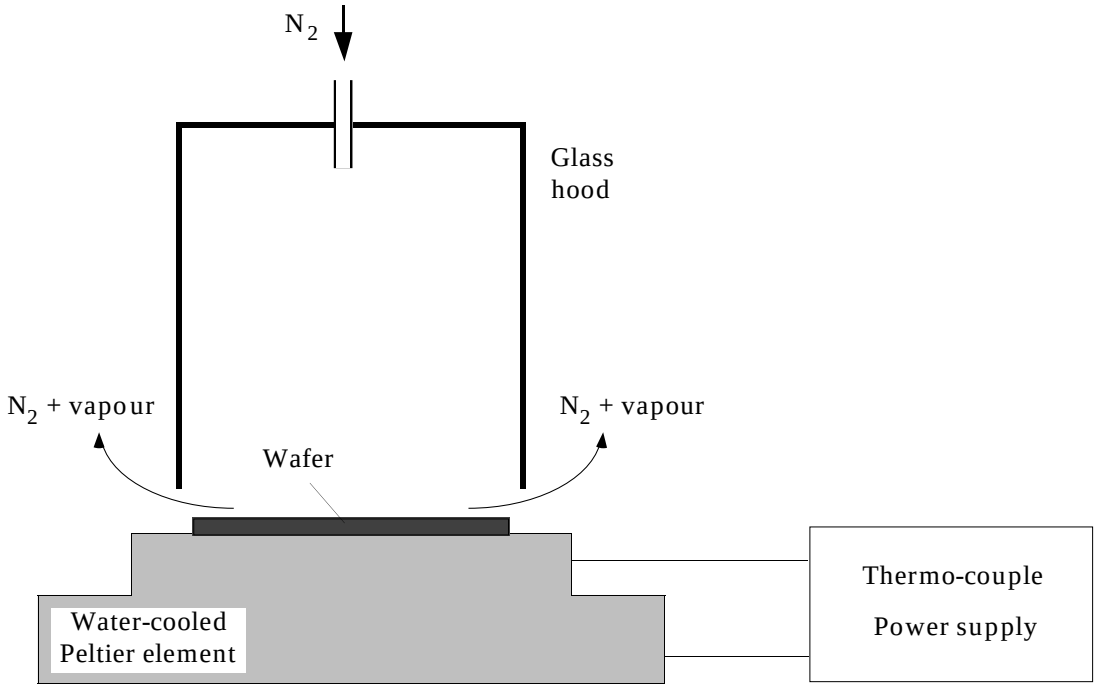

Fig. 2.9 *Schematic of the experimental freeze-drying set-up.*

Details of the rinse-freeze-sublimation procedure are as follows: After sacrificial layer etching in an HF-solution a dilution rinse in DI-water is performed to remove the etchant. Isopropyl alcohol (IPA) is added to keep the hydrophobic wafer surface wet after removal from the solution. The wafers are placed in another beaker containing IPA and are then placed in cyclohexane, the final rinse agent. The IPA serves as an intermediate mixing agent. After rinsing the wafer in cyclohexane, they are placed upon a Peltier element, which has already been cooled down to -10 ˚C and is located under a glass hood. A nitrogen flow aids the sublimation process by removing cyclohexane vapours, and prevents condensation of atmospheric water. After the sublimation is completed, the Peltier element is raised to room temperature. No residues have been observed by optical microscopy and SEM. It was found that temperatures of about -10 ˚C and high nitrogen flows of about several tens of litres / min produce a very high yield for low strain microbridges and cantilever beams with aspect ratios as high as respectively 2000 and 1000 at gap spacings of 2 μm (see fig. 2.10).

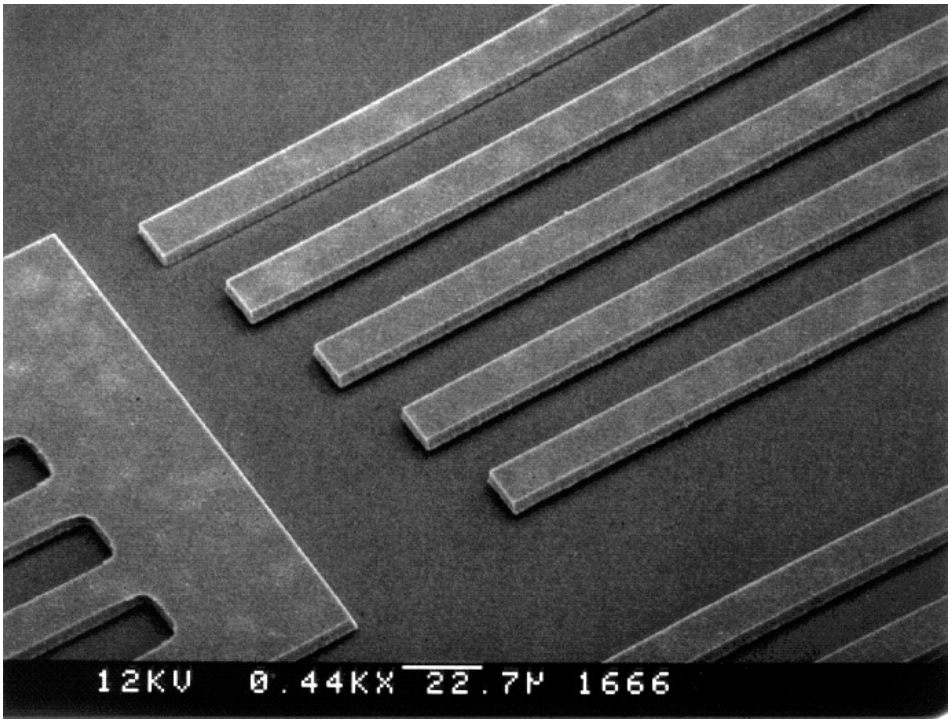

Fig. 2.10 *SEM photograph of 1 mm long polysilicon cantilever beams after the cyclohexane freeze drying technique. The thickness of the beams and the gap spacing is 2 µm. Only one of the beams is sticking.*

2.5 BASIC SURFACE MICROMACHINING PROCESSES

A number of surface micromachining processes will be described that have been used for successful fabrication of elementary components. These components are generally part of more complicated structures and mechanisms. These basic processes (or modifications of them) can be used in conjunction with structural materials other than polysilicon or can be combined together with other designs and processes in order to fabricate more complex micromechanisms.

The fabrication of free standing beams, cantilevers and membranes is based upon the fabrication process that has already been given in the introduction of this chapter. The structures can be used for movements in directions that are perpendicular or lateral to the wafer surface, for example comb drive structures [2.107]. Rotating structures can be fabricated by a center-pin or flange-bearing process [2.11, 2.14]. These fabrication schemes are also useful for the fabrication of sliding structures by extension of the center bearing [2.11]. Structures that rotate out of the wafer plane can be fabricated by a hinge fabrication process

[2.15]. An elegant way to create sealed cavities is the reactive sealing process that is based on surface micromachining techniques [2.7, 2.143, 2.161]. The fabrication steps of these processes will be briefly described below.

2.5.1 Center-pin process

The basic center-pin process uses two polysilicon and two silicon dioxide depositions as well as four lithography steps. Fig. 2.11 shows cross-sectional views of the design during the fabrication process. After a blanket deposition of silicon dioxide, the bushing moulds are time etched to the desired depth in the oxide. After a blanket deposition of polysilicon, the rotor is patterned. The bushings are formed automatically. After a second blanket deposition of silicon dioxide, the bearing anchor is opened. After a second blanket deposition of polysilicon, the center pin bearing is defined. At this point the sacrificial layers can be dissolved in hydrofluoric acid to release the rotor. The center pin process has the capability of producing self-aligned or non-self-aligned bearings.

2.5.2 Flange-bearing process

The basic flange bearing process uses two polysilicon and two silicon dioxide depositions as well as four lithography steps (see fig. 2.12). The overall process is similar to the center-pin process and uses only minor modifications. For the same number of film depositions, the flange bearing process provides more flexibility in design as compared with the center-pin process. After a blanket deposition of silicon dioxide, a blanket layer of polysilicon is deposited. The rotor or slider is patterned into the polysilicon layer. At this point the oxide at the inner (or outer or both) sides is under etched. After a second blanket deposition of silicon dioxide , the bearing anchor is opened. After a second deposition of polysilicon, the bearing is defined. Note that the flange in the bearing forms automatically and the bearing is self-aligned. After release the rotor rests on the bearing flange.

2.5.3 Hinge fabrication process

In fig. 2.13 a surface micromachining process is shown that allows structures to be rotated out of the plane of the wafer after fabrication. The structures rotate about hinges whose axes are in the plane of the wafer. The hinge fabrication process starts with the deposition and patterning of a first sacrificial layer. Then a structural polysilicon layer is deposited and patterned and a second sacrificial

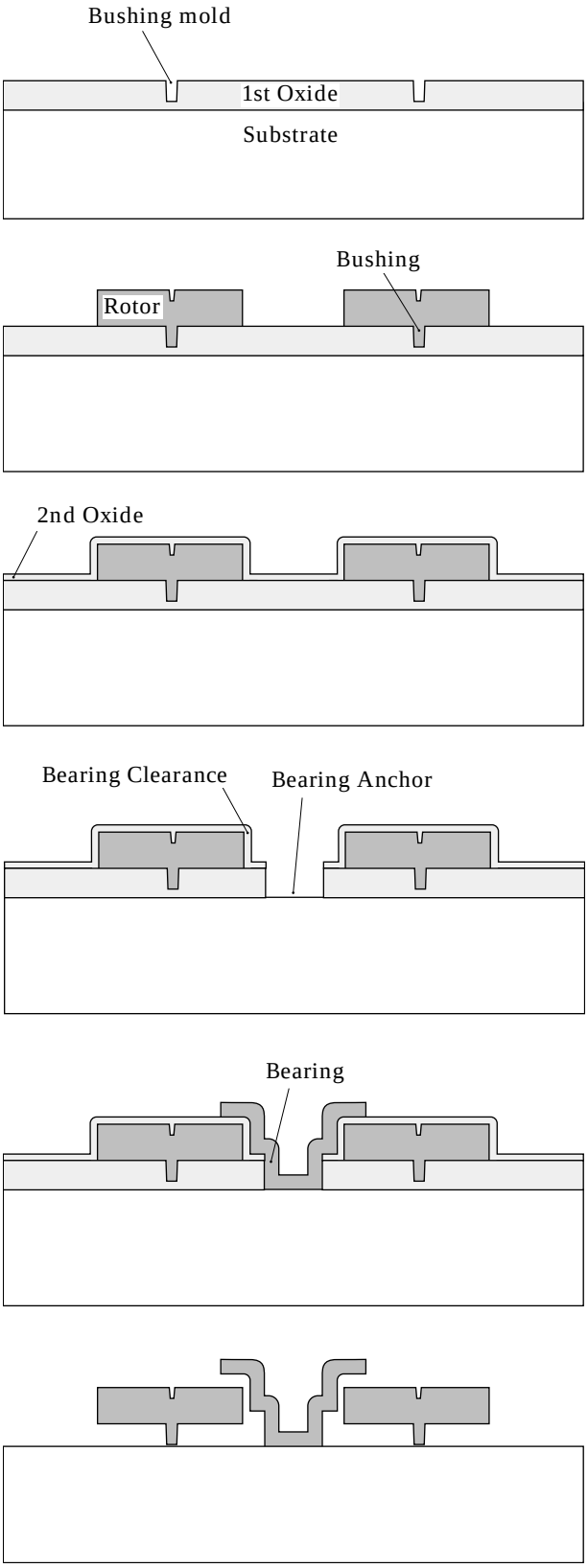

Fig. 2.11 *The center-pin process.*

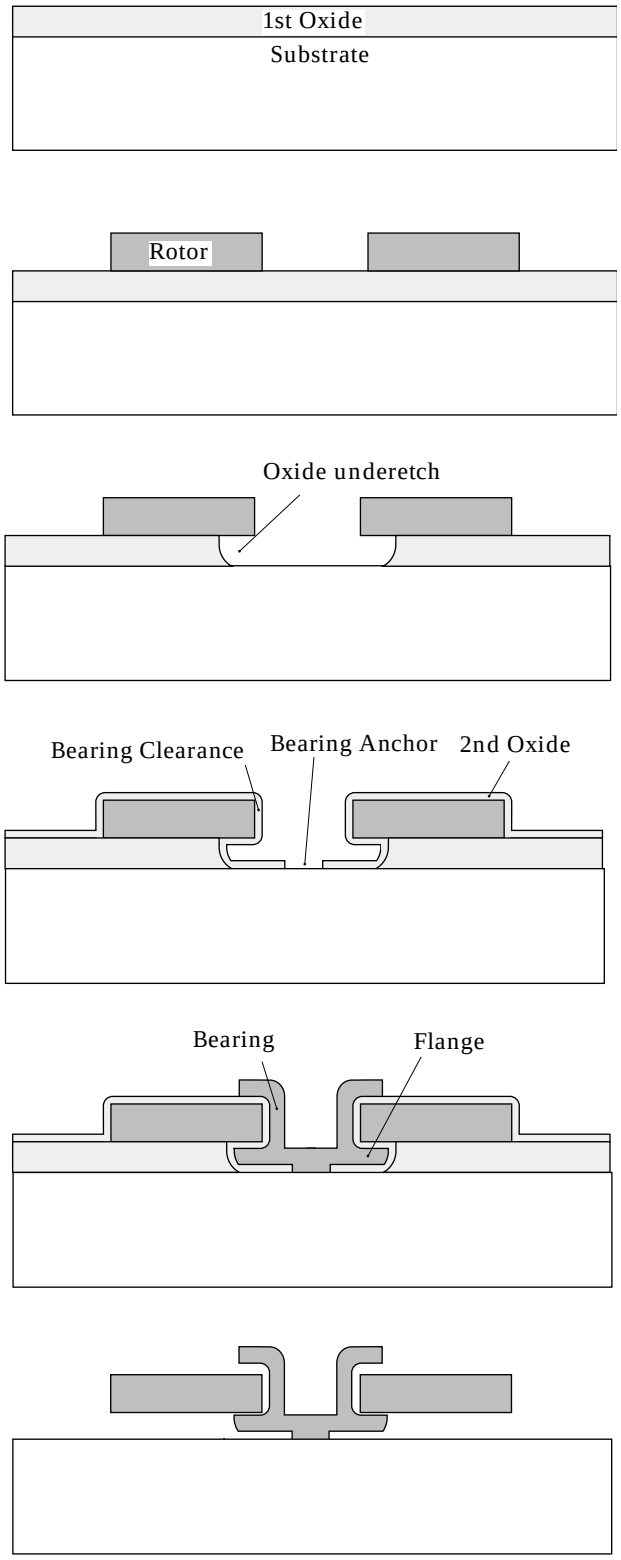

Fig. 2.12 *The flange-bearing process.*

layer is deposited and patterned. Anchors are etched and a second structural layer is deposited and patterned. An anneal step is used to remove polysilicon residual strain and dope the polysilicon layers when doped oxides are used as the sacrificial layers. Sacrificial layer etching in an HF solution frees the structures. Different types of hinges can be produced like a pin hinge, that hinges a piece of structural silicon to the substrate, and a scissor hinge, connecting two released pieces together.

2.5.4 Reactive sealing

The reactive sealing technique as developed by Guckel and Burns [2.7] can be used to create sealed cavities. These cavities may contain low pressures inside, depending on the sealing technique. Sealed cavities are made by defining thin regions of the sacrificial layer at the perimeter of the structure (see fig. 2.14). After removal of the sacrificial layer thin film deposition methods can be used to seal the narrow openings. The cavity pressure after sealing is a function of the processing conditions like pressure and temperature, and subsequent (out)diffusions and chemical reactions. The reactive sealing process starts with the deposition and patterning of a first sacrificial layer. Then a thin sacrificial layer is deposited and patterned to define anchors for the polysilicon cap structure. The next step is deposition of polysilicon that is subsequently patterned to form the cap structure. The sacrificial layers are etched which is followed by rinsing and drying procedures. Now the reactive sealing process will close the cavity. Typical processes that have been used for sealing are thermal oxidation, LPCVD of polysilicon and LPCVD of silicon nitride.

2.5.5 Special Techniques

Besides these basic fabrication processes some special techniques have been used. By adding an anisotropic etch step in the sacrificial layer highly compliant lateral suspensions using sidewall beams can be fabricated [2.162].

The attack of underlying oxide through defects in polysilicon grain boundaries in case of thin polysilicon films can be used to create permeable polysilicon etch-access windows [2.163] that are useful for fast removal of sacrificial layers and encapsulation purposes. With a combination of these two techniques it is possible to realise hollow polysilicon beams [2.164].

Deep anisotropic etching of the substrate can be used to create high aspect ratio milli-scale polysilicon structures by trench refill with the sacrificial and polysilicon layer [2.165]. Finally resistive cutting, welding and heating has been applied to attach, release and reshape polysilicon structures [2.166, 2.167].

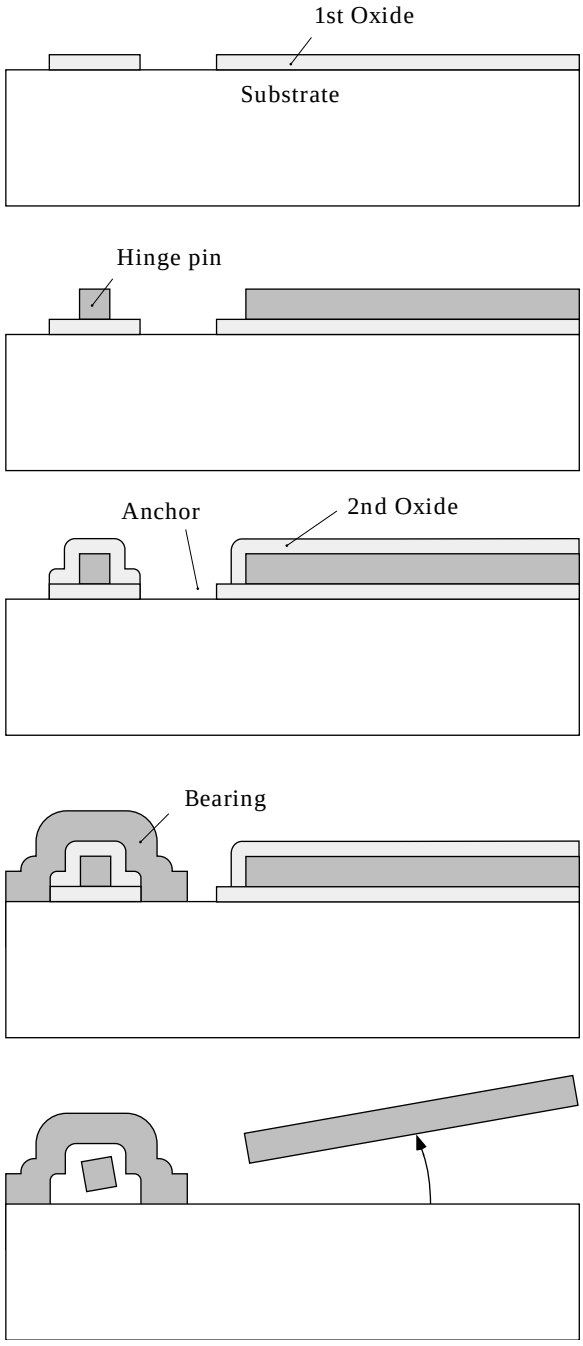

Fig. 2.13 *Hinge fabrication process.*

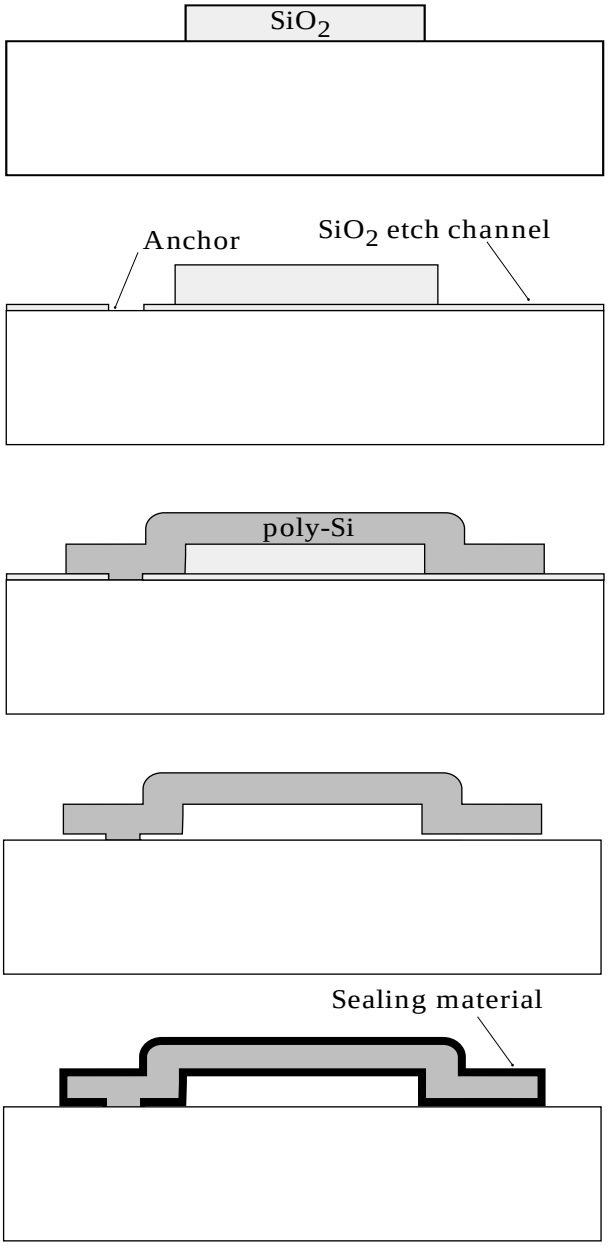

Fig. 2.14 *Reactive sealing process.*

2.6 CONCLUSIONS

Surface micromachining has extended the possibilities and applications of micromachining techniques. Mechanical structures with more than one degree of freedom can be realised with this technique. Polysilicon surface micromachining is based upon the selective removal of sacrificial layers from a multilayer sandwich of patterned thin films consisting of sacrificial silicon oxide layers and structural polysilicon thin films. The residual stress in polysilicon thin films can be controlled and most of the mechanical properties of polysilicon films have been characterised. The silicon oxide sacrificial layer etch process has been modelled and methods to prevent stiction have been developed. A variety of fabrication processes has been presented and the possibility to integrate electronics has been demonstrated. The feasibility of surface micromachining has already been illustrated by a large number of devices and applications. A wide variety of structures have been realised with applications in mechanical test structures, resonators, sensors, actuators, mechanical interconnections and electronics. This makes polysilicon surface micromachining a well developed and versatile technology. Further development and improvement of materials, fabrication techniques and processes will certainly lead to improved or new devices and applications of micromachining techniques.

REFERENCES

[2.1] K. E. Petersen, Silicon as a mechanical material, Proc. IEEE, 70 (198), pp. 420-457.

[2.2] H. Seidel, The mechanism of anisotropic silicon etching and its relevance for micromachining, Proc. Int. Conf. Solid-State Sensors and Actuators (Transducers '87), Tokyo, Japan, 1987, pp. 120-125.

[2.3] B. Hök, Micromechanics and micromachining of semiconductor sensors, Acta Polytechnica Scandinavia El. Eng. Series, E163 (1988), pp. 65-84.

[2.4] W. Ehrfeld, P. Bley, F. Götz. P. Hagmann, A. Maner, J. Mohr, H. O. Moser. D. Münchmeyer, W. Schelb, D. Schmodt and E. W. Becker, Fabrication of microstructures using the LIGA process, IEEE ,1987.

[2.5] H. Guckel, T. Christenson and K. Skrobis, Metal micromechanisms via deep X-ray lithography, electroplating and assembly, J. Micromech. Microeng., 2 (1992), pp. 225-228.

[2.6] A. Rogner, J. Eicher, D. Münchmeyer, R. P. Peters and J. Mohr, The LIGA technique-What are the new opportunities, J. Micromech. Microeng., 2 (1992), pp. 133-140.

[2.7] H. Guckel and D. W. Burns, A technology for integrated transducers, Proc. Int. Conf. Solid-State Sensors and Actuators (Transducers '85), Philadelphia, PA, U. S. A., June 11-14, 1985, pp. 90-92.

[2.8] R. T. Howe, Surface micromachining for microsensors and microactuators, J. Vac. Sci. Technol., B 6 (6) (1988), pp. 1809-1813.

[2.9] Surface micromachining, C. Linder, L. Paratte, M. A. Gretillat, V. P. Jaecklin and N. F. de Rooij, J. Micromech. Microeng., 2 (1992), pp. 122-132.

[2.10] R.S. Muller, Microdynamics, Proc. 5th Int. Conf. Solid-State Sensors and Actuators (Transducers '89), Montreux, Switzerland, June 25-30, 1989, pp. 1-8.

[2.11] L. S. Fan, Y. C. Tai and R. S. Muller, Integrated movable micromechanical structures for sensors and actuators, IEEE Trans. on El. Dev., 35 (6) (1988), pp. 724-730.

[2.12] M. Mehregany, K. J. Gabriel and W. S. N. Trimmer, Integrated fabrication of polysilicon mechanisms, IEEE Trans. on El. Dev., 35 (6) (1988), pp. 719-723.

[2.13] F. Behi, M. Mehregany and K. J. Gabriel, A microfabricated three-degree-of-freedom parallel mechanism, Proc. IEEE Micro Electro Mechanical Systems, Napa Valley, CA, U.S.A., Feb. 11-14, 1990, pp. 159-165.

[2.14] M. Mehregany and Y. C. Tai, Surface micromachined mechanisms and micromotors, J. Micromech. Microeng., 1 (1991), pp. 73-85.

[2.15] K. S. J. Pister, M. W. Judy, S. R. Burgett and R. S. Fearing, Microfabricated hinges, Sensors and Actuators A, 33 (1992), pp. 249-256.

[2.16] H. C. Nathanson, W. E. Newell, R. A. Wickstrom and J.R. Davis jr., The resonant gate transistor, IEEE Trans. on El. Dev., ED-14 (1967), pp. 117-133.

[2.17] R.T. Howe and R.S. Muller, Polycrystalline silicon micromechanical beams, J. Electrochem. Soc., 130 (1983), pp. 1420-1423.

[2.18] H. Guckel, D. K. Showers, D. W. Burns and C. R. Rutigliano, Deposition techniques and properties of strain compensated LPCVD silicon nitride films, Proc. IEEE Solid-State Sensors Workshop, Hilton Head Island, SC, U.S.A., June 2-5, 1986.

[2.19] M. A. Schmidt, R. T. Howe and S. D. Senturia, Surface micromachining of polyimide / metal composites for a shear-stress sensor, Proc. IEEE Micro Robots and Teleoperators Workshop, Hyannis, MA, U.S.A., Nov. 9-11, 1987.

[2.20] L. Y. Chen, Z. L. Zhang, J. J. Yao, D. C. Thomas and N. C. MacDonald, Selective chemical vapor deposition of tungsten for microdynamic structures, Proc. IEEE Micro Electro Mechanical Sytems, Salt Lake City, Utah, February 20-22, 1989, pp. 60-65.

[2.21] K. Hjort, J. Schweitz and B. Hök, Bulk and surface micromachining of GaAs structures, Proc. IEEE Micro Electro Mechanical Systems, Napa Valley, CA, U.S.A., Feb. 11-14, 1990, pp. 73-76.

[2.22] Y. W. Kim and M. G. Allen, Surface micromachined platforms using electroplated sacrificial layers, Proc. Int. Conf. on Solid-State Sensors and Actuators, (Transducers '91), San Fransisco, CA, U. S. A., June 24-27, 1991, pp. 651-654.

[2.23] S. Chang, W. Eaton, J. Fulmer, C. Gonzalez, B. Underwood, J. Wong and R.L. Smith, Micromechanical structures in amourphous silicon, Proc. Int. Conf. on Solid-State Sensors and Actuators, (Transducers '91), San Fransisco, CA, U. S. A., June 24-27, 1991, pp. 751-754.

[2.24] R. C. Anderson, R.S. Muller and C.W. Tobias, Laterally grown porous polycrystalline silicon:a new material for transducer applications, Proc. Int. Conf. on Solid-State Sensors and Actuators, (Transducers '91), San Fransisco, CA, U. S. A., June 24-27, 1991, pp. 747-750.

[2.25] K. Yamada and T. Kuriyama, A new modal mode controlling method for a surface format surrounding mass accelerometer, Proc. Int. Conf. on Solid-State Sensors and Actuators, (Transducers '91), San Fransisco, CA, U. S. A., June 24-27, 1991, pp. 655-658.

[2.26] O. Tabata, K. Shimaoka and S. Sugiyama, In situ observation and analysis of wet etching process for micro electro mechanical systems, Proc. IEEE Micro Electro Mechanical Systems, Ford Lauderdale, Florida, U.S.A., Feb. 7-10, 1993, pp. 99-102.

[2.27] K. Petersen, D. Gee, F. Pourahmadi, R. Craddock, J. Brown and L. Christel, Surface micromachined structures fabricated with silicon fusion bonding, Proc. Int. Conf. on Solid-State Sensors and Actuators, (Transducers '91), San Fransisco, CA, U. S. A., June 24-27, 1991, pp. 397-399.

[2.28] P.R. Scheeper, W. Olthuis and P. Bergveld, Fabrication of a subminiature silicon condenser microphone using the sacrificial layer technique, Proc. 6th Int. Conf. Solid-State Sensors and Actuators (Transducers '91), San Fransisco, CA, USA, June 24-27, pp. 408-411.

[2.29] Z. L. Zhang and N. C. MacDonald, An RIE process for submicron, silicon electromechanical structures, Proc. Int. Conf. on Solid-State Sensors and Actuators, (Transducers '91), San Fransisco, CA, U. S. A., June 24-27, 1991, pp. 520-523.

[2.30] R.H. Hackett, L.E. Larson and M.A. Melendes, The integration of micro-machine fabrication with electronic device fabrication on III-V semiconductor materials, Proc. Int. Conf. on Solid-State Sensors and Actuators, (Transducers '91), San Fransisco, CA, U. S. A., June 24-27, 1991, pp. 51-54.

[2.31] T. Hirano, T. Furuhata and H. Fujita, Dry releasing of electroplated rotational and overhang structures, Proc. IEEE Micro Electro Mechanical Sytems, Fort Lauderdale, Fl, U.S.A., February 7-10, 1993, pp. 278-283.

[2.32] J. Bernstein, S. Cho, A.T. King, A Kourepenis, P. Maciel and M. Weinberg, A micromechanical comb-drive tuning fork rate gyroscope, Proc. IEEE Micro Electro Mechanical Systems, Ford Lauderdale, Florida, U.S.A., Feb. 7-10, 1993, pp. 143-148.

[2.33] SOI (SIMOX) as a substrate for surface micromachining of single crystalline silicon sensors and actuators, Proc. Int. Conf. om Solid-State Sensors and Actuators (Transducers '93), Yokohama, Japan, June 7-10, 1993,pp. 233-236.

[2.34] C. W. Stroment, D. A. Borkholder, V. A. Westerlind, J. W. Suh, N. I. Maluf and G. T. A. Kovacs, Flexible, dry-released process for aluminum electrostatic actuators, Journal of Microelectromechanical Systems, Vol. 3, No. 3, Sept. 1994, pp. 90-96.

[2.35] L. S. Fan, S. J. Woodman, R. C. Moore, L. Crawforth, T. C. Reiley and M. A. Moser, Batch fabricated area-efficient milli-actuators, Proc. Solid-State Sensor and Actuator Workshop, Hilton Head Island, SC, U. S. A., June 13-16, 1994, pp. 38-42.

[2.36] J. Buhler, J. Funk, F.P. Steiner, P.M. Sarro and H. Baltes, Double pass metallization for CMOS aluminum actuators, Proc. 8th Int. Conf. Solid-State Sensors and Actuators (Transducers '95), Stockholm, Sweden, June 25-29, 1995, Vol. 2, pp. 360-363.

[2.37] R. T. Howe and R. S. Muller, Resonant-microbridge vapor sensor, IEEE Trans. Electron Devices, ED-33 (1986), pp. 499-506.

[2.38] M. Parameswaran, H. P. Baltes and A. M. Robinson, Polysilicon microbridge fabrication using standard CMOS technology, Proc. Solid-State Sensor and Actuator Workshop, Hilton Head Island, SC, U. S. A., June 6-9, 1988, pp. 148-150.

[2.39] M. W. Putty, S. C. Chang, R. T. Howe, A. L. Robinson and K. D. Wise, One-port active polysilicon resonant microstructures, Proc. IEEE Micro Electro Mechanical Sytems, Salt Lake City, Utah, February 20-22, 1989, pp. 60-65.

[2.40] J.M. Bustillo, G.K. Fedder, C.T.C. Nguyen and R.T. Howe, Process technology for the modular integration of CMOS and polysilicon microstructures, Microsystem Technologies, Vol. 1, 1994, pp. 30-41.

[2.41] M.A. Gretillat, P. Thiebaud, N.F. deRooij and C. Linder, Electrostatic polysilicon microrelays integrated with MOSFETs, Proc. IEEE Micro Electro Mechanical Systems, Oiso, Japan, Jan. 25-28, 1994, pp. 97-101.

[2.42] M. Biebl, T. Scheiter, C. Hierold, H.v. Philipsborn and H. Klose, Micromechanics compatibel with an 0.8 μm CMOS process, Sensors and Actuators, A46-47, 1995, pp. 593-597.

[2.43] R.T. Howe, Polysilicon integrated microsystems: technologies and applications, Proc. 8th Int. Conf. Solid-State Sensors and Actuators (Transducers '95), Stockholm, Sweden, June 25-29, 1995, Vol. 1, pp. 43-46.

[2.44] C. T. Rosenmayer, F. R. Brotzen and R. J. Gale, Mechanical testing of thin films, Proc. Materials Research Society Symp., Boston, MA, U.S.A., November 28-30, 1988, Vol. 130, pp. 77-86.

[2.45] F. Maseeh, M. A. Schmidt, M. G. Allen and S. D. Senturia, Calibrated measurements of eleastic limit, modulus and the residual stress of thin films using micromachined suspended structures, Proc. IEEE Solid-State Sensor and Actuator Workshop, Hilton Head Island, SC, U. S. A., June 6-9, 1988, pp. 84-87.

[2.46] J. Koskinen, J.E. Steinwall, R. Soave and H.H. Johnson, Microtensile testing of free-standing polysilicon fibers of various grain sizes, J. Micromech. Microeng., Vol. 3, 1993, pp. 13-17.

[2.47] G. G. Stoney, The tension of metallic films deposited by electrolysis, Proc. Roy. Soc. London, Vol. 9 (1909), p. 172.

[2.48] N.A. Winfree, Y.C. Tai, W. Hsieh and R. Wu, The effects of boundary conditions on implementing the Stoney formula for stress measurement, Proc. 7th Int. Conf. Solid-State Sensors and Actuators (Transducers '93), Yokohama, Japan, June 7-10, pp. 179-182.

[2.49] Y.S. Chen and H. Fatemi, Stress measurements on multilevel thin film dielectric layers used in Si integrated circuits, J. Vac. Sci. Technol. A, 4 (3), 1986, pp. 645-649.

[2.50] E. I. Bromley, J. N. Randall, D. C. Flanders and R. W. Mountain, A technique for the determination of stress in thin films, J. Vac. Sci. Technol. B 1 (4), Oct.-Dec. (1983), pp. 1364-1366.

[2.51] O. Tabata, K. Kawahata, S. Sugiyama and I. Igarashi, Mechanical property measurements of thin films using load-deflection of composite rectangular membrane, Proc. IEEE Micro Electro Mechanical Systems, Salt Lake City, Utah, U.S.A., Feb. 20-22, 1989, pp. 152-156.

[2.52] M. Mehregany, M. G. Allen and S. D. Senturia, The use of micromachined structures for the measurement of mechanical properties and adhesion of thin films, Proc. IEEE Solid-State Sensor and Actuator Workshop, Hilton Head Island, SC, U. S. A., June 2-5, 1986.

[2.53] S. Hong, T. P. Weihs, J. C. Bravman and W. D. Nix, Measuring stifnesses and residual stresses of silicon nitride thin films, Journal of Electronic Materials, Vol. 19, No. 9, 1990, pp. 903-909.

[2.54] M. K. Small, J. J. Vlassak, S. F. Powell, B. J. Daniels and W. D. Nix, Accuracy and reliability of bulge test experiments, Proc. Materials Research Society Symp., San Francisco, CA, U.S.A., April 12-16, 1993, Vol. 308, pp. 159-164.

[2.55] D. Maier-Schneider, J. Maibach and E. Obermeier, Computer-aided characterization of the elastic properties of thin films, J. Micromech. Microeng., Vol. 2, 1992, pp. 173-175.

[2.56] J. Y. Pan, P. Lin, F. Maseeh and S. D. Senturia, Verification of FEM analysis of load-deflection methods for measuring mechanical properties of thin films, Proc. IEEE Solid-State Sensor and Actuator Workshop, Hilton Head Island, SC, U. S. A., June 4-7, 1990, pp. 70-73.

[2.57] Y. C. Tai and R. S. Muller, Measurement of Young's modulus on microfabricated structures using a surface profiler, Proc. IEEE Micro Electro Mechanical Systems, Napa Valley, CA, U.S.A., Feb. 11-14, 1990, pp. 147-152.

[2.58] R.P. Vinci and J.C. Bravman, Mechanical testing of thin films, Proc. 6th Int. Conf. Solid-State Sensors and Actuators (Transducers '91), San Fransisco, CA, USA, June 24-27, pp. 943-948.

[2.59] T. P. Weihs, S. Hong, J. C. Bravman and W. D. Nix, Measuring the strength and stiffness of thin film materials by mechanically deflecting cantilever microbeams, Proc. Materials Research Society Symp., Boston, MA, U.S.A., November 28-30, 1989, Vol. 130, pp. 87-92.

[2.60] J. Schweitz, Characterization of mechanical properties of thin films, Proc. 3rd European workshop on micromachining, micromechanics and microsystems,m Leuven, Belgium, June 1-2, 1992, pp. 56-85.

[2.61] K. E. Crowe and R. L.Smith, A new technique for determination of tensile stress in thin films, J. Electrochem.Soc. , Vol. 136, No. 5, May 1989, pp. 1566-1568.

[2.62] K. E. Petersen and C. R. Guarnieri, Young's modulus measurements of thin films using micromechanics, J. Appl. Phys. 50 (11), Nov. 1979, pp. 6761-6766.

[2.63] L. M. Zhang, D. Uttamchandani and B. Culshaw, Measurements of the mechanical properties of silicon microresonators, Sensors and Actutors A, 29, 1991, pp. 79-84.

[2.64] L. Kiesewetter, J.M. Zhang, D. Houdeau and A. Steckenborn, Determination of Young's moduli of micromechanical thin films using the resonance method, Sensors and Actuators, A 35, 1992, pp. 153-159.

[2.65] H. A. C. Tilmans and R. Legtenberg, Electrostatically driven vacuum-encapsulated polysilicon resonators-Part II Theory and performance, Sensors and Actuators A, 45 (1994), pp. 67-84.

[2.66] J Elders, H.A.C. Tilmans, S. Bouwstra and M. Elwenspoek, Mechanical parameter extraction using resonant structures, Proc. Materials Research Society Symp., San Francisco, CA, U.S.A., April 12-16, 1993, Vol. 308, pp. 171-176.

[2.67] H. Guckel, T. Randazzo and D. W. Burns, A simple technique for the determination of mechanical strain in thin films with application to polysilicon, J. Appl. Phys, 57 (5) (1985), pp. 1671-1675.

[2.68] H. Guckel, D. Burns, C. Rutigliano, E. Lovell and B. Choi, Diagnostic microstructures for the measurement of intrinsic strain in thin films, J. Micromech. Microeng. 2 (1992), pp. 86-95.

[2.69] R. Mutikainen and M. Orpana, Silicon surface micromachined structures for the stress measurement of thin films, Proc. Materials Research Society Symp., San Francisco, CA, U.S.A., April 12-16, 1993, Vol. 308, pp. 153-158.

[2.70] T. A. Lober, J. Huang, M. A. Schmidt and S.D. Senturia, Characterization of the mechanisms producing bending moments in polysilicon micro-cantilever beams by interferometric deflection measurements, Proc. IEEE Solid-State Sensor and Actuator Workshop, Hilton Head Island, SC, U. S. A., June 6-9, 1988, pp. 92-95.

[2.71] L.S. Fan, R.S. Muller, W. Yun, R.T. Howe and J. Huang, Spiral microstructures for the measurement of average strain gradients in thin films, Proc. IEEE Micro Electro Mechanical Systems, Napa Valley, CA, U.S.A., Feb. 11-14, 1990, pp. 177-181.

[2.72] M.A. Benitez, J. Esteve, M.S. Benrakkad, J.R. Morante, J. Samitier and J.A. Schweitz, Stress profile characterization and test structures analysis of single and double ion implanted LPCVD polycrystalline silicon, Proc. 8th Int. Conf. Solid-State Sensors and Actuators (Transducers '95), Stockholm, Sweden, June 25-29, 1995, Vol. 2, pp. 88-91.

[2.73] M. Mehregany, R. Howe and S. Senturia, Novel microstructures for the in situ measurement of the mechanical properties of thin films, J. Appl. Phys, Vol. 62 (9), 1987, pp. 3579-3584.

[2.74] B. P. van Drieënhuizen, J.F.L. Goosen, P.J. French and R.F. Wolffenbuttel, Comparison of techniques for measuring both compressive and tensile stress in thin films, Sensors and Actuators, A 37-38, 1993, pp. 756-765.

[2.75] L. Lin, R. T. Howe and A. P. Pisano, A passive, In situ micro strain gauge, Proc. IEEE Micro Electro Mechanical Systems, Fort Lauderdale, Fl, U. S. A., February 7-10, 1993, pp. 201-206.

[2.76] F. Ericson, S. Greek, J. Söderkvist and J.A. Schweitz, High sensitive internal film stress measurement by an improved micromachined indicator structure, Proc. 8th Int. Conf. Solid-State Sensors and Actuators (Transducers '95), Stockholm, Sweden, June 25-29, 1995, Vol. 2, pp. 84-87.

[2.77] Y. B. Gianchandani and K. Najafi, A compact passive strain sensor with a bent beam deformation multiplier and a complementary motion vernier, Proc. IEEE Solid-State Sensor and Actuator Workshop, Hilton Head Island, SC, U. S. A., June 13-16, 1994, pp. 116-118.

[2.78] R. I. Pratt, G. C. Johnson, R. T. Howe and J. C. Chang, Micromechanical structures for thin film characterization, Proc. Int. Conf. on Solid-State Sensors and Actuators, (Transducers '91), San Fransisco, CA, U. S. A., June 24-27, 1991, pp. 205-208.

[2.79] M. Biebl, G. Brandl and R.T. Howe, Young's modulus of in situ Phosphorus-doped polysilicon, Proc. 8th Int. Conf. Solid-State Sensors and Actuators (Transducers '95), Stockholm, Sweden, June 25-29, 1995, Vol. 2, pp. 80-83.

[2.80] K. Najafi and K. Suzuki, A novel method and structure for the measurement of intrinsic stress and Young's modulus of thin films, Proc. IEEE Micro Electro Mechanical Systems, Salt Lake City, Utah, U.S.A., Feb. 20-22, 1989, pp. 96-97.

[2.81] P. M. Osterberg, R. K. Gupta, J. R. Gilbert and S. D. Senturia, Quantitative models for the measurement of residual stress, Poisson ratio and Young's modulus using electrostatic pull-in of beams and diaphragms, Proc. IEEE Solid-State Sensor and Actuator Workshop, Hilton Head Island, SC, U. S. A., June 13-16, 1994, pp. 184-188.

[2.82] Y. C. Tai and R. S. Muller, Fracture strain of LPCVD polysilicon, Proc. IEEE Solid-State Sensor and Actuator Workshop, Hilton Head Island, SC, U. S. A., June 6-9, 1988, pp. 88-90.

[2.83] S. Greek, F. Ericson, S/ Johansson and J.A. Schweitz, In situ tensile strength measurement of thick-film and thin film micromachined structures, Proc. 8th Int. Conf. Solid-State Sensors and Actuators (Transducers '95), Stockholm, Sweden, June 25-29, 1995, Vol. 2, pp. 56-59.

[2.84] L.S. Fan, R.T. Howe and R.S. Muller, Fracture toughness characterization of brittle thin films, Proc. 5th Int. Conf. Solid-State Sensors and Actuators (Transducers '89), Montreux, Switzerland, June 25-30, 1989, pp. 872-874.

[2.85] J.M. Zhang, L. Kiesewetter, D. Houdeau and A. Steckenborn, In-situ measurement of the fracture strength of thin films, 3rd Int Conf. on Micro Electro, Opto, Mechanical Systems and Components (Microsystems '92), Berlin, Germany, Oct. 21-23, 1992, pp. 177-194.

[2.86] M. Biebl, H. von Philipsborn, Fracture strength of doped and undoped polysilicon, Proc. 8th Int. Conf. Solid-State Sensors and Actuators (Transducers '95), Stockholm, Sweden, June 25-29, 1995, Vol. 2, pp. 72-75.

[2.87] H.J. McSkimin, W.L. Bond, E. Buehler and G.K. Teal, Measurement of the elastic constants of silicon single crystals and their thermal coefficients, Phys. Rev, Vol. 83, 1951, p. 1080.

[2.88] L. S. Fan and R. S. Muller, As-deposited low-strain LPCVD polysilicon, Proc. IEEE Solid-State Sensor and Actuator Workshop, Hilton Head Island, SC, U. S. A., June 6-9, 1988, pp. 55-58.

[2.89] H. Guckel, D. W. Burns, H. A. C. Tilmans, D. W. DeRoo and C. R. Rutigliano, Mechanical properties of fine grained polysilicon: The repeatability issue, Proc. IEEE Solid-State Sensor and Actuator Workshop, Hilton Head Island, SC, U. S. A., June 6-9, 1988, pp. 96-99.

[2.90] S. Guo, D. Zou and W. Wang, Theoretical calculation for the Young's modulus of poly-Si and a-Si films, Mat. Res. Soc. Symp. Proc. Vol. 276, (1992), pp. 233-238.

[2.91] G.L. Pearson, W.T.Read and W.L. Feldmann, Deformation and fracture of small silicon crystals, Acta Metallurgica, Vol. 5, Apr. 1957, pp. 181-191.

[2.92] T.I. Kamins, Design Properties of polycrystalline silicon, Sensors and Actuators, A21-A23 (1990), pp. 817-824.

[2.93] R. T. Howe and R. S. Muller, Stress in polycrystalline and amorphous silicon thin films, J. Appl. Phys., 54 (8) (1983), pp. 4674-4675.

[2.94] H. Guckel, D. W. Burns, C. C. G. Visser, H. A. C. Tilmans and D. W. deRoo, Fine grained polysilicon films with built-in tensile strain, IEEE trans. Electron Devices, Vol. ED-35, 1988, p. 800.

[2.95] T.I. Kamins, Structure and properties of LPCVD silicon films, J. Electrochem. Soc. Vol. 127, No. 3, March 1980, pp. 686-690.

[2.96] R. Bisaro, J. Magariño and N. Proust, Structure and crystal growth of atmospheric and low-pressure chemical-vapor-deposited silicon films, J. Appl. Phys., 59 (4), Feb. 1986, pp. 1167-1178.

[2.97] J. Huang, P. Krulevitch, G.C. Johnson, R.T. Howe and H.R. Wenk, Investigation of texture and stress in undoped polysilicon films, Proc. Materials Research Society Symp., San Fransisco, CA, U.S.A., April 17-19 1990, Vol. 182, pp. 201-206.

[2.98] P. Krulevitch, R. T. Howe, G. C. Johnson and J. Huang, Stress in undoped LPCVD polycrystalline silicon, Proc. Int. Conf. on Solid-State Sensors and Actuators, (Transducers '91), San Fransisco, CA, U. S. A., June 24-27, 1991, pp. 949-952.

[2.99] P. Krulevitch, T.D. Nguyen, G.C. Johnson, R.T. Howe, H.R. Wenk and R. Gronsky, LPCVD polycrystalline silicon thin films: the evolution of structure, texture and stress, Proc. Materials Research Society Symp., Boston, MA, U.S.A., Nov. 26-Dec. 1 1990, Vol. 202, pp. 167-172.

[2.100] P. Krulevitch, G. C. Johnson and R. T. Howe, Stress and microstructure in LPCVD polycrystalline silicon films: experimental results and closed form modelling of stresses,

Proc. Materials Research Society Symp., Boston, MA, U.S.A., Dec. 2-5 1991, Vol. 239, pp. 13-18.

[2.101] P. Krulevitch, G. C. Johnson and R. T. Howe, Stress and microstructure in phosphorus doped polycrystalline silicon, Proc. Materials Research Society Symp., San Fransisco, CA, U.S.A., April 12-16, 1992, Vol. 276, pp. 79-84.

[2.102] D.G. Oei and S.L. McCarthy, The effect of temperature and pressure on residual stress in LPCVD polysilicon films, Proc. Materials Research Society Symp., San Fransisco, CA, U.S.A., April 28-30 1992, Vol. 276, pp. 85-90.

[2.103] A. Benitez, J. Bausells, E. Cabruja, J. Esteve and J. Samitier, Stress in low pressure vapour deposition polycrystalline silicon thin films deposited below 0.1 Torr, Sensors and Actuators, A 37-38, 1993, pp. 723-726.

[2.104] T.I. Kamins, M.M. Mandurah and K.C. Saraswat, Structure and stability of low pressure chemically vapor-deposited silicon films, J. Electrochem. Soc., Vol. 125, No. 6, June 1978, pp. 927-932.

[2.105] D. Maier-Schneider, J. Maibach and E. Obermeier, Variations in Young's modulus and intrinsic stress of LPCVD-polysilicon due to high temperature annealing, Proc. 5th European workshop on micromachining, micromechanics and microsystems (MME 94), Pisa, Italy, Sept. 5-6, 1994, pp. 65-68.

[2.106] W. Huber, G. Borionetti and C. Villani, The behaviour of polysilicon thin film stress and structure under rapid thermal processing conditions, Proc. Materials Research Society Symp., Boston, MA, U.S.A., Nov. 28-30, 1988, Vol. 130, pp. 389-393.

[2.107] W.C. Tang, T.C.H. Nguyen and R.T. Howe, Laterally driven polysilicon resonant microstructures, Proc. IEEE Micro Electro Mechanical Systems, Salt Lake City, Utah, U.S.A., Feb. 20-22, 1989, pp. 53-59.

[2.108] M. Orpana and A. O. Korhonen, Control of residual stress of polycrystalline polysilicon thin films by heavy doping in surface micromachining, Proc. Int. Conf. on Solid-State Sensors and Actuators, (Transducers '91), San Fransisco, CA, U. S. A., June 24-27, 1991, pp. 957-960.

[2.109] O. Ruiz, S. Marco, J. Samitier, J. R. Morante and J. Bausells, Effect of boron implantation on the structure and residual stress of LPCVD polysilicon films, Proc. 3rd European workshop on micromachining, micromechanics and microsystems, Leuven, Belgium, June 1-2, 1992, pp. 86-88.

[2.110] S. P. Murarka and T. F. Retajczyk, Effect of phosphorus doping on stress in silicon and polycrystalline silicon, J. Appl. Phys., Vol. 54 (4), April 1983, pp. 2069-2072.

[2.111] M. S. Choi and E. W. Hearn, Stress effects in boron-implanted polysilicon films, J. Electrochem. Soc., Vol. 131 (10), Oct. 1984, pp. 2443-2446.

[2.112] Y. Wada and S. Nishimatsu, Grain growth mechanism of heavily phosphorous-implanted polycrystalline silicon, J. Electrochem. Soc., Vol. 125, No. 9, Sept. 1978, pp. 1499-1504.

[2.113] L. Mei, M. Rivier, Y. Kwark and R.W. Dutton, Grain-growth mechanisms in polysilicon, J. Electrochem. Soc., Vol. 129 (8), August 1982, pp. 1791-1795.

[2.114] M. Biebl, G.T. Mulhern and R.T. Howe, In Situ Phosphorus doped polysilicon for integrated MEMS, Proc. 8th Int. Conf. Solid-State Sensors and Actuators (Transducers '95), Stockholm, Sweden, June 25-29, 1995, Vol. 1, pp. 198-201.

[2.115] D.J. Monk, D.S. Soane and R.T. Howe, Sacrificial layer SiO_2 wet etching for micromachining applications, Proc. Int. Conf. on Solid-State Sensors and Actuators, (Transducers '91), San Fransisco, CA, U. S. A., June 24-27, 1991, pp. 647-650.

[2.116] D.J. Monk and D.S. Soane, Determination of the etching kinetics for the hydrofluoric acid / silicon dioxide system, J. Electrochem. Soc., Vol. 140, No. 8, August 1993, pp. 2339-2345.

[2.117] D.J. Monk, D.S. Soane and R.T. Howe, Hydrofluoric acid etching of silicon dioxide sacrificial layers, I. Experimental observations, J. Electrochem. Soc., Vol. 141, No. 1, January 1994, pp. 264-269.

[2.118] D.J. Monk, D.S. Soane and R.T. Howe, Hydrofluoric acid etching of silicon dioxide sacrificial layers, II. Modeling, J. Electrochem. Soc., Vol. 141, No. 1, January 1994, pp. 641-646.

[2.119] J. Liu, Y.C. Tai, J. Lee, K.-C. Pong. Y. Zohar and C.-M. Ho, In-Situ monitoring and universal modelling of sacrificial PSG etching using hydrofluoric acid, Proc. of Micro Electromechanical Systems Workshop, Ft. Lauderdale, FL, U.S.A., 1993, p. 71-76.

[2.120] D. J. Monk, D. S. Soane and R. T. Howe, Enhanced removal of sacrificial layers for silicon surface micromachining, Proc. Int. Conf. om Solid-State Sensors and Actuators (Transducers '93), Yokohama, Japan, June 7-10, 1993,pp. 280-283.

[2.121] D. Poenar, P.J. French, R. Mallée, P.M. Sarro and R.F. Wolffenbuttel, PSG layers for surface micromachining, Sensors and Actuators, A 41-42, 1994, pp. 304-309.

[2.122] J.J. Gajda, Annu. Proc. Reliab. Phys., 12th, 1974, p. 30.

[2.123] Riedel de Haehn, art. nr. 17551.

[2.124] P.J. French and R.F. Wolffenbuttel, Low-temperature BPSG reflow compatible with surface micromachining, Proc. 5th European workshop on micromachining, micromechanics and microsystems (MME 94), Pisa, Italy, Sept. 5-6, 1994, pp. 69-72.

[2.125] W. Hoffmeister and M. Zügel, Determination of the etch rate of silicon in buffered HF using a ^{31}Si silicon tracer method, Int. J. of Appl. Rad. and Isotopes, Vol. 20, 1969, pp. 139-140.

[2.126] S.M. Hu and D.R. Kerr, J. Electrochem. Soc., Vol. 114, 1967, pp. 414.

[2.127] T. A. Lober and R.T. Howe, Surface-micromachining processes for electrostatic microactuator fabrication, Proc. IEEE Solid-State Sensor and Actuator Workshop, Hilton Head Island, SC, U. S. A., June 6-9, 1988, pp. 59-62.

[2.128] J. A Walker, K. J. Gabriel and M. Mehregany, Mechanical integrity of polysilicon films exposed to hydrifluoric acid solutions, Proc. IEEE Micro Electro Mechanical Systems, Napa Valley, CA, U.S.A., Feb. 11-14, 1990, pp. 57-59.

[2.129] D. J. Monk, P. Krulevitch, R. T. Howe and G. C. Johnson, Stress-corrossion cracking and blistering of thin polycrystalline silicon films in hydrofluoric acid, Proc. Materials Research Society Symp., San Fransisco, CA, U.S.A., April 12-16 1993, Vol. 308, pp. 641-646.

[2.130] H. Guckel, J.J. Sniegowski and T.R. Christenson, Advances in processing techniques for silicon micromechanical devices with smooth surfaces, Proc. IEEE Micro Electro Mechanical Systems, Salt Lake City, Utah, U.S.A., June 6-9 1989, pp. 71-75.

[2.131] R. Legtenberg, H.A.C. Tilmans, J. Elders and M. Elwenspoek, Stiction of surface micromachined structures after rinsing and drying: model and investigation of adhesion mechanisms, Sensors and Actuators A, 43 (1994), pp. 230-238.

[2.132] C.H. Mastrangelo and C.H. Hsu, Mechanical stability and adhesion of microstructures under capillary forces-Part I: Basic theory, Journal of microelectromechanical systems, Vol. 2, No. 1, March 1993, pp. 33-43.

[2.133] C.H. Mastrangelo and C.H. Hsu, Mechanical stability and adhesion of microstructures under capillary forces-Part II: Experiments, Journal of microelectromechanical systems, Vol. 2, No. 1, March 1993, pp. 44-55.

[2.134] R.L. Alley, G.J. Cuan, R.T. Howe and K. Komvopoulos, The effect of release-etch processing on surface microstructure stiction, Proc. IEEE Solid-State Sensors and Actuators Workshop, Hilton Head Island, SC, U.S.A. June 22-25, 1992, pp. 202-207.

[2.135] C. Linder and N.F. deRooij, Investigations on free-standing polysilicon beams in view of their application as transducers, Proc. 5th Int. Conf. Solid-State Sensors and Actuators (Transducers '89), Montreux, Switzerland, June 25-30, 1989, pp. 1053-1059.

[2.136] P.R. Scheeper, J.A. Voorthuyzen, W. Olthuis and P. Bergveld, Investigation of attractive forces between PECVD silicon nitride microstructures and an oxidized silicon substrate, Sensors and Actuators A, 30 (1992) 231-239.

[2.137] C.H. Mastrangelo and C.H. Hsu, A simple experimental technique for the measurement of the work of adhesion of microstructures, Proc. IEEE Solid-State Sensors and Actuators Workshop, Hilton Head Island, SC, U.S.A. June 22-25, 1992, pp. 208-212.

[2.138] A. Torii, M. Sasaki, K. Hane and S. Okuma, Adhesive force of the microstructures measured by the atomic force microscope, Proc. IEEE Micro Electro Mechanical Systems, Ford Lauderdale, Florida, U.S.A., Feb. 7-10,1993, pp. 111-116.

[2.139] K. L. Yang, D. Wilcoxen and G. Gimpelson, The effects of post-process techniques and sacrificial materials on the formation of free standing polysilicon structures, Proc. IEEE Micro Electro Mechanical Systems, Salt Lake City, Utah, U.S.A., Feb. 20-22, 1989, pp. 66-70.

[2.140] H. Guckel, J. J. Sniegowski, T. R. Christenson, S. Mohney and T. F. Kelly, Fabrication of micromechanical devices from polysilicon films with smooth surfaces, Sensors and Actuators, 20 (1989) 117-122.

[2.141] N. Takeshima, K. J. Gabriel, M. Ozaki, J. Takahasji, H. Horiguchi and H. Fujita, Electrostatic parallelogram actuators, Proc. 6th Int. Conf. Solid-State Sensors and Actuators (Transducers '91), San Fransisco, CA, USA, June 24-27, 1991, pp. 63-66.

[2.142] D. Kobayashi, T. Hirano, T. Furuhata and H. Fujita, An integrated lateral tunneling unit, Proc. IEEE Micro Electro Mechanical Systems, Travemünde, Germany, Feb. 4-7, 1992, pp. 214-219.

[2.143] R. Legtenberg and H.A.C. Tilmans, Electrostatically driven vacuum encapsulated polysilicon resonators: Part I Design and fabrication, Sensors and Actuators A, 45 (1994), pp. 57-66.

[2.144] G.T. Mulhern, D. S. Soane and R.T. Howe, Supercritical carbon dioxide drying of microstrutures, Proc. 7th Int. Conf. Solid-State Sensors and Actuators (Transducers '93), Yokohama, Japan, June 7-10, 1993, pp. 296-299.

[2.145] M. Orpana and A.O. Korhonen, Control of residual stress of polysilicon thin films by heavy doping in surface micromachining, Proc. 6th Int. Conf. Solid-State Sensors and Actuators (Transducers '91), San Fransisco, CA, USA, June 24-27, 1991, pp. 957-960.

[2.146] D. Kobayashi, C.J. Kim and H. Fujita, Photoresist-assisted release of movable microstructures, Proc. 7th Int. Conf. Solid-State Sensors and Actuators (Transducers '93), Yokohama, Japan, June 7-10, 1993, abstracts of late news papers, pp. 14-15.

[2.147] C.H. Mastrangelo and G.S. Saloka, A dry-release method based on polymer columns for microstructure fabrication, Proc. IEEE Micro Electro Mechanical Systems, Fort Lauderdale, Florida, U.S.A., Feb. 7-10,1993, pp. 77-81.

[2.148] A. Kovacs, A. Stoffel, Process optimization of free-standing polysilicon microstructures, Proc. 3rd European workshop on micromachining, micromechanics and microsystems (MME 92), Leuven, Belgium, June 1-2, 1992, pp. 114-117.

[2.149] F. Kozlowski, N. Lindmair, Th. Scheiter, C. Hierold and W. Lang, A novel method to avoid sticking of surface micromachined structures, Proc. 8th Int. Conf. Solid-State Sensors and Actuators (Transducers '95), Stockholm, Sweden, June 25-29, 1995, Vol. 1, pp. 220-223.

[2.150] T. Abe, W.C. Messner and M.L. Reed, Effective methods to prevent stiction during post-release-etch processing, Proc. IEEE Micro Electro Mechanical Systems, Amsterdam, The Netherlands, Jan. 29-Feb. 2, 1995, pp. 94-99.

[2.151] R.A. Brennen, M.G. Lim, A.P. Pisano and A.T. Chou, Large displacement linear actuator, Proc. IEEE Solid-State Sensors and Actuators Workshop, Hilton Head Island, SC, U.S.A. June 4-7, 1990, pp. 135-139.

[2.152] G. K. Fedder and R. T. Howe, Thermal assembly of polysilicon microstructures, Proc. IEEE Micro Electro Mechanical Systems, Nara, Japan, Jan. 30-Feb. 2,1991, pp. 63-68.

[2.153] M.A. Benitez, S.Q. Shen and J. Esteve, A new process for releasing micromechanical structures in surface micromachining, Berenschot, M.C. Elwenspoek and J.H.J. Fluitman, The electrostatic shuffle motor, Proc. 6th European workshop on micromachining, micromechanics and microsystems (MME '95), Copenhagen, Denmark, Sept. 3-5, 1995, pp. 43-46.

[2.154] M. Offenberg, B. Elsner and F. Lärmer, Electrochem. Soc. Fall meeting, 1994, Ext. Abstr., No. 671.

[2.155] M.R. Houston, R. Maboudian and R.T. Howe, Ammonium fluoride anti-stiction treatments for polysilicon microstructures, Proc. 8th Int. Conf. Solid-State Sensors and Actuators (Transducers '95), Stockholm, Sweden, June 25-29, 1995, Vol. 1, pp. 210-213.

[2.156] F.S.A. Sandejas, R.B. Apte, W.C. Banyai and D.M. Bloom, Surface microfabrication of deformable grating light valves for high resolution displays, Proc. 7th Int. Conf. Solid-State Sensors and Actuators (Transducers '93), Yokohama, Japan, June 7-10, 1993, abstracts of late news papers, pp. 6-7.

[2.157] R.L. Alley, P Mai, K. Komvopoulos and R.T. Howe, Surface roughness modification of interfacial contact in polysilicon microstructures, Proc. 7th Int. Conf. Solid-State Sensors and Actuators (Transducers '93), Yokohama, Japan, June 7-10, 1993, pp. 288-291.

[2.158] Y. Yee, K. Chun and J.D. Lee, Polysilicon surface modification technique to reduce sticking of microstructures, Proc. 8th Int. Conf. Solid-State Sensors and Actuators (Transducers '95), Stockholm, Sweden, June 25-29, 1995, Vol. 1, pp. 206-209.

[2.159] B.P. Gogoi and C.H. Mastrangelo, Post-processing release of microstructures by electromagnetic pulses, Proc. 8th Int. Conf. Solid-State Sensors and Actuators (Transducers '95), Stockholm, Sweden, June 25-29, 1995, Vol. 1, pp. 214-217.

[2.160] A. Boyde and C. Wood, Preparation of animal tissues for surface-scanning electron microscopy, J. Microsc., 90 (1969), 221-249.

[2.161] K. Ikeda, H. Kuwayama, T. Kobayashi, T. Watanabe, T. Nishikawa and T. Yoshida, Three dimensional micromachining of silicon resonant strain gauge, Proc. 7th Sensor Symp., Tokyo, Japan, 1988, pp. 55-58.

[2.162] M.W. Judy and R.T. Howe, Highly compliant lateral suspensions using sidewall beams, Proc. 7th Int. Conf. Solid-State Sensors and Actuators (Transducers '93), Yokohama, Japan, June 7-10, pp. 54-57.

[2.163] K.S. Lebouitz, R.T. Howe and A.P. Pisano, Permeable polysilicon etch-access windows for microshell fabrication, Proc. 8th Int. Conf. Solid-State Sensors and Actuators (Transducers '95), Stockholm, Sweden, June 25-29, 1995, Vol. 1, pp. 224-227.

[2.164] M.W. Judy and R.T. Howe, Polysilicon hollow beam lateral resonators, Proc. IEEE Micro Electro Mechanical Systems, Ford Lauderdale, Florida, U.S.A., Feb. 7-10, 1993, Pp. 265-271.

[2.165] C. Keller and M. Ferrari, Milli-scale polysilicon structures, Proc. IEEE Solid-State Sensors and Actuators Workshop, Hilton Head Island, SC, U.S.A., June 13-16, 1994, pp. 132-137.

[2.166] G.K. Fedder, J.C. Chang and R.T. Howe, Thermal assembly of polysilicon microactuators with narrow-gap electrostatic comb drive, Proc. IEEE Solid-State Sensors and Actuators Workshop, Hilton Head Island, SC, U.S.A. June 22-25, 1992, pp. 63-68.

[2.167] Y. Fukuta, T. Akiyama and H. Fujita, A reshaping technology with Joule heat for three dimensional silicon structures, Proc. 8th Int. Conf. Solid-State Sensors and Actuators (Transducers '95), Stockholm, Sweden, June 25-29, 1995, Vol. 1, pp. 174-177.

Chapter Three

STICTION OF SURFACE MICROMACHINED STRUCTURES AFTER RINSING AND DRYING*

In this chapter the mechanisms causing stiction of polysilicon structures fabricated by surface micromachining techniques are investigated. It is found that during drying from rinse liquids attractive dynamic capillary forces are responsible for bringing micromechanical structures into contact with the underlying substrate. Measured adhesion energies of sticking microbridges after complete drying indicate that van der Waals forces are responsible for the stiction of hydrophobic surfaces and that hydrogen bridging is an additional adhesion mechanism for hydrophilic surfaces.

3.0 INTRODUCTION

A notorious problem of surface micromachined structures using the sacrificial layer etching technique is the permanent attachment of slender structures to the underlying substrate after drying. This phenomenon is known as sticking or stiction [3.1-3.6]. It is assumed that during drying attractive capillary forces bring micromechanical structures into contact with the substrate. After complete drying the structures remain stuck to the substrate. It has been suggested that etch residues [3.1, 3.2], electrostatic forces [3.3] and condensation of water between the structures [3.4, 3.5] may be responsible for sticking. An understanding of the sticking phenomena is important for both static (beams) and dynamic (rotors) applications of surface micromachined structures with respect to technological realisation and tribological aspects.

In this chapter a model is presented which describes the pull-in behaviour of beams during drying from liquids, characterised by a *pull-in length* defined as the maximum length beyond which beams are forced into physical contact with the underlying substrate. Surface micromachined polysilicon microbridges have been fabricated and the pull-in length has been measured.

* presented at the 7th Int. Conf. on Solid-State Sensors and Actuators (Transducers '93), Yokohama, Japan, June 7-10, 1993, pp. 198-201, published in Sensors and Actuators A, 43 (1994) 230-238.

After drying, beams with a length greater than the so called *detachment length* remain stuck to the substrate. A relation between the detachment length of microbridges and the corresponding adhesion energy is given. The resulting bond strength has been determined from measured detachment lengths and is correlated to possible adhesion mechanisms.

3.1 PULL-IN BY CAPILLARY FORCES

During drying, the surface tension of the diminishing liquid induces an attractive capillary force which is inversely proportional to the gap spacing between the beam and the substrate, see fig. 3.1.

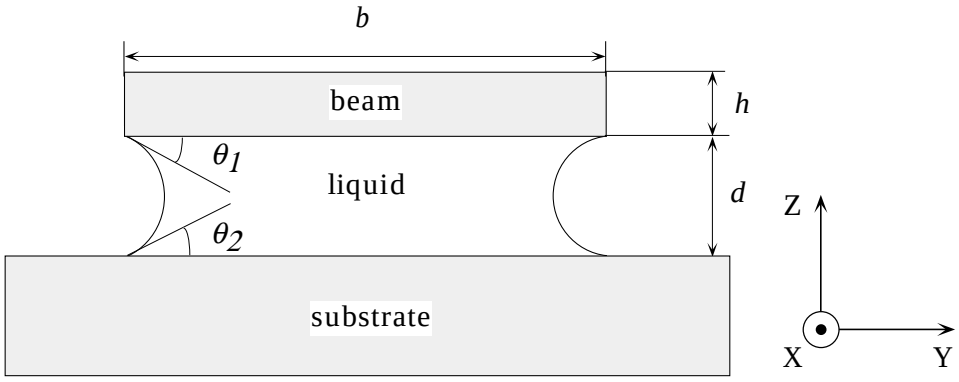

Fig. 3.1 *Cross section of the beam during drying.*

The restoring force consists of the bending and stretching stiffness of the beam. An increase in the deflection of the beam results in a decrease of the gap spacing and thus an increase in the capillary force. If the restoring force is not able to counterbalance the capillary force, the deflection does not reach an equilibrium position and increases until physical contact with the substrate is made. This behaviour is similar to the electrostatic attraction between two conducting surfaces as a result of an applied d.c. voltage as described in [3.7] and can be modelled in a similar way. In the following analysis, the process is assumed to be quasi-static.

The differential equation for the static deflection *w(x)* of a prismatic wide beam subjected to an axial (x) load *N* and a transverse (z) capillary pressure *q* is given by:

$$\widehat{E}I\,\frac{\partial^4 w(x)}{\partial x^4} - N\,\frac{\partial^2 w(x)}{\partial x^2} = q = \frac{\gamma(\cos\theta 1 + \cos\theta 2)\,b}{d - w\,(x)} \qquad (3.1)$$

where $\hat{E}=E_y/(1-\nu^2)$ is the plate modulus and E_y and ν are the Young's modulus and Poisson's ratio of the beam material, respectively, $I=bh^3/12$ is the second moment of inertia, γ is the surface tension of the liquid, θ_1 is the contact angle between the liquid and the beam, θ_2 is the contact angle between the liquid and the substrate, d is the zero displacement gap spacing, b the beam width and h is the beam thickness.

An approximate solution can be obtained using the Rayleigh-Ritz method. A deflection profile is assumed which satisfies the geometric boundary conditions (zero displacement and rotation at the supports). The total potential energy Π can be expressed as:

$$\Pi = U_{bending} + U_{stretching} + U_{surface\ tension} \tag{3.2}$$

where $U_{bending}$, $U_{stretching}$ are the strain energy terms due to bending and stretching respectively and $U_{surface\ tension}$ is the potential energy due to the surface tension or capillary force of the fluid, given by:

$$U_{bending} = \frac{1}{2}\int_0^l \hat{E}I\left(\frac{d^2w(x)}{dx^2}\right)^2 dx \tag{3.3}$$

$$U_{stretching} = \frac{1}{2}\int_0^l N\left(\frac{dw(x)}{dx}\right)^2 dx \tag{3.4}$$

$$U_{surface\ tension} = -\int_0^l \int_0^{w(x)} \frac{\gamma(\cos\theta 1 + \cos\theta 2)\, b}{(d-w)}\, dw\, dx \tag{3.5}$$

where l is the beam length. Trigonometric functions are very convenient in solving problems of clamped-clamped beams. An appropriate deflection profile is:

$$w(x) = a\left(1-\cos\frac{2\pi x}{l}\right) \tag{3.6}$$

where a is a coefficient that has to be determined. For a system at equilibrium, the first derivative of the total energy with respect to a is equal to zero. For a stable equilibrium the total potential energy must be at a (local) minimum,

implying that the second derivative with respect to a has to be positive definite. The transition to an unstable system occurs when the second derivative equals zero. Solving these equations simultaneously yields the following expression for the pull-in length L_{PI} and the corresponding value for a:

$$L_{PI} = \left\{ \pi^2 C d^2 \left[N + \left(\frac{8 \hat{E} I}{C d^2} + N^2 \right)^{\frac{1}{2}} \right] \right\}^{\frac{1}{2}} \qquad \text{where} \quad C = \frac{0.1549}{\gamma (\cos\theta 1 + \cos\theta 2)\, b} \qquad (3.7)$$

and $a = 0.2950\, d$

The effect of geometry and of the residual strain $\varepsilon_0 = N/Ebh$ on the pull-in length is shown in fig. 2. For the condition that $8\hat{E}I/Cd^2 >> N^2$, the influence of the residual strain on the pull-in length can be neglected and expression (3.7) becomes:

$$L_{PI} = 1.059 \left[\frac{8 . \hat{E} . d^2 . h^3}{\gamma . (\cos\theta 1 + \cos\theta 2)} \right]^{\frac{1}{4}} \qquad (3.8)$$

Note that the bracketed expression on the right hand side of equation (3.8) gives the pull-in length in case the problem is simplified and the beam is modelled as a spring-mass system. The spring stiffness k for this special case is given by $k = 384\hat{E}I/l^3$ and the active area is equal to the beam surface bl.

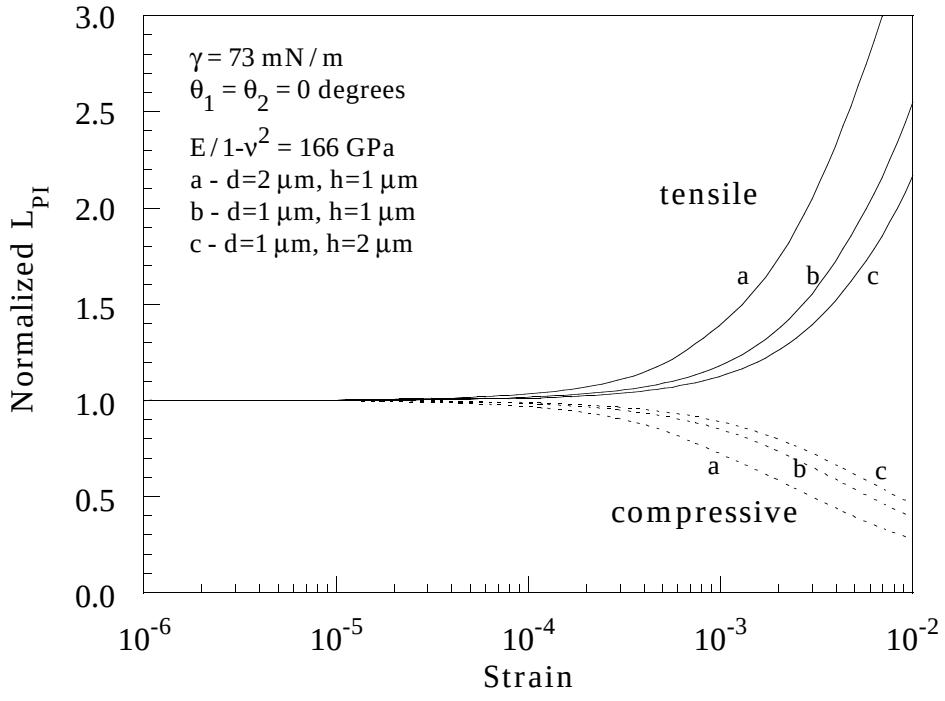

Fig. 3.2 *The influence of the mechanical strain on the pull-in length L_{PI} for different beam thicknesses and gap spacings normalised on the pull-in length at zero strain.*

3.2 DETACHMENT LENGTH

If the beam length exceeds the pull-in length physical contact with the substrate will be made during the drying of the liquid. Physical contact between the released microstructures and the underlying substrate induces an adhesive bond. If the strength of the adhesive bond exceeds the mechanical 'pull-off force', the structures remain permanently stuck to the substrate. The bonding strength of sticking beams can be determined from their detachment length as presented by Mastrangelo *et al* [3.5] for cantilever beams. It is evident, that the detachment length is always equal to or larger than the pull-in length, since sticking only occurs after physical contact has been made.

Using an array of beams with increasing length the detachment length is equal to the length where a transition occurs from sticking beams to free standing beams. The relation between the detachment length and the surface energy is derived as follows. The stored elastic energy in doubly clamped beams again consists of a bending and stretching term, see eqns. (3.3) and (3.4). The energy of adhesion is stored in the segment of the beam that is in physical contact with the substrate.

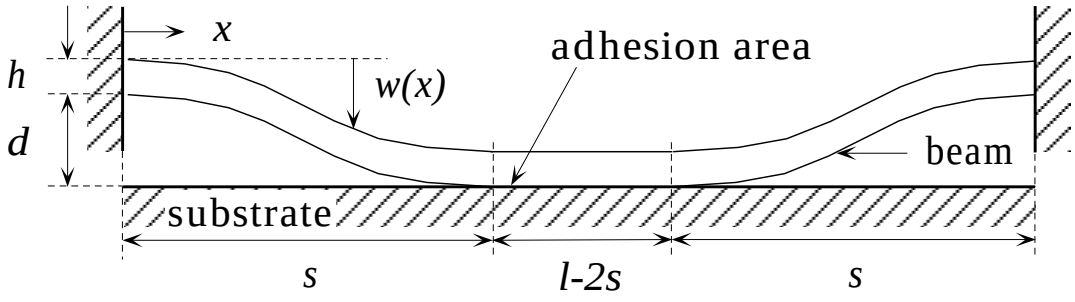

Fig. 3.3 *Sketch of a polysilicon beam adhering to the substrate.*

At equilibrium the total energy of the system is minimised with respect to *s* (see fig. 3.3) and an expression for the bondstrength γ_S can be found. In this case an appropriate deflection profile of the beam is:

$$w(x) = \frac{1}{2} d \left(1 - \cos \frac{\pi x}{s}\right) \tag{3.9}$$

where *s* is the region near the support of the beam that is not sticking. We find for the total energy of this system:

$$\Pi = \frac{\pi^4 . \hat{E} . I . d^2}{8 . s^3} + \frac{\pi^2 . N . d^2}{8 . s} - \gamma_s . (l - 2s) b \tag{3.10}$$

Equilibrium is found by setting $dU_{total}/ds = 0$, yielding the value for s at which the energy is minimal. The energy has a single equilibrium point if $s < l/2$ and no equilibrium point if $s > l/2$, i.e. the beam is sticking to the substrate in the former case and is free standing in the latter case. At the transition from sticking to free standing beams, s is equal to $l/2$ giving the following relation between the bondstrength γ_S and the detachment length L_{det}:

$$\gamma_S = \frac{\pi^4 . \hat{E} . h^3 . d^2}{4 . L_{det}^4} + \frac{\pi^2 . \varepsilon_0 . E . h . d^2}{4 L_{det}^2} \qquad (3.11)$$

The influence of the residual strain ε_0, both compressive and tensile, on the detachment length is very small when $\varepsilon_0 L_{det}^2 / \pi^2 h^2 << 1$. In this case the second term on the right hand side of equation (3.11) can be neglected.

3.3 ADHESION OF SOLIDS

The bondstrength can be determined by measuring the detachment length of samples with different combinations of gap spacing and beam thickness. From the measured value of the bondstrength, as determined from the detachment length, information about the adhesion mechanisms that are present can be deduced.

The contents of this section is based upon the adhesion theories described in references [3.8-3.12]. Interactions between solids which bring about adhesion can be classified as follows [3.8]. Firstly there are long-range attractive interactions, including capillary forces, van der Waals forces and electrostatic forces, which establish the adhesive contact area. Secondly there are short range interactions caused by hydrogen bonds, chemical bonds and metallic bonds. Interfacial interactions based on diffusion and alloying are generally very slow at room temperature and will not be considered.

After HF etching, the hydrophobic silicon surface consists mainly of Si-H bonds which are chemically stable. The silicon surface shows a logarithmic growth rate up to roughly half a monolayer equivalent of silicon oxide during exposure to water or air. This growth rate increases after 3 hrs exposure to water and after nearly one week exposure to air [3.13, 3.14]. On further exposure the surface becomes hydrophilic. Because the surfaces are contaminated, strong ionic interactions between silicon surface atoms are screened out. Chemical reactions between surface hydroxyl groups only start to play a role at elevated temperatures [3.15].

For comparison, a system consisting of two solids, each one having the form of an infinitely extended half space, will be considered. The bonding energy per unit area due to the most relevant adhesion mechanisms is discussed below. Figure 3.4 shows the bondstrength for each mechanism as a function of the separation.

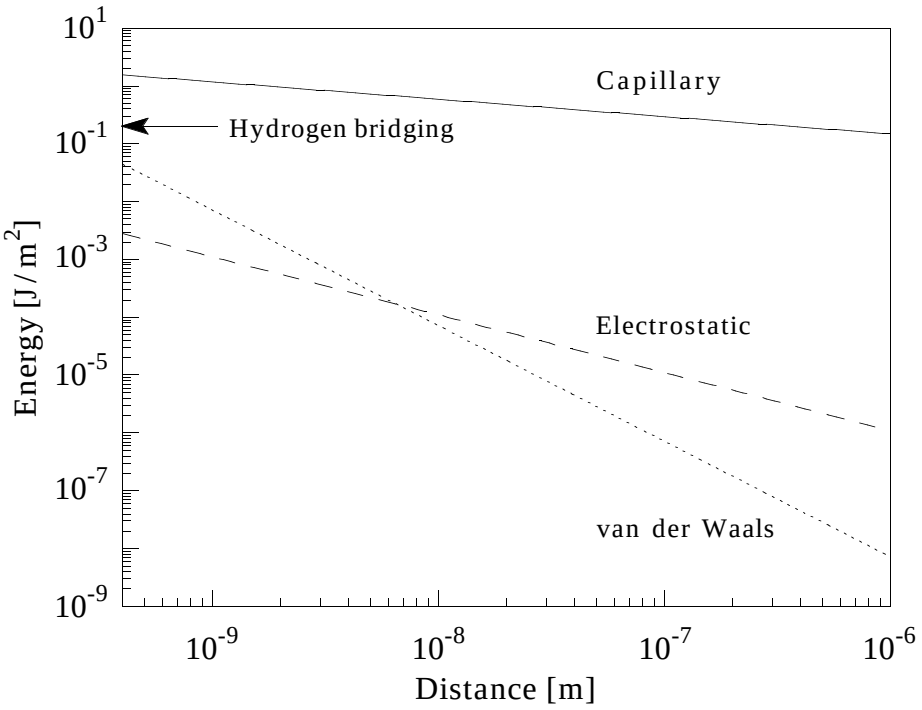

Fig. 3.4 *Bonding energy versus separation. The capillary energy was calculated for water using a surface tension of 73 mN/m and a contact angle of zero degrees with a reference distance δr of 2 μm. For the electrostatic energy a voltage difference of 0.5 V was used and for the van der Waals energy a Hamaker's constant of silicon in air equal to 27 10^{-20} J has been used.*

van der Waals forces:

Van der Waals forces result from the interaction between instantaneous dipole moment of atoms and can be described by the Lifshitz theory [3.8, 3.9]. The expression for the van der Waals energy is given by the following equation for separations in the non-retarded regime (δ < 20 nm):

$$E_{vdW} = \frac{H}{12.\pi.\delta^2} \qquad (3.12)$$

where H is the Hamaker's constant and δ is the separation distance.

The surface energy due to van der Waals forces between two solid surfaces in contact can be predicted by:

$$\gamma_s = \frac{1}{2} E_{vdW} = \frac{H}{24.\pi.D_0^2} \qquad (3.13)$$

where D_0 is a cut-off distance of about 0.2 nm [3.9]. This yields a surface energy for silicon of 90 mJ/m^2 using a Hamaker's constant of silicon in air of 27.10^{-20} J [3.8].

Capillary forces:

The energy as a result of capillary forces is given by:

$$E_{capillary} = \int_{\delta}^{\delta_r} - \frac{\gamma.(\cos\theta 1 + \cos\theta 2)}{\delta} d\delta \qquad (3.14)$$

where γ is the surface tension of the liquid and θ_1 and θ_2 are the contact angles of the liquid with the two surfaces. As opposed to the other mechanisms, the reference distance δ_r of the capillary energy cannot be chosen infinite but it is readily shown that, under conditions of meniscus forces, the capillary energy exceeds all other adhesive components (see fig. 3.4). When two hydrophilic surfaces are in contact or close to being in contact in a humid environment, water will capillary condense in the small gap between them until the meniscus radius reaches the Kelvin radius as determined by the Kelvin equation [3.9].

Electrostatic forces:

Electrostatic forces can arise from Coulomb attraction between charged objects or from the contact potential between two surfaces caused by differences in the local energy states and electron work functions. Its energy is given by:

$$E_{el.} = \frac{\varepsilon_{air}.U^2}{2.\delta} \qquad (3.15)$$

where U is the potential difference between the surfaces separated by an air gap with permitivity ε_{air}. At small separations electrostatic pressures equal van der Waals pressures only for extremely large surface charge densities (> 10^{13} elementary charges per cm^2) and large contact-potential differences (> 0.5 V) and are unlikely ever to exceed them [3.8], see fig. 3.4.

Hydrogen bridging:

Hydrophilic silicon surfaces contain a large number of hydroxyl groups. The hydroxyl groups can form strong hydrogen bonds as the separation between both surfaces becomes small. The density of hydrogen-bonding sites is given by the number of silanol groups and is found to be 5.0 ± 0.5 per nm^2 for fully hydrated silica surfaces [3.16]. The strength of most hydrogen-bonds lie between 10 and 40 kJ/mol [3.9], thus yielding adhesion energies between 0.1 and 0.3 J/m^2 for these surfaces.

Other aspects:

Besides the mentioned bonding mechanisms Alley *et al* [3.2] suggested that polysilicon structures stick together due to a silicon oxide residue, left behind after a chemical reaction of the silicon surface with water. In this case an intermediate material is introduced between the silicon substrate surface and the polysilicon beam surface. The adhesive strength of solid bridging is high [3.17] but difficult to estimate and is dependent on the type and amount of residue material. In addition, all attractive forces except the meniscus forces decrease rapidly with increasing distance. In practice, the surfaces exhibit a surface roughness which strongly influences the real contact area and nominal separation [3.18]. The surface roughness has a significant effect on the adhesion of elastic solids [3.19] and small increases of the surface roughness are sufficient to reduce the adhesion to very small values.

3.4 EXPERIMENTAL

3.4.1 Fabrication

Test structures consisting of an array of doubly clamped undoped polysilicon beams have been fabricated. First, a PECVD silicon oxide layer was grown on a n-type (100) silicon wafer (5-10 Ωcm) from a 2 percent SiH_4 in N_2 gas mixture and N_2O gas at a pressure of 650 mTorr and a temperature of 300 ˚C. This layer was patterned using BHF to form the beam anchors. Next, an undoped polysilicon layer was grown by LPCVD from SiH_4 at a pressure of 250 mTorr and a temperature of 590 ˚C. The wafers were then annealed at 1100 ˚C in N_2 for one hour to obtain a low residual stress (typically on the order of 10 ppm). The polysilicon layer was patterned by RIE using a SF_6 plasma to form the beams with lengths ranging from 10 to 200 μm in steps of 1 μm and widths of 20 and 50 μm. The polysilicon and silicon oxide thickness ranged from 0.5 to 2 μm in steps of 0.5 μm resulting in a 4X4 matrix of the gap spacing *d* and the

beam thickness *h*. Samples were cleaned prior to sacrificial layer etching. Sacrificial layer etching was done in a 50 % HF solution for 25 minutes. After this, different treatments have been used. Special care was taken to keep the wafers wet and as clean as possible. Dilution rinsing for 15 minutes in DI water and drying, yields hydrophobic wafers dried from H_2O. Adding isopropylalcohol (IPA) to the water keeps the wafers wet after removal from the solution. Next they were rinsed in IPA for 15 minutes and withdrawn from the liquid. This procedure gives hydrophobic wafers dried from IPA. A set of hydrophilic wafers was also produced by adding nitric acid after DI dilution rinsing. At a concentration of 70 % nitric acid the solution was heated to 100 ˚C for one hour to render the silicon surface hydrophilic. After dilution rinsing for 15 minutes in DI water a set of hydrophilic wafers dried from H_2O was obtained. The same procedure followed by an IPA rinse as described above gives hydrophilic wafers dried from IPA.

3.4.2 Measurements

Pull-in length:

To verify the model for the pull-in length, hydrophobic and hydrophilic wafers dried from IPA have been used. Wet samples were placed under a microscope connected to a video camera system. The drying process has been recorded and pull-in was made visible using interference contrast during slow replay. The shortest beam showing pull-in due to the surface tension represents the pull-in length which has been determined in this way. The results are shown in fig. 3.5.

The contact angle of a droplet of IPA on a hydrophobic or hydrophilic silicon surface was measured to be smaller than 5 degrees. The measured contact angles of water on hydrophobic silicon and water on hydrophilic silicon were 70±5 and 5±5 degrees, respectively.

Detachment length:

After drying, not all the beams that pulled-in during drying deflect upward again but some remain permanently attached to the substrate. The transition from sticking to free standing beams after drying, the detachment length, has also been determined by interference contrast microscopy. For the detachment length experiments samples have been dried from two commonly used rinsing liquids, namely H_2O and IPA, to see whether or not the rinse liquid has an effect on the detachment length. Drying from these solutions was done for hydrophobic and hydrophilic samples. The results of these measurements are shown in fig. 3.6.

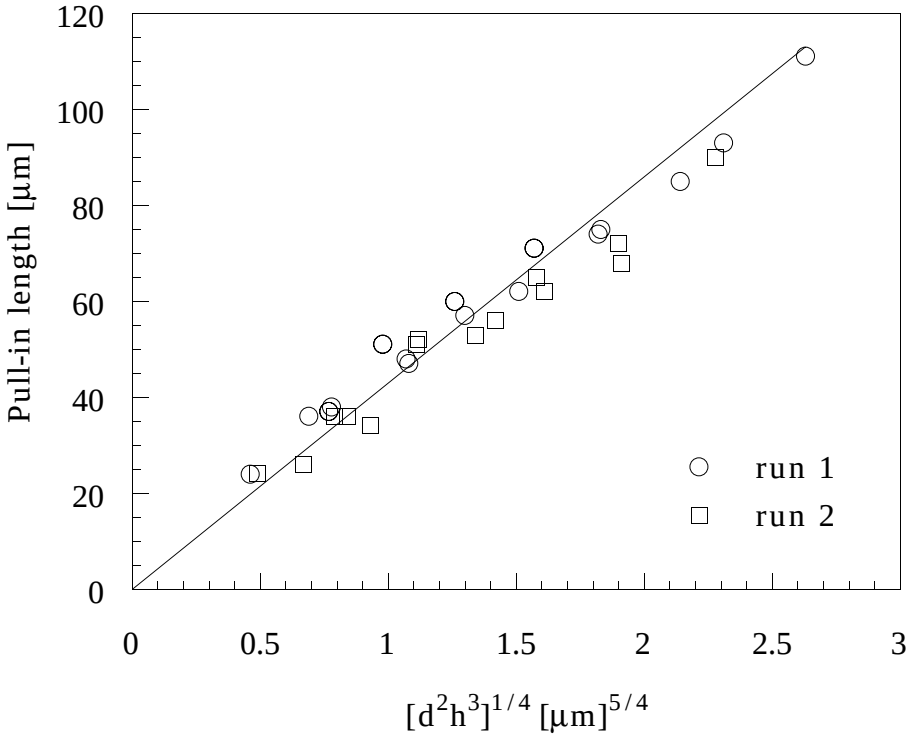

Fig. 3.5 *Measured pull-in length as a function of* $[d^2h^3]^{1/4}$ *for polysilicon beams dried from IPA. Measurements were performed on two separate fabrication runs, each resulting in a 4x4 matrix of polysilicon beams with a gap spacing d and a beam thickness h .*

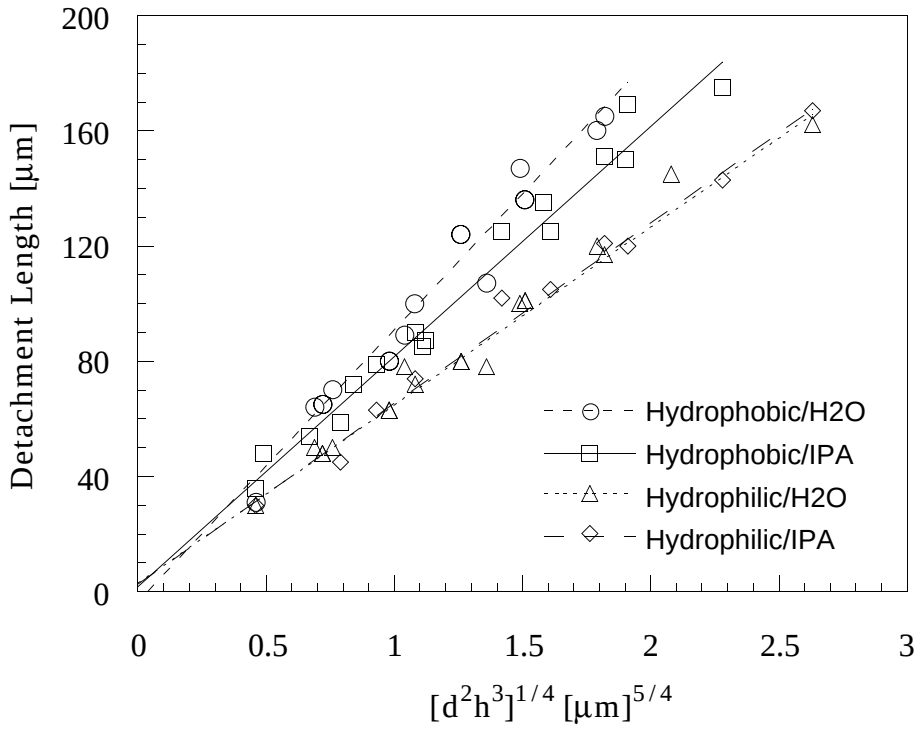

Fig. 3.6 *Detachment length as a function of* $[d^2h^3]^{1/4}$ *for hydrophobic and hydrophilic samples dried from water (*H_2O*) and isopropanol (IPA).*

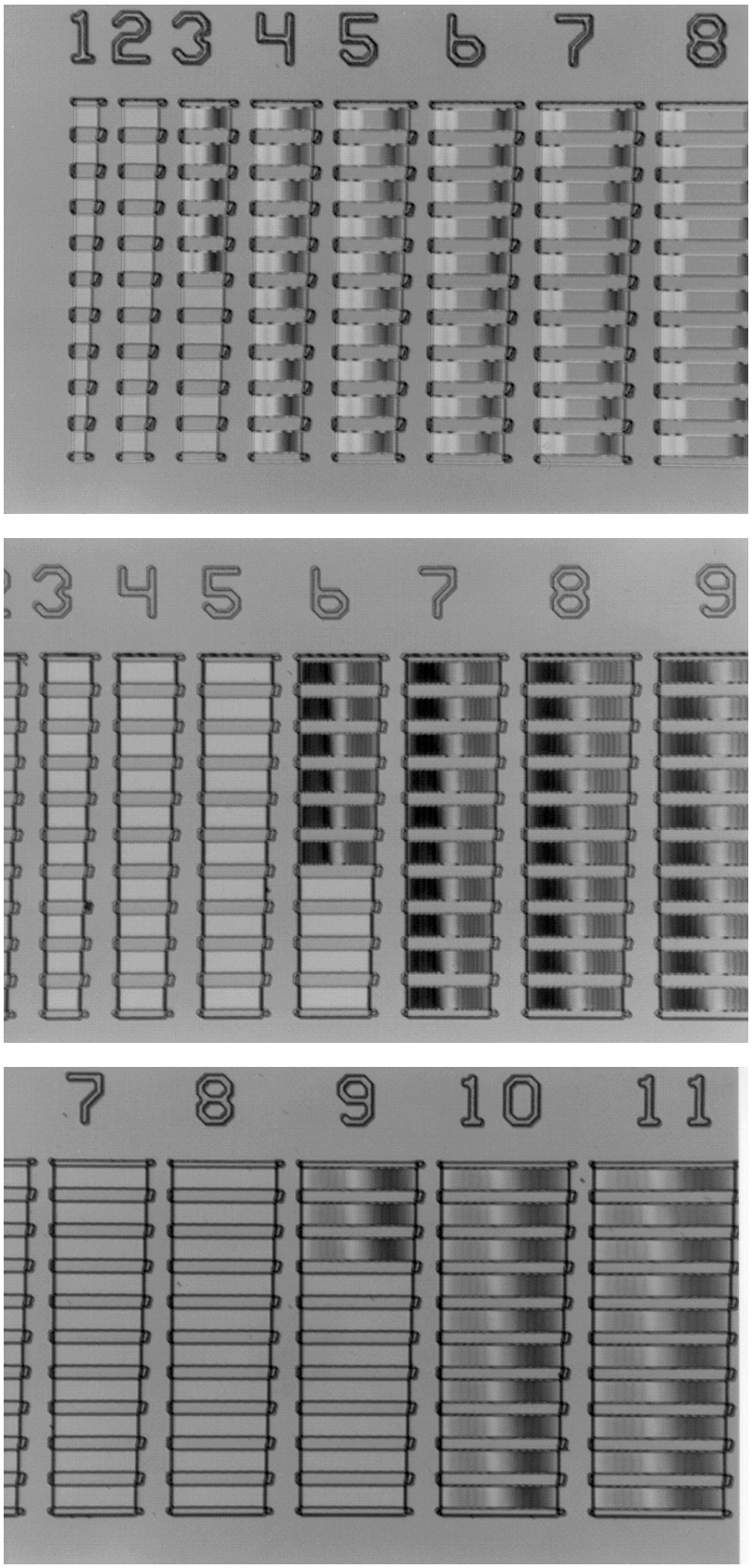

Fig. 3.7 *Photographs showing the transition from free standing to sticking beams which is clearly visible by interference patterns.*

Interference contrast photographs of some test samples are shown in fig. 3.7. The residual strain of the polysilicon layer was measured by ring and buckled beam structures and was typically found to be on the order of 10 ppm. For the dimensions of the samples in this paper and the measured residual strain, the conditions to neglect the influence of the residual strain are generally satisfied (see previous section).

The detachment length showed a large spread, especially the hydrophobic samples dried from water. Often long beams are free standing while shorter beams are sticking. Disturbances because of local surface asperities, dust particles, etc. strongly reduce adhesion resulting in errors that lead to an increase of the detachment length. In our experiments, the detachment length was determined from the shortest sticking beams (i.e. giving the highest bonding strength). From the detachment length the surface energy can be calculated by eq. (3.11). The slope of the curves in fig. 3.7 is equal to $[\pi^4 \hat{E}/4\gamma_S]^{1/4}$. The corresponding surface energies for hydrophobic and hydrophilic samples are listed in table 3.1.

	Surface energy [J/m^2]	
liquid	Hydrophobic	Hydrophilic
H_2O	0.05 ± 0.05	0.26 ± 0.1
IPA	0.10 ± 0.05	0.24 ± 0.1

Table 3.1 *Surface energy of the different samples calculated from formula (11). A value of 166 GPa was used for the plate modulus $\hat{E}$. Residual strain is on the order of 10 ppm and can be neglected in our experiments.*

The errors in the surface energies are worst case values and are mainly determined by the error in the slopes of the curve fits.

Because the roughness is important with respect to the adhesion properties, as discussed before, the surface roughness was measured by Atomic Force Microscopy. The root mean square values of the surface roughness of the bottom side of the microbridges varied from about 1 to 3 nm, depending on the thickness of the silicon oxide and polysilicon layer. The surface roughness of the silicon substrate after sacrificial layer etching was 0.2 nm. Measurement examples are shown in fig. 3.8. These values are very small and imply that the measured surface energies are only weakly influenced by the surface roughness of the samples. Some samples were inspected by SEM to see if etch residues were left behind after the etching and rinsing procedures, but only smooth and

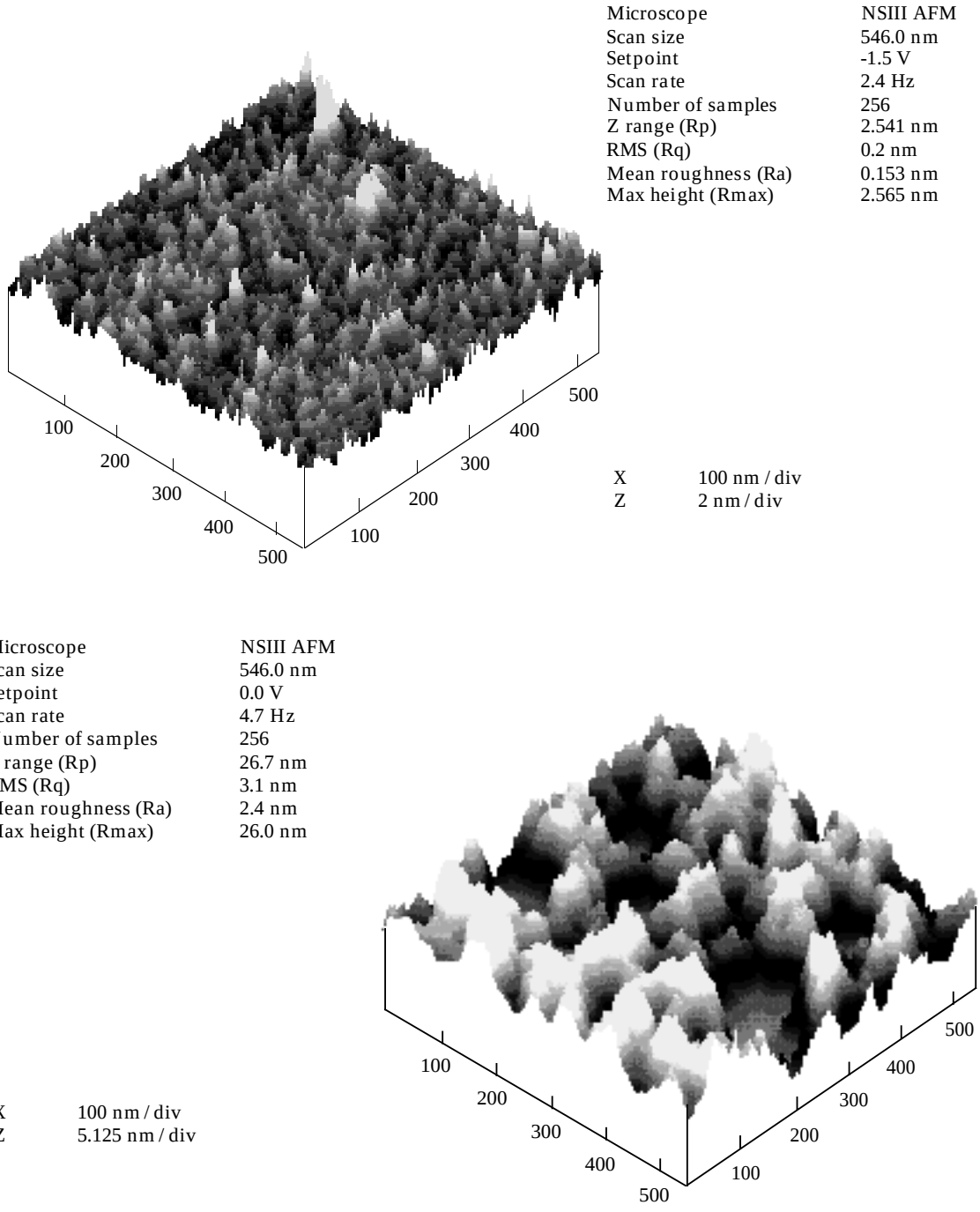

Fig. 3.8 *AFM scanning images of a silicon wafer and the bottom side of a polysilicon beam. Top figure: silicon wafer surface with RMS surface roughness of 0.2 nm. Bottom figure: bottom surface of polysilicon beam with RMS surface roughness of 3.1 nm, the beam thickness is 1.67 μm and silicondioxide thickness before release was 1.69 μm.*

clean surfaces were observed. Fig. 3.9 shows a SEM photograph of the disappearing gap spacing between a sticking beam and the substrate.

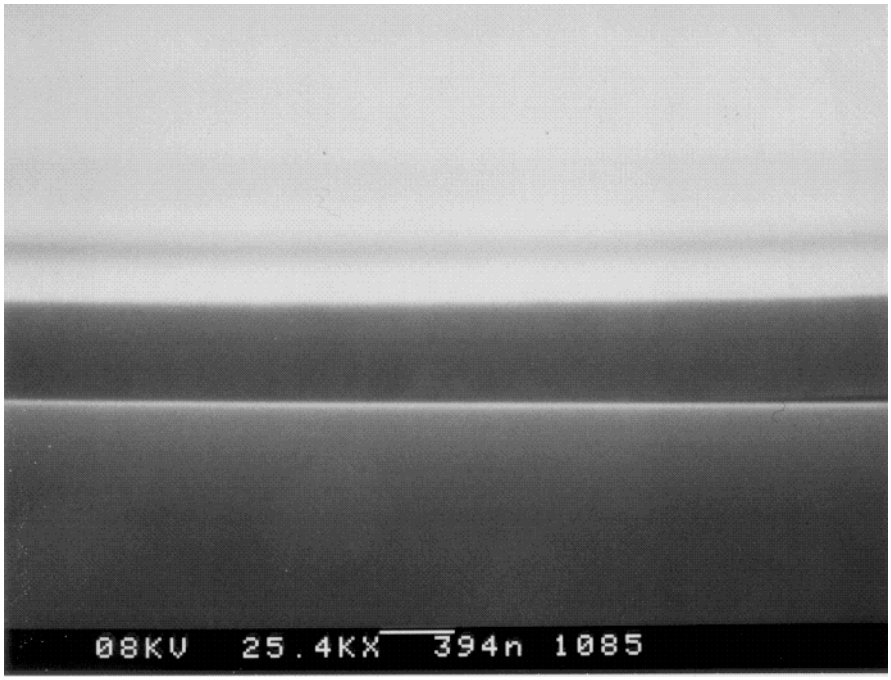

Fig. 3.9 *SEM Photograph of the disappearing gap spacing between a sticking beam and the substrate.*

3.5 DISCUSSION

From fig. 3.5 it can be seen that the measured pull-in length shows a linear fit with the parameter $[d^2h^3]^{1/4}$ as predicted by the theory. However, the slope of the curve is 41 $\mu m^{-1/4}$, which is lower than the theoretical value of 79 $\mu m^{-1/4}$, calculated from eq. (3.8) by using a plate modulus $\hat{E}$ of 166 GPa, a surface tension γ for IPA of 21.7 mN/m [3.20] and zero degrees contact angles θ_1 and θ_2. The influence of the step-up boundary of the fabricated microbeams or other assumptions for the deflection profile have been considered and only lead to small variations in the pull-in length and are thus unlikely to cause the discrepancy. The difference might be due to the non-equilibrium situation that exists during drying. The value used for the surface tension is only valid for IPA at thermodynamical equilibrium. During drying however, the liquid is not in equilibrium. Dynamic effects such as spreading may lead to in an increase of the capillary forces. In case of spreading, the difference can be enormous, and is about 60 mN/m for organic liquids on oxides and 300 mN/m for water on metallic oxides [3.21]. In our situation the increase would be 270 mN/m as determined from the pull-in measurements.

The measured surface energies of sticking beams (table 3.1) can be compared with theoretically calculated values to determine which adhesion mechanisms are present. After the rinsing and drying procedures, as described above, no residues have been observed by microscopic- or SEM inspection indicating that adhesion by solid bridging is not present. From table 3.1 one can see that the rinsing liquids which have been used hardly effect the adhesion energy and that it is mainly determined by the surface properties (i.e. hydrophobic or hydrophilic) of the materials which have been used. Although meniscus forces play an important role in the initiation of the physical contact between the beam and the substrate, the measured bonding energies are too small to be associated with meniscus forces from a thin liquid film, remaining after drying or initiated by microcapillary effects. Chemical bonding is also precluded for the same reason. As already discussed, electrostatic forces are unlikely to exceed van der Waals forces at small separations and are disregarded as a possible cause for stiction. This leaves van der Waals forces and hydrogen bonding as the possible causes for stiction.

The measured surface energies indicate that van der Waals forces are responsible for the hydrophobic bonded surfaces and hydrogen bridging is an additional bond mechanism for the hydrophilic bonded surfaces. The values for the surface energy show a good correlation with hydrophobic and hydrophilic wafer bonding experiments [3.15]. In this case energies are found of 0.04 to 0.1 J/m^2 for hydrophobic wafers and 0.14 to 0.2 J/m^2 for hydrophilic wafers bonded at room temperature.

In summary, stiction is accomplished in a two step process. First a temporary physical contact between surface micromachined structures and the substrate is induced by dynamic capillary forces during the drying of the rinse liquid. After this, permanent attachment is caused by van der Waals forces and hydrogen bridges which are induced by the small separation distance during this contact.

The maximum free standing length, the detachment length, is a function of the adhesion energy of the beam to the substrate surface and the mechanical stiffness of the structures. The maximum free standing length can easily be increased by increasing the beam thickness and the sacrificial layer thickness and using larger tensile residual strains.

Stiction can be prevented or reduced in several ways which has already been discussed in the previous chapter. The methods are based upon the prevention of physical contact between the structures and the substrate during the fabrication process and on the reduction of the adhesional forces.

3.6 CONCLUSIONS

It has been shown that during the drying process, attractive capillary forces are responsible for bringing micromechanical structures into contact with the substrate. A model for the surface tension forces during drying has been developed and applied to doubly clamped beams. For these beams a pull-in length exists beyond which the beams are forced into contact with the underlying substrate. Measurements of the pull-in length are in qualitative agreement with the theory. The measured values of the pull-in length are somewhat lower than predicted by the theory. This is probably due to dynamical effects during the drying process.

After complete drying, structures remain stuck to the substrate. The measured adhesion energy of the resultant bond has been determined using the detachment length of the beams after complete drying. The resulting bonding strength's were independent of the used rinsing liquids, water and isopropanol. The adhesion energy ranged from 0.05 to 0.10 J/m^2 for hydrophobic silicon surfaces and 0.24 to 0.26 J/m^2 for hydrophilic silicon surfaces. These energies indicate that van der Waals forces are responsible for the hydrophobic surfaces and hydrogen bridging is the dominant bond mechanism in case of the hydrophilic surfaces. These results are in agreement with wafer bonding experiments.

REFERENCES

[3.1] H. Guckel, J.J. Sniegowski and T.R. Christenson, Advances in processing techniques for silicon micromechanical devices with smooth surfaces, Proc. IEEE Micro Electro Mechanical Systems, Salt Lake City, Utah, U.S.A., June 6-9 1989, pp. 71-75.

[3.2] R.L. Alley, G.J. Cuan, R.T. Howe and K. Komvopoulos, The effect of release-etch processing on surface microstructure stiction, Proc. IEEE Solid-State Sensors and Actuators Workshop, Hilton Head Island, SC, U.S.A. June 22-25, 1992, pp. 202-207.

[3.3] C. Linder, E. Zimmerman and N.F. de Rooy, Capacitive polysilicon resonator with MOS detection circuit, Sensors and Actuators A, 25-27 (1991), 591-595.

[3.4] P.R. Scheeper, J.A. Voorthuyzen, W. Olthuis and P. Bergveld, Investigation of attractive forces between PECVD silicon nitride microstructures and an oxidized silicon substrate, Sensors and Actuators A, 30 (1992) 231-239.

[3.5] C.H. Mastrangelo and C.H. Hsu, A simple experimental technique for the measurement of the work of adhesion of microstructures, Proc. IEEE Solid-State Sensors and Actuators Workshop, Hilton Head Island, SC, U.S.A. June 22-25, 1992, pp. 208-212.

[3.6] W.C. Tang, T.C.H. Nguyen and R.T. Howe, Laterally driven polysilicon resonant microstructures, Proc. IEEE Micro Electro Mechanical Systems, Salt Lake City, Utah, U.S.A., Feb. 20-22,1989, pp. 53-59.

[3.7] H. A. C. Tilmans, Micro-mechanical sensors using encapsulated built-in resonant strain gauges, Ph.D. thesis, University of Twente, January 1993, ch. 4.

[3.8] H. Krupp, Adv. Coll. Interf. Sci., 1 (1967), pp. 111-239.

[3.9] J. Isrealachvilli, Intermolecular and Surface Forces, Academic Press, 2nd ed., 1991.

[3.10] J.Isrealachvilli, P. McGuiggan and R. Horn, Basic physics of interactions between surfaces in dry, humid and aqueous environments, Proc. The Electrochem. Soc. First Int. Symp. on Semiconductor Wafer Bonding, Phoenix, AZ, U.S.A., October 13-18, 1991, pp. 33-47.

[3.11] A.D. Zimon, Adhesion of dust and powders, 2nd ed., Consultants Bureau, New York, 1979.

[3.12] R.A. Bowling, An analysis of particle adhesion on semiconductor surfaces, J. Electrochem. Soc., Vol. 132, No. 9 (1985), pp. 2208-2214.

[3.13] D. Gräf, M. Grundner and R. Schultz, The reaction of water with hydrofluoric acid treated silicon (111) and (100) surfaces, J. Vac. Sci. Technol. A 7 (3), May/Jun 1989, pp. 808-813.

[3.14] M. Grundner, D. Gräf, P.O. Hahn and A. Schnegg, Wet chemical treatment of Si Surfaces: chemical composition and morphology, Solid State Technology, Feb. 1991, pp. 69-75.

[3.15] Y. Bäcklund, K. Herrmansson and L. Smith, Bond strength measurements related to silicon surface hydrophilicity, Proc. The Electrochem. Soc. First Int. Symp. on Semiconductor Wafer Bonding, Phoenix, AZ, U.S.A., October 13-18, 1991, pp. 82-87

[3.16] R.K. Iler, The chemistry of silica, Wiley, New York, 1979, p. 177.

[3.17] A Torii, M. Sasaki, K. Hane and S. Okuma, Adhesive force of the microstructures measured by the atomic force microscope, Proc. IEEE Micro Electro Mechanical Systems, Fort Lauderdale, Florida, U.S.A., Feb. 7-10,1993, pp. 111-116.

[3.18] J.A. Greenwood and J.B.P. Williamson, Contact of nominally flat surfaces, Proc. R. Soc. Lond. A 295 (1966), pp. 300-319.

[3.19] K.N.G. Fuller and D. Tabor, The effect of surface roughness on the adhesion of elastic solids, Proc. r. Soc. Lond., A 345 (1975), pp. 327-342.

[3.20] Handbook of chemistry and physics, 66 th ed., CRC press, 1985-1986

[3.21] P.G. de Gennes, Wetting: statics and dynamics, Rev. Mod. Phys., Vol. 57, No. 3, Part 1, July 1985, pp. 827-863.

Chapter Four

ANISOTROPIC REACTIVE ION ETCHING OF SILICON USING SF6/ O2/ CHF3 GAS MIXTURES*

Reactive ion etching of silicon, using $SF_6/O_2/CHF_3$, plasmas in an RF parallel plate system has been studied. Etching behaviour was found to be a function of loading, the cathode material and the mask material. Good results with respect to reproducability and uniformity have been obtained by using silicon as the cathode material and silicon dioxide as the masking material for mask designs where most of the surface is etched. Etch rate, selectivity, anisotropy and self-bias voltage have been examined as a function of SF_6 flow, O_2 flow, CHF_3 flow, pressure and the RF power, using response surface methodology, in order to optimise anisotropic etching conditions. The effect of the variables on the measured responses is discussed. The anisotropic etch mechanism is based on ion-enhanced inhibitor etching. SF_6 provides the reactive neutral etching species, O_2 supplies the inhibitor film forming species and SF_6 and CHF_3 generate ion species that suppress the formation of the inhibitor film at horizontal surfaces. Anisotropic etching of high aspect ratio structures with smooth etch surfaces has been achieved. The technique is applied to the fabrication of three dimensional micromechanical structures.

4.0 INTRODUCTION

Dry anisotropic etching of silicon is an important technology for the fabrication of micromechanical devices. Dry etch characteristics are not constrained by crystal planes as in the case of wet anisotropic etching for example by KOH solutions. This has the advantage that not only single crystalline-silicon but also poly-crystalline silicon and amorphous-silicon can be used for the fabrication of three-dimensional micromechanical structures. Dry etching techniques can be utilized to etch arbitrarily shaped mask designs. This is especially usefull for the fabrication of electrostatically driven microactuators that often exhibit complex shapes and require small gap sizes with high aspect ratio's.

Dry anisotropic etching of silicon has been achieved with Cl and Br containing gas mixtures such as SF_6-$CBrF_3$ [4.1], SF_6-$C_2Cl_3F_3$ [4.2] and SF_6-C_2ClF_5 [4.3, 4.4]. Etching of silicon with SF_6 at very low temperatures [4.5] or at

* published in J. Electrochem. Soc., Vol. 142, No. 6, June 1995, pp. 2020-2028.

very low pressures [4.6] can also be used to produce anisotropic etch profiles. Furthermore SF_6/O_2 gas mixtures [4.7-4.14] were found to anisotropically etch silicon. The last technique has the advantage of being a fluorine based etch chemistry that can be used in common reactive ion etch systems. Generally, however, rough etch surfaces are produced that make the process less useful.

In this study the objective was to optimise the anisotropic etching of silicon by SF6-O2 plasmas and produce smooth etch surfaces by response surface methodology, using the etch system described below. This was accomplished by the addition of CHF_3 to the SF_6/O_2 plasma. The process is applied in the fabrication of micromechanical structures with high aspect ratio's.

4.1 EXPERIMENTAL

4.1.1 Equipment

Etching experiments were performed in an Electrotech, Plasmafab 310-340 twin deposition/etch system. The RIE part consists of a parallel-plate system with a RF generator operating at 13.56 MHz and an automatic RF matching network. The pumping system consists of a turbo-pump in series with a rotary-pump. The spacing between the electrodes is fixed at 8.0 cm. The chamber walls consist of aluminium and the powered electrode has a diameter of 19 cm and is covered with a titaniumdioxide coated, aluminium (styros) plate. The temperature of the lower electrode can be controlled from 10 to 60 ˚C, by backside heating or cooling, using a temperature controlled oil-bath system. The flow rates of the gases were maintained with standard mass flow controllers. The pressure during processing is monitored with a capacitive manometer and controlled automatically with a throttle valve.

4.1.2 Initial experiments

Loading:

Initial experiments showed that the etch behaviour of silicon in SF6/O2 gas mixtures is loading dependent with regard to macroloading (i.e. the amount of wafers) and with regard to microloading (i.e. with regard to the pattern density on the wafers). This effect has been investigated by several researchers [15-18]. For our purpose we are interested in positive mask pattern designs that are equally distributed over the wafer, and where most of the wafer surface will be etched. The loading was kept constant at one 3" wafer per run in our experiments.

Cathode material:

The etching behaviour is also depending on the cathode material [4.15]. Three cathode materials; styros, graphite and silicon have been examined. The graphite and silicon electrode cover the styros electrode that is normally present in the reactor. Styros is a non-consumable material in contrast to graphite and silicon that are etched in fluorine based plasmas. With the styros cathode, the etch rate at the wafer edge was twice as high compared to the etch rate at the center of the wafer. This non-uniformity is a result of gradients in local reactant concentrations and is controlled by the relative etch rates of the wafer *vs.* the cathode material [4.15]. The uniformity in case of the graphite cathode was measured to be about 20 percent. The use of the consumable silicon cathode resulted in a uniformity of a few percent across the wafer. In this case the silicon etching rate as well as the selectivity to silicon dioxide were found to be lower than in case of the other cathode materials. Because of the good uniformity, the silicon cathode was used for further experiments.

Mask material:

During initial experiments, it was observed that etching is also affected by the mask material. It has been suggested that the mask material may act as a catalyst for SF_6 to generate fluorine [4.19, 4.20], thereby affecting the process conditions. For this reason a non catalytic mask material is preferred. In our experiments silicon dioxide has been used as the etch mask material.

CHF_3 addition:

Anisotropic etching with SF_6/O_2 plasmas normally produces rough etch surfaces. The silicon etch surfaces sometimes showed a black color as a result of large surface roughness (black silicon). This phenomenon has also been reported by other investigators [4.7, 4.9, 4.11]. It was found that the addition of CHF_3 to the SF_6/O_2 plasma produced smooth etch surfaces. Therefore this gas mixture has been used in our experiments.

4.1.3 Sample preparation

In all of the experiments, the samples prepared were 3" diam., <100> oriented, p-type (5-10 Ωcm) silicon wafers. A 3000 Å thick SiO_2 layer was grown by wet oxidation at 1000 ˚C. This layer was patterned by lithography and RIE using CHF_3 gas with a flow of 10 sccm, a process pressure of 20 mTorr, and an RF power of 50 Watt. The temperature of the oil bath, that controls the

temperature of the lower electrode, was set at 25 ˚C. After the etching of the SiO_2 layer the resist was stripped by oxygen ashing. Before the etching experiments the etching chamber was manually cleaned with ethanol and by an oxygen plasma cleaning step. Before each experiment the wafer was given an HF-dip ($HF:H_2O$ = 1:100) for one minute to remove the native oxide layer. The gas flows and process pressure were allowed to stabilize for five minutes before etching was performed.

4.1.4 Experimental design

The characteristics of the etch process are explored using a statistical experimental design [4.21, 4.22] and are modelled empirically by response surface methodology. In general a design should be chosen that will support a full quadratic model, which includes linear terms, two factor interactions, and quadratic terms for curvature. The general form of the full quadratic model is:

$$Y = b_0 + \sum_{i=1}^{f} b_i X_i + \sum_{i=1}^{f} b_{ii} X_i^2 + \sum_{i=1}^{f-1} \sum_{j=2}^{f} b_{ij} X_i X_j \qquad (4.1)$$

where the X_i represent the independant input variables (i.e., process parameters), the b_i are the coefficients for the linear terms, the b_{ii} are the coefficients for the quadratic terms, and the b_{ij} are the coefficients for the cross terms. A more elucidated discussion of surface response methodology is given in Appendix A.

For the optimisation of the RIE process the SF_6 flow, the O_2 flow, the CHF_3 flow, the pressure and the RF power have been chosen as the process variables. These process variables have been varied within the limits of our etching system. The temperature of the oil-bath that controls the cathode temperature was set at 25 ˚C. No special clamping or temperature control of the wafer was used. The loading was constant at one 3" wafer. A central composite rotatable second order design was used for the experiment. The monitored responses are the self-bias voltage, the silicon etch rate, the uniformity, the etch surface roughness, the selectivity and the anisotropy. The normalized experimental design information is given in table 4.1 whereas table 4.2 shows the actual parameter settings. The order of performing the experimental trials was randomized to minimize the effect of any systematic error.

Run #	SF_6	O_2	CHF_3	p	P
1	-1	-1	-1	-1	+1
2	+1	-1	-1	-1	-1
3	-1	+1	-1	-1	-1
4	+1	+1	-1	-1	+1
5	-1	-1	+1	-1	-1
6	+1	-1	+1	-1	+1
7	-1	+1	+1	-1	+1
8	+1	+1	+1	-1	-1
9	-1	-1	-1	+1	-1
10	+1	-1	-1	+1	+1
11	-1	+1	-1	+1	+1
12	+1	+1	-1	+1	-1
13	-1	-1	+1	+1	+1
14	+1	-1	+1	+1	-1
15	-1	+1	+1	+1	-1
16	+1	+1	+1	+1	+1
17	-2	0	0	0	0
18	+2	0	0	0	0
19	0	-2	0	0	0
20	0	+2	0	0	0
21	0	0	-2	0	0
22	0	0	+2	0	0
23	0	0	0	-2	0
24	0	0	0	+2	0
25	0	0	0	0	-2
26	0	0	0	0	+2
27	0	0	0	0	0
28	0	0	0	0	0
29	0	0	0	0	0
30	0	0	0	0	0
31	0	0	0	0	0
32	0	0	0	0	0

Table 4.1 *Nonrandomized experimental design for five normalized parameters.*

Variable	-2	-1	0	1	2
SF_6 flow [sccm]	10	20	30	40	50
O_2 flow [sccm]	2	6	10	14	18
CHF_3 flow [sccm]	2	7	12	17	22
pressure [mTorr]	20	60	100	140	180
power [Watt]	20	60	100	140	180

Table 4.2 *Variable settings used for the experimental design.*

4.1.5 Data aquisition

The thickness of the SiO_2 layer was measured by ellipsometry before and after the etching process to determine the etch rate of this layer. A correction was made for the HF-dip which was measured to remove about 50 Å of the oxide layer before the experiments. After etching, the etch depth of the silicon was measured with a Dektak surface profiler. The result was corrected for the remaining thickness of the oxide layer. The etch depth was measured at the center and at four points at 1 cm from the edge of the wafer to obtain an indication of the uniformity of the etch process. The selectivity was found from the ratio of the silicon etch depth and the difference in the SiO_2 thickness before and after the experiment. To determine the anisotropy, the samples were broken and their cross-section was examined by SEM. Several different etch profiles have been obtained. Depending on the process conditions not only mask undercut, but outward sloped profiles have also been observed. The anisotropy is defined by:

$$A = 1 - \frac{V}{H} \qquad (4.2)$$

where H is the etch depth and V is the maximal undercut of the mask or, in case of outward sloped profiles, the lateral extension of the sidewall as shown in fig. 4.1. This definition of the anisotropy does not give information whether the anisotropy is due to mask undercut or to outward sloped profiles. However the expression in equation (4.2) is generally used and therefore preferred for a comparison with results from other workers. A value of 1 represents a perfect vertical sidewall with no mask undercut.

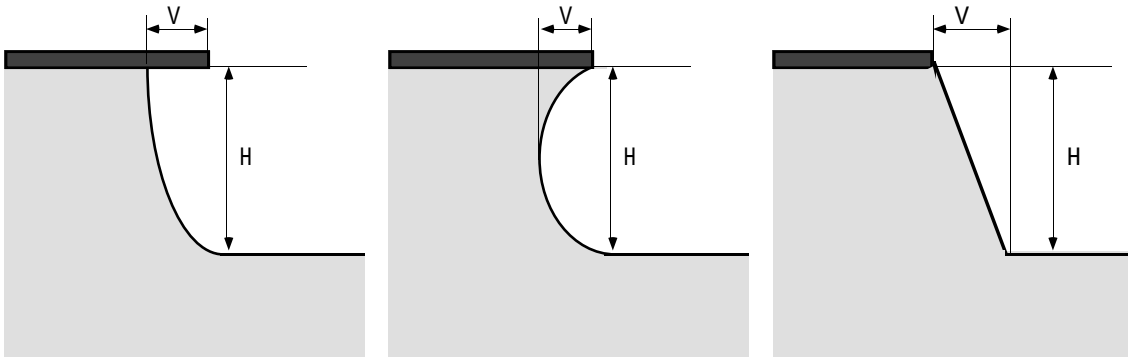

Fig. 4.1 *Definition of anisotropy.*

The roughness of the etch surface was only regarded qualitatively by means of the visual reflectivity of the silicon surface after etching, and by examining the etch surface of the cross-sectional SEM photographs.

In our experiments post structures and lines and spacings of 1,2 and 5 µm have been used to determine the etch rate and anisotropy for etch depth of about 2 µm. At these dimensions no feature size dependent etch effects have been noticed. However effects like RIE lag and charging, may affect etch results at larger etch depth's [4.17].

4.2 RESULTS AND DISCUSSION

The responses of the factorial design are shown in table 4.3. The independent input variables in formula (4.1) have been normalized as follows:

$$X_i = \left(\phi_i - \overline{\phi_i}\right) / \sigma_i \qquad (4.3)$$

Where X_i is the normalized value for the variable setting ϕ_i, $\overline{\phi_i}$ is the centerpoint value of that variable and σ_i is the step of the variable that has been used in the factorial design (see table 4.2).

The responses of the self-bias voltage, the silicon etch rate, the selectivity, and the anisotropy are fitted by the quadratic model (formula 4.1). The regression coefficients b_i,b_{ii},b_{ij} and the fit coefficient R^2 for the quadratic model are shown in table 4.4. Graphical representation of the responses and SEM photographs of sample cross sections are shown in fig. 4.2-4.8. In the graphs all parameters except for the specific parameters being varied are fixed at the center point of the design.

Run #	Bias Voltage [V]	Rate [µm/min]	Selec-tivity	Aniso-tropy	Unifor-mity [%]	Sur-face
1	477	0.430	5.9	0.590	1.0	smooth
2	47	0.320	13	0.690	2.4	smooth
3	232	0.200	4.7	0.940*	2.8	rough
4	339	0.670	10	0.880	3.9	smooth
5	224	0.200	5.2	0.810	2.0	smooth
6	343	0.460	5.1	0.620	3.9	smooth
7	517	0.420	6.3	0.980	5.8	smooth
8	72	0.310	10	0.960	1.2	smooth
9	31	0.120	14	0.886*	1.9	rough
10	50	0.550	11	0.560	4.2	smooth
11	224	0.400	6.0	0.810*	1.3	rough
12	27	0.0550	13	0.700	2.7	smooth
13	154	0.350	5.6	0.640	8.1	smooth
14	28	0.130	30	0.460	1.9	smooth
15	42	0.190	12	0.886*	2.7	rough
16	64	0.580	10	0.940	4.9	smooth
17	366	0.240	5.1	0.881*	3.6	rough
18	47	0.490	12	0.690	2.3	smooth
19	62	0.360	6.4	0.940	7.6	smooth
20	108	0.350	11	0.970*	1.2	rough
21	58	0.360	9.3	0.938*	2.2	rough
22	135	0.360	7.7	0.830	5.2	smooth
23	448	0.360	5.9	0.730	3.8	smooth
24	35	0.270	20	0.844*	3.7	rough
25	23	0.00680	6.8	0.900	3.3	smooth
26	356	0.600	7.2	0.660	3.5	smooth
27	88	0.450	9.7	0.970	5.5	smooth
28	85	0.440	10	0.940	6.3	smooth
29	86	0.430	9.2	0.950	3.8	smooth
30	84	0.450	10	0.970	2.3	smooth
31	87	0.430	8.9	0.970	3.7	smooth
32	85	0.430	9.4	0.960	3.9	smooth

Table 4.3 *Responses of the factorial design. In case of outward sloped etch profiles the anisotropy is marked by an asterisk.*

Coef.	Rate	Selec-tivity	Aniso-tropy	DCB
b0	0.434	9.34	0.969	87
b1	0.052	2.34	-0.066	-65
b2	0.010	-0.36	0.079	11
b3	0.004	-0.14	0.004	7
b4	-0.043	2.90	0.008	-102
b5	0.147	-1.72	-0.043	89
b11	-0.014	-0.05	-0.040	29
b22	-0.017	-0.01	-0.013	-1
b33	-0.016	-0.06	-0.023	2
b44	-0.027	1.05	-0.035	38
b55	-0.030	-0.44	-0.056	25
b12	0.003	-0.90	0.029	-6
b13	-0.008	0.60	0.004	4
b14	-0.016	0.65	-0.039	23
b15	0.035	-1.11	0.058	-14
b23	0.028	0.16	0.054	-17
b24	-0.007	-1.34	-0.016	2
b25	0.018	1.70	0.035	5
b34	0.022	1.29	-0.019	7
b35	-0.023	-1.15	0.028	-3
b45	0.027	-1.93	0.008	-46
s	0.01	0.5	0.01	1.5
R^2	0.99	0.90	0.95	0.99

Table 4.4 *Fitted coefficients of the quadratic model for the reponses. The s value at the bottom of each column is an estimate of the standard deviation for that response. The* R^2 *index indicates the agreement between model and data. A value of 1.00 denotes an ideal fit.*

4.2.1 Etch Rate

In fig. 2 the effect of the SF_6 and O_2 flow, and the effect of the pressure and RF power, on the etch rate of silicon are shown. The silicon etch rate shows a quadratic dependency on the SF_6 flow, the O_2 flow, the process pressure and the RF power. The rate is independent of the CHF_3 flow. The accuracy of the model is indicated by the squared multiple R^2 which is 0.99 and represents a good fit.

To understand the etch behaviour, some background of the etch mechanism is needed. It is well known that plasma etching of silicon with fluorinated compounds is primarily due to free fluorine [4.23]. The dissociation of SF_6 is assumed to involve electron impact dissociation reactions of the form:

$$e + SF_{x_g} \rightarrow SF_{x-1_g} + F_g + e \; (x = 3\text{–}6) \tag{4.4}$$

The etching of silicon occurs by a reaction with F atoms. The overall stochiometry of etching by atomic F is [4.24]:

$$Si + 4\,F \rightarrow SiF4 \tag{4.5}$$

The etch rate R_{Si} can be written as:

$$R_{Si} = k\,\beta_{Si}\,n_F \tag{4.6}$$

where k is a constant, β_{Si} is the reaction probability of fluorine at the surface and n_F is the density of fluorine atoms. Higher SF_6 flows will increase the fluorine concentration in the gas mixture, resulting in higher etch rates. At high flows, the fluorine concentration can decrease due to higher convective losses (see section on total flow rate) and the etch rate will start to decrease.

The influence of oxygen addition to SF_6 plasmas has been investigated by several authors [4.11-4.14, 4.25-4.27]. With an SF_6-O_2 mixture in the absence of silicon, the final reaction products are F_2, SOF_4, and SO_2F_2. When Si is etched, SiF_4 is the only stable silicon-containing etch product and SOF_2 is formed in oxygen-poor mixtures. It was found that oxygen additions drastically increase the conversion of the feed gas, evidently by reacting with fluorosulfur radicals and thus preventing their recombination with fluorine to reform SF_6 [4.12].

$$SF_x + F \rightarrow SF_{x-1} \; (x = 5\text{–}1) \tag{4.7}$$

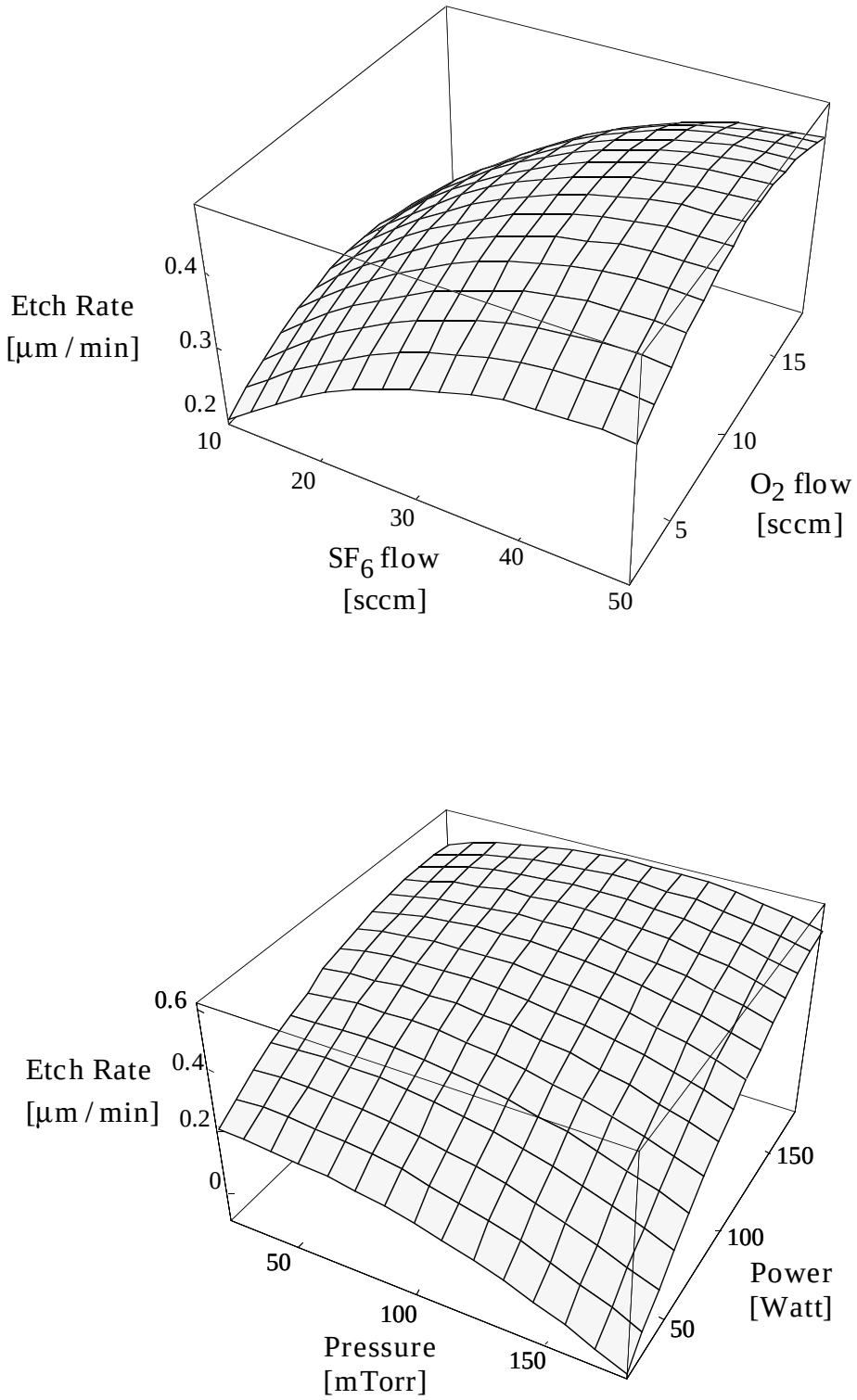

Fig. 4.2 *Surface plots showing the silicon etch rate as a function of the SF_6 and O_2 flow, and as a function of the process pressure and the RF power. All parameters except for the specific parameters being varied are fixed at the center point of the design.*

This leads to a net increase of F atoms. As the feed is made more O_2 rich, SO_2F_2 increases with respect to SOF_4 while the F-atom concentration first increases, reaches a maximum, and then decreases. These results closely parallel analogous trends in the carbon-based CF_4-O_2 system [4.24].

When silicon is exposed to the discharge, a significant change in the product composition is observed. SOF_2 is formed in oxygen-poor mixtures, SiF_4 appears, and the concentration of molecular fluorine is depressed [4.13]. As the quantity of oxygen is increased, the etch rate goes through a maximum and subsequently decreases.

In the presence of oxygen, oxygen species compete with F for active surface sites. This has been explained by a quantitative model which takes oxygen adsorption into account to relate the etch rate to the fluorine concentration for silicon and SiO_2 etching in CF_4-O_2 plasmas [4.24]. The decrease of the reaction probability was found to be:

$$\beta' = \frac{\beta}{1 + C\, n_O / n_F} \tag{4.8}$$

where β' is the reaction probability in the presence of oxygen, n_O is the density of oxygen atoms and C is a constant. Maneschijn [4.28] showed that this model also represents the data for SF_6-O_2 gas mixtures quite well.

Thus at higher O_2 flows the etch rate will be depressed as a result of the competition of oxygen atoms with fluorine atoms for chemisorption on the silicon surface.

As was pointed out by Tzeng [4.11], increasing the RF power leads to a significant increase of the atomic fluorine concentration while the oxygen concentration increases only slightly. This explains the increased silicon etching rate with increasing RF power.

At low RF power the etch rate decreases with increasing pressure, while at high RF power the etch rate first increases, reaches a maximum and finally decreases with increasing pressure. These results agree with the experiments of Kopalidis [4.12]. By measuring the effect of pressure on the discharge composition of SF_6-O_2 plasmas they found that the main effect of increasing pressure is to enhance the oxyfluoride production rates, thus reducing the recombination reactions. In accordance with our results, the self-bias was found to decrease strongly with increasing pressure. Assuming that ion bombardment contributes significantly to the overall etching rate (the synergistic effect of ion bombardment and chemical etching), the decrease in

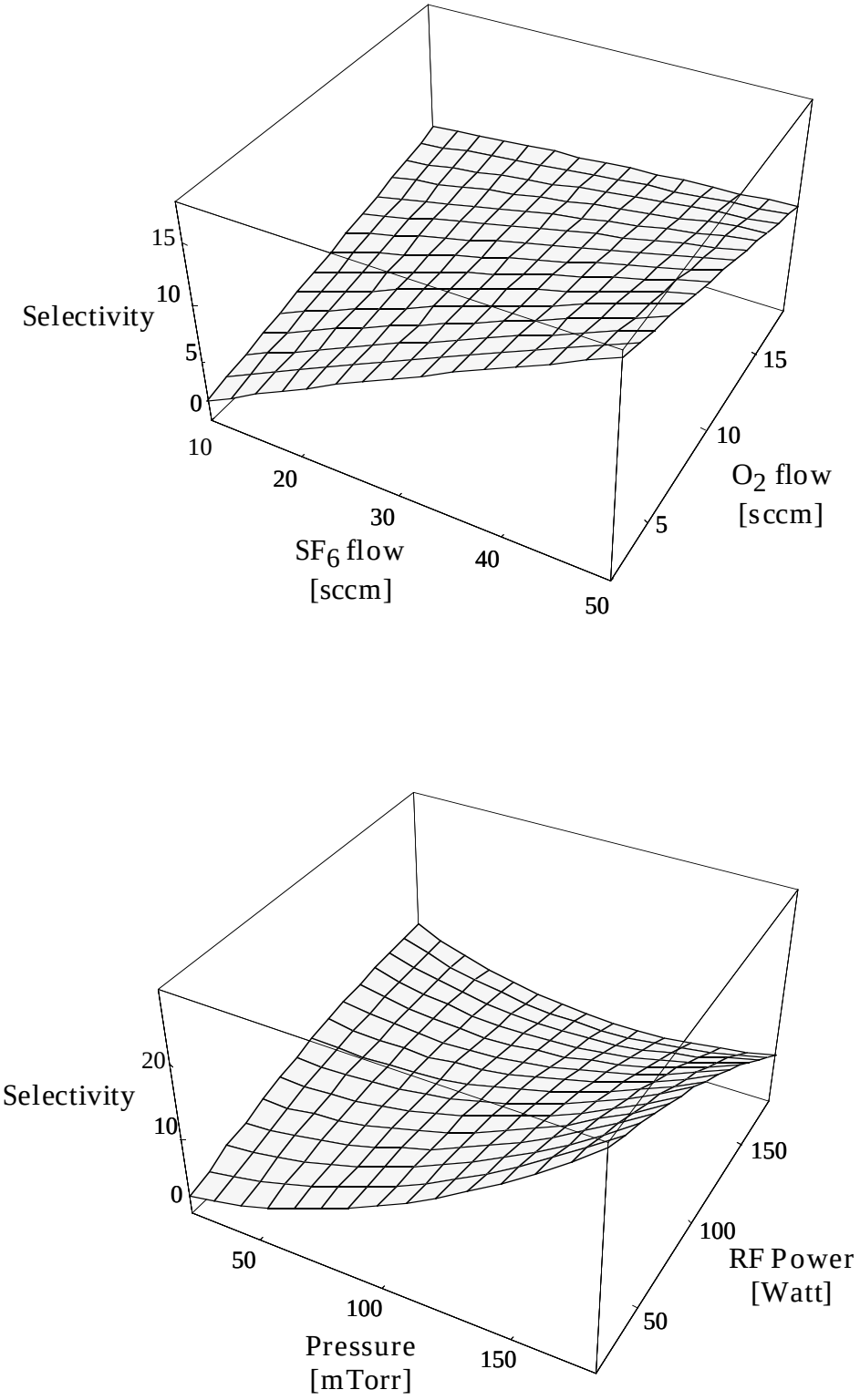

Fig. 4.3 *Surface plots showing the selectivity as a function of the SF_6 and the O_2 flow, and as a function of the process pressure and the RF power.*

the etch rate with increasing pressure can be explained by the decrease in ion bombardment at higher pressures.

At high RF power the initial increase of the etch rate with increasing pressure may be the result of an increasing F concentration and ion density that leads to a larger ion flux towards the substrate.

4.2.2 Selectivity

The selectivity linearly increases with the SF_6 flow and linearly decreases with the O_2 flow and the RF power, and only sligthly decreases with increasing CHF_3 flow. It shows a quadratic dependancy on the pressure. Surface plots showing the selectivity as a function of the SF_6 and the O_2 flow, and as a function of the process pressure and the RF power are shown in fig. 4.3. The R^2 index indicates a good model fit.

The selectivity is the quotient of the etch rates of silicon and silicon dioxide. The effect of the process parameters on the silicon etch rate have been discussed. The etch rate of SiO_2 is to a large extent due to direct etching by reactive ions. It was reported that the etch rate of SiO_2 in a CHF_3-O_2 plasma was found to follow the ion density and to be fairly independant of the plasma chemistry under most experimental conditions [4.29]. Ion bombardment increases with increasing RF power and with decreasing pressure. This results in a decrease of the SiO_2 etch rate with increasing RF power and an increase of the SiO_2 etch rate with increasing pressure. Assuming that the SiO_2 etch rate in this process is also fairly independent of the plasma chemistry, this leads to an increase of the selectivity with increasing SF_6 flow and increasing pressure (more chemical etching) and a decrease of the selectivity with increasing RF power and O_2 flow and CHF_3 flow (more physical etching).

4.2.3 Anisotropy

Responses of the anisotropy are shown in fig. 4.4. The anisotropy shows a linear increase with the O_2 flow. It is quadratically dependent on the process pressure, the RF power and the SF_6 flow. Furthermore the anisotropy shows a weak quadratic dependency on the CHF_3 flow. Again the fit between the data and the model is good.

Fig. 4.5 shows a selection of the sidewall profiles, which have been obtained in our experiments. These photographs clearly demonstrate that it is difficult to obtain a straightforward definition of the anisotropy. Depending on process conditions profiles may vary from isotropic to outward sloped profiles.

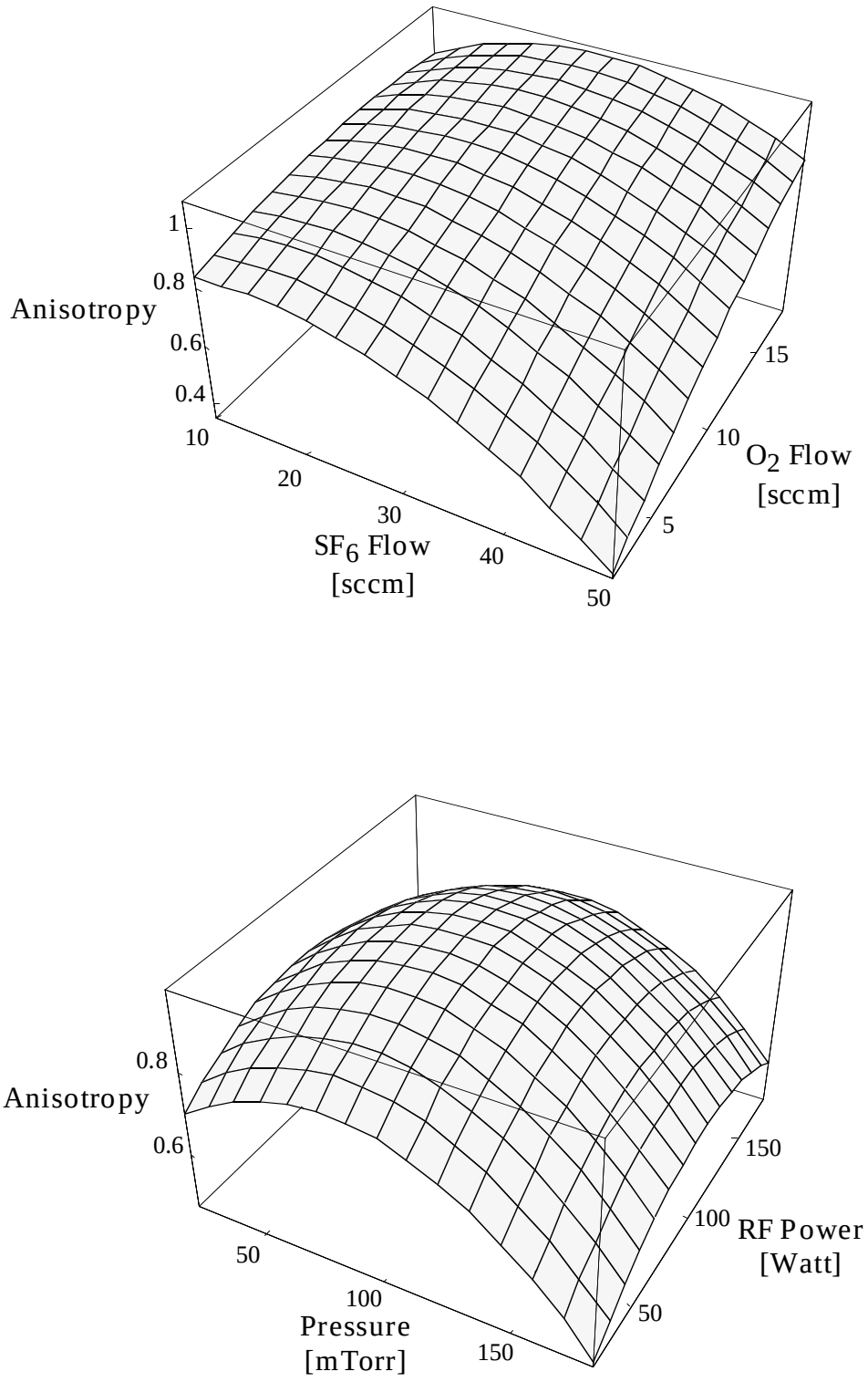

Fig. 4.4 *Surface plots showing the anisotropy as a function of the SF_6 and O_2 flow, and as a function of the process pressure and the RF power.*

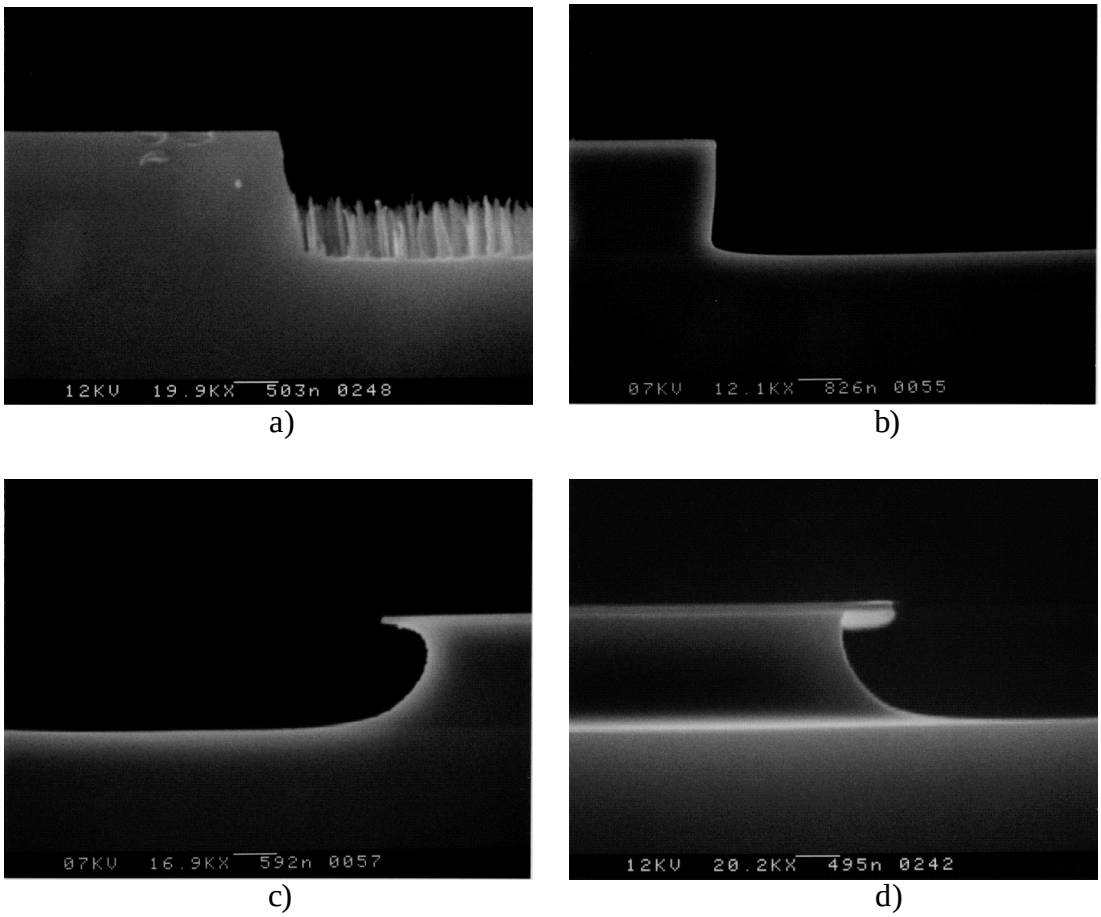

Fig. 4.5 *Sidewall profiles obtained under different process conditions. The parameter settings are shown in tabel 1 and 2 for: a) fact. nr. 24, b) fact. nr. 27, c) fact. nr. 13 and d) fact. nr. 6.*

Note that at high pressures and high O_2 flows the value of the anisotropy, as defined before, may be lower because of outward sloped etch profiles.

Auger Electron Spectroscopy (AES) data, taken within 15 minutes after the etch process, from the sidewall and bottom etch surface of a center point run is shown in fig. 4.6. Approximately equal amounts of sulfur and carbon were detected on both surfaces. Sulfur is most likely a product of the SF_6 gas and carbon may result from the CHF_3 gas or from organic contamination. The presence of fluorine was not observed. However, this may be due to electron stimulated desorption of fluorine atoms as a result of the measurement. Oxygen is present on both surfaces. The amount of oxygen on the sidewall surface is much higher than the amount of oxygen on the bottom surface. This clearly indicates a sidewall passivation effect by oxygen species, as proposed by Zhang [4.14]. On the horizontal silicon surfaces, adsorption of oxygen residue can be readily attacked through the physical bombardment of active ion species like SF_x^+ and CF_x^+. While on the the vertical Si surfaces (sidewalls), the removal of sidewall material is not significant because of the less directional kinetic energy in this orientation. These results are in agreement with other investigations [4.7, 4.30, 4.31].

Surface and interfacial residue films formed on polycrystalline silicon and silicon dioxide by reactive ion etching with SF_6-10% O_2 at 100 mTorr have been investigated using x-ray photoemission spectroscopy [4.30]. Composition and chemistry at the surface were found to be variations of SiO_xF_y. The thickness varied from 7 to 13 Å with a decreasing etch rate. Silicon surfaces etched in CF_4-O_2 plasma have been characterised with the use of in situ x-ray photoemission spectroscopy [4.31]. It was found that a SiO_xF_y layer on elemental silicon was formed under all conditions. For oxygen percentages greater than 5% in the feed gas, the oxygen content of the film and the film thickness increased, whereas the fluorine content of the film decreased.

These observations may explain the increase of the anisotropy with increasing O_2 flow and the decrease of the anisotropy with increasing SF_6 flow by affecting the formation of the sidewall passivation layer. At high O_2 flows and low SF_6 flows, profiles are positively tapered (outward sloped) and the anisotropy shows an initial increase with the SF_6 flow. In this region, the formation of the passivation layer is very pronounced and outward sloped etch profiles are obtained that may be the result of an orientation dependant etch rate. Increasing the SF_6 flow at high O_2 flows, increases the F concentration, thereby reducing the formation of the passivation layer on outward sloped profiles which leads to a more vertical etch profile that has a higher anisotropy.

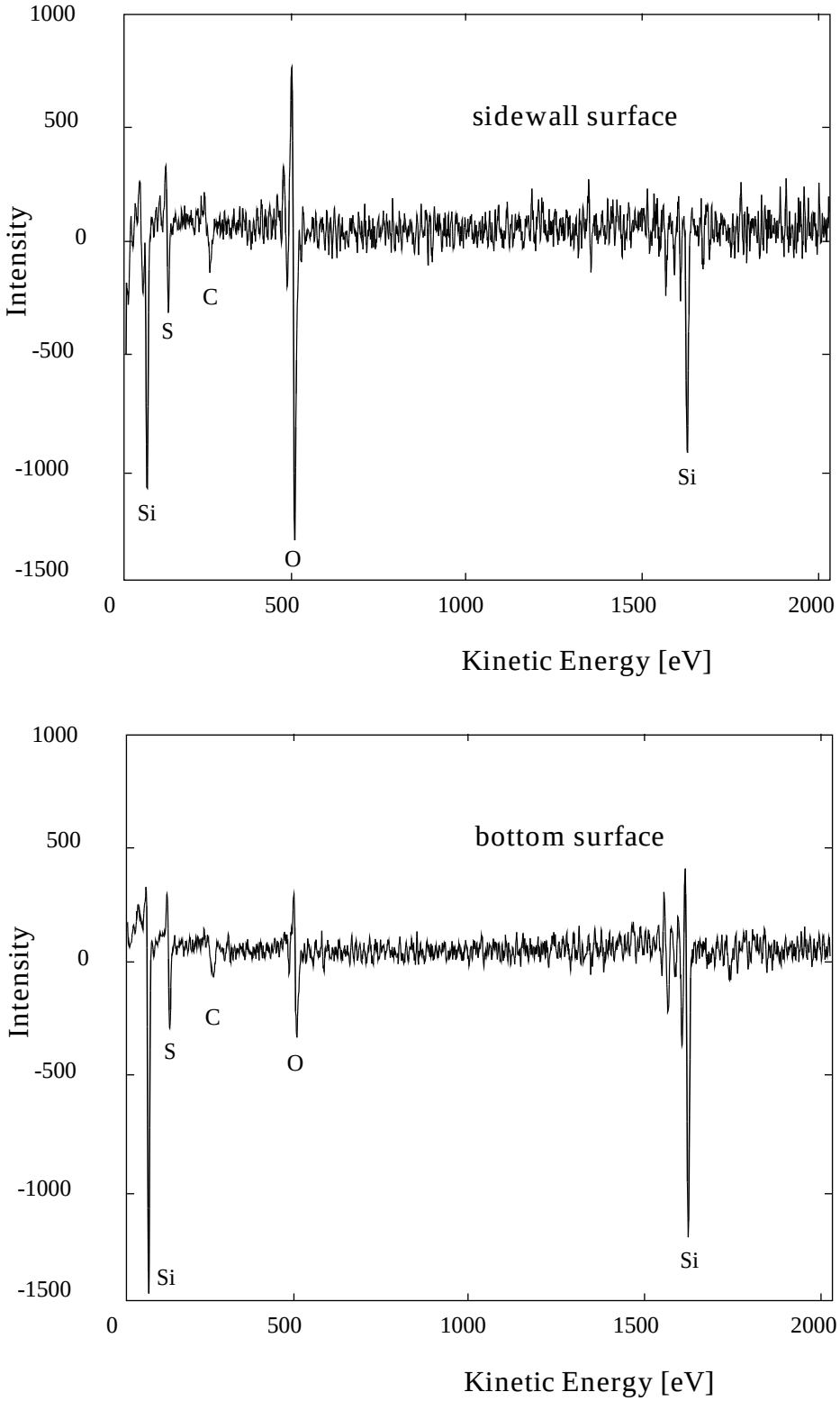

Fig. 4.6 *AES data of the sidewall and bottom etch surface after etching of a center point run.*

It has been found that increasing the pressure increases the atomic fluorine concentration and decreases the ion bombardment [4.12]. Both effects lead to a reduction of the anisotropy in agreement with our results at high pressures. At low pressures, however, the anisotropy increases with increasing pressure until it reaches a maximum. This may be explained by a low silicon surface coverage by oxygen atoms. The surface coverage is a function of the pressure and increases with increasing pressure. Apparently the oxygen concentration at low pressures is too small to result in a surface coverage that is high enough to form a stable passivation layer.

The RF power gives an initial increase, reaches a maximum and then results in a decrease of the anisotropy with increasing RF power. Increasing the RF power increases the F concentration as well as the ion bombardment on the horizontal surface. At low RF power it seems that the effect of the increase in ion bombardment is stronger than the effect of the increasing F concentration, giving a net increase in the anisotropy. At higher RF power the increase in the F concentration probably becomes dominant and reduces the formation of the passivation layer. This leads to a decrease in the anisotropy with increasing RF power.

Adding CHF_3 to the SF_6-O_2 plasma may influence the O to F concentration. In CHF_3-O_2 plasmas the major reaction products are CF_x species, CO, CO_2 and COF_2 [4.31]. These reactions will lower the O atom concentration. Since the selectivity (i.e the SiO_2 etch rate) is only sligthly affected by the CHF_3 addition it is suggested that the formation of the passivation layer is suppressed by an additional competition of oxygen with CF_x species on the surface. This effect is assumed to be more pronounced at the horizontal surfaces because the etch mechanism of silicon oxide, by CF_x species, is ion enhanced where ions are the main reactants in the etch reaction [4.29]. For high CHF_3 flows the reduction of the O atom concentration and passivation layer formation eventually result in more isotropic etching profiles (see fig. 4.8).

4.2.4 Total gas flow

It should be noted that the total gas flow in the experiments is not constant and changes, depending on the SF_6, O_2 and CHF_3 gas flow settings, from a minimum value of 32 sccm to a maximum value of 72 sccm. As a result, the residence time of the gases is not constant. Longer residence times will lead to a higher conversion of the etch gases into lower molecular weigth products. The etch rate dependency as a function of the total flow rate for SF_6/O_2 gas

mixtures has been studied by Tandon, and Kopalidis [4.8, 4.32]. At low pressures an increase in total flow rate is accompanied by an increase in the dissociation of SF_x molecules and radicals. The etch rate is limited by the supply of fluorine atoms while at high flow rate, the etch rate decreases due to convective losses. At high pressure and low flow rate, etchant production is at its maximum and increasing flow rates causes the fluorine concentration to decrease due to higher convective losses (active species are pumped away before they have an opportunity to react).

4.2.5 Uniformity

As shown in tabel 4.4 the uniformity does not show a large variation when the parameter settings are changed. Only a few points per wafer have been used to determine the uniformity leading to a relatively large standard error. The average uniformity of the etch rate is 3.5 percent with a standard deviation of 1.4 percent. A small increase is observed for high SF_6 flows and high pressures. The uniformity is mainly a function of loading and cathode material as discussed in the section on initial experiments.

4.2.6 Self-Bias Voltage

The bias voltage is quadratically dependent on the SF_6 flow, the RF power and the pressure. It increases linearly with the O_2 flow and the CHF_3 flow. The model fit of the experimental values is very good as indicated by the R^2 index which equals 0.99. The results are presented graphically in fig. 4.7.

SF_6 is used as a gaseous insulator because of its electronegativity. Increasing the SF_6 flow makes the discharge more electronegative due to a lower ratio of electrons to positive ions and the self-bias voltage decreases.

The decrease of the DC bias voltage with pressure is a result of a decrease in the electron energy as the pressure is increased [4.12]. The increase of the DC Bias with increasing O_2 flow and CHF_3 flow, is a consequence of a shift of the electron energy distribution to higher values [4.12].

4.2.7 Etch surface roughness

It was observed that the etch surface roughness showed a correlation to wafer cleanliness. A cleaning step, followed by an HF-dip were sufficient to reduce the etch surface roughness in this case, indicating that etch residue from previous steps or native oxide could be responsible for this effect. In spite of

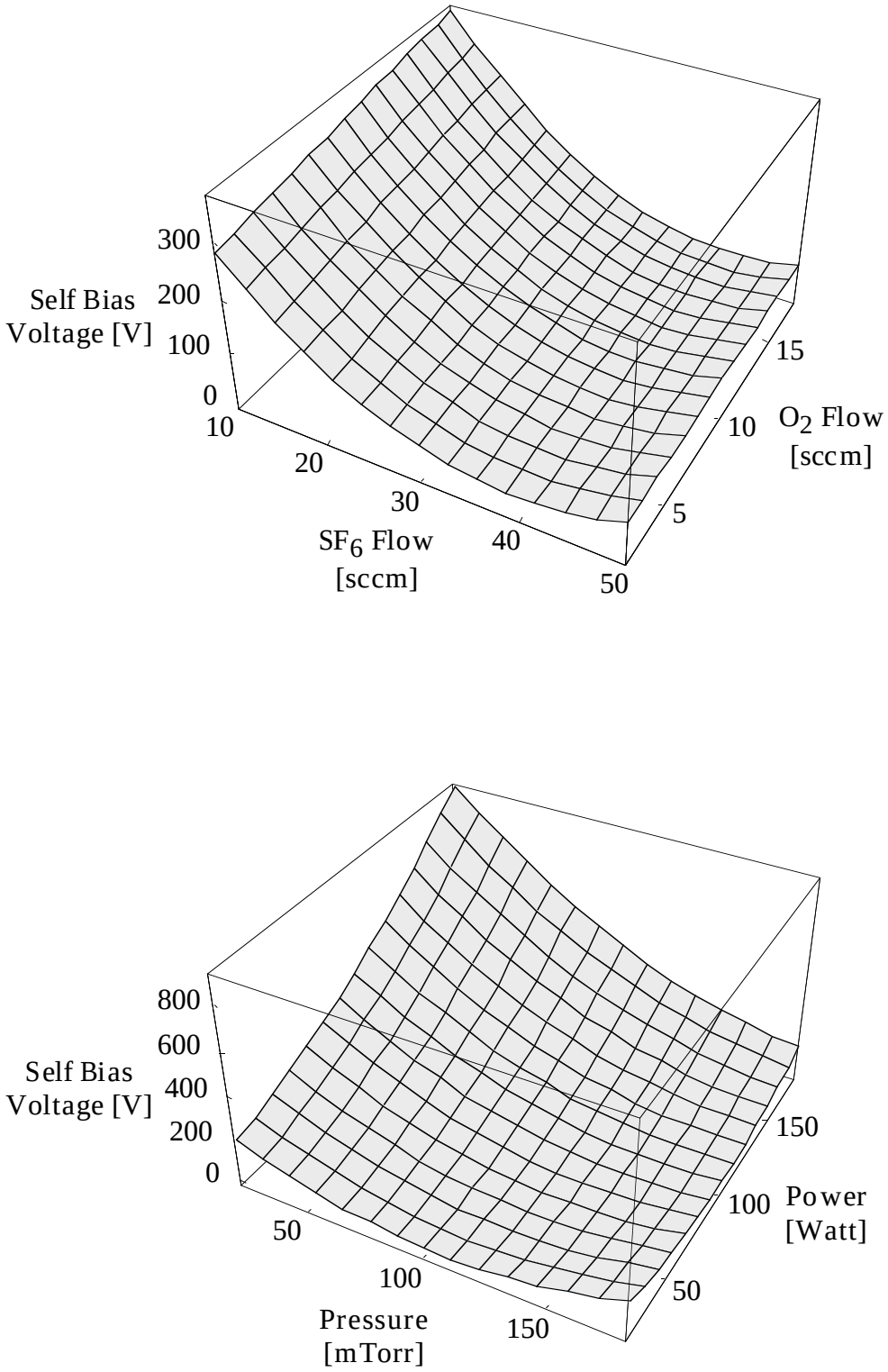

Fig. 4.7 *Surface plots showing the bias voltage as a function of the SF_6 and the O_2 flow, and as a function of the process pressure and the RF power.*

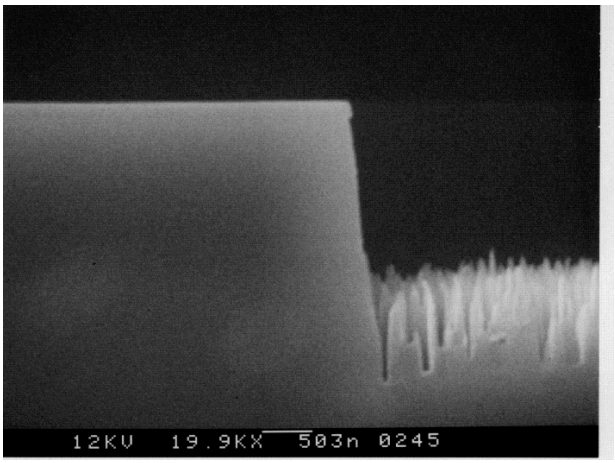

a)

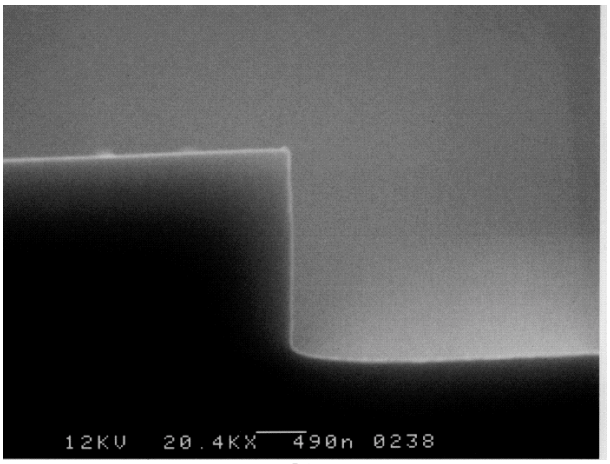

b)

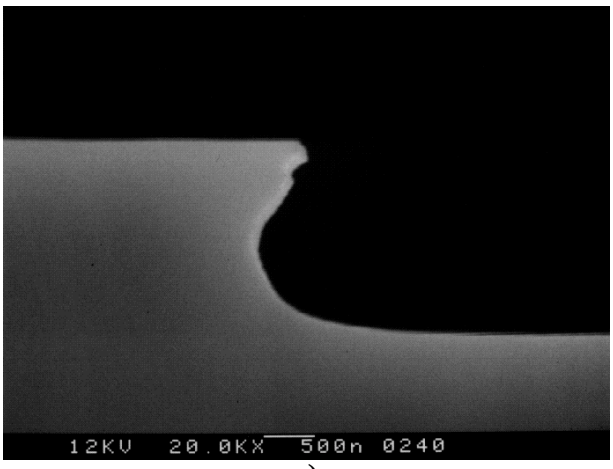

c)

Fig. 4.8 *SEM photograps showing the influence of the CHF_3 addition with respect to the surface roughness and etch profile. All parameter settings except for the CHF_3 flow are set at the center point, a) 2 sccm CHF_3; b) 12 sccm CHF_3; c) 22 sccm CHF_3.*

these precautions rough etch surfaces have been observed after the etching process and were found to be a function of the etch parameters. This indicates that rough etch surfaces are also generated by the etching process itself. At high pressures and high O_2 flows, in the anisotropic etching regime, the etch surface roughness increases. The addition of CHF_3 to an SF_6/O_2 gas mixture improves the etch surface quality, as shown in figure 4.8. When no CHF_3 is added, the etch surface roughness, in the anisotropic etch regime, is high as a result of "micrograss". The addition of CHF_3 results in smooth surfaces, only slightly affecting the anisotropy. At high CHF_3 flows, the anisotropy will be lost and more isotropic etching is obtained.

It is suggested that surface roughness is the result of silicon oxide micro masking. It has been shown that during etching in SF_6 plasmas, large amounts of Si particles are generated [4.33]. When oxygen is added to SF_6 plasmas these particles may also contain silicon oxide. Redeposition of these particles on the etch surfaces results in micromasking leading to the development of surface roughness (micrograss) in case of anisotropic etching. Another possibility is that the surface roughness results from variations in thickness of the oxyfluoride layer on the horizontal silicon surfaces.

The presence of CF_x species in the plasma may supress the formation and/or oxidation of the particles that are generated by the plasma or reduce their masking effect and suppresses the formation of the passivation layer on the horizontal surface by chemical and physical attack. Note that CF_x species may not only be produced by the etch gas but also by photoresist or reactor components like a graphite cathode.

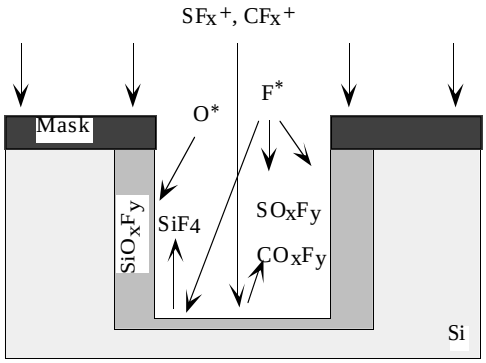

Fig. 4.9 *Schematic drawing of the SF_6, O_2, CHF_3 etch process.*

In summary it can be concluded that the anisotropic etch mechanism is based upon an ion-enhanced inhibitor etching process. This mechanism requires three ingredients: **1** reactive neutral species, **2** inhibitor film forming

species, and **3** vertical ion flux to the substrate to prevent growth or etch the inhibitor film at the horizontal surfaces. These mechanisms can be more or less controlled indepedently by the three etch gasses. SF6 produces the F radicals for the chemical etching of the silicon. O_2 creates the O radicals to passivate the silicon surface by silicon oxide species. CHF_3 produces CF_x ions that, in addition to SF_x ions, suppress the formation of the passivation layer at horizontal surfaces. The etch process is schematically shown in fig. 4.9.

4.3 APPLICATIONS

The process parameters optimized for high anisotropy are very usefull for the fabrication of deep trenches and micromechanical structures. The optimized process parameter settings result in an anisotropy of 0.98, an etch rate of 0.5 μm / min, a selectivity with SiO2 of 10 and a smooth etch surface. Not only monocrystalline silicon but also LPCVD polysilicon and sputtered silicon films have been used to fabricate micromechanical structures. In fig. 4.10 and 4.11 SEM photographs are shown that clearly demonstrate the usefullness of the RIE process for high aspect ratio structures. The selectivity of the silicon dioxide mask limits the etch depth. This problem can be solved by using metal etch masks. For instance with a chromium etch mask very high selectivities (>500) have been obtained, whereas etch characteristics are only slightly affected. Applications of this etch process, with respect to deep trench etching and other mask materials, has been presented elsewhere [4.34, 4.35].

4.4 CONCLUSIONS

Reactive ion etching using SF_6, O_2, CHF_3 gas mixtures for the anisotropic etching of silicon has been investigated. The etching behaviour was found to be affected by loading, the mask material and the cathode material. Reproducable and uniform results have been obtained by using a silicon cathode and a silicon dioxide mask. Surface response methodology was used to characterize etch rate, mask selectivity, bias voltage and anisotropy as a function of the RF power, the process pressure, the SF_6 flow, the O_2 flow and the CHF_3 flow in order to optimise anisotropic etching conditions. The effect of several variables on the measured responses has been discussed. The addition of CHF_3 can be used to produce smooth etch surfaces in the anisotropic regime and is usefull for a fine tuning of the anisotropy.

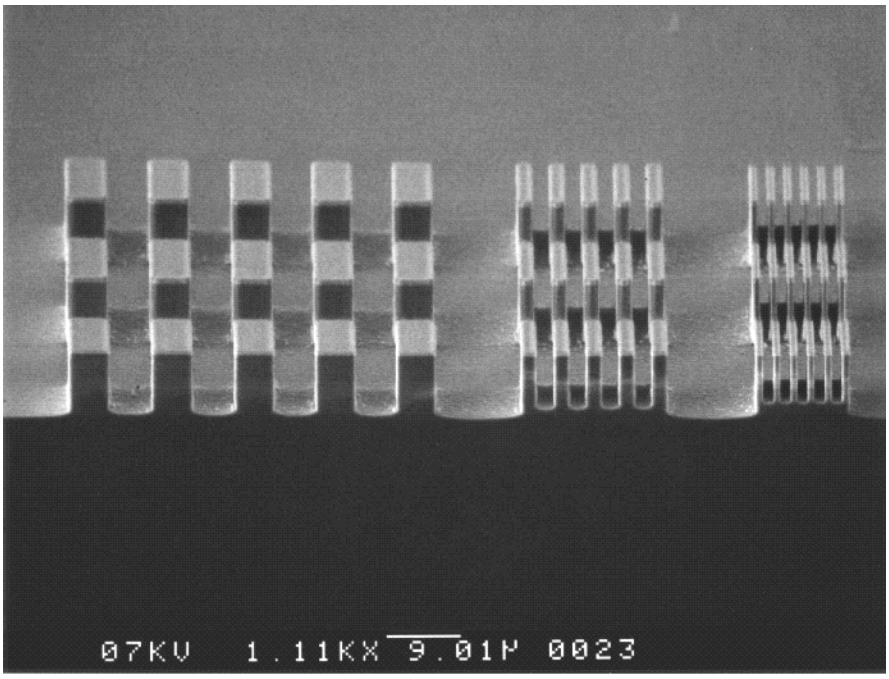

Fig. 4.10 *SEM photograph showing 1, 2 and 5 µm lines and spacings etched to a depth of plusminus 10 µm. For the 1 and 2 µm structures the effect of RIE lag is clearly visible.*

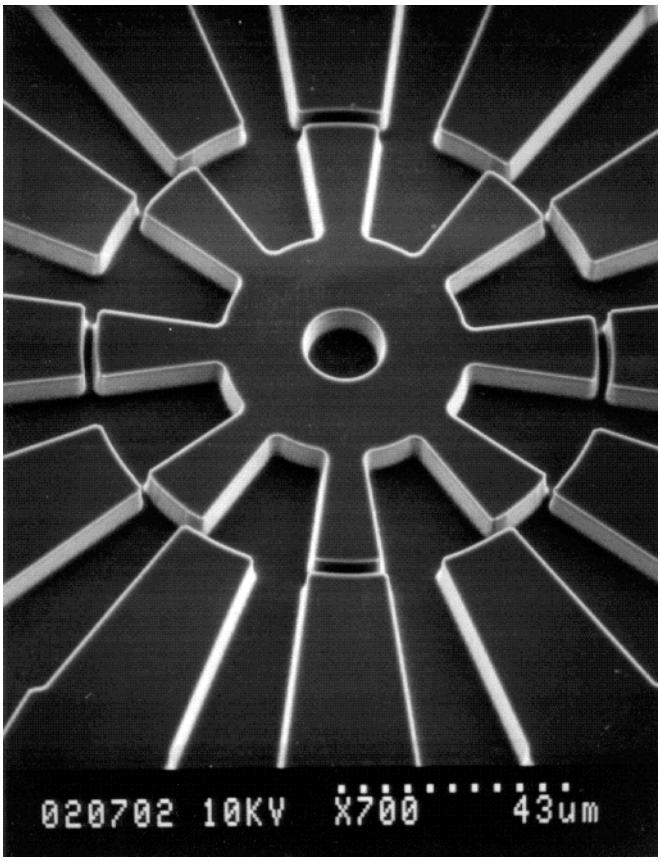

Fig. 4.11 *SEM photograph of a stator-rotor structure of an electrostatic micromotor. Diameter of the rotor is 100 µm, etch depth is 13 µm and the rotor-stator gap spacing is 2 µm.*

AES measurements indicate that anisotropic etching results from sidewall passivation by silicon oxide species. The anisotropic etch mechanism in SF_6, O_2, CHF_3 plasmas is based on ion-enhanced inhibitor etching. SF_6 provides the reactive neutral etching species, in the form of F atoms. O_2 supplies the inhibitor film forming species that passivate the surface with a SiO_xF_y layer. SF_6 and CHF_3 generate ion species, SF_x^+ and CF_x^+ respectively, that suppress the formation the inhibitor film at horizontal surfaces.

The fabrication of structures with aspect ratios of about 10 has been demonstrated. The process is applied to deep trench etching and fabrication of high aspect ratio structures used in micromachining.

REFERENCES

[4.1] A.M. Krings, K. Eden and H. Beneking, RIE etching of deep trenches in Si using $CBrF_3$ and SF_6 plasma, Microelectronic engineering, 6, 553-558 (1987).

[4.2] V.A. Yunkin, D. Fischer and E. Voges, Highly anisotropic selective reactive ion etching of deep trenches in silicon, Microelectronic Engineering, 23, 373-376 (1994).

[4.3] C. Linder, T Tschan and N.F. de Rooy, Deep dry etching techniques as a new IC compatible tool for silicon micromachining, Proc. of the 6th Int. Conf. on solid-state Sensors and Actuators (Transducers '91), June 24-27, 1991, San Fransisco, CA, U.S.A., pp. 524-527.

[4.4] J.P. McVittie and C. Gonzalez, Anisotropic etching of Si using SF_6:C_2ClF_5, Extended Anstracts, Fall meeting, Electrochem. Soc., Vol. 84-2, pp. 584-585.

[4.5] A.J. Watts and W.J. Varhue, Low temperature etching of silicon trenches with SF_6 in an electron cyclotron resonance reactor, J. Vac Sci Technol. A, 10, 1313-1317 (1992).

[4.6] C. Pomot, B. Mahi, B. Petit, Y. Arnal and J. Pelletier, Anisotropic etching of silicon using an SF_6/Ar microwave multipolar plasma, J. Vac. Sci. Technol. B, 4, 1-5 (1986).

[4.7] T. Syau, B. J. Baliga and R.W. Hamaker, Reactive ion etching of silicon trenches using SF_6/O_2 gas mixtures, J. Electrochem. Soc., 138, 3076-3081 (1991).

[4.8] U.S. Tandon and B.P. Pant, The characteristics of reactive ion etching of polysilicon using SF_6/O_2 and their interdependence, Vacuum, 42, 837-843 (1991).

[4.9] R. Pinto, K.V. Ramanathan and R.S. Babu, Reactive ion etching in SF_6 gas mixtures, J. Electrochem. Soc., 134, 165-175 (1987).

[4.10] C.P. D'Ernic, K.K. Chan and J. Blum, Deep trench plasma etching of single crystal silicon using SF_6/O_2 gas mixtures, J. Vac. Sci. Technol. B, 10, 1105-1110 (1983).

[4.11] Y. Tzeng and T.H. Lin, Dry etching of silicon materials in SF_6 based plasmas, roles of N_2O and O_2 gas additives. J. Electrochem. Soc., 134, 2304-2309 (1987).

[4.12] P. M. Kopalidis and J. Jorne, Langmuir probe measurements and characterization of silicon etching in SF_6/O_2 discharges. J. Electrochem. Soc., 139, 839-844 (1992).

[4.13] R. d'Agostino and D.L. Flamm, Plasma etching of Si and SiO_2 in SF_6-O_2 mixtures, J. Appl. Phys., 52, 162-167 (1981).

[4.14] M. Zhang, J.Z. Li, I. Adesida and E.D. Wolf, Reactive ion etching for submicron structures of refractory metal silicides and polycides, J. Vac. Sci. Technol. B, 1, 1037-1042 (1983).

[4.15] A.G. Nagy, Radial etch rate nonuniformity in reactive ion etching, J. Electrochem. Soc., 131, 1871-1875 (1984).

[4.16] C.J. Mogab, The loading effect in plasma etching, J. Electrochem. Soc., 124, 1262-1268 (1977).

[4.17] R.A. Gotscho and C.W. Jurgensen, Microscopic uniformity in plasma etching, J. Vac. Sci. Technol. B, 10, 2133-2147 (1992).

[4.18] R.W. Light and H.B. Bell, Profile control of polysilicon lines with an SF_6/O_2 plasma etch process, J. Electrochem. Soc., 130, 1567-1571 (1983).
[4.19] G.W. Grynkewich, T.H. Fedynyshyn and R.H. Dumas, The effect of aluminium masks on the plasma etch rates of polysilicon and silicon nitride, J. Vac. Sci. Technol. B8 , 5-9 (1990).
[4.20] T.H. Fedynyshyn, G.W. Grynkewich and Tso-Ping Ma, The effect of aluminium vs. photoresist masking on the etch rates of silicon and silicon dioxide in fluorine containing plasmas, J. Electrochem. Soc., 134, 2580-2585 (1987).
[4.21] W.G Cochran and G.M. Cox, Experimental designs, 2 nd ed., John Wiley & Sons, Inc. 1964.
[4.22] G.E.P. Box, W.G. Hunter and J.S. Hunter, Statistics for experimentors, John Wiley & Sons, Inc.
[4.23] Y. Lii and J. Jorné, Plasma etching of silicon in SF_6, J. Electrochem. Soc., 137, 3633-3639 (1990).
[4.24] C.J. Mogab, A.C. Adams and D.L. Flamm, Plasma etching of Si and SiO_2-The effect of oxygen additions to CF_4 plasmas, J. Appl. Phys., 49, 3796-3803 (1978).
[4.25] K.R. Ryan, Aspects of the chemistry of SF_6-O_2 plasmas, Plasma chemistry and Plasma Processing, 9, 483-497 (1989).
[4.26] K.R. Ryan and I.C. Plumb, A model for the etching of silicon in SF_6/O_2 plasmas, Plasma chemistry and plasma processing, 10, 207-229 (1990).
[4.27] W. W. Brandt and T. Honda, Mass spectrometric transient study of DC plasma etching of Si in SF_6/O_2 mixtures, J. Appl. Phys., 60, 1595-1601 (1986).
[4.28] A. Maneschijn, Ion bombardment and ion-assited etching in RF discharges, Ph.D. dissertation, Technical University of Delft, 3 October 1991.
[4.29] Ch. Steinbrüchel, H.W. Lehmann and K. Frick, Mechanism of dry etching of silicon dioxide, J. Electrochem. Soc., 132, 180-186 (1985).
[4.30] J.H. Thomas and B. Singh, X-ray photoemission study of SF_6/O_2 triode reactive ion etching of polysilicon, silicon dioxide and their interface, J. Vac. Sci. Technol. A, 10, 3039-3047 (1992).
[4.31] G.S. Oehrlein, S.W. Robey and J.L. Lindström, Appl. Phys. Lett., 52, 1170-1172 (1988).
[4.32] P. M. Kopalidis and J. Jorné, Modeling and experimental studies of reactive ion etching using SF_6/O_2 chemistry, J. Electrochem. Soc., 140, 3037-3045 (1993)
[4.33] M.M. Smadi, G.Y. Kong, R.N. Carlile and S.E. Beck, Particle contamination of silicon in SF_6 and CF_4/O_2 RF etch plasmas, J. Electrochem. Soc., 139, 3356-3363 (1992).
[4.34] H. Jansen, M. de Boer, R. Legtenberg and M. Elwenspoek, The black silicon method: a universal method for determining the parameter setting of a fluorine-based reactive ion etcher in deep silicon trench etching with profile control, Proc. Micro Mechanics Europe (MME '94), Pisa, Italy, September 5-6, 1994, pp. 60-64.
[4.35] H. Jansen, M. de Boer, J. Burger, R. Legtenberg and M. Elwenspoek, The black silicon method II: The effect of mask material and loading on the reactive ion etching of deep silicon trenches, Proc. Micro and Nano Engineering (MNE), Davos, Switzerland, Sept. 26-29, 1994, pp. 475-480.

Chapter Five

ELECTROSTATIC CURVED ELECTRODE ACTUATORS*

The design and performance of an actuator design that is based on the deformation of a movable micromechanical structure, which is deflected by electrostatic forces along a fixed curved electrode, is presented. The behaviour of this type of actuators is studied by using cantilever beam structures. A theoretical description of the static behaviour of a deformable cantilever beam that is forced into contact with a rigid structure by means of electrostatic forces is given. Modelling of the static behaviour was done by a simplified model based on energy methods and by 3D coupled electromechanical simulations using CoSolve-EM. The shape of the curved electrode was found to have a strong influence on the actuator performance. The models are in qualitative agreement with each other and predict stable actuator behaviour when the beam deflection becomes constrained by the curved electrode geometry before electrostatic pull-in can occur. Actuators that generate displacements in a direction lateral to the wafer surface were fabricated by polysilicon surface micromachining techniques. Experiments were performed in order to verify theoretical results. Relative large displacements and forces can be generated by curved electrode actuators. Depending on the design, or as a result of geometrical imperfections, instable regions in the deflection behaviour are present.

5.0 INTRODUCTION

Electrostatic actuation is very attractive for micro-electro-mechanical systems because of good its scaling properties to small dimensions, high energy densities and its relative ease of fabrication. However, electrostatic actuators which are able to generate relatively large displacements and large forces are difficult to design as a result of a geometric discrepancy. Large displacement actuators (e.g. comb drive structures) require displacements perpendicular to the major field lines, leading to small forces. Large force actuators (e.g. parallel plate structures) require small gaps and a displacement in the direction of the major field lines, thus implying small displacements. Several actuator designs

* presented at the IEEE Micro Electro Mechanical Systems Workshop, Amsterdam, the Netherlands, Jan 29-Feb. 2, 1995, pp. 37-42.

have been reported employing curved structures in order to generate large displacement and large forces. A curved electrode has been applied in microactuators for aligning optical fibers [5.1]. Actuators have been presented where a large vertical displacement is obtained by a S-shaped film sandwiched between planar electrodes [5.2]. Another design employs a deformed membrane which is pulled against a glass plate by electrostatic forces [5.3]. Active joints that employ a bend beam electrode that is pulled against a rigid counter electrode have also been proposed [5.4]. Furthermore a distributed electrostatic microactuator using wave-like electrodes [5.5] and an electrostatic moving wedge actuator for use in a microrelay [5.6] have been presented. All these actuators use curved structures with a specific shape that are deflected by electrostatic forces towards a counter electrode and generate displacements that are normal to the wafer surface.

In order to investigate the basic phenomena of these actuators, the static behaviour of cantilever beam structures that are deformed by electrostatic forces along curved electrodes has been studied. Special attention has been given to the effect of the electrode curvature on the static behaviour of the actuators. The dynamic properties of comparable structures have been presented elsewhere [5.7]. Devices, that generate displacements in a direction lateral to the wafer surface, have been fabricated by polysilicon surface micromachining techniques. Experimental data obtained from these structures is compared with theoretical results.

5.1 DESIGN

The design of curved electrode actuators includes a movable electrode structure, a cantilever beam, and a mechanically fixed curved counter electrode as shown in fig. 5.1. The gap distance between both electrodes is small near the clamped edge of the beam and increases with a position along the length of the beam. When a voltage is applied across the gap, an electrostatic force is created that will deform the beam along the outline of the curved electrode. The displacement is parallel to the wafer surface. To prevent short circuiting between the beam and the curved electrodes, electrical insulation is required e.g. by applying a dielectric layer between the structures or by using stand-off bumper structures that prevent physical contact of the electrodes.

For the shape of the curved electrode simple polynomials have been used that are normalised to a maximum tip deflection of the cantilever beam.

As will be shown in the next section the performance of these actuators is dependent on the electrode curvature and can become unstable after the so-called pull-in voltage. Although this work is focused on cantilever beam structures, similar actuators can be fabricated by using microbridges or membranes.

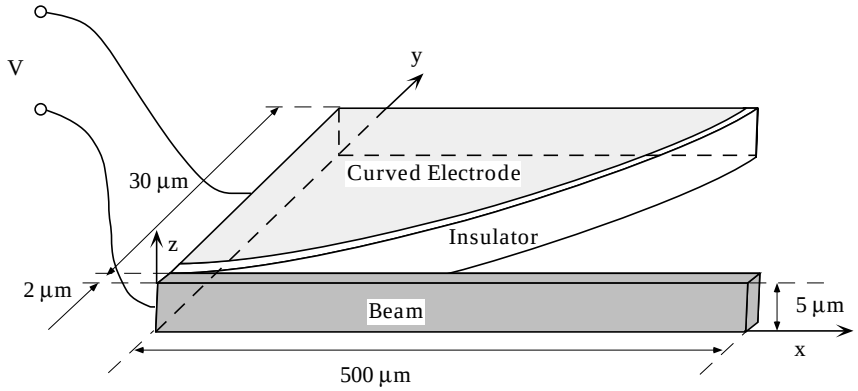

Fig. 5.1 *Schematic view of the curved electrode actuator.*

5.2 ENERGY MODEL

5.2.1 Unloaded and unconstrained static behaviour

Because the gap spacing is small with respect to the electrode length it is assumed that the electric field lines cross the gap only in the y-direction, i.e. a parallel plate approximation.

When a d.c. polarisation voltage is applied between the capacitor electrodes, an electrostatic force is developed that is inversely proportional to the square of the gap spacing. This makes the force dependent on the deflection, leading to non-linear behaviour. The static deflection $w_{(x)}$ of a prismatic beam with a transverse pressure $q_{(x,V)}$ can be described by the following non-linear differential equation of equilibrium:

$$E_y I \frac{d^4 w(x)}{dx^4} = q_{(x,V)} = \frac{1}{2} \frac{\varepsilon_0 \, h \, V^2}{\left[\frac{d}{\varepsilon_r} + s_{(x)} - w_{(x)} \right]^2} \tag{5.1}$$

where $q_{(x,V)}$ denotes the static electrostatic force per unit beam length as a function of the position x and the drive voltage V, $E_y I$ is the bending stiffness, d is the thickness of the insulator, ε_0 the dielectric constant in air, h the width of the beam, ε_r is the dielectric constant of the insulator and $s_{(x)}$ the shape of the

electrode as a function of the position x. An analytical closed-form solution of the above equation cannot be found and numerical solutions or a simplified model based on the method of total potential energy using small deflection theory has to be applied e.g. the Rayleigh-Ritz method, were an approximate solution to the differential equation is constructed in the form of admissible trial functions [5.8, 5.9]. The total potential energy, denoted by Π , can be expressed as:

$$\Pi = U_b + V_{el} \tag{5.2}$$

where U_b and V_{el} are the strain energy term of bending and the potential energy of the electrostatic force $q_{(x,V)}$ given by:

$$U_b = \frac{1}{2}\int_0^L E_y I \left[\frac{d^2 w_{(x)}}{dx^2}\right]^2 dx \tag{5.3}$$

and

$$V_{el} = -\frac{1}{2}\int_0^L \frac{\varepsilon_0 \, h \, V^2}{\frac{d}{\varepsilon_r} + s_{(x)} - w_{(x)}} dx \tag{5.4}$$

The deflection profile of a uniformly loaded cantilever beam has been used for the admissible trial function:

$$\tilde{w}(x) = c \, g(x) = c \, x^2 \, (6 \, L^2 - 4 \, L \, x + x^2) \tag{5.5}$$

where c is a constant that has to be determined. The applied shape of the curved electrodes have been simple polynomials, described by the following expression:

$$s(x) = \delta_{max}\left[\frac{x}{L}\right]^n \tag{5.6}$$

where δ_{max} is the maximum gap distance of the curved electrode and n is the polynomial order of the curve, $n \geq 0$.

The system is in equilibrium when the first variation of the total potential energy with respect to the constant c equals zero. By solving this equation the unknown c can be found giving the approximate deflection profile. Whether this equilibrium is stable or unstable is determined by the second variation of the potential energy with respect to c. At the transition from a stable to an unstable equilibrium the first and the second derivative of the potential energy with respect to c are zero. Solving these equations simultaneously yields the pull-in voltage V_{PI} of the cantilever and an implicit expression for the constant c_{PI} at pull-in:

$$V_{PI}^{\,2} = \frac{E_y I}{\varepsilon_0 h} \frac{\int_0^L \left[\frac{d^2 g_{(x)}}{dx^2}\right]^2 dx}{\int_0^L \frac{g_{(x)}^{\,2}}{\left(\frac{d}{\varepsilon_r} + s_{(x)} - c_{PI}\, g_{(x)}\right)^3} dx} \tag{5.7}$$

$$\int_0^L \frac{c_{PI}\, g_{(x)}^{\,2}\, dx}{\left(\frac{d}{\varepsilon_r} + s_{(x)} - c_{PI}\, g_{(x)}\right)^3} = \int_0^L \frac{g_{(x)}\, dx}{\left(\frac{d}{\varepsilon_r} + s_{(x)} - c_{PI}\, g_{(x)}\right)^2} \tag{5.8}$$

The calculated pull-in voltages for different polynomial orders obtained by this energy method are listed in table 5.1.

n	V_{PI} [V]	c_{PI} [$*10^7$ m^{-3}]
0	141.7	7.63
0.5	115.2	7.66
1.0	86.2	7.56
1.5	59.5	6.88
2.0	40.0	5.54

Table 5.1 *Calculated pull-in voltages from the energy model, for polysilicon (E_y=150 GPa) cantilever beams (h*t*L=5*2*500 μm) with a minimum gap spacing d of 2 μm and a maximum deflection δ_{max} of 30 μm. A relative dielectric constant of the insulator ε_r equal to 1 has been used.*

Equations (5.7) and (5.8) give little insight into the effect of different parameters. Some aspects will be discussed here. Increasing the polynomial order *n* of the electrode curve decreases the pull-in voltage, while the maximum displacement just before pull-in stays about the same. Thus, by using curved electrodes the pull-in voltage can be lowered significantly resulting in large amplitude motion at lower driving voltages as compared to a parallel plate structure *(n=0)*. At voltages above the pull-in voltage the displacement cannot be controlled because of unstable behaviour. The maximum tip displacement at pull-in is independent of the beam properties and only depends on the gap geometry. The tip displacement at pull-in, calculated from the examples in table 5.1, is about one third of the maximum gap spacing δ_{max} which is comparable to the stable to unstable deflection boundary for a lumped parallel-plate spring model [5.10]. The pull-in voltage strongly decreases with a decreasing initial gap spacing at the clamped edge of the beam or an increasing dielectric constant of the insulating layer between the electrodes.

5.2.2 Constrained static behaviour

The pull-in voltage decreases with increasing polynomial order. However for polynomial orders above two it was found that the deflection profile of the beam becomes constrained by the geometry of the curved electrode before the pull-in voltage is reached. In this situation, the model needs to be adjusted. In addition, a force *P*, that is acting on the tip of the beam, has been added in order to perform external work. In addition to the electrostatic forces, this force will deform the beam in that part where the beam is not in contact with the curved electrode.

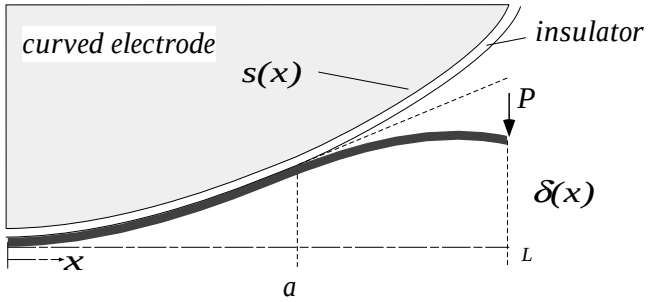

Fig. 5.2 *Sketch of the constrained beam deflection model with external loading force P.*

It is assumed that the beam will partly be in contact with the curved electrode and will partly be free standing; and is clamped at point *a,* as sketched in fig. 5.2. The problem will have a variable boundary condition with respect to

the free standing length of the beam. Therefore the system has to be divided in two regions. From the clamped edge of the beam to point a , the beam is assumed to be in physical contact with the curved electrode and the deflection profile $w_{(x)}$ will be equal to the shape of the electrode $s_{(x)}$. The distance between the electrodes is equal to d, the thickness of the insulator. Beyond point a, the beam is free and deflected by electrostatic forces and the external force.

The expressions for the strain energy of bending and the potential energy of the electrostatic force become:

$$U_b = \frac{1}{2}\int_0^a E_y I\left[\frac{d^2 s_{(x)}}{dx^2}\right]^2 dx + \frac{1}{2}\int_a^L E_y I\left[\frac{d^2 w_{(x)}}{dx^2}\right]^2 dx \tag{5.9}$$

and

$$V_{el} = -\frac{1}{2}\int_0^a \frac{\varepsilon_r \varepsilon_0 h V^2}{d}\, dx - \frac{1}{2}\int_a^L \frac{\varepsilon_0 h V^2}{\frac{d}{\varepsilon_r} + s_{(x)} - w_{(x)}}\, dx \tag{5.10}$$

An additional term has to be added to the total potential energy, given in expression (5.2). This term is the work from the external force acting on the tip of the beam, given by:

$$V_P = P\, w(L) \tag{5.11}$$

The admissible trial function of the deflection profile of the cantilever beam is now also dependent on the contact distance a and bending from force P:

$$\tilde{w}_{(x)} = s_{(x)} \qquad \text{for } 0 < x \le a \tag{5.12}$$

$$\tilde{w}_{(x)} = c(x\text{-}a)^2\left[6(L\text{-}a)^2 - 4(L\text{-}a)(x\text{-}a) + (x\text{-}a)^2\right] - \frac{P(x\text{-}a)^2\left[3(L\text{-}a)\text{-}(x\text{-}a)\right]}{6EI} + \left[s_{(x)}\right]_{x=a} + \left[\frac{ds}{dx}\right]_{x=a}(x-a) \qquad \text{for } a < x < L \tag{5.13}$$

This system, is in equilibrium when the first variation of the potential energy with respect to the contact distance a equals zero and the first variation of the potential energy with respect to the constant c equals zero. Solving both

equations simultaneously by numerical iteration gives the values of *a* and *c* at a certain driving voltage.

The tip deflection versus driving voltage for unloaded designs with a polynomial order ranging from two to four is shown in fig. 5.3. For designs with a polynomial order above 2, a stable behaviour up to the maximum tip deflection is found. This is the result of the constrained beam deflection which makes the beam zip along the curved electrode.

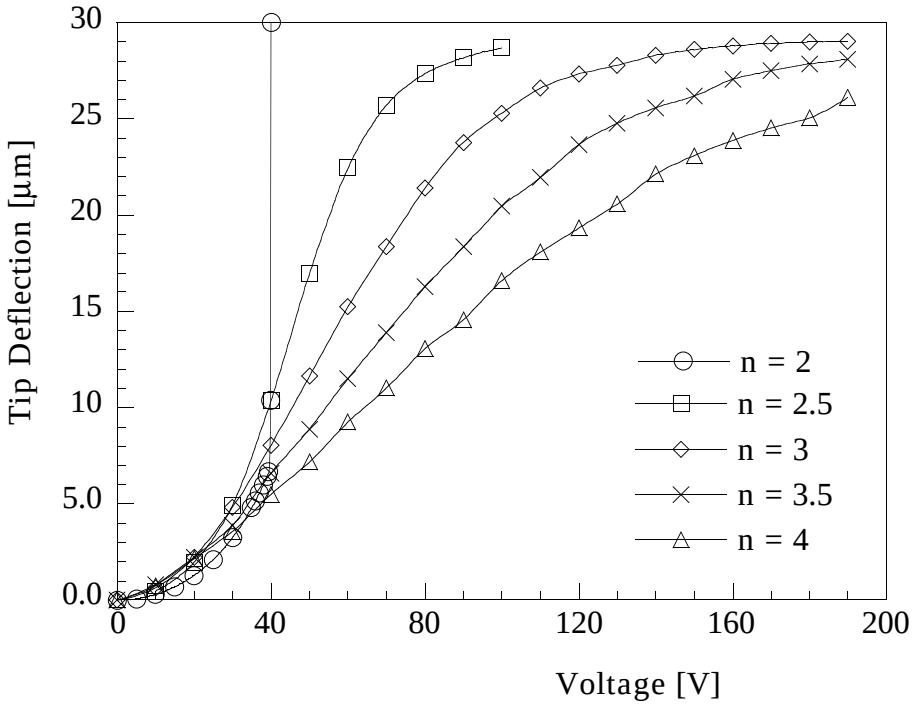

Fig. 5.3 *Modelled tip deflection as a function of the applied voltage for several polynomial orders n of the curved electrode. When the polynomial order is larger than 2 the behaviour becomes stable up to the maximum tip deflection. Otherwise a pull-in voltage exists. Variable settings that have been used are:* E_y*=150 GPa, h=5 µm, t=2 µm, L=500 µm, d=2 µm,* δ_{max}*=30 µm and* ε_r*=1.*

5.2.3 Force generation

The force generated by the actuator is a function of the displacement of the tip. It can also be found by numerical iteration from the first variation of the potential energy, with respect to the contact distance *a* and the constant *c*, that equals zero. The external force needed to keep the tip fixed at a certain position is shown in fig. 5.4 for different tip positions. Actuator dimensions are given in the figures and the effect of the dielectric constant of the insulating layer between the electrodes is also shown. Forces are typically a few µN for this example but increase with decreasing gap distance and increasing dielectric

constant of the insulating layer. The deformation of the beam is illustrated in fig. 5.5. In this case the tip is fixed at zero deflection. When the actuator is loaded by displacement dependent forces like e.g. a spring, the problem can be solved by substitution of the force to displacement relation.

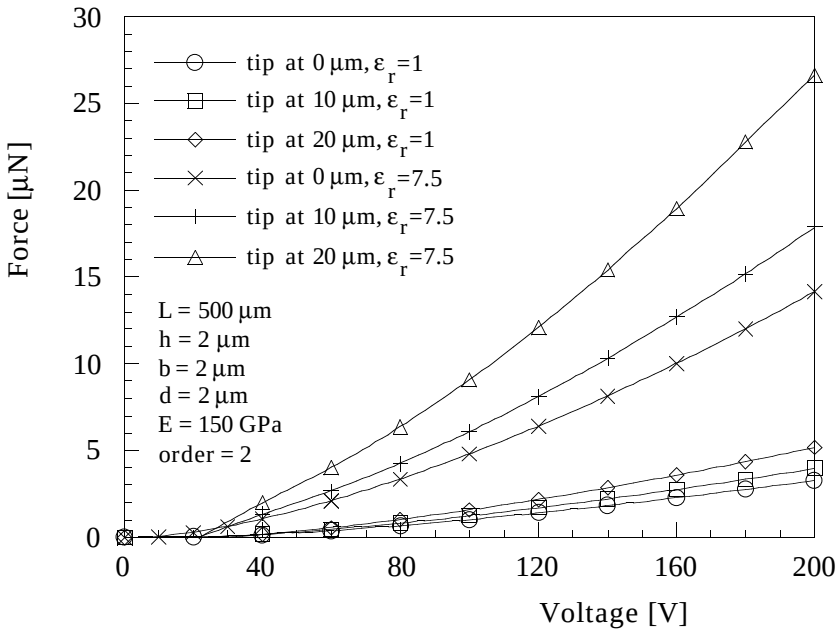

Fig. 5.4 *Theoretical force generation of a quadratic order electrode curvature as a function of driving voltage. The tip deflection is fixed at 0 ,10 and 20 µm. The effect of the relative dielectric constant of the insulating layer is also shown. Unless given in the graph, variable settings equal to fig. 5.3 have been used.*

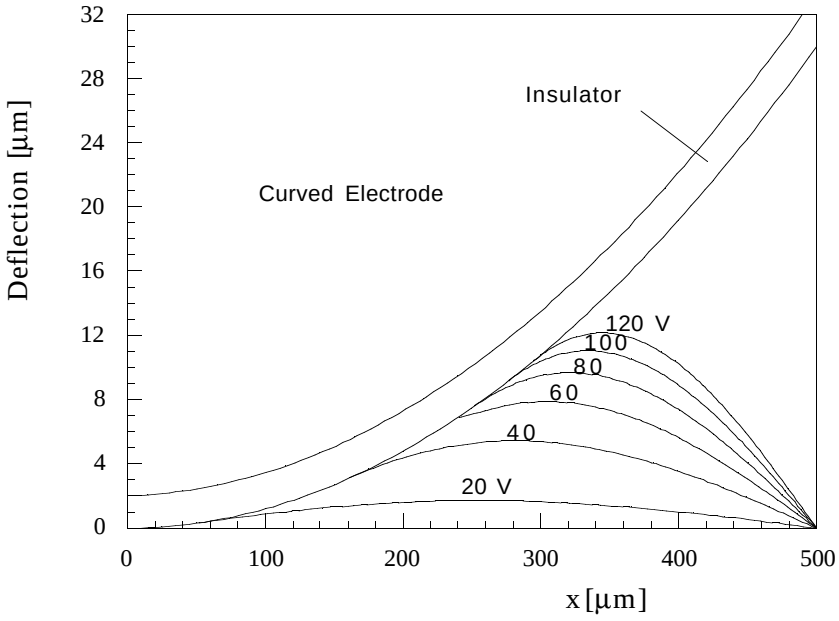

Fig. 5.5 *Deflection profiles of the cantilever beam in fig. 5.4 for several driving voltages when the tip is constrained at zero deflection.*

5.3 3D COUPLED ELECTROMECHANICAL SIMULATIONS

In order to study 3D effects like fringing fields and the effect of a groundplane below the actuator, which will be present after fabrication by surface micromachining techniques, simulations have been performed by CoSolve-EM.

CoSolve-EM is a software package that is capable of doing self-consistent electromechanical analysis of complex three-dimensional structures [5.11]. The approach is based on a relaxation scheme combining a fast multipole-accelerated scheme for the electrostatic analysis (FASTCAP) with a standard finite-element method for the mechanical system analysis (ABAQUS). An example of a geometric model of the actuator is shown in fig. 5.6. The models consist of a movable cantilever beam, a groundplane and different types of curved electrodes.

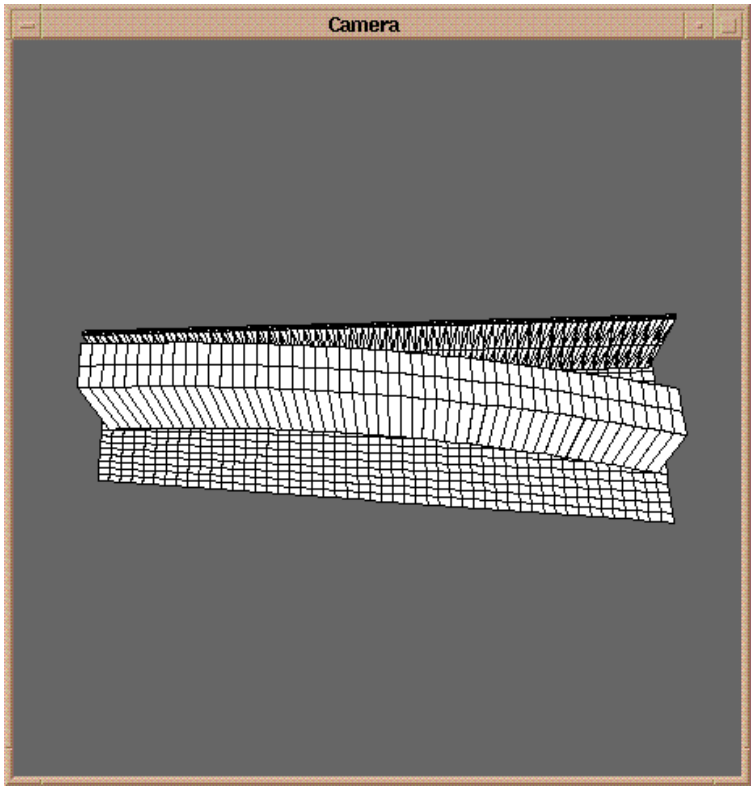

Fig. 5.6 *Geometric model used in the CoSolve-EM simulations.*

In the model, *x* is along the length of the beam, *y* is in a direction normal to the groundplane and the principal motion of the beam is in *z*-direction towards the curved electrode. Because the cantilever beam contacts the curved electrode, an interface had to be inserted between the electrodes using CoSolve-EM. Because of this contact problem the levitation in z-direction of the beam

had to be suppressed in order to obtain proper convergence [5.11]. The modelled tip deflection to driving voltage behaviour for quadratic, cubic and fourth order curvatures with an initial gap distance of 1 µm are shown together with results from the numerical energy model in fig. 5.7.

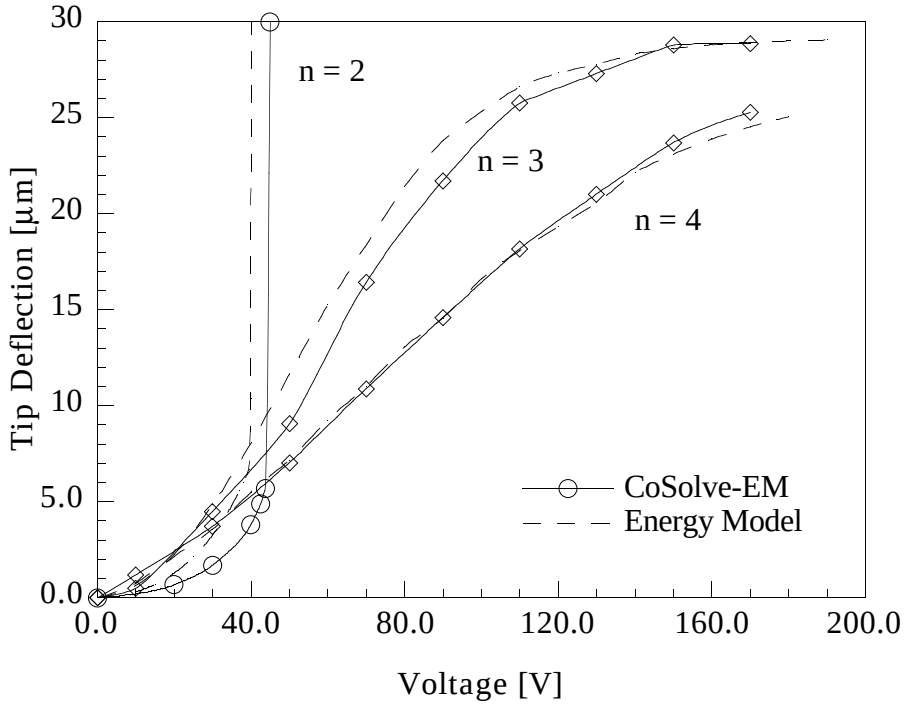

Fig. 5.7 *Results of the unloaded tip deflection versus voltage behaviour for the energy model using a parallel plate approximation and the 3D finite element model in the presence of the groundplane. The dielectric constant of the spacer is 1, and a Young's modulus* E_y *of 150 GPa, a Poisson's ratio* ν *of 0.3, beam dimensions (h*t*L) of 5*2*500* μm*, a minimal gap spacing d of 2* μm*, and maximum gap spacing* δ_{max} *of 30* μm *have been used in the calculations.*

It can be concluded that the results from the numerical energy model and the 3D coupled electro-mechanics are qualitatively in good agreement with each other. The presence of the groundplane reduces the tip deflection and increases the pull-in voltage. Simulations without a groundplane showed to increase the tip deflection of the beam because of electrostatic fringing fields compared to the parallel plate approximation that was used in the energy model.

Actuators have been fabricated that employ polysilicon bumper structures instead of a continuous insulating layer between the electrodes to simplify the fabrication process. The static behaviour of these complex structures can easily be simulated by CoSolve-EM by attaching interface nodes at the corresponding bumper positions.

5.4 FABRICATION

A one mask fabrication process has been developed where electrical insulation between the electrodes is obtained by polysilicon bumper structures or by a sidewall silicon nitride layer.

The fabrication starts with a (100) p-type 3" silicon wafer. The first step is wet thermal oxidation at 1150 ˚C to obtain a 2 µm thick SiO_2 sacrificial layer. Next a 5 µm thick polysilicon layer is grown by LPCVD at a temperature of 590 ˚C, a pressure of 250 mTorr and a silane flow of 50 sccm. This polysilicon layer is heavily doped with boron by deposition of a BSG layer and indiffusion at 1150 ˚C for 3 hours. This yields a sheet resistance of about 4.5 Ω/□ and also results in a small residual strain and strain gradient of the polysilicon layer. After boron indiffusion the BSG layer is stripped in a buffered HF-solution. A 0.6 µm thick PECVD SiO_2 layer is grown that serves as an etch mask for the polysilicon. After patterning this SiO_2 layer by RIE using CHF_3 gas, the polysilicon is anisotropically etched using a SF_6, O_2, CHF_3 gas mixture. After a cleaning step the sacrificial layer is etched in a buffered HF solution for 30 minutes. This releases thin beams but leaves larger structures attached to the substrate. Drying is done by means of a special freeze drying method to prevent stiction of free structures to the substrate [5.12]. Finally a 1 µm thick aluminum layer is evaporated for backside contact. The final result for bumper designs is shown in fig. 5.8.

By introducing a deposition of LPCVD stress reduced silicon nitride after anisotropically etching the polysilicon and a subsequent anisotropic RIE step in CHF_3 gas, silicon nitride sidewall layers are obtained that act as a continuous insulating layer between the electrodes. Examples of devices having silicon nitride sidewall insulation are shown in fig. 5.9.

5.5 EXPERIMENTAL RESULTS AND DISCUSSION

5.5.1 Experimental Set-up:

The tip deflection as a function of the applied driving voltage has been measured for different electrode curves using an experimental set-up that consisted of a probe station with a microscope and a digital voltage supply. The beam electrode and the substrate are connected to ground potential while the

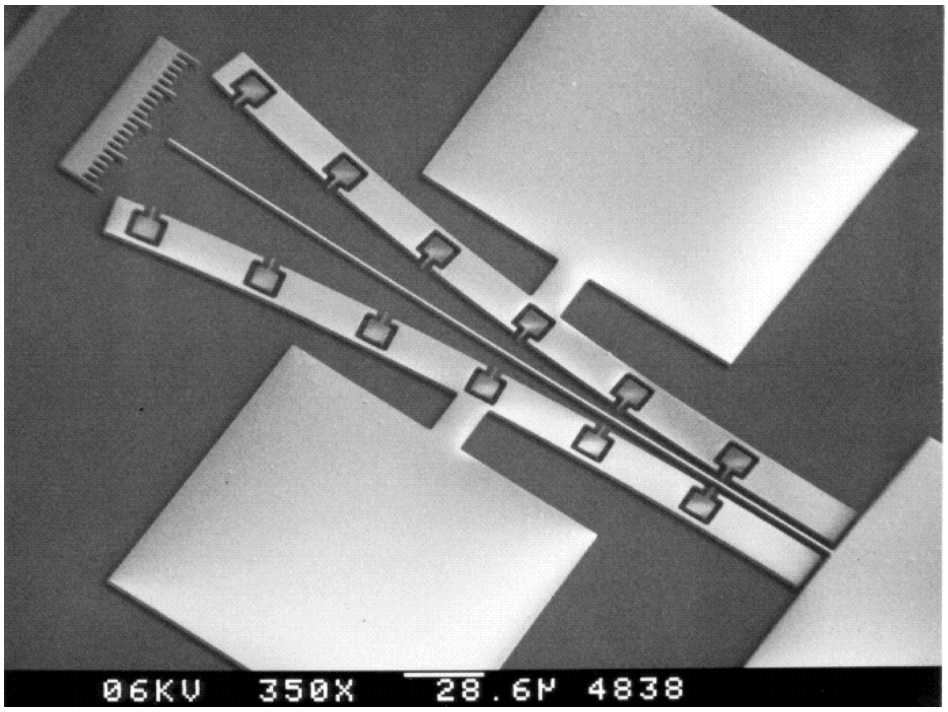

Fig. 5.8 a) *SEM photograph of curved electrode actuator with stand-off bumpers.*

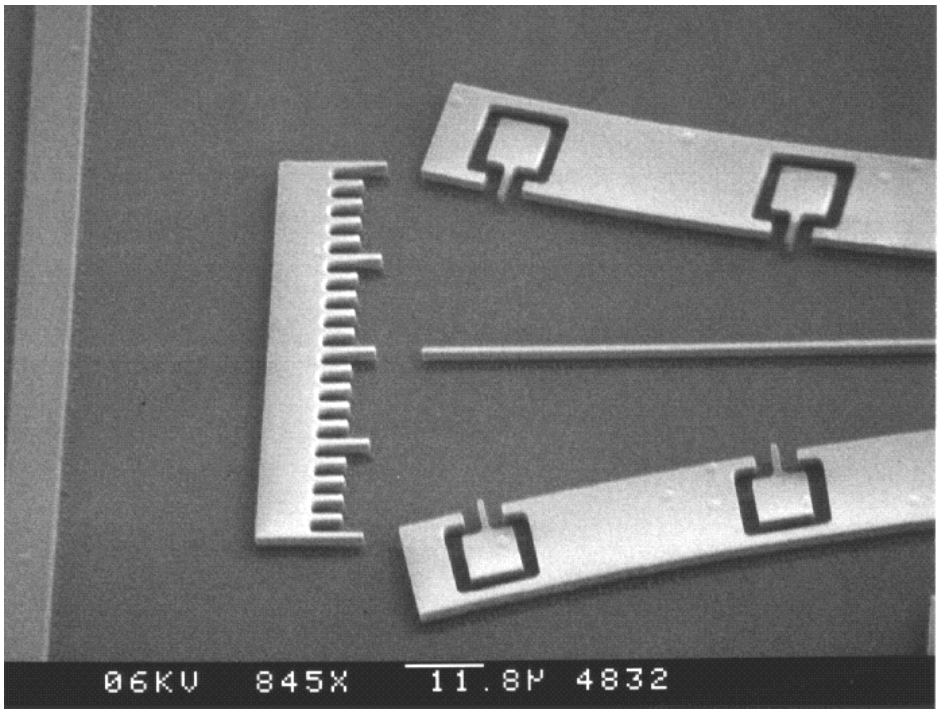

Fig. 5.8 b) *Close-up of the free standing actuator tip and the stand-off bumper structures.*

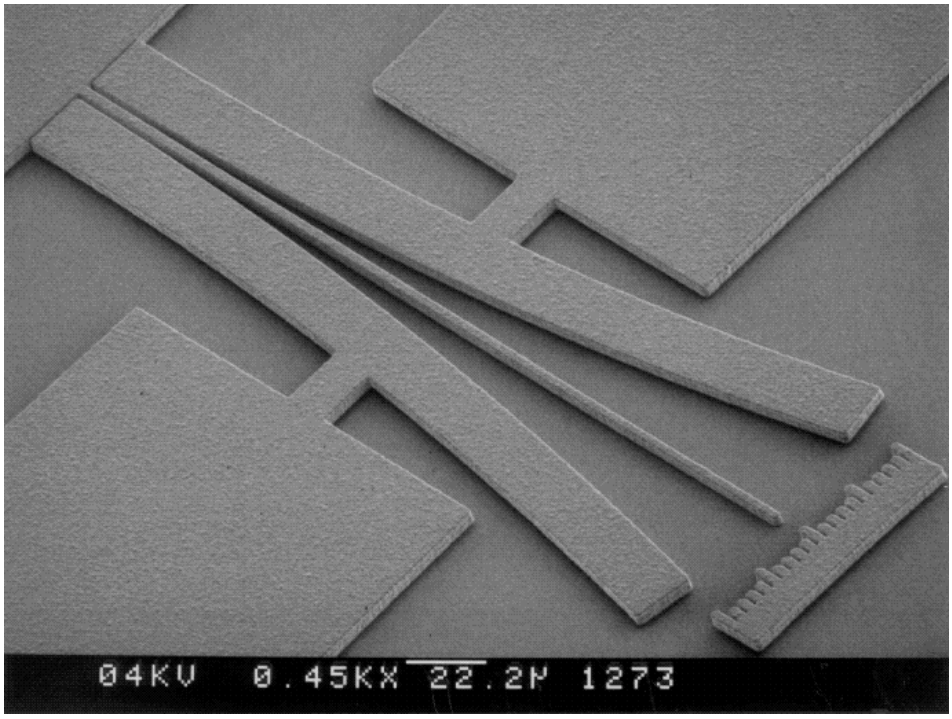

Fig. 5.9 a) *SEM photograph of curved electrode actuator with a silicon nitride sidewall insulation.*

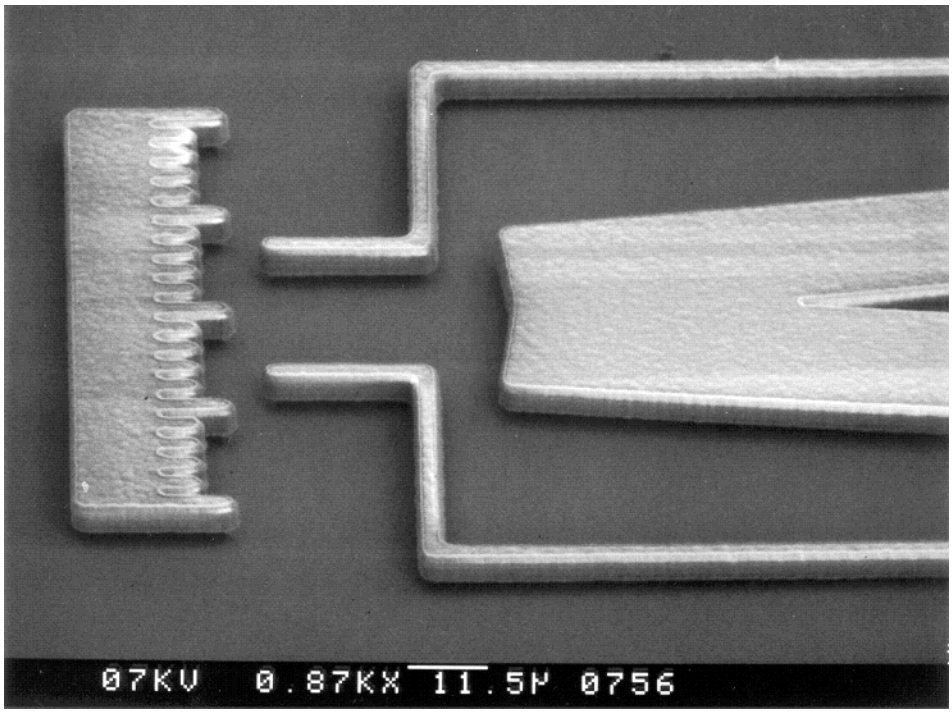

Fig. 5.9 b) *SEM photograph of a microgripper employing curved electrode structures for actuation.*

curved electrode is connected to a positive voltage. Deflections and dimensions have been measured using a micrometer eyepiece.

5.5.2 Pull-in voltage of instable bumper designs:

To determine the pull-in voltage, the driving voltage was slowly increased until the beam deflection became unstable. The results are shown fig. 5.10 and the pull-in voltages are listed in table 5.2. The calculated pull-in voltages as obtained from the energy model are smaller than the measured values. The difference is increasing with a decreasing order of the electrode curvature. This effect can be explained by three dimensional electrostatic field effects.

Electrostatic fringing fields will increase the electrostatic forces and will result in lower pull-in voltages than calculated by our simple parallel plate approximation. However, the presence of the groundplane gives rise to an unbalanced electrostatic field distribution [5.13]. This effect reduces the electrostatic forces, especially for large gaps, and induces a levitation of the surface micromachined structure. The pull-in voltage will increase by the presence of the groundplane and this effect will be stronger for increasing gap distances. Therefore it is difficult to give accurate quantitative predictions of the pull-in voltage by a simple one-dimensional model and makes 3D simulations necessary.

Note that the pull-in voltage is very sensitive to the thickness of the cantilever beam and the initial gap spacing. For instance a change in beam thickness of 0.1 µm results in a change of about 10 percent in the pull-in voltage of a second order polynomial design.

order	Pull-in Voltage V_{PI} [V]	
	Cantilever	
	Exp.	Energy
0	223	130
1.0	98	79
2.0	40	37

Table 5.2 *Pull-in voltage of polysilicon (E_y=150 GPa) cantilever beams using bumper structures with a maximum deflection δ_{max} of 30 µm. The measured thickness of the poly layer is 4.6 µm (width of the beam), the thickness of the sacr. layer is 1.6 µm. The thickness t of the different beams is 1.6, 1.7 and 1.8 µm and the initial gap is 2.2, 3.2 and 3.3 µm for the 0,1 and 2 order polynomial designs respectively.*

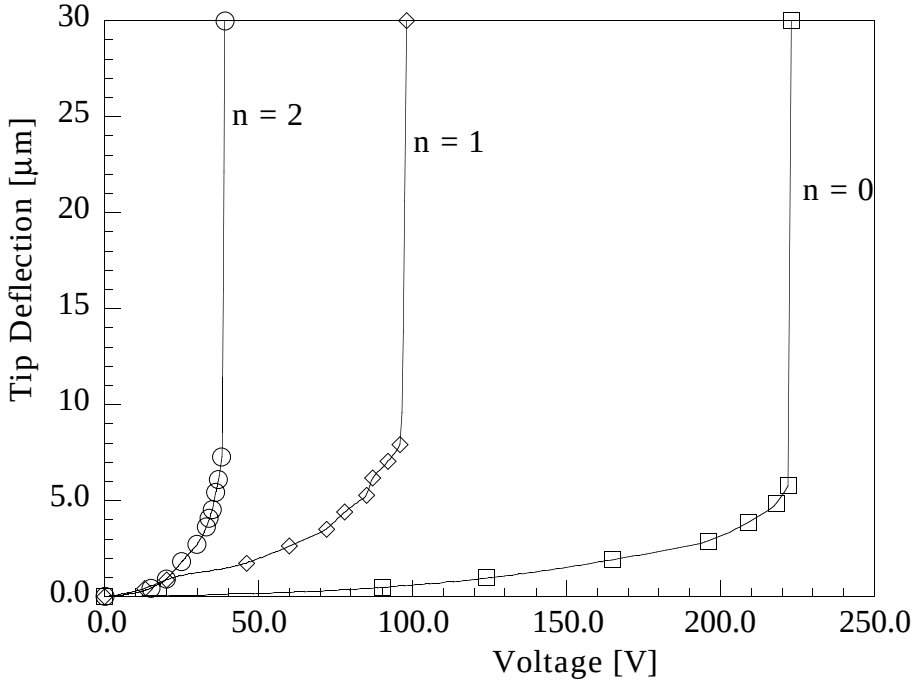

Fig. 5.10 *Measured tip deflection versus driving voltage for instable electrode profiles. The polynomial orders are 2, 1 and 0. Measured dimensions are given in table 5.2.*

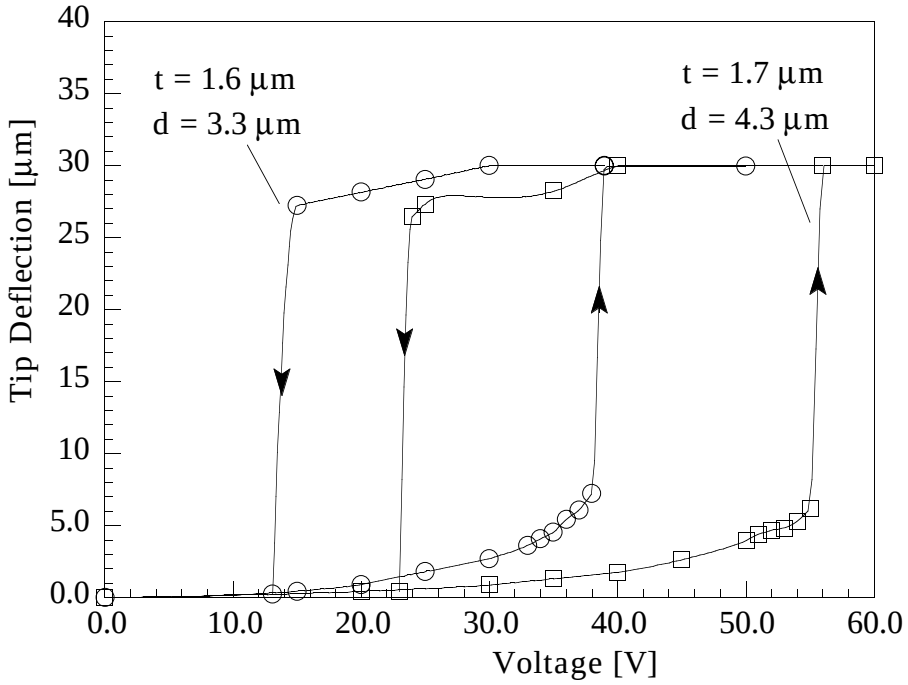

Fig. 5.11 *Measurement of the hysteresis effect for second order polynomial designs. Beam length and width are respectively 500 µm and 4.6 µm. Beam thickness and initial gap spacing are 1.6, 3.3 µm and 1.7, 4.3 µm respectively.*

The behaviour of the actuators show a hysteresis effect for increasing and decreasing voltages. This has been studied in more detail for the second order polynomial electrodes and the experimental results are shown in fig. 5.11. The origin of the hysteresis comes from a difference in the electrostatic field distribution between a beam before and after pull-in. Once the beam has collapsed, the electrostatic forces strongly increase as a result of the decreased gap spacing and a large decrease in the driving voltage is needed before bending forces overcome the electrostatic forces again.

5.5.3 Constrained bumper designs:

When the polynomial order becomes larger than 2 the deflection of the beam becomes constrained by the geometry of the curved electrode as discussed earlier. The measured deflection behaviour of a third and fourth order polynomial curvature design with bumper structures at every 50 µm is shown in fig. 5.12 for beams with a length of 500 µm. The application of bumpers results in a stepwise behaviour where the cantilever beam reaches an instable point from bumper to bumper. In fig. 5.12 also simulated results, as obtained from CoSolve-EM, are shown for the third order design. The model is in fair agreement with the data.

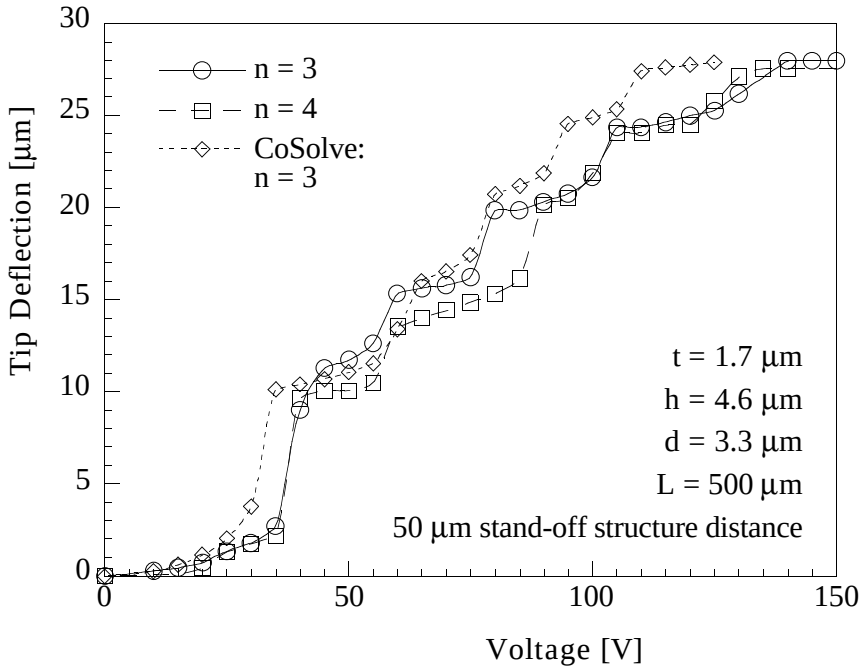

Fig. 5.12 *Experimental results of curved electrodes with stand off bumper structures where the beam deflection becomes constrained by the electrode geometry (bumpers). The polynomial orders are 3 and 4. Also the results of a CoSolve-EM simulation for a cubic electrode design with a gap spacing of 3.1 µm employing bumper structures spaced apart at every 50 µm and 2 µm away from the curved electrode are shown.*

The CoSolve model is systematically somewhat overestimating the electrostatic force on the beam. This is probably a result from the suppression of the levitation of the beam or a too small theoretical Young's modulus.

5.5.4 Constrained sidewall insulator designs:

An example of the measurement results from an actuator with continuous sidewall insulation is shown in fig. 5.13. In contrast to our theoretical results, devices with a continuous sidewall insulator did not show completely stable behaviour. Fabricated devices show a behaviour that is more or less identical to the constrained bumper designs. Steplike instable and stable regions are also observed. Furthermore, a large variation in behaviour of identical designs has been observed.

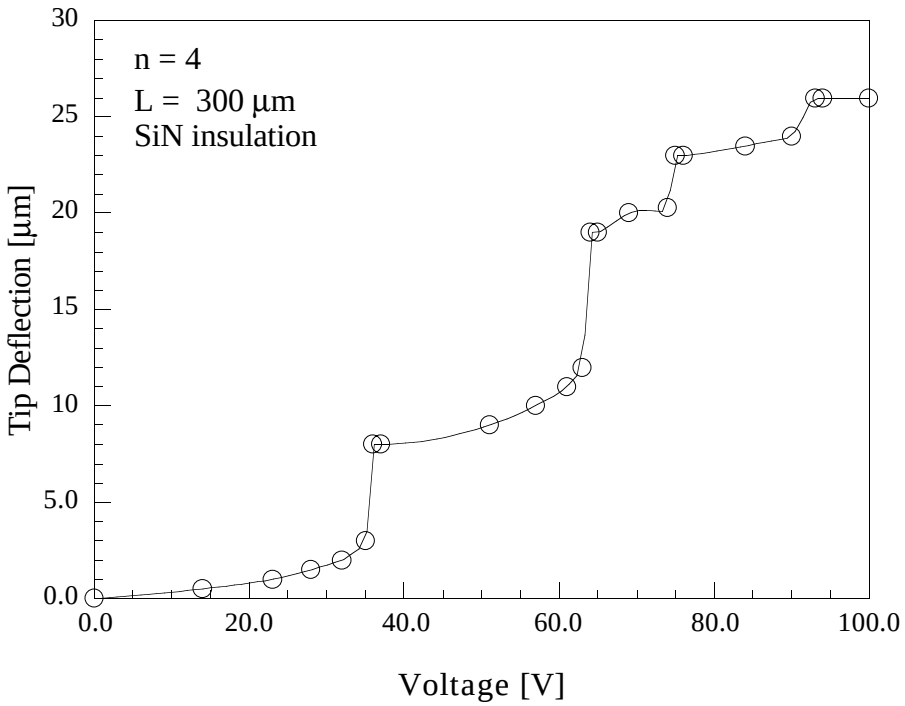

Fig. 5.13 *Example of the measured tip deflection as function of the driving voltage for a fourth order design with a silicon nitride sidewall layer.*

It is suggested that these results are caused by imperfections at the sidewall surfaces such as surface asperities, and entrapped particles and residues between the electrodes after the fabrication process. A close up of a beam with silicon nitride sidewall insulation is shown in fig. 5.14. Small protrusions strongly affect the behaviour of the actuators and prevent the movable beam from smoothly zipping along the curved electrode and act like small bumpers which leads to instabilities. For successful constrained designs smooth

electrodes surfaces are required. This may be difficult to realise by the proposed fabrication process and is, in general, a fabrication problem for this type of actuators.

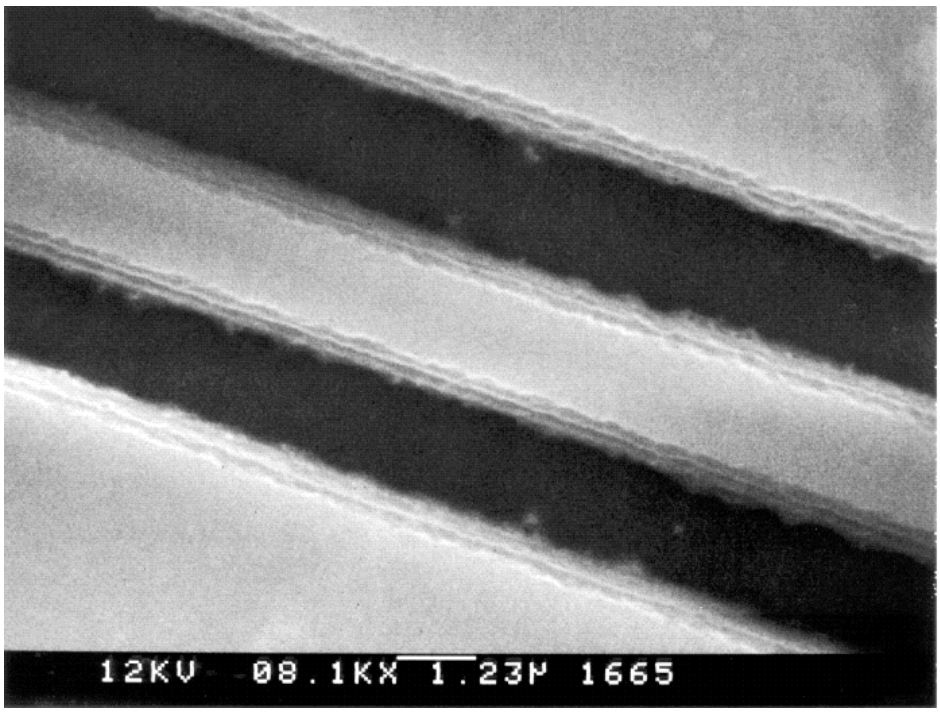

Fig. 4.14 *Close-up SEM top-view of a cantilever beam with silicon nitride sidewall passivation. The presence of relative large surface roughness, residue and particles is suggested to induce instabilities in the actuator behaviour.*

5.6 CONCLUSIONS

An electrostatic actuator design has been presented where a deformable mechanical structure is bent around a fixed curved electrode by means of electrostatic forces. Such a design is attractive because relatively large deflections and force generation can be obtained.

For the shape of the curved electrode simple polynomials have been used. A theory based upon energy methods is presented to describe the static behaviour of the actuator. Furthermore 3D coupled electromechanical simulations using CoSolve-EM have been performed. The results from both models are in qualitative agreement with each other. When the beam deflection is not constrained by the curved electrode geometry, instable behaviour occurs at a certain pull-in voltage and a hysteresis exists to release the structure after pull-in. For polynomial designs, with an order above two, it was found that the

beam deflection becomes constrained by the curved electrode geometry before pull-in occurs. Our models predict completely stable behaviour in this situation.

Curved electrode actuators have been fabricated from polysilicon by surface micromachining techniques using a one-mask process. Electric insulation has been realised by stand off bumper structures between the movable beam and the fixed electrode or by a silicon nitride sidewall layer. Measurements of non-constrained beam deflections show that the qualitative behaviour of the energy model is in agreement with theory but that the pull-in voltages are higher than theoretically predicted. This effect is a result of the presence of a groundplane as shown in 3D coupled electromechanical simulations.

Constrained designs employing bumper structures show a stepwise behaviour as a result of a number of stable positions at the bumper positions. The static behaviour of these designs has been modelled by CoSolve-Em and was found to be in fair agreement with experimental data.

Experimental data of samples with a continuous sidewall insulator did not show stable behaviour up to maximal deflection in contrast to our theoretical results. It is suggested that this is caused by imperfections at the sidewall surfaces, as a result of the fabrication process, which prevent the movable beam from smoothly zipping along the curved electrode and act like small bumpers leading to local instabilities.

In practice, curved electrode structures are therefore mainly suited for bi-stable actuator applications such as microswitches, microgrippers, microvalves and micro pumps.

5.7 REFERENCES

[5.1] R. Jebens, W. Trimmer and J. Walker, Microactuators for aligning optical fibers, Sensors and Actuators, 20, 1989, pp. 65-73.

[5.2] K. Sato and M. Shikida, Electrostatic film actuator with large vertical displacement, Proc. IEEE Micro Electro Mechanical Systems, Travemunde, Germany, February 4-7, 1992, pp. 1-5.

[5.3] J. Branebjerg and P. Gravesen, A new electrostatic actuator providing improved stroke length and force, Proc. IEEE Micro Electro Mechanical Systems, Travemunde, Germany, February 4-7, 1992, pp. 6-11.

[5.4] M. Elwenspoek, L. Smith and B. Hök, Active joints for microrobot limbs, J.Micromech. Microeng., 2 (1992), pp. 221-223.

[5.5] M. Yamaguchi, S. Kawamura, K. Minami and M. Esashi, Distributed electrostatic micro actuator, Proc. IEEE Micro Electro Mechanical Systems, Fort Lauderdale, Florida, U.S.A., February 7-10, 1993, pp. 18-23.

[5.6] J. Schimkat, L. Kiesewetter, H.J. Gevatter, F. Arndt, A. Steckenborn and H.F. Schlaak, Moving wedge actuator: An electrostatic actuator for use in microrelay, Proc. 4th Int. Conf. and Exhibition on Micro Electro, Opto, Mechanical Systems and Components, Berlin, Germany, October 19-21, 1994, pp. 989-996.

[5.7] M. Elwenspoek, M. Weustink and R. Legtenberg, Static and dynamic properties of active joints, Proc. 8th Int. Conf. on Solid-State Sensors and Actuators, Stockholm, Sweden, June 25-29, 1995, pp. 412-415.

[5.8] I.H. Shames and C.L. Dym, Energy and finite element methods in structural mechanics, McGraw-Hill, New York, 1985.

[5.9] H. Tilmans and R. Legtenberg, Electrostatically driven vacuum encapsulated polysilicon resonators-Part II, Sensors and Actuators, A45, 1994, pp. 67-84.

[5.10] P. Osterberg, H. Yie, X. Cai, J. White and S. Senturia, Self consistent simulation and modelling of electrostatically deformed diaphragms, Proc. IEEE Micro Electro Mechanical Systems, Oiso, Japan., February 25-28, 1994, pp. 28-32.

[5.11] J.R. Gilbert, R. Legtenberg and S.D Senturia, 3D coupled electro-mechanics for MEMS: Applications of CoSolve-EM, Proc. IEEE Micro Electro Mechanical Systems, Amsterdam, The Netherlands, January 30-February 2, 1995.

[5.12] R. Legtenberg and H.A.C. Tilmans, Electrostatically driven vacuum encapsulated polysilicon resonators-Part I, Sensors and Actuators, A45, 1994, pp. 57-66.

[5.13] W.C. Tang, M.G. Lim and R.T. Howe, Electrostatic comb drive levitation and control method, J. of Micro Electro Mechanical Systems, Vol. 1, 1992, pp. 170-174

Chapter Six

COMB-DRIVE ACTUATORS FOR LARGE DISPLACEMENTS*

The design, fabrication and experimental results of lateral comb-drive actuators for large displacements at low driving voltages is presented. A comparison of several suspension designs is given, and the lateral large deflection behaviour of clamped-clamped beams and a folded flexure design is modelled. An expression for the axial spring constant of folded flexure designs including bending effects from lateral displacements, which reduce the axial stiffness, is also derived. The maximum deflection that can be obtained by comb-drive actuators is bounded by electromechanical side-instability. Expressions for the side-instability voltage and the resulting displacement at side-instability are given. The electromechanical behaviour around the resonance frequency is described by an equivalent electric circuit. Devices are fabricated by polysilicon surface micromachining techniques using a one mask fabrication process. Static and dynamic properties are determined experimentally and are compared with theory. Static properties are determined by displacement-to-voltage, capacitance-to-voltage and pull-in voltage measurements. Using a one-port approach, dynamic properties are extracted from measured admittance plots. Typical actuator characteristics are deflections of about 30 μm at driving voltages around 20 V, a resonance frequency around 1.6 kHz and a quality factor of approximately 3.

6.0 INTRODUCTION

Comb drive actuators consist of two interdigitated finger structures, where one comb is fixed and the other one is connected to a compliant suspension. Applying a voltage difference between the comb structures will result in a deflection of the movable comb structure by electrostatic forces. Comb drive actuators have been used as resonators [6.1-6.3], electromechanical filters [6.4], optical shutters [6.5-6.7], microgrippers [6.8] and voltmeters [6.9]. They have also been used as the driving element in e.g. vibromotors [6.10] and micromechanical gears [6.11].

Voltage controlled comb drive actuators exert a lateral electrostatic force which is independent of position making them attractive for micro positioning applications like, for instance, xy-microstages [6.12-6.14]. Together

* submitted to J. Micromech. Microeng.

with nanotools like microtips, integrated systems can be fabricated with applications in scanning microscopy and data storage [6.15, 6.16]. In most devices actuator deflections have been limited to a few microns but in many cases micropositioning over larger distances is attractive. For this reason the design and fabrication of large displacement comb drive actuators is investigated.

A suspension that is compliant in the aimed direction of displacement and stiff in the orthogonal directions is required. Electrostatic forces increase with decreasing gap spacing and increasing number of comb fingers. However, due to fabrication processes, dimensions are limited by minimum feature size constraining e.g. the minimum beam width and gap spacing. These and other design constraints are discussed in order to obtain large-displacement, low-driving-voltage comb-drive actuators.

6.1 SPRING DESIGNS

6.1.1 Introduction

Different types of spring designs have been applied in comb drive actuators [6.1, 6.12, 6.17]. In this section the following spring designs will be discussed; clamped-clamped beams, a crab-leg flexure and the folded beam flexure. In most cases, it is desirable to have a structure which is very compliant in one direction while being very stiff in the orthogonal directions. This can be expressed as a stiffness ratio. Most polysilicon micromechanical flexures constrain motion to a rectilinear direction, and are created from straight beams. When a concentrated load is applied the linear spring constant is defined as:

$$k_i = \frac{F_i}{\delta_i} \tag{6.1}$$

where F_i and δ_i are respectively the force and the deflection in the i-direction. The lateral spring constants and stiffness ratio of a clamped-clamped beam, a crab-leg flexure and a folded flexure design will be discussed. The analysis assumes that there is no residual stress present in the spring structures.

6.1.2 Clamped-clamped beam

A clamped-clamped beam with rectangular cross section is shown in fig. 6.1. A concentrated force is applied to the center of the shuttle. The axial displacement along the x-axis can be found directly from Hooke's law and the

lateral displacement along the *y*-axis is obtained from small deflection theory [6.18].

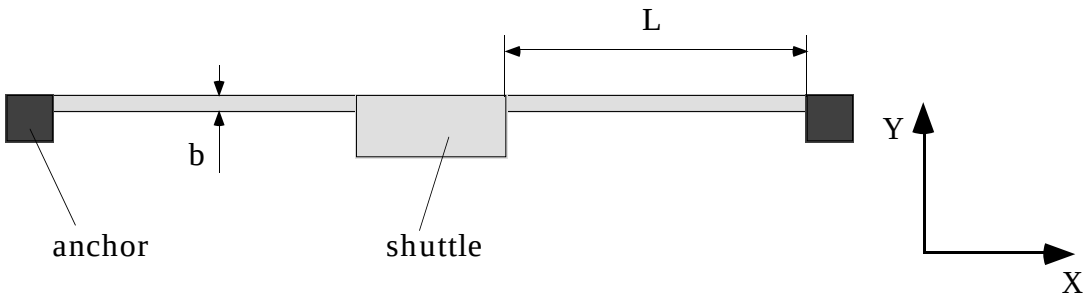

Fig. 6.1 *Clamped-clamped beam.*

The spring constants for a concentrated force in *x*- and *y*-direction are given by:

$$k_x = \frac{2\,E_y\,h\,b}{L} \tag{6.2}$$

$$k_y = \frac{2\,E_y\,h\,b^3}{L^3} \tag{6.3}$$

where E_y is the Young's modulus, h is the beam width, b is the beam thickness and L is the length of one beam segment. The stiffness ratio is:

$$\frac{k_x}{k_y} = \left(\frac{L}{b}\right)^2 \tag{6.4}$$

The stiffness ratio of a clamped-clamped beam can be very high. For example, the stiffness ratio is $1.25\ 10^5$ for a beam with a length of 500 µm and a width of 2 µm. For large displacements, however, extensional axial forces develop in the beam that result in a non-linear force-to-displacement relation. In this case non-linear effects have to be included that strongly increase the stiffness of the beam with increasing deflection. This spring design is therefore not suitable for large deflections. However, it is useful in applications that require measurement of axial forces; for instance in order to determine residual stresses or measure externally applied axial stresses as in sensing applications.

A derivation of the large deflection behaviour of clamped-clamped beams can be found in [6.19, Appendix B]. The center deflection for a concentrated load P at the center can be found by simultaneously solving the next equations:

$$P_y = \frac{E_y\,I\,b}{L^3}\,\sqrt{8/3}\,u^3\left(\frac{3}{2} - \frac{1}{2}\,Tanh^2 u\; - \frac{3}{2}\,\frac{Tanh\,u}{u}\right)^{-\frac{1}{2}} \tag{6.5}$$

$$\delta_y = b\sqrt{2/3}\,(u - Tanh\,u)\left(\frac{3}{2} - \frac{1}{2}\,Tanh^2 u - \frac{3}{2}\,\frac{Tanh\,u}{u}\right)^{-\frac{1}{2}} \qquad (6.6)$$

with

$$u = \sqrt{N\,/\,E_y I}\,\frac{L}{2} \qquad (6.7)$$

where N is the normal force that develops in the beam as a result of the applied force and I is the second moment of inertia of the beam. The normalised deflection to force behaviour is shown in fig. 6.2. This graph shows that the small deflection theory is valid for deflections up to about a quarter of the beam thickness. For larger deflections non-linear theory has to be used.

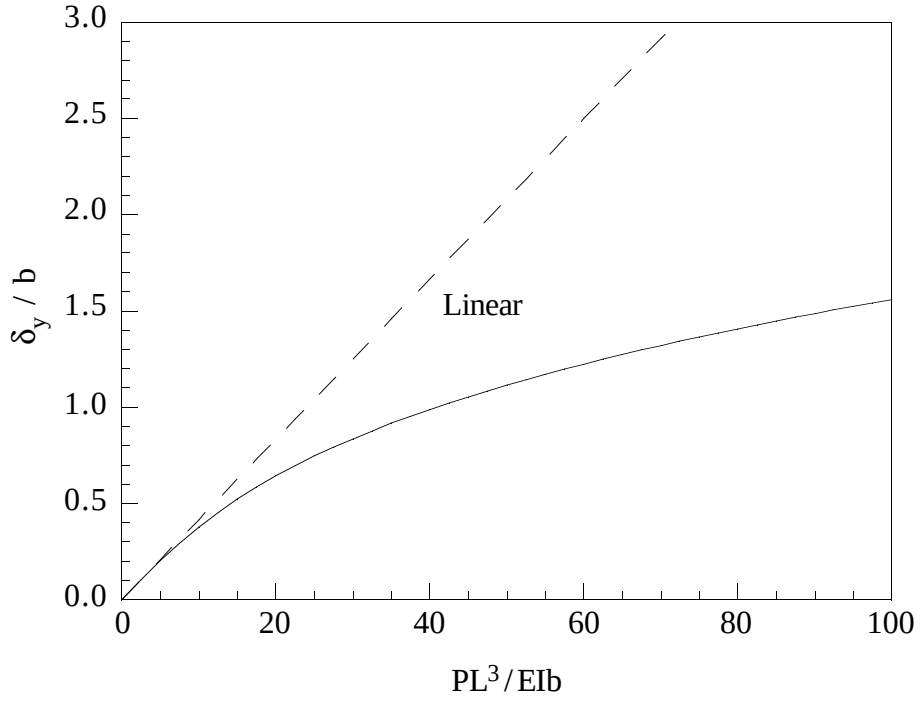

Fig. 6.2 *Normalised deflection of a clamped-clamped beam with dimensions (h*b*2L) of 5*2*1000 μm under a force P at the center.*

6.1.3 Crab-leg flexure

In order to reduce the extensional axial forces a crab-leg flexure can be used. A sketch of a crab-leg flexure is shown in fig. 6.3. The thigh segment has a second moment of inertia I_1 and a length L_1; the shin segment has a second moment of inertia I_2 and a length L_2. The spring constants, as a result of a concentrated force on the shuttle, in x- and y-direction are given by:

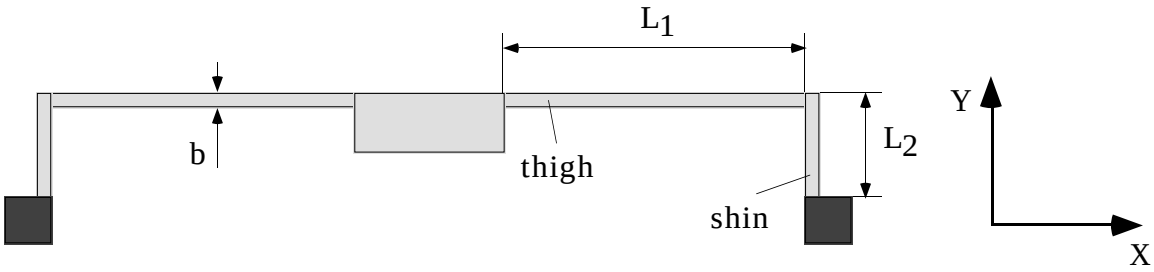

Fig. 6.3 *Crab-leg flexure.*

$$k_x = \frac{12\,E_y\,I_2}{L_2^{\,3}}\left\{\frac{L_1\,I_2 + 2\,L_2\,I_1}{2\,L_1\,I_2 + L_2\,I_1}\right\} \tag{6.8}$$

$$k_y = \frac{24\,E_y\,I_1}{L_1^{\,3}}\left\{\frac{L_1\,I_2 + L_2\,I_1}{L_1\,I_2 + 4\,L_2\,I_1}\right\} \tag{6.9}$$

When the shin and thigh have the same width and thickness, the stiffness ratio can be obtained from:

$$\frac{k_x}{k_y} = \frac{1}{2}\,\frac{L_1^{\,3}}{L_2^{\,3}}\left\{\frac{L_1^{\,2} + 6\,L_1\,L_2 + 8\,L_2^{\,2}}{2\,L_1^{\,2} + 3\,L_1\,L_2 + L_2^{\,2}}\right\} \tag{6.10}$$

Although this design increases the linear deflection region to a certain extent, a large reduction of the stiffness ratio is introduced. A design that has a shin length of 50 µm and thigh dimensions equal to our previous clamped-clamped beam example, has a stiffness ratio that is already several orders of magnitude smaller. A flexure design that is less susceptible to a decrease in the stiffness ratio is the folded flexure design [1].

6.1.4 Folded flexure

A sketch of the folded beam design is shown in fig. 6.4. The beams are anchored near the center and the trusses allow expansion or contraction of the beams along the *x*-axis. The length of the inner and outer beams is identical otherwise problems may arise because the structure is statically indeterminate.

Assuming rigid trusses, the spring constant of the folded flexure design in axial and lateral direction can be found from:

$$k_x = \frac{2\,E_y\,h\,b}{L} \tag{6.11}$$

$$k_y = \frac{2\,E_y\,h\,b^3}{L^3} \tag{6.12}$$

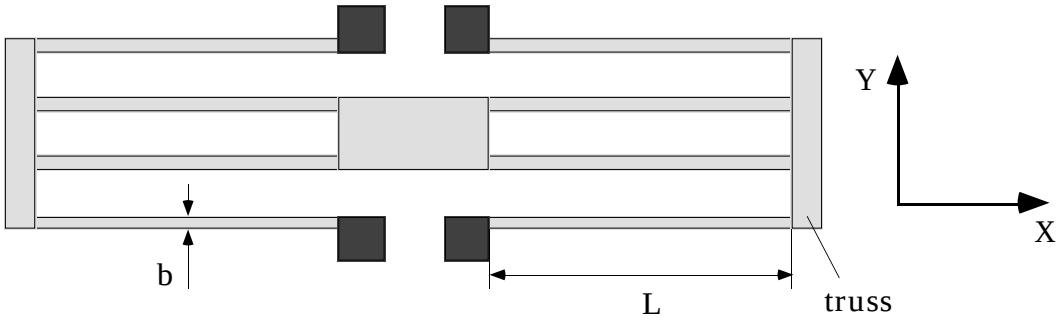

Fig. 6.4 *Folded flexure design.*

and the stiffness ratio is:

$$\frac{k_x}{k_y} = \left(\frac{L}{b}\right)^2 \tag{6.13}$$

The folded flexure design strongly reduces the development of axial forces and exhibits a much larger linear deflection range. The stiffness ratio for small deflections is equal to the stiffness ratio of a clamped-clamped beam. This design is therefore very suitable for large deflection actuators. For a more extensive analysis of folded beams, including the effect of compliant trusses, the reader is referred to [6.20] and [6.21]. The large deflection behaviour of a folded flexure design can be obtained by considering the folded flexure as four folded beams in parallel. Each folded beam is a combination of two clamped-guided beams connected in series. By solving the elastica for a clamped-guided beam the large deflection behaviour of the folded flexure can be described by the following set of equations:

$$\delta_y = 8\sqrt{\frac{E_y I}{P}} \int_{\phi_1}^{\pi/2} \frac{\left(2\,p^2\,Sin\phi - 1\right) d\phi}{\sqrt{1 - p^2\,Sin\,\phi}} \tag{6.14}$$

where p can be found from numerical iteration and solving of:

$$\begin{aligned} \frac{1}{4} L \sqrt{\frac{P}{E_y I}} &= \int_{\phi_1}^{\pi/2} \frac{d\phi}{\sqrt{1 - p^2\,Sin^2\,\phi}} \\ \phi_1 &= ArcSin\sqrt{2\,p^2 - 1} \end{aligned} \tag{6.15}$$

A detailed derivation of these formulas is given in appendix C. In these equations p and ϕ result from a change in variables to bring the equations in

the standard form of elliptic integrals. The normalised deflection to force behaviour of a folded flexure and cantilever beam is shown in fig. 6.5.

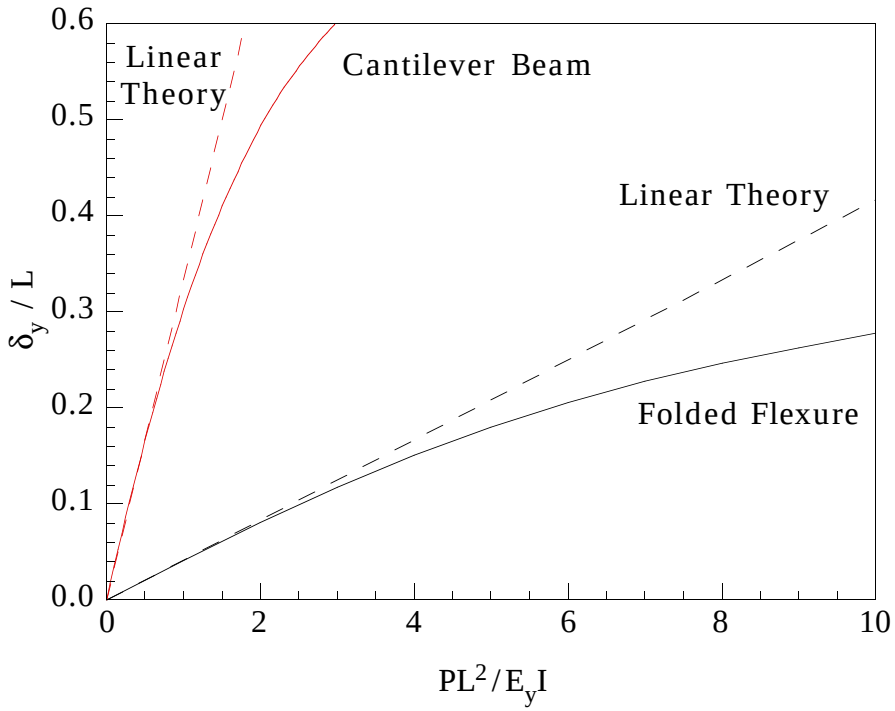

Fig. 6.5 *Normalised large deflection behaviour of a beam with a length 2L that is clamped at one side and guided along the x-axis at the other end and loaded at its center by a concentrated load P. Assuming rigid trusses the behaviour of such a beam resembles the deflection behaviour of a folded flexure. The deflection of a cantilever beam with a length L loaded at the tip is also shown.*

The small deflection theory is valid for lateral deflections up to approximately 10 percent of the beam length, which is considerably larger than in case of the clamped-clamped beam.

Another important effect that has to be considered is that the stiffness of the folded beam flexure in the *x*-direction decreases with increasing displacement in the *y*-direction. Thus, expressions (6.2), (6.8) and (6.11) are, in fact, upper limits of the axial spring constants at zero lateral deflection which decrease with increasing lateral deflection. In order to include lateral deflection effects in the axial spring constant of the folded flexure the problem is simplified. Because of the folded beam symmetry only one beam segment is considered (see fig. 6.6).

It is assumed that the beam has an initial deflection given by the function $w_{0(x)}$. The known admissible trial function of the initial deflection profile is:

$$w_{0(x)} = a\,x^2\left(6\,L - 4\,x\right) \tag{6.16}$$

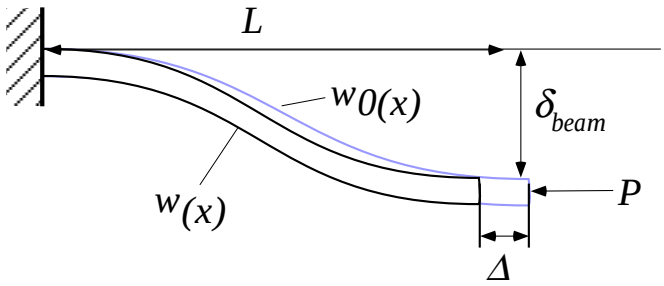

Fig. 6.6 *Decrease of the stiffness in the x-direction with increasing displacement in the y-direction.*

The function of the deflection is approximated by the following admissible trial function:

$$w_{(x)} = b\,x^2\left(6\,L - 4\,x\right) \tag{6.17}$$

where b is an unknown constant. The total potential energy Π for the beam is:

$$\Pi = \frac{1}{2}\,E_y I \int_0^L \left[\frac{d^2\left(w - w_0\right)}{dx^2}\right]^2 dx - P\,\Delta \tag{6.18}$$

where P is the axially applied load. The contraction of the beam Δ can be expressed as [6.22]:

$$\Delta = \frac{1}{2}\int_0^L \left(\frac{dw}{dx}\right)^2 dx - \frac{1}{2}\int_0^L \left(\frac{dw_0}{dx}\right)^2 dx \tag{6.19}$$

After extremisation of the potential energy with respect to b, this contraction is given by:

$$\Delta = \frac{3\,\delta_{beam}^{\,2}}{5\,L}\left\{\frac{1}{\left(1 - \frac{P}{P_{cr}}\right)^2} - 1\right\} \tag{6.20}$$

where δ_{beam} is the deflection of the initial beam curvature and the buckling load P_{cr} is:

$$P_{cr} = \frac{10\,E\,I}{L^2} \tag{6.21}$$

In case of forces that are much smaller than the critical load P_{cr} (i.e. P/P_{cr}«1), the axial deflection of a beam segment can be found from:

$$\Delta = \frac{3\,P\,L\,\delta_{beam}^{\,2}}{25\,E_y\,I} \tag{6.22}$$

The spring constant for the folded beam flexure as a result of lateral deflections can be found by combining forces and deflections of the beam segments resulting in:

$$k_x = \frac{200\,E_y\,I}{3\,L\,\delta_y^{\,2}} \tag{6.23}$$

From this expression, it can easily be seen that the spring constant in the *x*-direction decreases with increasing beam displacement in the *y*-direction. As a result the stiffness ratio also decreases with increasing lateral beam deflection. The total spring constant is a series connection of the lateral displacement dependant spring constant in eq. (6.23) and the axial spring constant resulting from Hooke's law (eq. 6.11).

6.2 ELECTROMECHANICAL BEHAVIOUR

6.2.1 Static behaviour

In the comb actuator a movable set (rotor) and a stationary set (stator) of comb fingers are engaged. A ground plane is located under the comb fingers which is normally connected to the same potential as the rotor in order to prevent electrostatic pull-down forces to the substrate. An engaged pair of fingers, being one cell, of a comb actuator is shown in fig. 6.7. To simplify modelling the electrostatic field between the rotor and stator is approximated by a one dimensional parallel plate model between the engaged parts of the comb fingers. Therefore 3D effects like fringing fields, comb finger end effects and the groundplane levitation effect are neglected [6.23]. In our case these effects will lead to lateral electrostatic forces underestimated by about 5 %, as will be discussed later.

Lateral deflection

The capacitance between the stator and the rotor can be expressed as:

$$C = \frac{2\,n\,\varepsilon_0\,h\left(y+y_0\right)}{d} \tag{24}$$

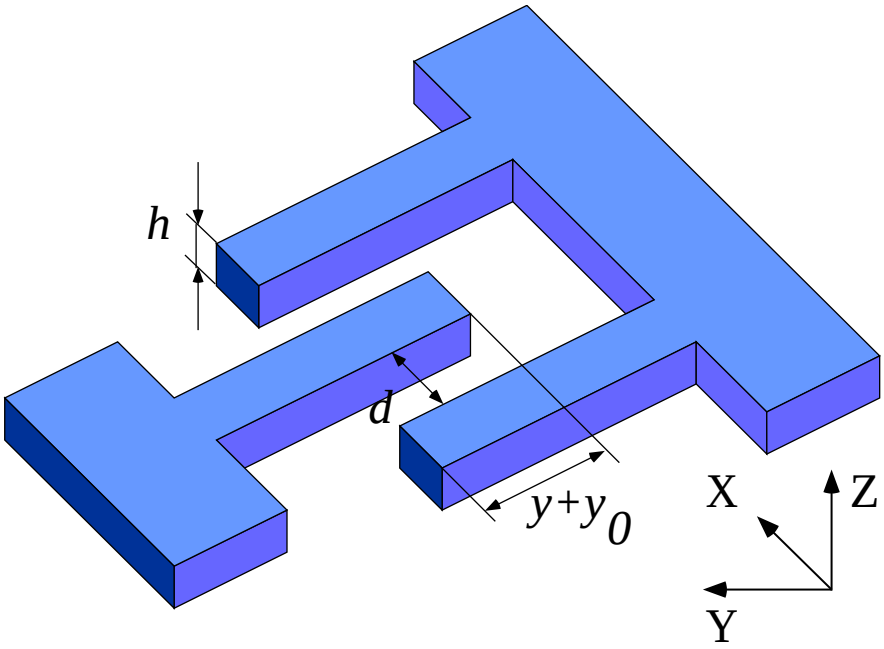

Fig. 6.7 *Cell of engaged comb finger arrays.*

where n is the number of fingers, ε_0 is the dielectric constant in air, h is the height of the comb fingers, y_0 is the initial comb finger overlap, y is the comb displacement and d is the gap spacing between the fingers. The lateral electrostatic force in the y-direction is equal to the negative derivative of the electrostatic co-energy with respect to y:

$$F_{el} = \frac{1}{2}\frac{\partial C}{\partial y} V^2 = \frac{n\,\varepsilon_0\,h}{d} V^2 \qquad (6.25)$$

where V is the applied voltage between the stator and the rotor. This force is acting on the spring to which the rotor is connected resulting in a deflection:

$$y = \frac{n\,\varepsilon_0\,h}{k_y\,d} V^2 \qquad (6.26)$$

Side instability

Besides electrostatic forces along the y-axis, electrostatic forces pulling the stator and rotor fingers together are also present. The electrostatic force in the axial direction is:

$$F_{el} = \frac{n\,\varepsilon_0\,h\left(y+y_0\right)}{2\left(d-x\right)^2} V^2 - \frac{n\,\varepsilon_0\,h\left(y+y_0\right)}{2\left(d+x\right)^2} V^2 \qquad (6.27)$$

The forces on both sides of the comb fingers normally cancel each other. However, when the first derivative of the electrostatic force with respect to x becomes larger than the restoring spring constant in the *x*-direction a side-instability of the comb drive is introduced. Hence stable comb operation is bounded by:

$$k_x > \left[\frac{\partial F}{\partial x}\right]_{x \to 0} = \frac{2\, n\, \varepsilon_0\, h \left(y+y_0\right)}{d^3}\, V^2 \qquad (6.28)$$

When the driving voltage exceeds the so-called side-instability voltage V_{SI} the comb drive becomes unstable leading to side sticking of the rotor and stator fingers. By combining eq. (6.26) and (6.28) the voltage at which side-instability occurs can be expressed as:

$$V_{SI}^{\,2} = \frac{d^2\, k_y}{2\, \varepsilon_0\, h\, n}\left(\sqrt{2\,\frac{k_x}{k_y} + \frac{y_0^{\,2}}{d^2}} - \frac{y_0}{d}\right) \qquad (6.29)$$

By neglecting the second term in the root (when $k_x >> k_y$), the maximum deflection y_{SI} that can be obtained before pull-in will occur is:

$$y_{SI} = d\,\sqrt{\frac{k_x}{2\, k_y}} - \frac{y_0}{2} \qquad (30)$$

From this equation it can be seen that the side-instability voltage and maximum deflection are proportional to the gap spacing and increase with the spring stiffness ratio. This shows that comb drive structures with small gap spacings are more susceptible to side instability [6.24] and that spring designs with a large stiffness ratio are preferred for large deflection comb drive actuators. Other sources of instability may result from sideways pull-in of compliant fingers themselves and pull-in by the finger front ends when the stator and rotor are almost completely engaged [6.25]. Instabilities have to be avoided by proper design of the comb structure and flexure; and supply together with maximum deflection, driving voltage and minimum feature size, the main constraints on comb actuator design. Large deflection comb drive actuators at low driving voltages should employ compliant springs with a high stiffness ratio and a large amount of comb fingers. In our comb drive design a folded flexure has been used which is connected at the center to a beam that is able to hold a large number of comb fingers.

6.2.2 Dynamic behaviour

Equation of motion

Using lumped elements the differential equation of motion is given by:

$$M_{eq}\,\ddot{y} + \alpha\,\dot{y} + k_y\,y = F_{el} = \frac{n\,\varepsilon_0\,h}{d}\left[V_P + v(t)\right]^2 \qquad (6.31)$$

where M_{eq} is the equivalent mass of the comb drive actuator, α is the equivalent viscous drag parameter and V_P is the d.c. polarisation voltage and $v(t)$ the a.c. voltage.

The fundamental frequency

The fundamental frequency of the structure can be obtained from Rayleigh's quotient [6.22]. Using the static deflection profile for the approximate fundamental mode shape function of the beams yields the following expression for the fundamental resonance frequency ω_0:

$$\omega_0 = \sqrt{\frac{k_y}{M_{shuttle} + \frac{1}{2}\,M_{truss} + \frac{96}{35}\,M_{beam}}} \qquad (6.32)$$

where the denominator of the fraction under the root sign resembles the equivalent mass M_{eq} in which $M_{shuttle}$ is the mass of the shuttle, M_{truss} is the mass of a single truss and M_{beam} is the mass of a single beam. The resonant frequency is ideally independent of V_P and $v(t)$.

Electric Admittance - Equivalent Circuit

If the comb drive is operated in a one-port configuration, the dynamic behaviour can be described by the electric admittance $Y(j\omega)$. The voltage is chosen as the independent variable because the electrodes define equipotential surfaces making the voltage independent of position. The constitutive equations of the electrostatic transducer, describing interactions between the mechanical and electrical variables can be expressed as:

$$\begin{bmatrix} dq \\ dF \end{bmatrix} = \begin{bmatrix} \frac{2\,n\,\varepsilon_0\,h\,(y_0+y_{00})}{d} & \frac{2\,n\,\varepsilon_0\,h\,V_P}{d} \\ -\frac{2\,n\,\varepsilon_0\,h\,V_P}{d} & k_y \end{bmatrix} \cdot \begin{bmatrix} du \\ dy \end{bmatrix} \qquad (6.33\ a,b)$$

where dq is the change in charge on the electrodes, dF is the change in electrostatic force, du is the change in voltage, dy is the change in displacement and y_{00} denotes the static deflection caused by the polarisation voltage V_P. Combining eq. (6.31) and (6.33a) the admittance is equal to:

$$Y(j\omega) = \frac{i}{v} = j\omega C_0 + \frac{j\omega C_1}{H(j\omega)} \tag{6.34}$$

with

$$C_0 = \frac{2\, n\, \varepsilon_0\, h\, (y_0 + y_{00})}{d} \tag{6.35}$$

$$C_1 = \frac{4\, n^2\, \varepsilon_0{}^2\, h^2\, u_0{}^2}{k_y\, d^2} \tag{6.36}$$

$$H(j\omega) = \left(\frac{j\omega}{\omega_0}\right)^2 + \frac{j\omega}{Q\,\omega_0} + 1 \tag{6.37}$$

where C_0 and C_1 denote the static and motional capacitance, respectively, and Q denotes the quality factor. An equivalent electrical circuit has been used to describe the electromechanical behaviour of the comb drive actuator around the resonance frequency. This is shown in fig. 6.8.

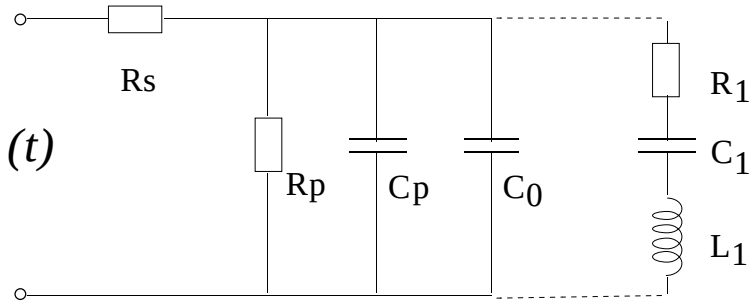

Fig. 6.8 *Equivalent circuit representation of the electrostatic comb drive actuator including parasitic loads. for C_1 see expr. (6.36), $L_1 = 1/\omega_0{}^2 C_1$, $R_1 = \frac{1}{Q}\sqrt{L_1/C_1}$, C_p = parasitic capacitance, R_p = parallel resistance, and R_S = series resitance .*

The corresponding values of resistors, capacitors and inductors can be determined by parameter extraction from measured polar admittance characteristics [6.26].

6.3 FABRICATION

Fabrication starts with a (100) p-type 3" silicon wafer. The first step is wet thermal oxidation at 1150 ˚C to obtain a 2 µm thick SiO_2 layer. Next a 5 µm thick polysilicon layer is grown by LPCVD at a temperature of 590 ˚C, a pressure of 250 mTorr and a silane flow of 50 sccm. This polysilicon layer is heavily doped with boron by solid source indiffusion at 1100 ˚C for 3 hours. This yields a sheet resistance of about 4.5 Ω/□ and also results in a small residual strain and strain gradient of the polysilicon layer. After boron indiffusion the BSG layer is stripped in a buffered HF-solution. A 0.6 µm thick PECVD silicon oxide layer is grown that serves as an etch mask for the polysilicon. After patterning the silicon oxide by RIE using CHF_3 gas, the polysilicon is anisotropically etched using a SF_6, O_2, CHF_3 gas mixture. After a cleaning step the sacrificial layer is etched for 50 minutes in a buffered HF solution. Drying is done by means of a cyclohexane freeze drying method to prevent stiction of free structures to the substrate. Finally a 1 µm thick aluminium layer is evaporated for backside contact. The final result is shown in fig. 6.9-6.12.

6.4 MEASUREMENTS

In the experiments, both the substrate and the rotor electrode were connected to ground potential while the stator electrode was connected to a positive driving voltage. From static measurements, flexure spring constants have been determined and the Young's modulus of the boron doped polysilicon lateral to the wafer surface has been calculated. From the dynamic measurements the resonance frequency and quality factor are extracted using the equivalent circuit parameters.

6.4.1 Extraction of Young's modulus

The displacement as a function of the driving voltage was measured using a microscope while applying a d.c. voltage between the rotor and the stator/substrate electrodes. Fig. 6.13 shows the results for two crab-leg flexure designs. As expected the deflection is proportional to the voltage squared. If the amount of comb fingers, finger thickness and gap spacing are known, the spring constant of the beams can be calculated from the slope of the deflection-

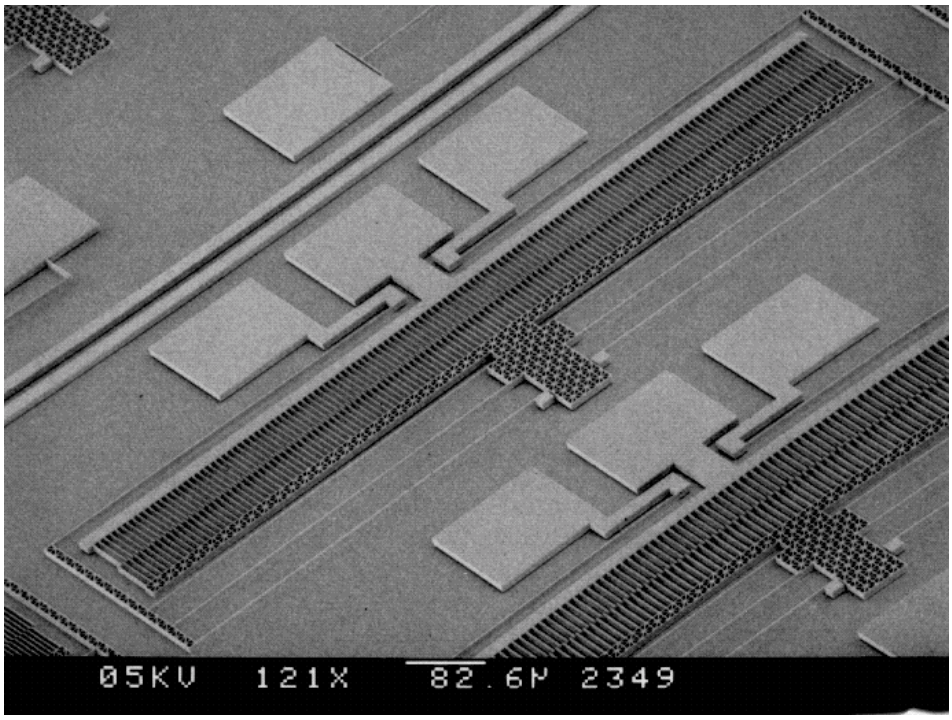

Fig. 6.9 *SEM photographs of fabricated comb drive actuators. The total length of the actuator is about 1 mm.*

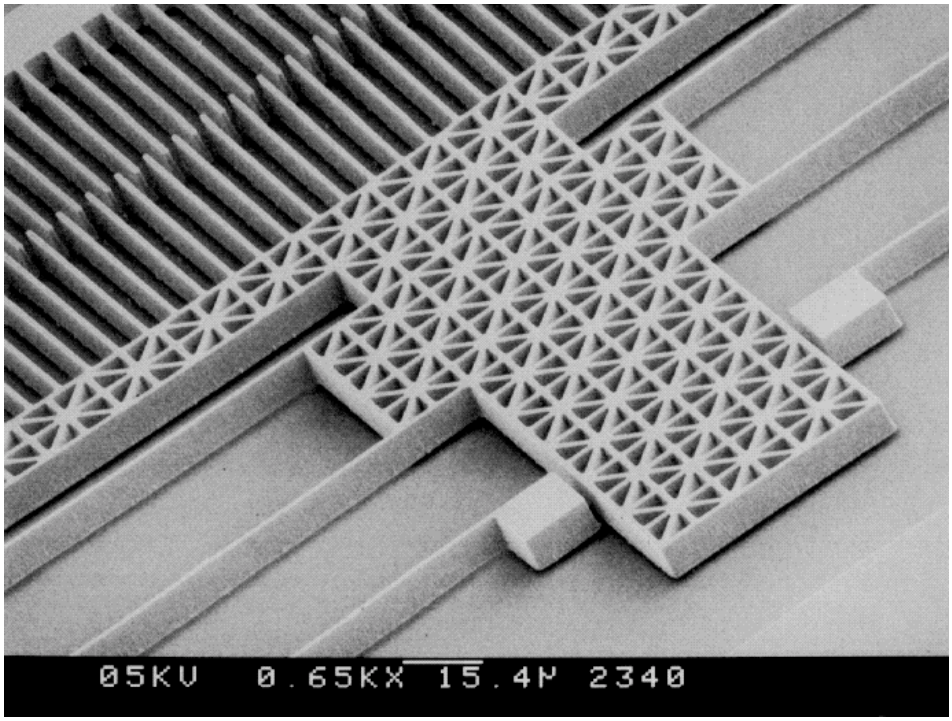

Fig. 6.10 *Close-up view showing the comb finger array, the movable shuttle, the beam anchors and free standing beams. A skeleton structure has been used to enhance sacrificial layer etching.*

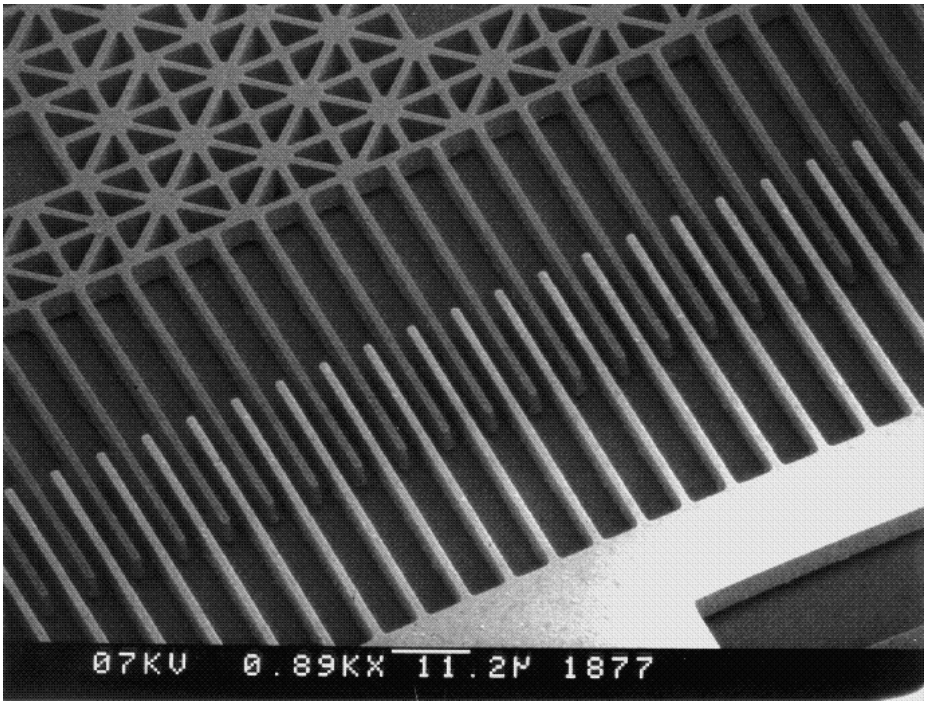

Fig. 6.11 *Close-up view of comb fingers of comb structure deflected by electrostatic forces.*

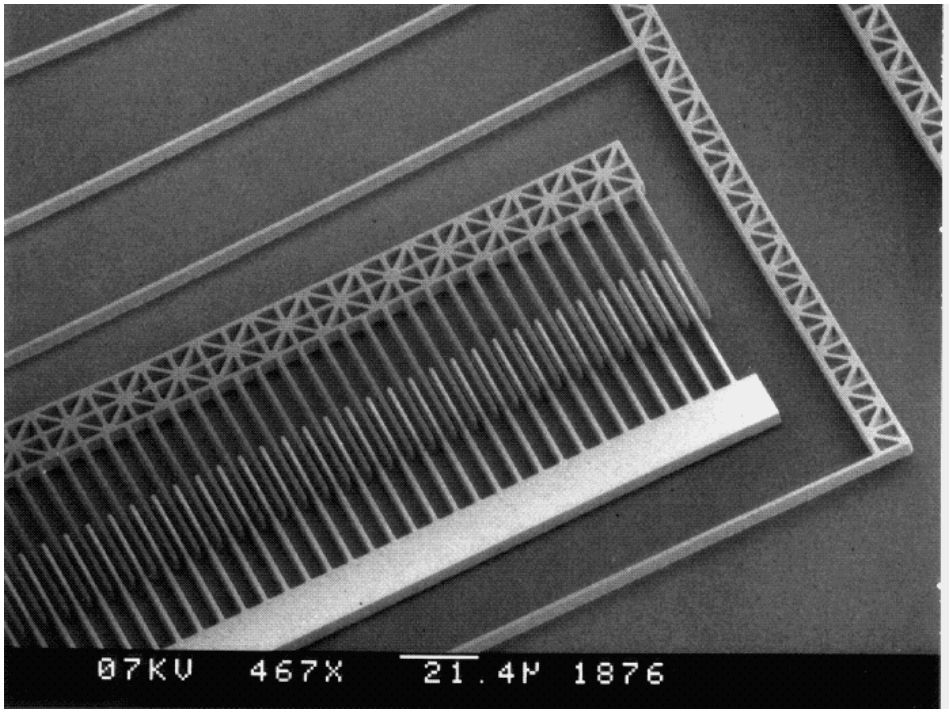

Fig. 6.12 *Close-up view of comb fingers, truss and deformed beams of a deflected comb structure.*

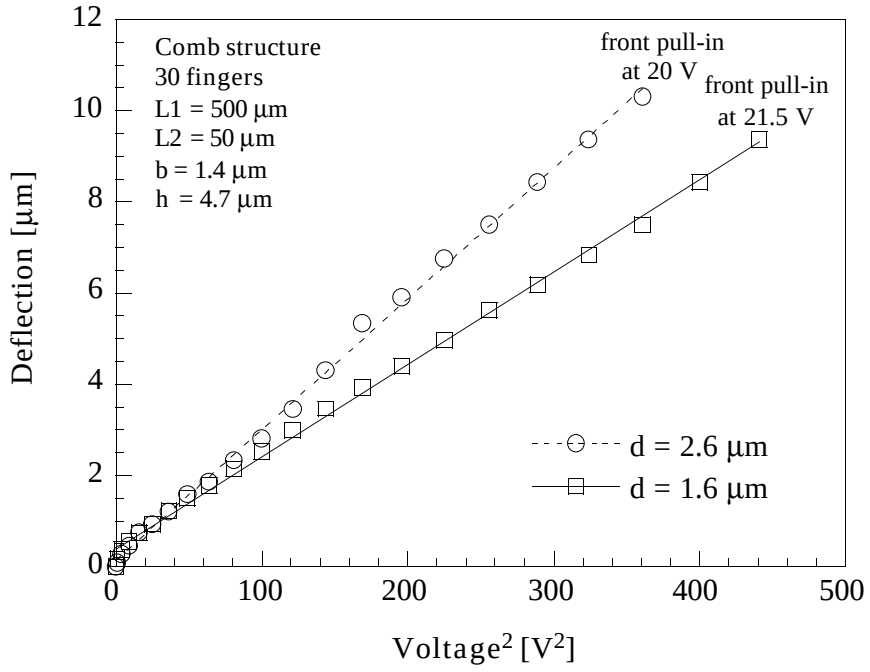

Fig. 6.13 *Measured deflection as a function of the driving voltage for two crab-leg flexure designs. The comb consisted of 30 fingers with a gap spacing d of 1.6 and 2.6 µm. The crab-leg structure consisted of a thigh segment with a length L1 of 500 µm and a shin with a length L2 of 50 µm. Measured beam width h was 4.7 µm and the beam thickness b was 1.4 µm.*

to-voltage curves. The lateral Young's modulus of the polysilicon layer can be extracted from known beam dimensions using the measured spring constant. This yields a lateral Young's modulus of 160±20 GPa for the polysilicon in our fabrication process. The large uncertainty in this value is mainly a result from the measurement error in the beam thickness. The Young's modulus is underestimated by a small factor because the electrostatic forces are somewhat larger as a result of fringing fields which have not be taken into account in our model. To obtain an indication of 3D effects, approximate expressions as derived by Johnson and Warne that include fringing fields and groundplane effects have been used [6.27]. For comb fingers with a height of 5 µm, a width of 2 µm, a gap spacing of 2 µm and a groundplane that is located 2 µm below the fingers, their expression yields an electrostatic force of: $F_{el} = 2.6225\, n\, \varepsilon_0\, V^2$. This approximated 3D force is about 5 % larger than the parallel plate approximation. After correction for 3D effects a final value of 170±20 GPa for the lateral Young's modulus has been calculated. This value lies well within the range of reported values [6.1, 6.28]. It is in good agreement with a theoretically calculated value of 164 GPa, which has been obtained by averaging of well known mono-crystalline properties, over the measured grain orientations in our polysilicon thin films.

The measured deflection to voltage behaviour of the folded flexure actuator designs is shown in fig. 6.14. The number of comb fingers in these designs has been increased resulting in lower driving voltages. Deflections of about 30 μm are obtained at driving voltages around 20 Volts.

6.4.2 Pull-in measurements

Another way to determine the static behaviour is by measuring the capacitance of the comb structure as a function of the d.c. bias voltage. Capacitance to voltage measurements have been performed using a HP4194A impedance analyser. The change in capacitance of some folded beam designs is shown in fig. 6.15. When the pull-in voltage is reached the comb drive becomes unstable and the capacitance suddenly changes as shown in the figure.

The measured pull-in voltage and deflection at pull-in for different folded flexure designs is summarised in table 6.1.

Design	fingers	V_{SI} [V]	δ [μm]
C2-2	136	20.0	39.9
C2-3	105	22.8	39.9
C2-4	88	24.3	39.8
C2-5	74	26.1	39.7

Table 6.1 *Measured pull-in voltage and deflection at pull-in for different comb drive designs. The initial finger overlap y_0 is 4.6 μm, the gap spacing d is 2.2 μm, the height h of the structures is 4.8 μm and the thickness b of the beams is 1.5 μm.*

The spring constants of the beam in the *x*- and *y*-direction can be determined from these measurements; the measured spring constants k_x and k_y are respectively 17 N/m and 0.029 N/m. The theoretical values using measured dimensions and Young's modulus, are determined from eq. (6.23) and (6.12), giving respectively k_x=19.2 N/m and k_y=0.044 N/m.

The measured spring constant along the *y*-axis is somewhat lower than the calculated value. This could result from the fact that the trusses are not rigid, as assumed in the theoretical model, or by a non-rectangular cross section of the beams as a result of underetching. The measured spring constant along the *x*-axis is in good agreement with the calculated value. A spring constant as obtained directly from Hooke's law (eq. 6.11), would result in a large overestimation of the spring constant in the x-direction yielding a theoretical value fork_x that is equal to almost 9000.

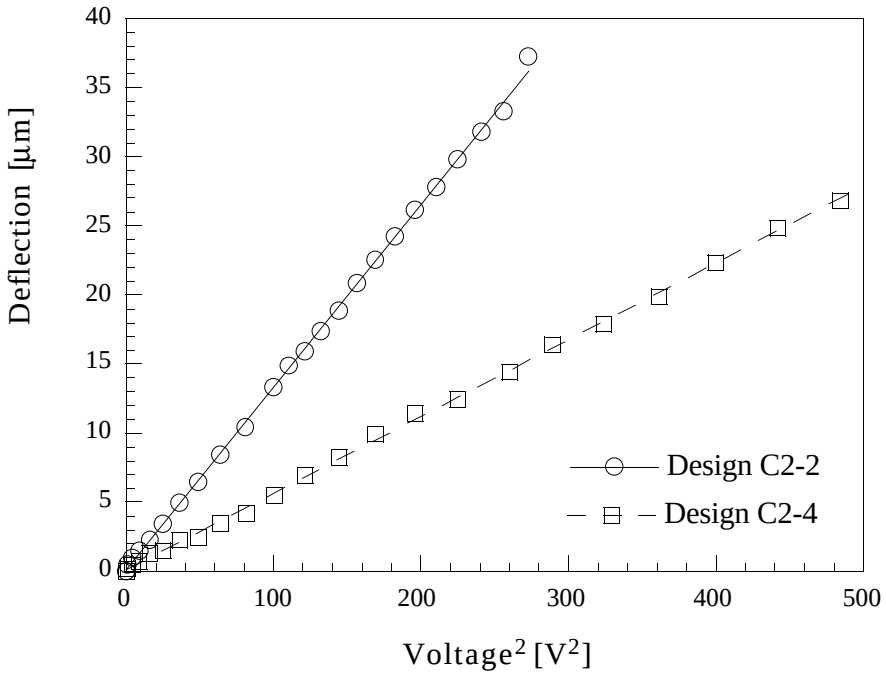

Fig. 6.14 *Measured deflection as a function of the driving voltage for several folded flexure designs. Design C2-2, C2-4 employed comb structures with respectively 136 and 88 fingers. The gap spacing d equals 2.2 µm and the length of the beams in the folded flexure is 500 µm. The beam width h is 4.8 µm and the beam thickness b is 1.5 µm.*

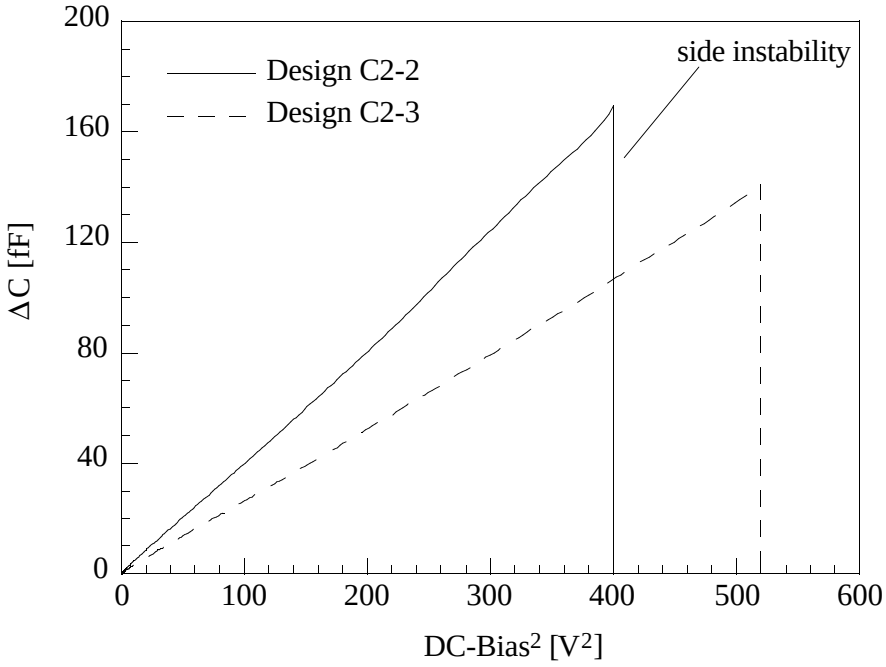

Fig. 6.15 *Capacitance change of folded beam comb drive designs as a function of the driving voltage squared. At a certain voltage pull-in of the comb structure occurs because of side instability. Design C2-2 and C2-3 employed comb structures with respectively 136 and 105 fingers. Oher parameters have already been given in fig. 6.13.*

6.4.3 Frequency response

The admittance of the comb actuators was also measured using the HP 4194A impedance analyser. Fig. 6.16 shows the measured and modelled polar admittance plot of a comb drive actuator around the resonance frequency. Neglecting the series resistance R_s, which has a small contribution compared to the other admittances, the following parameter values have been extracted from a best fit of the measured response: C_0+C_p=414.5 fF, C_1=145.6 fF, L_1=68.4 kH, R_1=205 MΩ and R_p=17.6 GΩ. This gives a resonance frequency f≈1.60 kHz and a quality factor Q≈3.34.

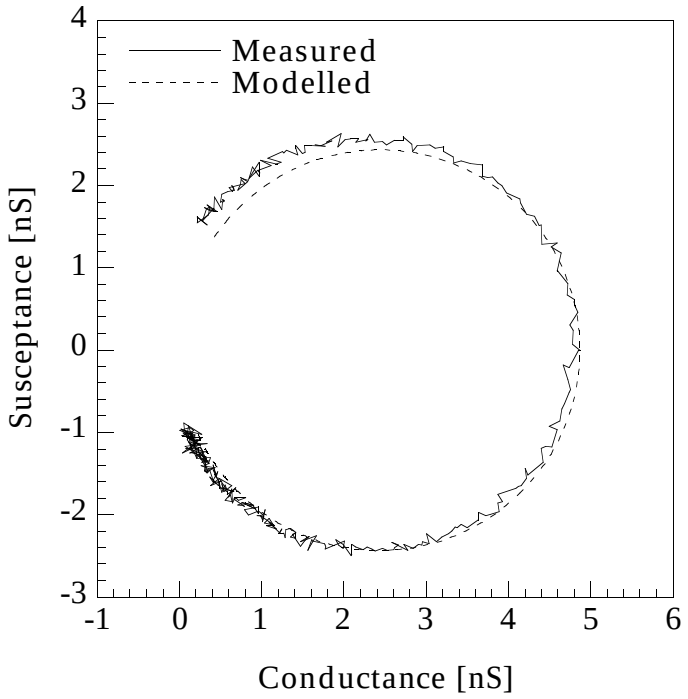

Fig. 6.16 *Measured and calculated admittance of comb actuator C2-2, having a beam length of 500 µm, a beam height of 4.8 µm, a beam thickness of 2 µm, a gap spacing of 2.2 µm and 136 comb fingers. The d.c. polarization voltage was equal to 15 V and the a.c. drive voltage was equal to 0.5V. The dashed line is a theoretical curve using extracted parameter values: C_0+C_p=414.5 fF, C_1=145.6 fF, L_1=68.4 kH, R_1=205 MΩ, R_p=17.6 GΩ.*

6.5 POSITION CONTROL

An important topic for further work is position control. In micropositioning, position feedback is desirable in order to reduce external disturbances and improve system response time and accuracy. In xy-stages, for example, springs are mechanically coupled and deflections in one direction may cause small but unwanted deflections in the orthogonal directions. A first study on feedback

control of comb drive actuators has been done [6.29, 6.30]. The position can easily be obtained by measuring the capacitance of the comb drive itself. The capacitance of the comb-drive can be measured by the superposition of a high frequency measurement signal to the driving signal. The measurement frequency needs to be much higher than the bandwidth of the system. In order to study control aspects, it is convenient to consider the comb drive actuator as a fourth order system in order to obtain information about feedback limitations. The system is generally underdamped; to increase the system damping (stability) it is necessary to use e.g. a P(I)D controller. Important aspects are that single comb drives can only be one-sided controlled and that the maximum driving voltage is limited by side-instability of the comb drive which put constrains on feedback control.

6.6 CONCLUSIONS

A large deflection, low driving voltage comb drive actuator has been designed and fabricated by a one mask fabrication process using boron doped polysilicon as the structural material and silicon dioxide for the sacrificial spacer. The lateral Young's modulus of the polysilicon layer has been obtained from static displacement-to-voltage measurements and turned out to be approximately 170 GPa. Theoretical lateral spring constants of clamped-clamped, crab-leg and folded beam flexure designs have been determined and were investigated on their large deflection behaviour. Actuator behaviour is limited by electromechanical side instability and expressions for the side-instability voltage and deflection are given. A one-port approach using electrostatic excitation and detection to generate and measure dynamical properties has been used. The electromechanical behaviour around the resonance frequency was described by an equivalent electric circuit. The modelled lateral spring constant of the folded beam design was somewhat larger than experimentally determined values. This is likely to be a result of compliant trusses in our fabricated design in contrast to rigid trusses that have been assumed in our theoretical model, or by a non-rectangular cross section of the beams as a result of underetching. The theoretical axial spring constant of a folded beam which includes a reduction in spring constant with increasing lateral deflection was found to be in good agreement with experimental results in contrast to theoretical spring constants simply determined from Hooke's law. The electromechanical behaviour can be well described by the presented equivalent circuit which was used to extract the resonance frequency and

quality factor from admittance measurements. An approach towards position control and feedback was briefly discussed.

REFERENCES

[6.1] W.C. Tang, T.C. Nguyen and R.T. Howe, Laterally driven polysilicon resonant microstructures, Sensors and Actuators, 20 (1989), pp. 25-32.

[6.2] R.A. Brennen, A.P. Pisano and W.C. Tang, Multiple mode micromechanical resonators, Proc. Micro Electro Mechanical Systems, Napa Valley, CA, U.S.A. , Feb. 11-14, 1990, pp. 9-14.

[6.3] M.W. Judy and R.T. Howe, Polysilicon hollow beam lateral resonators, Proc. IEEE Micro Electro Mechanical Systems, Fort Lauderdale, FL, U.S.A., Feb. 7-10, 1993, pp. 265-271.

[6.4] L. Lin, C.T.C. Nguyen, R.T. Howe and A.P. Pisano, Micro-electromechanical filters for signal processing, Proc. IEEE Micro Electro Mechanical Systems, Travemünde, Germany, Feb. 4-7, 1992, pp. 226-231.

[6.5] V.P. Jaecklin, C. Linder, N.F. de Rooij, J.M. Moret and R. Vuilleumier, Optical microshutters and torsional micromirrors for light modulator arrays, Proc. IEEE Micro Electro Mechanical Systems, Fort Lauderdale, Florida, U.S.A., Feb. 7-10, 1993, pp. 124-127.

[6.6] O. Tabata, R. Asahi, N. Fujitsuka, M. Kimura and S. Sugiyama, Electrostatic driven optical chopper using SOI, Proc. 7th Int. Conf. Solid-State Sensors and Actuators (Transducers '93), Yokohama, Japan, June 7-10,1993, pp. 124-127.

[6.7] P.Y. Chen and R.S. Muller, Microchopper-modulated IR microlamp, Proc. IEEE Solid-State Sensors and Actuators Workshop, Hilton Head Island, SC, U.S.A., June 13-16, 1994, pp. 239-242.

[6.8] C.J. Kim, A.P. Pisano and R.S. Muller, Overhung electrostatic micro gripper, Journal of Microelectromechanical Systems, Vol. 1, No. 1, March 1992, pp. 31-36.

[6.9] D.P. Loconto and R.S. Muller, High-sensitive micromechanical electrostatic voltmeter, Proc. 7th Int. Conf. Solid-State Sensors and Actuators (Transducers '93), Yokohama, Japan, June 7-10, pp. 878-881.

[6.10] A.P. Lee and A.P. Pisano, Polysilicon angular microvibromotors, Journal of Microelectromechanical Systems, Vol. 1, No. 2, June 1992, pp. 70-76.

[6.11] E.J. Garcia and J.J. Sniegowski Surface micromachined microengine as the driver for micromechanical gears, 8th Int. Conf. on Solid-State Sensors and Actuators (Transducers '95), Stockholm, Sweden, June 25-29, 1995, pp. 365-368.

[6.12] V.P. Jaecklin, C. Linder, N.F. de Rooij, J.M. Moret, R. Bischot and F. Rudolf, Novel polysilicon comb actuators for xy-stages, Proc. IEEE Micro Electro Mechanical Systems, Travemünde, Germany, Feb. 4-7, 1992, pp. 147-149.

[6.13] V.P. Jaecklin, C. Linder, N.F. de Rooij, Comb actuators for xy-microstages, Sensors and Actuators, Vol. A 39, 1993, pp. 83-89.

[6.14] H. Jansen, R. Verhagen and M. Elwenspoek, The black silicon method III: Design rules, modelling, optimisation, and performance of precision position systems for scanning probe, gripping and other MEMS applications, Seminar on Handling and Assembly of Microparts, Vienna, Austria, Nov. 14, 1994.

[6.15] J. Brugger, V.P. Jaecklin, C. Linder, N. Blanc, P.F. Indermühle and N.F. de Rooij, Microfabricated tools for nanoscience, J. Micromech. Microeng., Vol. 3, 1993, pp. 161-167.

[6.16] Y. Xu, S.A/ Miller and N.C. MacDonald, Microelectromechanical scanning tunneling microscope, Proc. 8th Int. Conf. Solid-State Sensors and Actuators (Transducers '95), Stockholm, Sweden, June 25-29, pp. 640-643.

[6.17] A.P. Pisano and Y.H. Cho, Mechanical design issues in laterally-driven microstructures, Sensors and Actuators, Vol. A21-A23, 1990, pp. 1060-1064.

[6.18] J.M. Gere and S.P. Timoshenko, Mechanics of Materials, 2nd ed., Van Nostrand Reinhold (UK) Co. Ltd., 1987.

[6.19] R. Frisch-Fay, Flexible bars, Butterworths (London), 1962.

[6.20] M.W. Judy, Micromechanisms using sidewall beams, Ph.D. dissertation, Faculty of Electrical Engineering and Computer Sciences, University of California at Berkeley, 1994.

[6.21] G.K. Fedder, Simulation of Microelectromechanical Systems, Ph.D. dissertation, Faculty of Electrical Engineering and Computer Sciences, University of California at Berkeley, 1994.

[6.22] I.H. Shames and C.L. Dym, Energy and finite element methods in structural mechanics, McGraw-Hill, New York, 1985.

[6.23] W.C. Tang, M.G. Lim and R.T. Howe, Electrostatic comb drive levitation and control method, Journal of Microelectromechanical Systems, Vol. 1, No. 4, Dec. 1992, pp. 170-178.

[6.24] T. Hirano, T. Furuhata, K.J. Gabriel and H. Fujita, Design, fabrication and operation of sub-micron gap electrostatic comb-drive actuators, Journal of Microelectromechanical Systems, Vol. 1, No. 1, March 1992, pp. 52-59.

[6.25] V.P. Jaecklin, C. Linder, N.F. de Rooy and J.M. Moret, Micromechanical comb actuators with low driving voltage, J. Micromech. Microeng., Vol. 2, 1992, pp. 250-255.

[6.26] H.A.C. Tilmans, Micromechanical sensors using encapsulated built-in resonant strain gauges, Ph.D. dissertation, Faculty of Electrical Enginnering, University of Twente, 1993.

[6.27] W.A. Johnson and L.K. Warne, Electrophysics of micromechanical comb actuators, Journal of Microelectromechanical Systems, Vol. 4, No. 1, March 1995, pp. 49-59.

[6.28] R. I. Pratt, G. C. Johnson, R. T. Howe and J. C. Chang, Micromechanical structures for thin film characterization, Proc. Int. Conf. on Solid-State Sensors and Actuators, (Transducers '91), San Fransisco, CA, U. S. A., June 24-27, 1991, pp. 205-208.

[6.29] A.W. Groeneveld, Electromechanical behaviour and study towards position control of electrostatic comb drive actuators, Master Thesis, University of Twente, December, 1995.

[6.30] R. Legtenberg, A.W. Groeneveld and M. Elwenspoek, Towards position control of electrostatic comb drives, Proc. 6th Workshop on Micromachining Micromechanics and Microsystems (MME '95), Copenhagen, Denmark, 3-5 September, 1995, pp. 124-127.

Chapter Seven

AN ELECTROSTATIC LOWER STATOR AXIAL GAP POLYSILICON WOBBLE MOTOR*

This chapter presents the design, modelling, fabrication and first performance characteristics of electrostatically driven axial-gap polysilicon wobble motors. Aspects such as the gear ratio, torque generation, excitation schemes and torque coverage, normal forces, friction, rotor kinetics and dynamical behaviour are addressed. The fabrication is based on a four mask process using polysilicon surface micromachining techniques. Three to twelve stator pole wobble motor designs are realised with rotor radii of 50 and 100 micrometer. Motors are operated successfully at driving voltages of only a few Volts and are capable of generating torque's in the nNm range at high electrostatic fields. The motor performance is characterised by gear ratio measurements and measuring starting and stopping voltages. The motor design and fabrication process are suited to the integration of gear linkages with respect to mechanical power transmission.

7.0 INTRODUCTION

Initial micromechanical motor design and fabrication attempts have been axial-gap architectures because of large estimated driving torques [7.1-7.4]. These designs, however, suffered from instabilities in tilting, to a lesser extent in vertical pertubations, and fabrication complexity that finally led to the development of radial-gap or side-drive micromotors [7.5-7.8]. Salient-pole and wobble side-driven micromotors have successfully been fabricated.

Although the performance of these micromotors is still improving, they do exhibit some drawbacks. The rotor to stator overlap is small, resulting in small driving torque's. Typically a few pNm for salient pole micromotors and a few tens of pNm for wobble motors. This is merely the result of the rotor and stator thickness that is generally only a few microns. Furthermore, it is difficult to implement the radial gap design into a system with respect to mechanical power transmission. In outer stator designs, the stator completely surrounds

* presented at the 8th Int. Conf. on Solid-State Sensors and Actuators (Transducers '95), Stockholm, Sweden, June 25-29, 1995, Vol. 2, pp. 404-407. submitted to Journal of Microelectromechanical Systems.

the rotor making it difficult to transfer the mechanical energy to another structure when using planar fabrication techniques. While for inner stator designs, it is difficult to make the electrical stator connections [7.9, 7.10].

A number of different side-driven wobble motors have been investigated [7.9-7.13]. Wobble motors are able to generate a larger driving torque's compared to salient pole micromotors because of their gear ratio. The gear ratio increases the driving torque at the cost of a decreasing angular speed. Also, in wobble motors friction is expected to be lower because of a rolling motion instead of sliding.

A lower stator axial gap wobble motor design probably can solve some of the limitations of the radial-gap or side-drive design. This design was first presented by Paratte [7.14-7.16]. The tilting-, vertical- and radial rotor instabilities of this lower stator axial gap design are constrained by the bearing and stator geometry. The larger rotor to stator overlap results in a larger torque generation and successful drive of a gear train has already been realised by a hybrid design based on electroplating and assembling techniques [7.17].

In this paper the design, modelling, a fabrication process based on polysilicon surface micromachining techniques and first performance characteristics of electrostatically driven axial-gap lower-stator polysilicon micromotors is presented. The motor design and fabrication process lend itself for on-chip micromotor driven micro mechanical systems.

7.1 OPERATION PRINCIPLE

The motor is sketched in fig. 7.1. The rotor is resting in its centre at a pin- or ball bearing. When a voltage is applied between the rotor and one of the stator poles, the rotor will be pulled down towards a contact point at the angular centre of the excited stator pole.

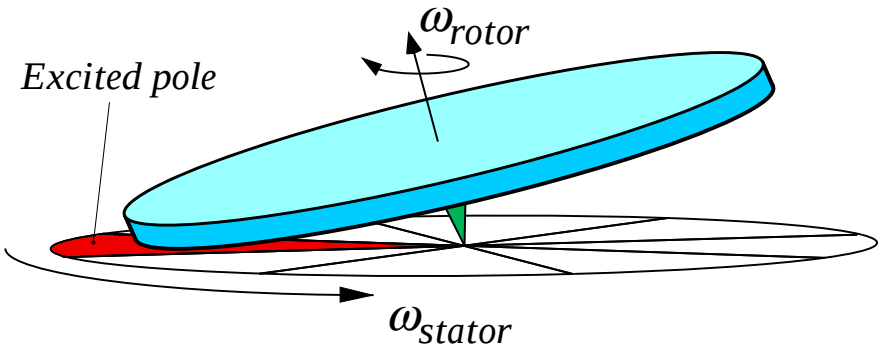

Fig. 7.1 *Sketch of the operation principle.*

Switching to other stator poles will move this contact point around and the rotor is forced to roll at its outer radius resulting in a rocking motion.

Because of a difference in radius between the rotor and the resulting contact point circle, the rotor will be rotated by a small angle after one sequential activation of all stator poles. By proper commutation of the charge distribution on the stator electrodes and the rotor, continuous motion of the rotor can be achieved. The ratio between the angular speed of the stator poles and the rotor is called the gear ratio *n*.

7.2 THEORETICAL MODEL

7.2.1 Gear Ratio

For small rocking angles, in the absence of rotor slip and mechanical deformations, the harmonic reduction ratio of the angular velocity between the stator and rotor is given by the nominal gear ratio. The nominal gear ratio is dependent on motor dimensions and can be found from the ratio of the rotor radius and the difference between the rotor radius and the contact point radius. The radius of the resulting contact point circle R_C can be found from:

$$R_C = \sqrt{R^2 + d^2} + \left(h_b - d\right)\sin\theta \qquad (7.1)$$

where R is the rotor radius, d is the axial gap distance at the rotor centre, h_b is the height of the bearing pin and θ is the angle between the rotor and the stator surface which is approximately equal to d/R (see fig. 7.2).

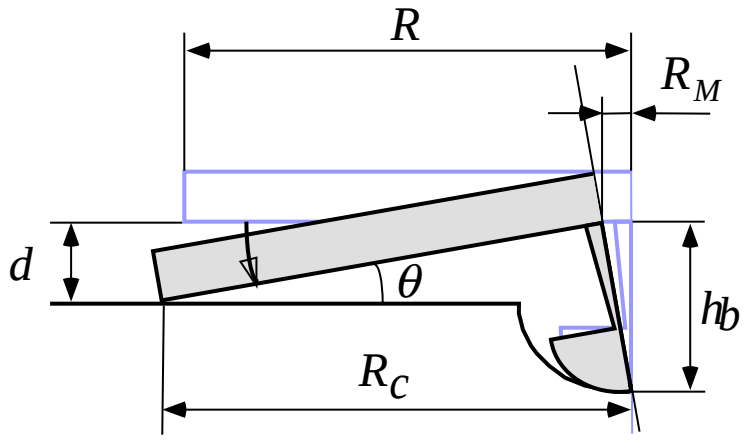

Fig. 7.2 *Schematic cross sectional view of the rotor.*

This yields the following expression for the nominal gear ratio:

$$n_0 = \frac{R}{R - R_C} \approx -\frac{2\,R^2}{2\,d\,h_b - d^2} \tag{7.2}$$

Note that the gear ratio is negative when R_c is larger than R which means that the rotor rotates in a direction opposite to the excitation of the stator poles.

7.2.2 Torque Generation

The tilt angle θ of the rotor is very small. Therefore the electrostatic field can be assumed to be vertical. Furthermore, fringing fields have been neglected and the rotor is assumed to be a rigid disk. An analytical model of the torque generation based on these assumptions has been shown to be in good agreement with FEM simulations for other axial gap motors [7.18]. The axial gap spacing g between the substrate and the rotor is equal to:

$$g = \left[R - r\cos(\varphi - \alpha)\right]\sin\theta \approx d\left[1 - \frac{r}{R}\cos(\varphi - \alpha)\right] \tag{7.3}$$

where r is the radius, φ is a variable for the angle and α is the contact point angle of the rotor. The electrostatic co-energy E'_{el} of an excited stator pole can be found by integration over the excited stator region from angle φ_1 to φ_2 and radius R_i to R_o yielding:

$$E'_{el} = -\frac{1}{2}\,C\,V^2 = -\frac{1}{2}\int_{\varphi_1}^{\varphi_2}\int_{R_i}^{R_o}\frac{\varepsilon_0\,r\,dr\,d\varphi}{g + \frac{d_{ins}}{\varepsilon_r}}\,V^2 \tag{7.4}$$

where ε_0 is the dielectric constant in air, d_{ins} is the thickness of the dielectric insulator between the stator and rotor, ε_r is the relative dielectric constant of this layer and V is the applied voltage. In the absence of rotor slip, the torque generated by the motor τ_{motor} can be found from the negative derivative of the electrostatic co-energy with respect to the rotor angle α:

$$\tau_{motor} = \frac{1}{2}\frac{dC}{d\alpha}\,V^2 \tag{7.5}$$

An example of the single phase torque as function of the rotor angle α is shown in fig. 7.3 for several stator pole designs. Dimensional values are given in the figure caption. The torque generation can be in the range of nNm at electrostatic fields of 10^8 V/m. The maximum torque is generated when the

rotor contact point is located at one of the edges of the excited stator pole. The driving torque can be increased by increasing the angular width of the excited stator poles up to π radians, by reducing the air gap spacing and the thickness of the dielectric layer between the rotor and the stator, by increasing the relative dielectric constants and by increasing the rotor diameter. The torque scales proportional to the third power with motor radius when the gear ratio and electric field strength are kept constant.

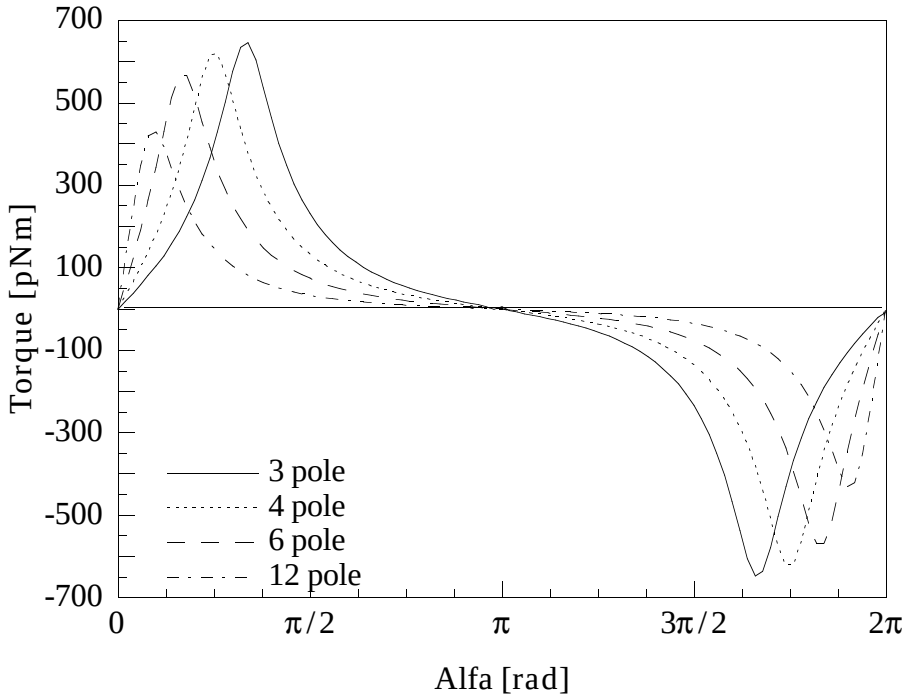

Fig. 7.3 *Single phase torque of a 3, 4, 6 and 12 stator pole design as function of the rotor angle. The driving voltage is equal to 100 Volts. The rotor radius R is 100 μm, the axial gap distance d is 2 μm, the thickness of the dielectric layer d_{ins} between the stator and rotor is 0.2 μm and has a relative dielectric constant of 7.5. The stator outer radius is equal to the rotor radius (R_O=R) and the inner stator radius R_i is equal to half the rotor radius (50 μm).*

7.2.3 Excitation Schemes and Torque Coverage

The stator needs a minimum of three poles in order to generate a driving torque. A stator with two poles with an angle of π radians will only result in a rocking motion but does not turn the rotor. To ensure a one directional rotation, a power supply with at least three independent phases is required. Below the independent phases are represented by alphabetical symbols, given in bold capitals when activated, and normal format when deactivated. The total amount of alphabetic symbols equals the number of stator poles. The overall torque generation $\tau_{coverage}$ for different driving schemes or excitation

patterns can be found from the enveloping curve of excited stator poles (see figs. 7.4 and 7.5). The average torque τ_{av} can be found from:

$$\tau_{av} = \frac{1}{2\pi} \int_0^{2\pi} \tau_{coverage}\, d\alpha \tag{7.6}$$

and the normalised torque ripple τ_{ripple} is:

$$\tau_{ripple} = \frac{\tau_{\max} - \tau_{\min}}{\tau_{av}} \tag{7.7}$$

The output power of the motor can be found from:

$$P_{motor} = \tau_{av}\, \omega_{rotor} \tag{7.8}$$

where ω_{rotor} is the angular speed of the rotor.

Open loop

The motor is operated in open-loop drive in our experiments. The simplest case for motor operation is a sequential excitation of the different stator poles which is called "single-pole open-loop excitation" (e.g. **A**bcd, a**B**cd, ab**C**d, abc**D** etc. for a four stator pole design). In this case the rotor rotates till it reaches the zero torque position at the angular center of the excited stator pole (when friction is neglected). Switching to the adjacent stator pole results in an inefficient position with respect to torque generation. This can be improved when using a "double-pole open-loop excitation". In this case two adjacent stator poles are excited simultaneously and in the next step this couple is rotated by one stator pole (e.g. **AB**cd, a**BC**d, ab**CD**, **A**bc**D** etc.). Now the starting position of the rotor is always at the edge of an excited stator couple where the torque generation is highest. The torque coverage of a four stator pole design in case of single-pole open-loop and double-pole open-loop excitation is shown in fig. 7.4.

Closed loop

Closed loop control requires a feedback of the rotor position in order to switch to the next stator pole at the right moment. Feedback of the rotor position is not implemented at this point. In case of closed loop control the torque ripple decreases with an increasing number of stator poles. However the maximum torque also decreases because the capacitor surface of

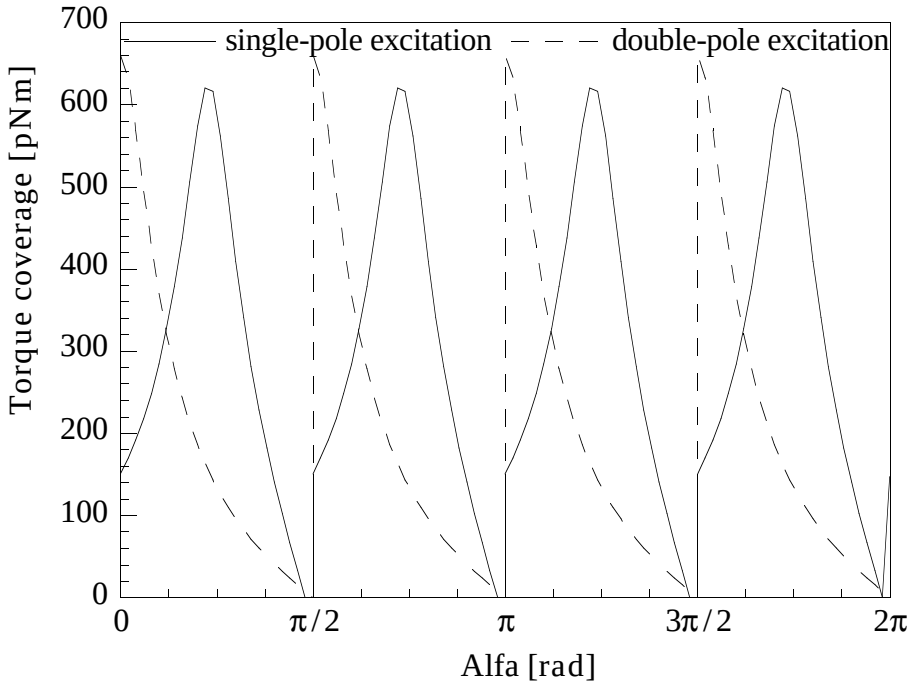

Fig. 7.4 *Torque coverage in case of open-loop single-pole and double-pole excitation for a four pole stator design with dimensions and variables as given in fig. 7.3. The average torque in case of single and double pole excitation is repectively 305 and 204 pNm.*

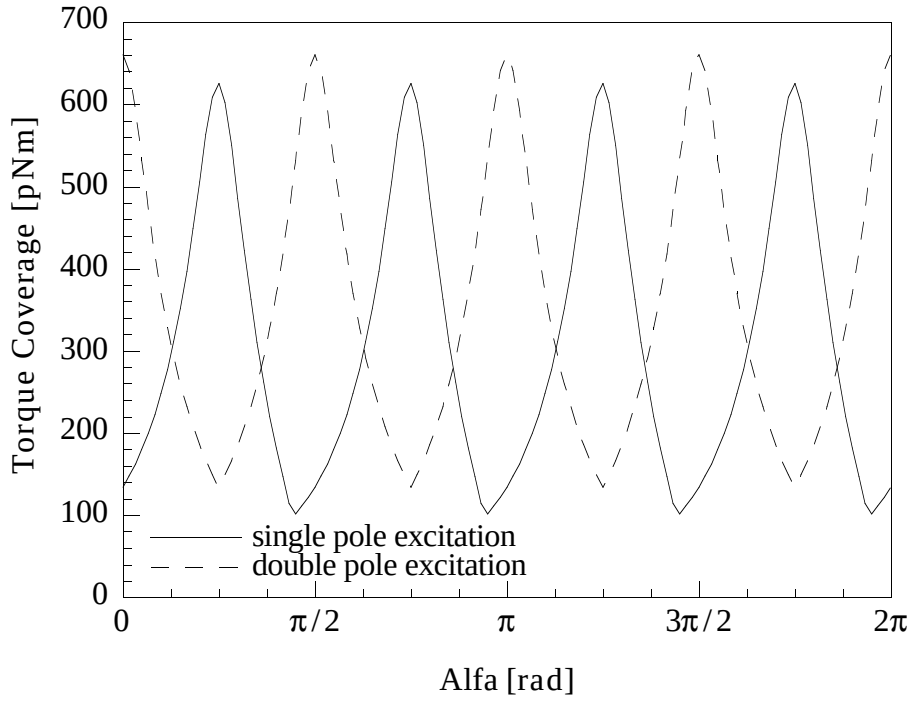

Fig. 7.5 *Torque coverage in case of closed-loop single-pole and double-pole excitation for a four pole stator design with dimensions and variables as given in fig. 7.3. The average torque for the single pole excitation is 313 pNm the average torque for the double pole excitation is 350 pNm.*

one stator pole decreases with an increasing number of poles. By simultaneously exciting a group of adjacent stator poles the maximum driving torque can be increased again. The torque generation in case of "single-pole closed-loop" and "double-pole closed-loop excitation" is shown in fig. 7.5 for a four stator pole design.

These single and grouped pole excitation schemes require a power supply with a number of independent phases that equals the number of stator poles. This may be a problem in case of a large number of stator poles which can be overcome by a parallel connection of stator poles. However, the simultaneous excitation of multiple stator groups will somewhat reduce the torque generation.

7.2.4 Normal Forces and Friction

If the friction torque balances the electrostatic torque τ_{motor} generated by the motor, rotor slip is avoided, resulting in a pure rolling motion. In fig. 7.6 forces and torques are shown when a small part dA of the stator is excited.

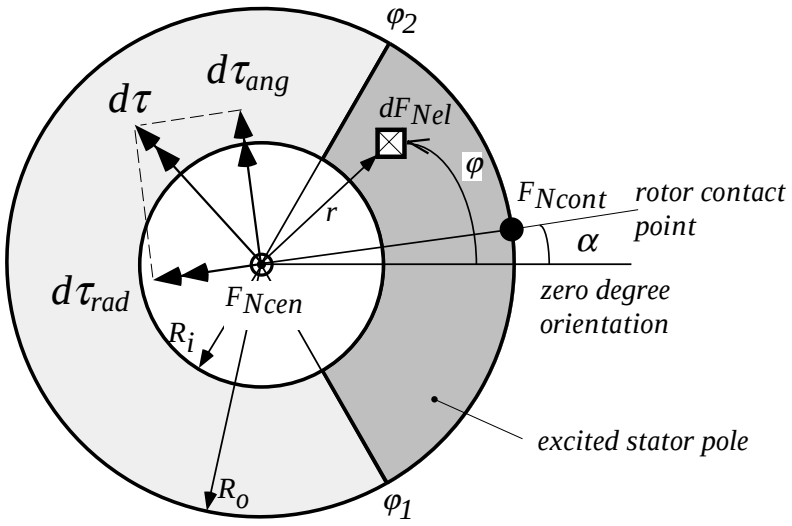

Fig. 7.6 *Sketch of the model parameters with forces and torques acting on the rotor.*

The axial electrostatic force dF_{Nel} is balanced by normal reaction forces at the rotor contact point $dF_{Ncontact}$ and the center bearing $dF_{Nbearing}$. The electrostatic force induces a torque $d\tau = dF_{Nel} \times r$ that can be divided in a component $d\tau_{ang}$ in the angular direction and a component $d\tau_{rad}$ in the radial direction. The normal bearing force $F_{Nbearing}$ and normal contact point force $F_{Ncontact}$ can be found from the angular torque balance and the force balance in the normal z-direction by integration of the electrostatic forces over the excited region. This

results in the following expressions for the normal force at the contact point and the normal force at the center bearing:

$$F_{Ncontact} = -\frac{1}{2}\,\varepsilon_0\,V^2 \int_{\varphi_1}^{\varphi_2} \int_{R_i}^{R_o} \frac{r^2 \cos(\varphi-\alpha)}{R\left(g+\frac{d_0}{\varepsilon_r}\right)^2}\,dr\,d\varphi \qquad (7.9)$$

$$F_{Nbearing} = -\frac{1}{2}\,\varepsilon_0\,V^2 \int_{\varphi_1}^{\varphi_2} \int_{R_i}^{R_o} \frac{r\left[R - r\cos(\varphi-\alpha)\right]}{R\left(g+\frac{d_0}{\varepsilon_r}\right)^2}\,dr\,d\varphi \qquad (7.10)$$

The radial torque τ_{rad} can be divided in a component that provides the rocking motion and a component in the z-direction (perpendicular to the stator surface) that provides the driving torque of the motor (see fig. 7.7):

$$\tau_{motor} = -\frac{1}{2}\,\varepsilon_0 \sin\theta\,V^2 \int_{\varphi_1}^{\varphi_2} \int_{R_i}^{R_o} \frac{r^2 \sin(\varphi-\alpha)}{\left(g+\frac{d_0}{\varepsilon_r}\right)^2}\,dr\,d\varphi \qquad (7.11)$$

This expression is equal to eq. (7.5) that was derived earlier. The normal force at the contact point $F_{Ncontact}$ and the normal force at the centerpoint $F_{Nbearing}$ are shown in fig. 7.8 for a four stator pole design as function of the contact point angle.

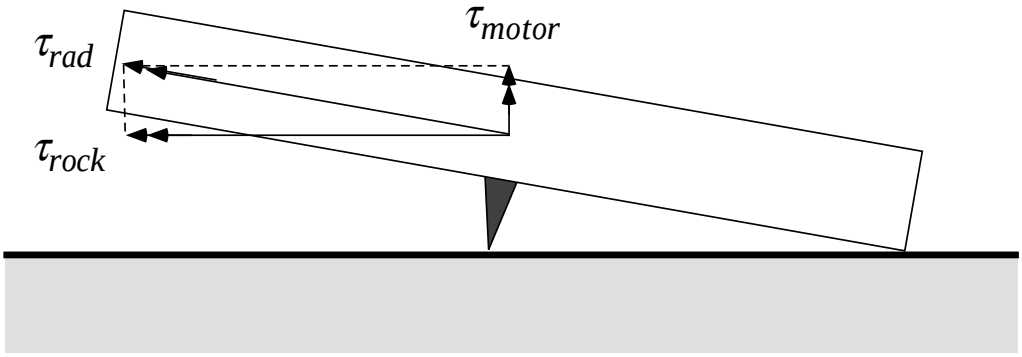

Fig. 7.7 *Decomposition of radial torque into motor torque and rocking torque.*

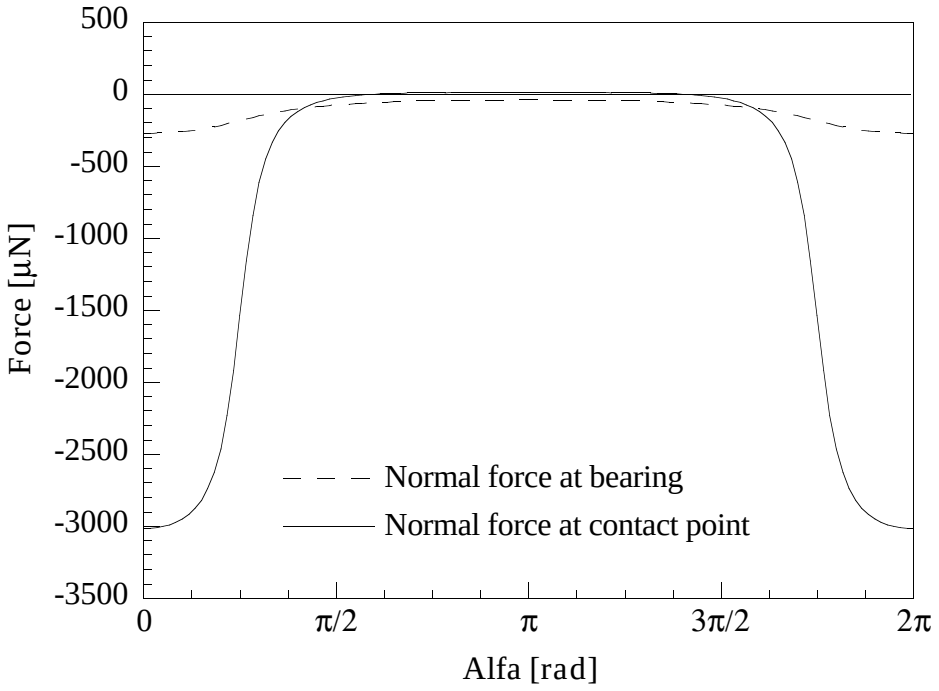

Fig. 7.8 *The normal force at the contact point $F_{Ncontact}$ and the normal force at the centerpoint $F_{Nbearing}$ as a function of the rotor contact angle α for a four pole stator design using the same parameter values as in fig. 7.3.*

Sliding and rolling friction results from two bodies that are respectively sliding or rolling against each other. The frictional forces are generally dependent on the normal forces between the two bodies. A pure rolling motion exists when the sliding frictional torque is larger than the electrostatic torque on the rotor. For the motor this no-slip condition is given by:

$$\mathrm{sgn}(\dot{\alpha})\left(F_{Ncontact}\, R\, \mu_{contact} + F_{Nbearing}\, r_{bearing}\, \mu_{bearing}\right) - \tau_{motor} \geq 0 \qquad (7.12)$$

where $\mu_{contact}$ and $\mu_{bearing}$ are the sliding frictional coefficients at respectively the contact point and the bearing.

Fig. 7.8 shows that the normal force at the contact point is very large around the region of the excited stator pole. It even changes sign when the contact point reaches a position at the opposite side of the excited stator pole because the rotor wants to flip over. In this region the frictional torque as a result of the normal force at the contact point will be zero. However, there is still a frictional torque in this region as a result of the normal force at the bearing. Provided the bearing radius and sliding frictional coefficient at the bearing

are large enough (for example: $R_{bearing}$=10 μm and $\mu_{bearing}$=0.3) the sliding frictional torque is still in the same range as the motive torque in this region. An appropriate choice of excitation scheme can be used to sustain continuous large normal forces that will prevent rotor slip. For example, an excitation scheme where the step angle is smaller than the totally excited angular region, like in the double pole excitation, will always operate at large normal forces. During normal operation our model suggests that the motor will always work under no-slip conditions.

7.2.5 Kinetic behaviour

The motion of a point on the rotor is a superposition of three movements. 1: a rotation of the rotor around its center, 2: a circular translation of the center itself and 3: the rocking motion of the rotor. The position of a fixed point on the rotor can be described by:

$$\begin{aligned}\bar{p} = &\left[R_M \cos\alpha + r\cos\left(\frac{\alpha}{n}+\varphi\right)\right] e_x + \\ &\left[R_M \sin\alpha + r\sin\left(\frac{\alpha}{n}+\varphi\right)\right] e_y + \\ &d\left[1-\cos\left(\alpha\,\frac{n-1}{n}+\varphi\right)\right] e_z\end{aligned} \tag{7.13}$$

where the radius of the center point rotation R_M is given by (see fig. 7.2):

$$R_M = \frac{h_b\, d}{R} \tag{7.14}$$

The kinetic behaviour is complex and the motion is related to a cycloid. The movement of a point at the outer radius of the motor is shown in fig. 7.9. As a result of the circular translation of the center, a point at the outer radius of the motor even moves in the opposite direction during short time intervals of a wobble cycle. This effect, which is also present in side driven wobble motors, is exaggerated in this figure by using a small gear ratio and may have consequences for certain applications of wobble motors.

7.2.6 Dynamic behaviour

The velocity of a point on the rotor can be found from the time derivative of the position. From this, the kinetic energy T of the rotor can be obtained:

$$T = \frac{\pi}{2}\rho\, h\, R_M^{\,2}\, R^2\, \dot{\alpha}^2 + \frac{\pi}{4}\,\frac{1}{n^2}\,\rho\, h\, R^4\, \dot{\alpha}^2 + \frac{\pi}{8}\left(\frac{n-1}{n}\right)^2 \rho\, h\, d^2\, R^2\, \dot{\alpha}^2 \tag{7.15}$$

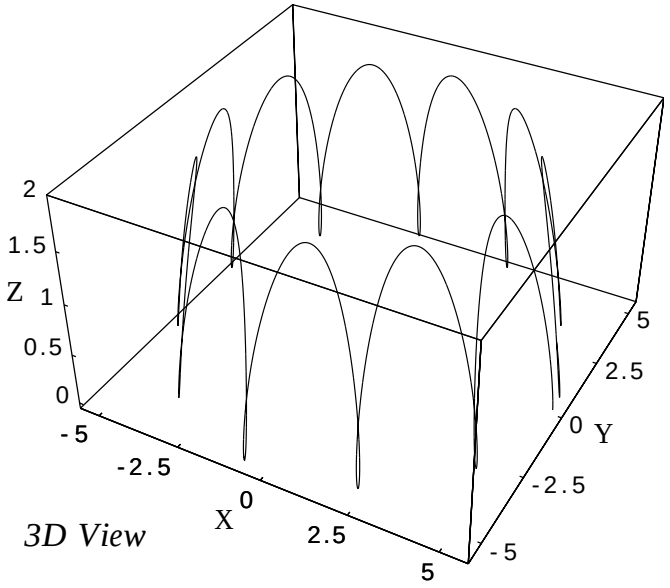

3D View

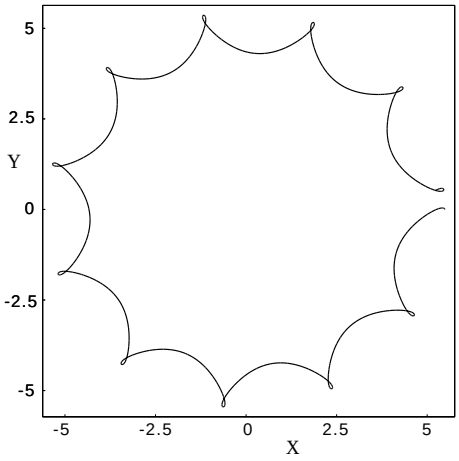

Top View

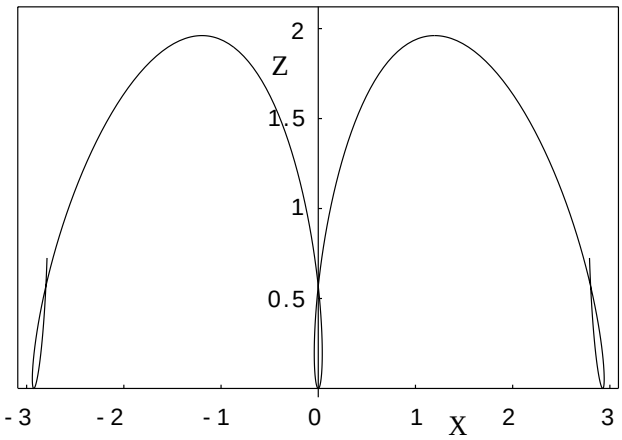

Side View

Fig. 7.9 *3D-, top- and side-view of the movement of a fixed point at the rotor outer radius in arbitrary units. A small gear ratio of about 11 has been used to clearly show the behaviour.*

The first term on the right is due to the motion of the center of the rotor. The second term is a result of the rotation of the rotor and the last term is caused by the rocking motion of the rotor. From Hamilton's principle [7.19], using the expressions for the electrostatic co-energy and kinetic energy as given in eqs. (7.4) and (7.15) respectively, the equation of motion for the rotor can be found. When additional terms are added to account for damping mechanisms this yields:

$$J\,\ddot{\alpha} + C_v\,\dot{\alpha} + \mathrm{sgn}\left(\dot{\alpha}\right)\left(C_{d1} + C_{d2}\,V^2\right) = \tau_{motive(\alpha)} \qquad (7.16)$$

where J is the rotational inertia of the rotor, related to the contact point angle, given by:

$$J = \pi\,\rho\,h\,R^2\left\{R_M{}^2 + \frac{R^2}{2\,n^2} + \left(\frac{n-1}{n}\right)^2\frac{d^2}{4}\right\} \qquad (7.17)$$

The rotational inertia of the rotor is mainly determined by its inertia about the rocking axes which is represented by the last term on the right hand side of eq. (7.17). The $\dot{\alpha}$ terms in eq. (7.16) have been added to include damping mechanisms. As proposed by Tai [7.20] and Bart [7.21] in case of side-driven micromotors, the next damping mechanisms have been used: C_v is the coefficient of viscous drag, C_{d1} is a constant coulombic friction term which results from constant normal forces like adhesion forces and gravity and C_{d2} is a voltage dependant coulombic friction term resulting from electrostatic normal forces as shown before and $\mathrm{sgn}(\dot{\alpha})$ is the sign function of angular velocity which is +1 if $\dot{\alpha} > 0$ and -1 if $\dot{\alpha} < 0$. For small oscillations around an equilibrium position, the differential equation (7.16) can be linearised. In that case the natural oscillating frequency of the rotor ω_N can be found from:

$$\omega_N = \sqrt{\frac{\left[\frac{d\tau}{d\alpha}\right]_{\alpha=0}}{J}} \qquad (7.18)$$

7.2.7 Viscous Damping

Because of the surrounding gas a damping torque will develop as a result of viscous drag. The viscous drag torque can be found by solving the Navier-Stokes equations. Because of the complex motion of the rotor this problem cannot be solved easily. Furthermore, realised rotor structures exhibit slots as a

result of the fabrication process. A 3-dimensional FEM fluid analysis of the problem is therefore required. To obtain an indication of the drag torque a strongly simplified approximation has been used. The rotor is assumed to be a thin rigid disk and the contributions due to the edges are ignored. The gas is treated as a continuous medium and is assumed to behave as a Newtonian fluid under laminar flow. The viscous drag forces are assumed to be mainly due to squeeze film damping in the small gap between the rotor and the stator surface as a result of the rocking motion of the rotor. With these assumptions the problem simplifies to a thin inclined rigid disk that is rotating over a horizontal surface where only the drag forces in the gap between the disk and the surface are considered. The rotational axis of the disk is perpendicular to the surface and the disk rotates with an angular speed equal to that of the contact point. The shear force dF_{shear} of a small part dA at the bottom of the disk is given by:

$$dF_{shear} = \frac{\mu\,\omega\,r}{g}\,dA \tag{7.19}$$

where μ is the viscosity of air and ω is the angular speed of the disk. This infinitesimal shear force results in a frictional torque $\tau_{viscous}$ that can be found by integrating $dF_{shear}.r$ over the rotor surface:

$$\tau_{viscous} = \int_0^R \int_0^{2\pi} \frac{\mu\,\omega\,r^3}{d\left(1 - \frac{r}{R}\cos\varphi\right)}\,dr\,d\varphi = \frac{4\,\pi\,\mu\,R^4\,\omega}{3\,d} \tag{7.20}$$

In case of a slider bearing a comparable approximation was found to be somewhat lower but accurate within a factor of two with a solution from the Navier-Stokes equations [7.22]. Therefore, the expression above is considered to be a reasonable estimate of the viscous drag torque on the rotor.

7.3 FABRICATION

Micromotor fabrication is based on a four mask process using polysilicon surface micromachining techniques which is schematically shown in fig. 7.10. The fabrication starts with a (100) p-type 3" silicon wafer. The first step is the deposition of a 1 μm thick stress reduced siliconnitride layer (Si_xN_y) by LPCVD

from a 70 sccm $SiCl_2H_2$ and a 18 sccm NH_3 flow at 850 ˚C and a pressure of 200 mTorr. The next step is the deposition of a 0.5 µm thick polysilicon layer, grown by LPCVD at a temperature of 590 ˚C, a pressure of 250 mTorr and a silane flow of 50 sccm. This polysilicon layer is heavily doped with boron by solid source drive-in diffusion for one hour at 1150 ˚C. This yields a sheet resistance of about 70 Ω/□. After boron diffusion the BSG layer is stripped in a buffered HF-solution. After patterning the doped polysilicon layer forms the stator poles (fig. 7.10 a).

Again a 0.5 µm thick stress reduced LPCVD silicon nitride layer is deposited that serves as an insulator between the stator and rotor. Contact windows are opened in this Si_xN_y layer by RIE in a CHF_3/O_2 gas mixture in order to make contact with the stator poles later on (fig. 7.10 b).

Now a 2 µm SiO_2 layer is grown by PECVD from a SiH_4/N_2O gas mixture at 300 ˚C, a pressure of 650 mTorr and RF power of 60 Watt (fig. 7.10 c). This layer defines the gap between the rotor and stator. The ball bearing is now formed by one lithography step and dry etching of the SiO_2, the Si_xN_y sandwich layer and dry isotropic underetching of the silicon wafer. This is done by RIE the SiO_2 layer using CHF_3 at a pressure of 20 mTorr and a RF power of 50 Watt and the Si_xN_y layer by RIE using a CHF_3/O_2 gas mixture at a pressure of 10 mTorr and a RF power of 75 Watt. The resist layer is removed by O_2 plasma ashing and the silicon is underetched by dry isotropic etching in a SF_6/N_2 gas mixture at 100 mTorr and 50 Watt (fig. 7.10 d). Next a 1 µm thick SiO_2 layer is deposited by LPCVD from TEOS at 700 ˚C and a pressure of 400 mTorr (fig. 7.10e). The bearing clearance is defined by this layer.

Now the rotor is constructed. This starts with the deposition of a 2 µm thick LPCVD polySi layer that is also doped by diffusion as previously described. The anneal step also reduces the residual stress of the polySi layer. After stripping the BSG layer in BHF a sheet resistivity of about 6 Ω/□ is obtained. The cross section of a ball bearing like groove at this point is shown in fig. 11.

The motor operation requires a rigid rotor design with respect to vertical deflections in order to prevent rotor deformation by axial electrostatic forces and stiction problems between the rotor and stator surface. In order to increase the stiffness of the rotor a 6 µm thick amourphous silicon layer is deposited by sputtering in Ar. This layer is annealed in a N_2 atmosphere at 450 ˚C for 1 hour to reduce residual stress [7.23]. A 0.6 µm thick PECVD silicon oxide layer is deposited that serves as an etch mask for the silicon sandwich layer. After patterning the silicon oxide by RIE using CHF_3 gas, the polysilicon is anisotropically etched using a SF_6, O_2, CHF_3 gas mixture (fig. 7.10f) [7.24].

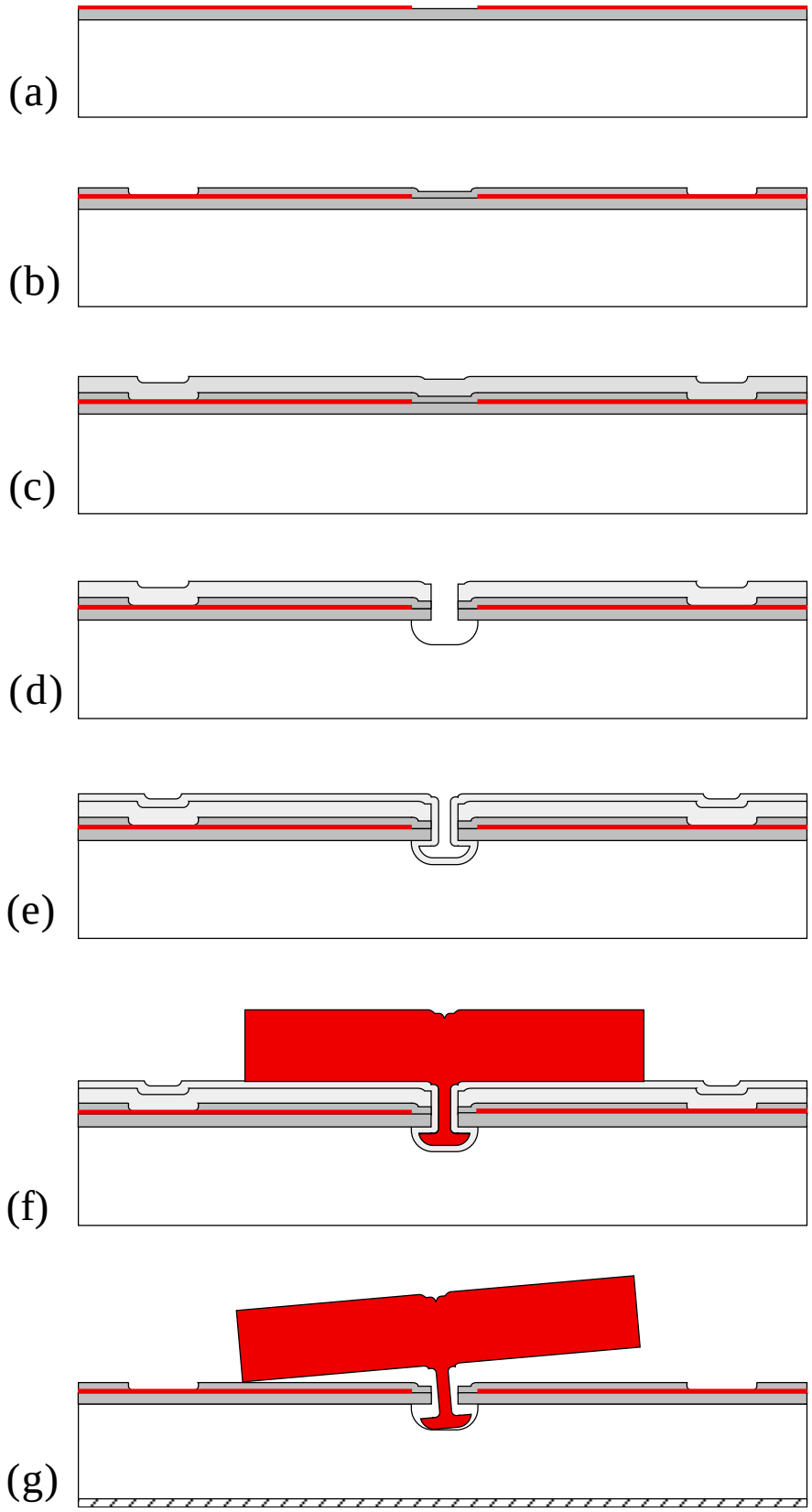

Fig. 7.10 *Processing sequence of the wobble motor. More details are given in the text. (a) LPCVD of SiN, LPCVD and etching of polySi, (b), LPCVD of SiN and contact window etching (c), PECVD of SiO_2 (d), RIE of SiO_2 and SiN and plasma etching of silicon wafer (e), LPCVD of SiO_2 (f), LPCVD of polySi, sputtering of Si and anisotropic etching (g) Sacrificial layer etching and backside metallization.*

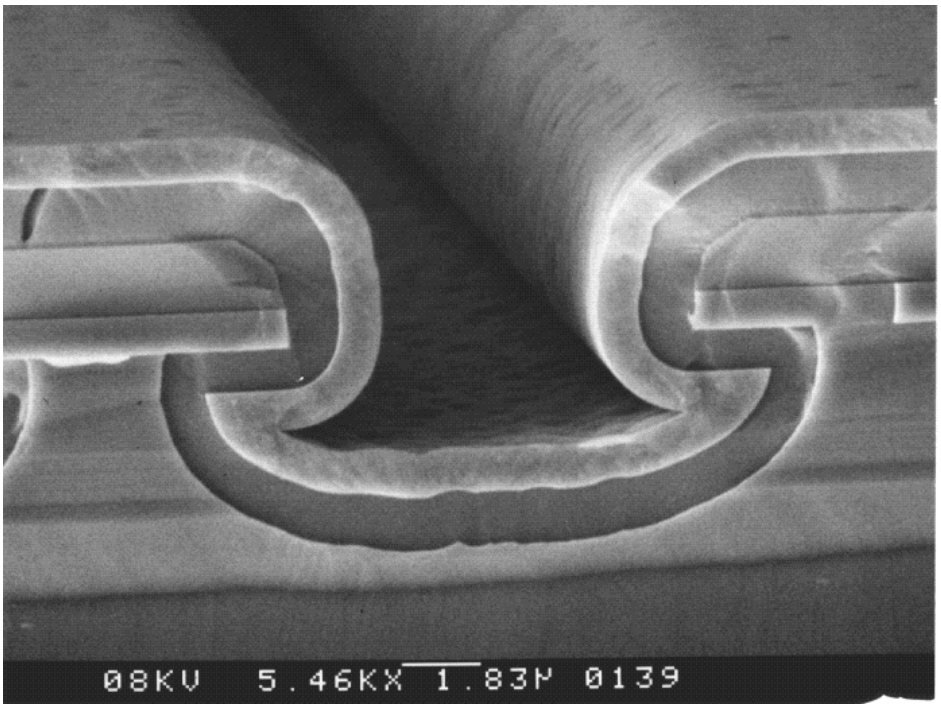

Fig. 7.11 *SEM photograph the cross section of a ball bearing like groove. The good step coverage of the TEOS silicon dioxide- and polysilicon layer is clearly visible.*

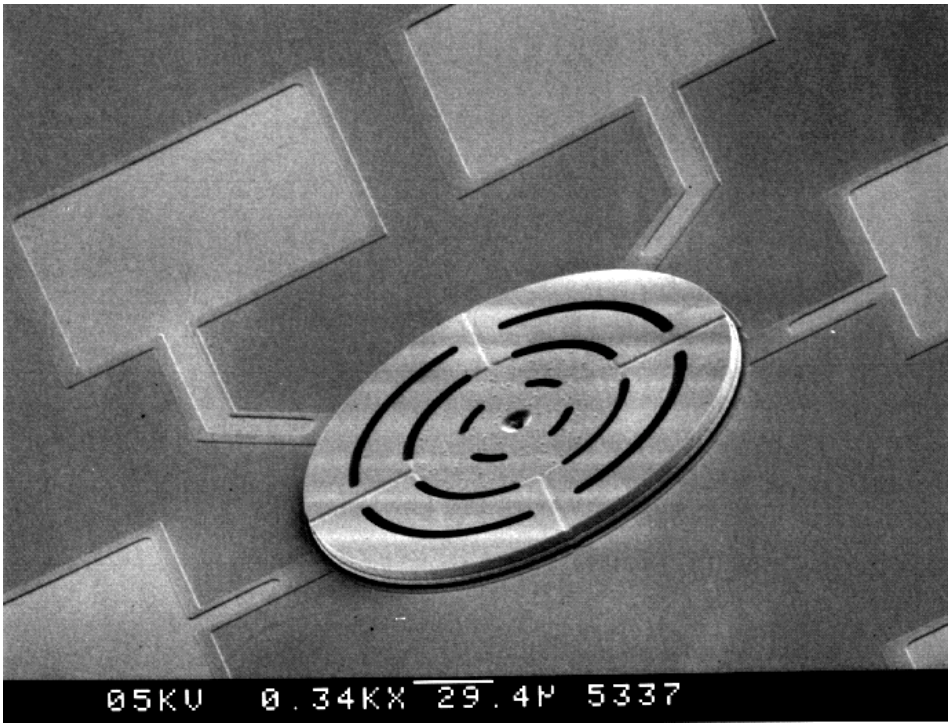

Fig. 7.12 *SEM photograph of an electrostatic axial gap wobble motor with four stator poles. The rotor diameter is 200 μm and rotor thickness is 8 μm.*

The accumulated layers at the backside are stripped by dry etching, followed by a standard cleaning procedure. The sacrificial layers are etched in an HF (50%) solution for 37.5 min., DI rinsed and spin dried. The last step is the evaporation of a 1 µm Al backside metallization layer (fig. 7.10g). The final result is shown in fig. 7.12.

A suitable center pin bearing for the rotor is the flange bearing design [7.25]. This, however, requires lithography over the patterned rotor structure. In order to prevent problems with photoresist step coverage a ball bearing design has been used. The ball bearing is, however, not self-aligned like the flange bearing design. But alignment within 1 µm should be possible and is not considered to affect the motor performance strongly. At this point no experimental or theoretical optimisation in order to minimise the rotor thickness has been done. For sufficiently thin rotors or good photoresist step coverage a flange bearing design for these type of motors can also be realised. Note that the ball bearing design can also be realised with LIGA or other moulding and electroplating techniques.

7.4 EXPERIMENTAL

In order to verify micromotor static and dynamic models, it is necessary to measure the torque and rotor transient response as it moves from one stator pole to the next. Unfortunately, measurement of the generated torque and detailed experimental measurement of rotor step transient is difficult for wobble micromotors, since torque measurements require mechanical power transmission and the rotor displacement associated with a step transient is very small. Instead the characteristic gear ratio of a wobble motor can be easily measured [7.25-7.29]. The gear ratio of a wobble motor is defined as the ratio of the electrical excitation frequency to the rotor rotational frequency. Starting and stopping voltages can also be determined from which frictional torque's can be extracted. Starting voltages are measured by increasing the driving voltage and observing at what voltage a motor starts to rotate. Similarly, the stopping voltages are measured by decreasing the driving voltage and observing at what voltage the motor operation fails. The motor lifetime was defined as the time to failure in which a motor could be operated at a fixed driving voltage.

To operate the electrostatic motors a programmable power supply which controls the driving schemes has been realised. The driving frequency of the

square wave signal of four independent output phases can be varied between 15 Hz and 10 kHz using the internal clock generator. Higher driving frequencies can be obtained by using an external clock generator. The amplitude of the driving voltage can be set between 0 and 100 V. The power supply is connected to the bonding pads of the stator poles using a probe station. The movements of the motor are recorded using a microscopic set-up that includes a camera and video recorder. Rotational speeds can easily be determined by video replay, from which the gear ratio is calculated. Single pole excitation schemes have been used in the measurements unless otherwise stated. Stator designs with a larger number of poles than the number of power supply phases are driven by symmetrically skipping the additional stator poles. Measurements have been performed in air under semi-cleanroom conditions after storage periods of up to several months.

7.5 RESULTS AND DISCUSSION

Table 7.1 shows measured starting and stopping voltages for motors with radii of 100 and 50 µm and four stator poles using a single-pole open-loop excitation at a frequency of 100 Hz. The effect of the driving frequency, the driving voltage and operating time on the gear ratio of the wobble motors has been measured. The results are shown in figs. 7.13 to 7.15. Experimentally determined gear ratios varied between 130 and 200 for the 50 µm rotor radius designs, and between 600 and 1000 for the 100 µm rotor radius designs. The large variation is due to the high sensitivity of the gear ratio to variations in the rotor radius as a result of underetching, to variations in the gap spacing and to changes in the bearing height because of etch and thin film non-uniformities.

7.5.1 Starting and stopping voltages

The static and dynamic frictional torque of the motor can be derived from the measured starting and stopping voltages (see table 7.1). The gap spacing of these samples was measured to be 2.3 µm, and the thickness of the silicon nitride layer was 0.46 µm. The motor will stop when the frictional torque equals the generated torque. The smallest torque will occur at the transition point of the individually excited stator poles. For the four stator pole design this transition point is located at approximately -0.2 radians from the angular center of the stator poles. From this the static friction is calculated to be equal to

Sample #	Radius [μm]	Starting Voltage [V]	Stopping Voltage [V]
1	100	6.0	4.4
2	100	8.1	5.9
3	100	8.1	5.1
4	100	7.4	5.6
5	50	13.1	10
6	50	21.9	18.5
7	50	16.7	12.0
8	50	19.9	15.5

Tabel 7.1 *Measured starting and stopping voltages of several motors with a four pole stator design and rotor diameters of 50 and 100 μm. A single-pole open-loop excitation with a square-wave voltage signal at 100 Hz was used.*

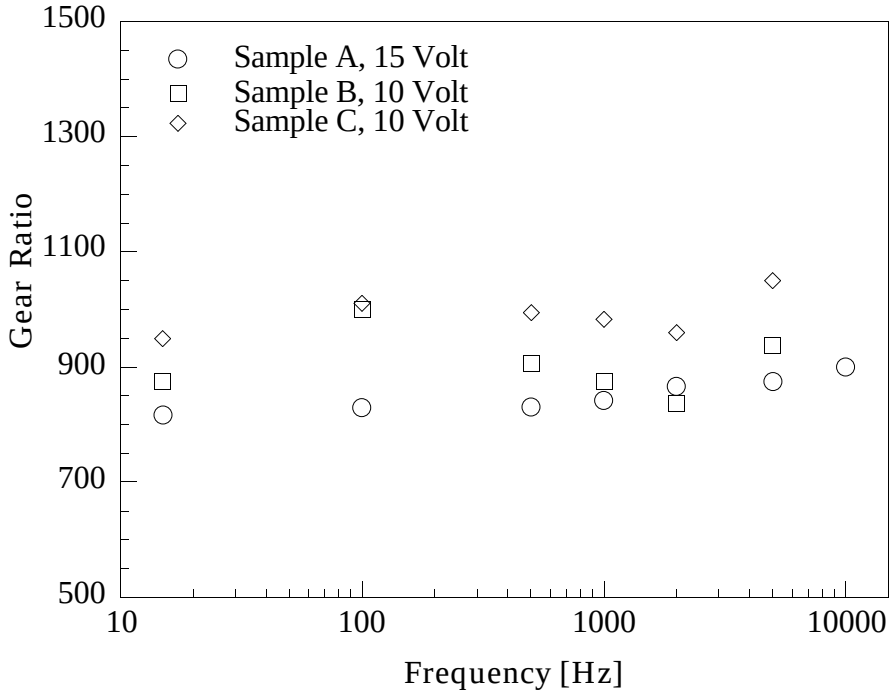

Fig. 7.13 *Gear ratio as a function of the excitation frequency, measured for three different micromotors.*

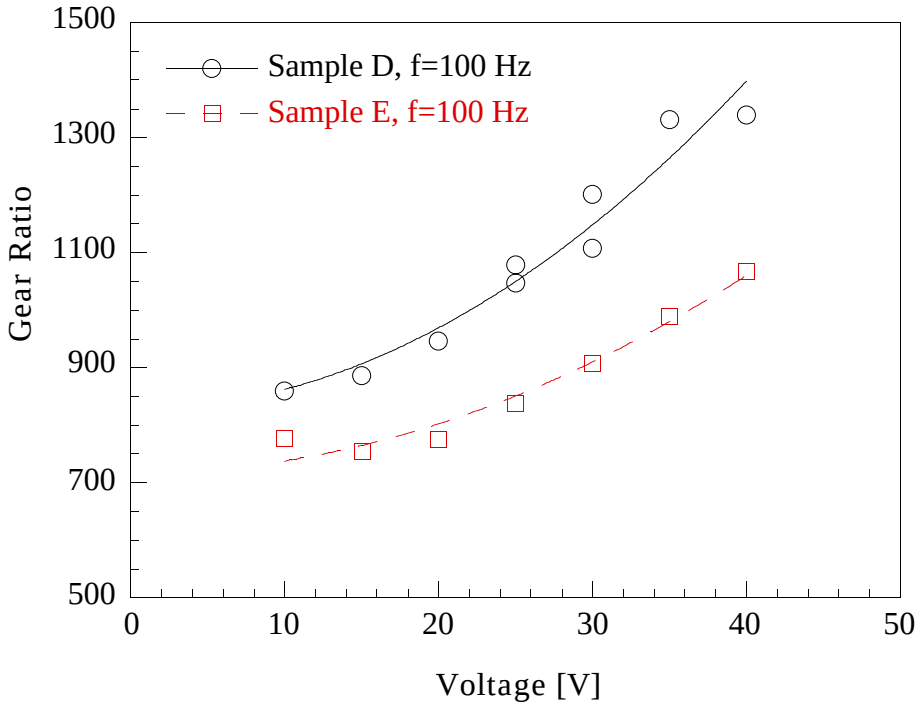

Fig. 7.14 *Measured gear ratio as a function of the driving voltage for two samples. Data has been fitted by the formula given in eq. (7.21).*

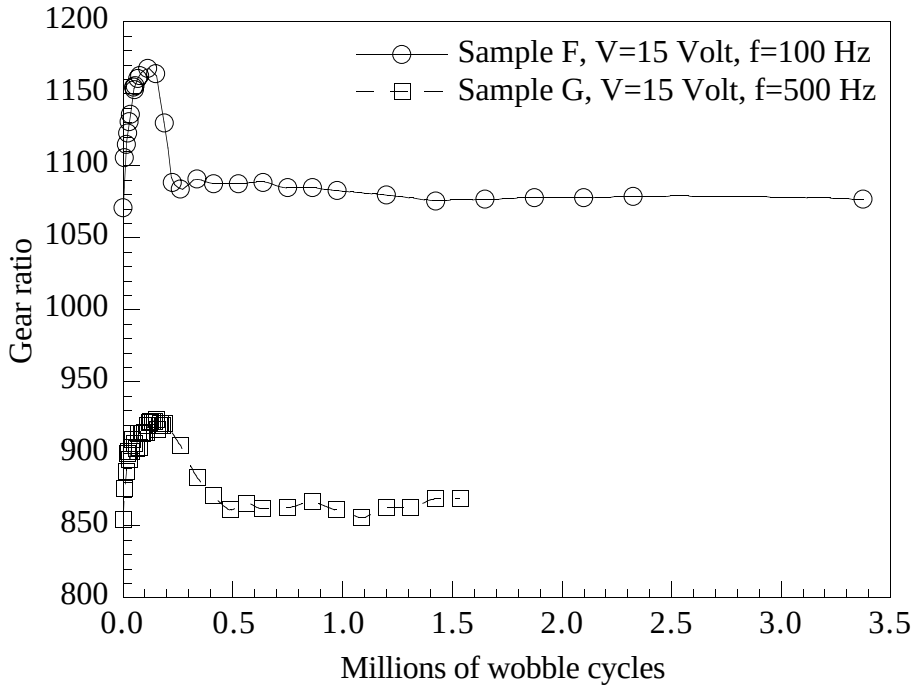

Fig. 7.15 *Gear ratio versus operation time in millions of wobble cycles for two motors. Both motors have been operated at 15 Volts with a driving frequency of 500 Hz and 100 Hz for respectively sample F and G. Total operation time until motor failure was 3.5 hours for sample F and 6.5 hours for sample G.*

0.71 and 0.48 pNm for the four stator pole motors, with rotor radii of respectively 50 and 100 micron. In the same way the average torque to overcome the dynamic friction is equal to 0.43 and 0.25 pNm for the small and large four stator pole motors respectively. The larger motors have smaller frictional torque's in contrast to their larger dimensions. This is a somewhat unexpected result. A possible reason may be the larger rocking angle of the small motors that leads to more friction at the ball bearing. The individual frictional forces at the contact point and the bearing of the rotors cannot, therefore, be extracted from these measurements. Rotor designs with identical rotor diameters but different bearings radii are expected to be more suited for extracting the frictional forces at the contact point and the bearing. The measured frictional torques are somewhat lower compared to their side-driven counterpart [7.25].

7.5.2 Frequency dependency of the gear ratio

The gear ratio as a function of the driving frequency has been measured for three different motors and is shown in fig. 7.13. Measurements have been performed up to a driving frequency of 10 kHz which is the maximum frequency of the internal clock generator in our power supply. At 10 kHz the angular speed of four pole stator motor designswith a radius of 100 μm is equal to about 150 rpm. Furthermore, gear ratios at higher frequencies are difficult to determine by our video system. In this case a stroboscope has to be implemented in our experimental set-up.

Some change in the gear ratio of the motors is present when the driving frequency is varied. However the behaviour is not the same for the different motors and the variations show little correlation with the driving frequency. The overall picture seems to be that the gear ratio is more or less independent of the driving frequency up to a frequency of 10 kHz.

7.5.3 Voltage dependency of the gear ratio

The voltage dependency of the gear ratio is shown in fig. 7.14. The gear ratio increases with increasing driving voltage. This behaviour is opposite to the behaviour of side driven wobble motors where the gear ratio decreases with increasing driving voltage as a result of a reduction in slip. It was observed that the gear ratio decreased somewhat when, instead of a double pole excitation, a single pole excitation scheme was used. As rotor slip leads to an increase in the gear ratio and double pole excitation will always operate at large normal forces

which exclude rotor slip, another effect must be responsible. Furthermore, our model predicts that the motors will normally operate under no-slip conditions. It is suggested that the axial electrostatic field will result in a deformation of the rotor structure. As illustrated in fig. 7.16 this will result in a small decrease of the contact point radius which results in an increase of the gear ratio. Motors that are excited over a larger region will exhibit a larger deformation explaining the increase in gear ratio when double pole excitation is used.

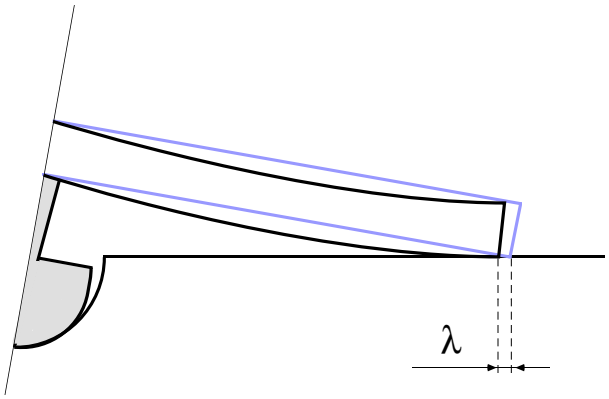

Fig. 7.16 *Sketch of rotor deformation by axial electrostatic forces. The rotor deformation results in a decrease of the contact point radius.*

The axial electrostatic forces are quadratically dependent on the applied voltage. Therefore the measured dependency has been fitted by the following equation:

$$n = n_0 + \gamma V^2 \qquad (7.21)$$

As shown in fig. 7.14 the experimental data can be fitted well by this equation. A change in gear ratio from 800 to 1500 is related to a change in the contact point radius of only 0.05 %. Additional measurements on rotors with different stiffnesses or coupled electromechanical simulations of the rotor deformation are necessary to verify our suggestion.

7.5.4 Time dependence of the gear ratio

The gear ratio-to-operation time dependency of two motors is shown in fig. 7.15. The gear ratio first increases, then decreases and then remains constant with increasing operation time until motor failure occurs. The initial increase and subsequent decrease in the gear ratio with operation time is expected to result from wear at the ball bearing and the surfaces at the contact circle and is caused by a run-in period. At the end of this period when the surface asperities

have worn off, the gear ratio remains constant till it stops rotating at the set voltage. The change in gear ratio, as a result of wear, can be expressed by:

$$n \approx n_0 \left[1 + \frac{2\, h_b\, \Delta h_b}{d^2 - 2\, d\, h_b} - \frac{2\left(h_b - d\right) \Delta d}{d^2 - 2\, d\, h_b} \right] \qquad (7.22)$$

where Δh_b is the change in bearing length as a result of wear and Δd is the wear between the stator surface and the rotor surface at the contact point. Wear at the ball bearing will result in a reduction of the bearing length Δh_b and a subsequent change in the axial gap distance. From eq. (7.22) it can be seen that this will lead to an increase of the gear ratio. Wear at the contact point circle, from surface roughness asperities at the bottom of the rotor and the stator surface, will result in an increase of the gap spacing with Δd. This results in a decrease of the gear ratio.

The time to motor failure showed large variations for the two process runs that have been done up to now and ranged from several ten thousands up to several millions of wobble cycles for different samples. As in side-driven wobble motors motor failure may be caused by wear particles [7.29]. At this point no SEM inspection of operated motors has been done. More work on wear is needed and other bearing designs, as well as other bearing materials, may lead to extended motor lifetime.

7.5.5 Dynamic behaviour

Measurements on the transient response of the rotor have not been performed. However, from measured and estimated parameters a theoretical prediction of the transient response can be given by using the equation of motion given in eq. (7.16). The rotational inertia for a rotor with a radius of 100 µm is calculated using eq. (7.17) from which a value of 8×10^{-22} kgm^2 is obtained. For an air viscosity of 1.83×10^{-5} kg/ms, the viscous damping constant C_v is estimated by eq. (7.20) to be about 3×10^{-15} Nms. Measurements on side driven wobble motors showed that coulombic friction is dominated by the voltage dependant term (i.e. $C_{d1} \ll C_{d2}$ V^2). From the measured dynamic frictional torque the value of C_{d2} is calculated to be 9×10^{-15} Nm/V^2 for the micromotors with a radius of 100 µm. The generated torque can be calculated for a given driving voltage from eq. (7.11). For ease of numerical computation, the function $\pi/2 \arctan(\alpha/10^{-4})$ has been used in place of $\mathrm{sgn}(\alpha)$. The transient

response of a four stator pole motor in case of a single-pole excitation is shown in fig. 7.17.

The response time is strongly dependent on the driving voltage. Because of coulombic friction the rotor does not reach the zero torque position of the excited stator pole but stops at an angle that is dependent on the driving torque. For decreasing driving voltages this stopping angle approaches about -0.2 radians as discussed before in the section on starting and stopping voltages.

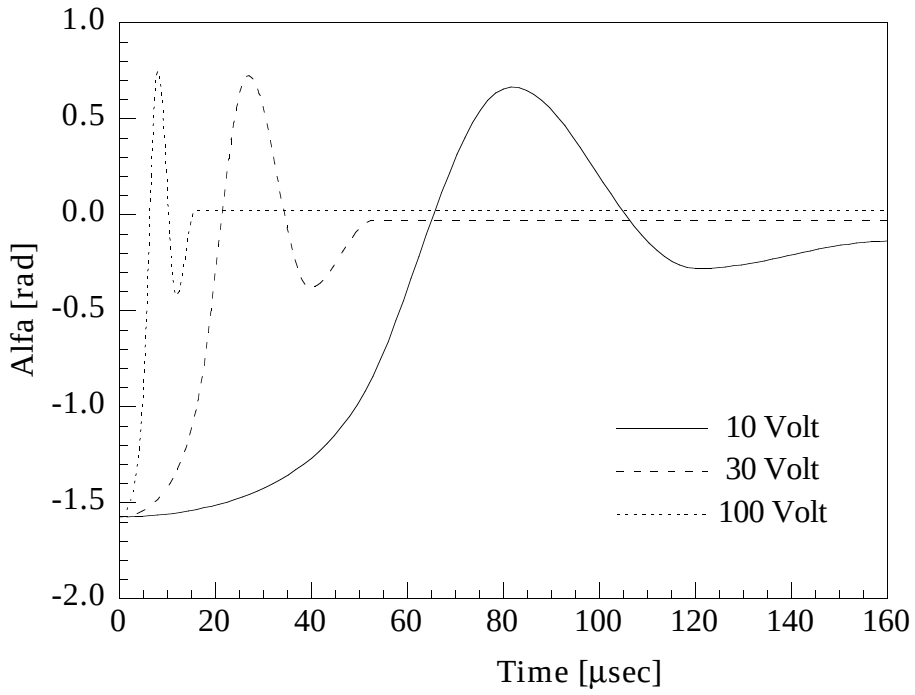

Fig. 7.17 *Transient response of a four stator pole design with single pole excitation for a driving voltage of 10, 30 and 100 Volts. Starting angle is -π/2 radians. R = 100 µm, R_i = 50 µm, R_o = 100 µm, d = 2.3 µm, d_{ins} = 0.46 µm, ε_r = 7.5, φ_1 = -π/4 rad, φ_2 = π/4 rad, J = 2.0×10^{-21} kgm/s^2, C_v = 4.1×10^{-18} Nms, C_{d1} = 0 Nm and C_{d2} = 9×10^{-15} Nm/V^2.*

7.6 CONCLUSIONS

The design and fabrication of an electrostatically driven lower-stator axial-gap wobble motor has been presented. In contrast to side drive motors, the stator poles are located underneath the rotor instead of surrounding the rotor sides. This results in a higher torque generation and easily accessible rotor structures that are suited to mechanical power transmission to other structures that can be fabricated on the same chip.

Based on small tilt angles, a rigid disk rotor and simplified electrostatic fields, a theoretical model describing the static and dynamic behaviour of the motor has been given. The torque generation is in the range of nNm at high electrostatic fields. The torque coverage for different excitation schemes in the case of both open-loop excitation and closed-loop excitation, which requires position feedback, is discussed. Because of large normal forces, generated by the axial electrostatic field, the motors can be easily operated in no-slip conditions at all times. The kinetic behaviour is complex and related to a cycloid. A fixed point at the rotor even moves opposite to the rotational direction of the rotor during small time intervals of a wobble cycle. This may have consequences for certain applications. Based on side-driven micromotor results an equation of motion for the rotor has been derived that includes rotational rotor inertia, viscous drag and coulombic frictional terms. The rotational inertia of the rotor is mainly determined by its inertia around the rocking axes.

Fabrication is based on a four mask process using polysilicon surface micromachining techniques. Silicon nitride has been used for electrical insulation between the rotor and stator poles and silicon oxides were used as sacrificial layers that have been removed in an HF solution. The rotor and stator poles have been constructed from doped polysilicon. In order to increase the stiffness of the rotor, it is made from polysilicon and a thick sputtered amorphous silicon film. A new ball bearing design, which is not self-aligned, has been used for the rotor in order to avoid photoresist step coverage problems.

Motors have been successfully operated at driving voltages of a few Volts. Motor performance has been characterised by measuring the gear ratio and start and stop voltage measurements using single pole, open-loop excitations with square-wave voltage signals. Although some variation in gear data has been observed for different motors, the gear ratio seems to be independent of the driving frequency up to a maximum measured frequency of 10 kHz. The gear ratio was found to be strongly dependent on the driving voltage. It is suggested that this is caused by the mechanical deformation of the rotor that results from the axial electrostatic forces. The gear ratio was also found to be dependent on operation time showing an initial increase and decrease of the gear ratio after which it remained constant until motor failure. This behaviour is suggested to result from wear at the ball bearing and the surfaces at the contact point circle. Motor lifetimes varied between a few ten thousand wobble cycles to some millions of wobble cycles for two different process runs. This resembles operation times ranging from a few minutes to several hours at

rotor speeds between a few and several hundred rpm. A theoretical prediction of the transient response of the motor has been given using measured and estimated calculated parameters in the equation of motion.

The presented theoretical and experimental results can be used as a framework for further development of axial-gap micromotors. Wear and motor lifetime should be especially investigated as well as other bearing designs and bearing materials in order to improve motor performance.

REFERENCES

[7.1] W.S.N. Trimmer, K.J. Gabriel and R. Mahadevan, Silicon electrostatic motors, Proc. 4th Int. Conf. on Solid-State Sensors and Actuators, Tokyo, Japan, June 2-5, 1987, pp. 857-860.

[7.2] J. H. Lang, M. F. Schlecht and R. T. Howe, Electric micromotors: electromechanical characteristics, IEEE Micro Robots and Teleoperators Workshop, Hyannis, Masschusetts, Nov. 9-11, 1987.

[7.3] S. F. Bart, T. A. Lober, R. T. Howe, J. H. Lang and M. F. Schlecht, Design considerations for microfabricated electric actuators, Sensors and Actuators, 14, 1988, pp. 269-292.

[7.4] T. A. Lober and R. T. Howe, Surface micromachining processes for electrostatic microactuator fabrication, Proc. IEEE Solid-State Sensor and Actuator Workshop, Hilton Head Island, SC, U.S.A. June 6-9, 1988, pp. 59-62.

[7.5] M. Mehregany and Y.C. Tai, Surface micromachined mechanisms and micromotors, J. Micromech. Microeng., 1, 1991, pp. 73-85.

[7.6] IC-processed electrostatic micromotors, L.F. Fan, Y.C. Tai and R.S. Muller, Sensors & Actuators, 20, 1989, pp. 41-47.

[7.7] M. Mehregany, S.D. Senturia, J.H. Lang and P. Nagarkar, Micromotor fabrication, IEEE Transactions on electron devices, 39, 1992, pp. 2060-2069.

[7.8] L.S. Tavrow, S.F. Bart and J.H. Lang, Operational characteristics of microfabricated electric micromotors, Sensors & Actuators, A35, 1992, pp.33-44.

[7.9] T. Furuhata, T. Hirano, L. H. Lane, R. E. Fontana, L. S. Fan and H. Fujita, Outer rotor surface-micromachined wobble motor, Proc. IEEE Micro Electro Mechanical Systems, Fort Lauderdale, Fl, U. S. A., February 7-10, 1993, pp. 161-166.

[7.10] K. Deng and M. Mehregany, Outer-rotor polysilicon wobble motors, Proc. IEEE MEMS, Oiso, Japan, January 25-28, 1994, pp. 269-272.

[7.11] W. Trimmer and R. Jebens, Harmonic electrostatic motors, Sensors and actuators, 20 (1989), pp. 17-24.

[7.12] S.C. Jacobsen, R.H. Price, J.E. Wood, T.H. Rytting and M. Rafaelof, A design overview of an eccentric-motion electrostatic microactuator, Sensors and actuators, 20 (1989), pp. 1-16.

[7.13] Operation of microfabricated harmonic and ordinary side-drive motors, M. Mehregany, P. Nagarkar, S. D. Senturia and J. H. Lang, IEEE?

[7.14] L. Paratte and N.F. de Rooij, A rigid ring electrostatic harmonic wobble motor with axial field, Proc. 6th Int. Conf. Solid-State Sensors and Actuators (Transducers '91), San Fransisco, CA, USA, June 24-27, pp. 890-893.

[7.15] L. Paratte and N.F. de Rooij, A rigid ring electrostatic harmonic wobble motor with axial field, Proc. 7th International Conference on Solid-State Sensors and Actuators, Abstracts of late news papers, Transducers '93, Yokohama, Japan, June 7-10, 1993, pp. 4-5.

[7.16] L. Paratte and N. F. de Rooij, Electrodeposited electrostatic rigid-rotor wobble motors on silicon, Sensors and Actuators, A43, 1994, pp. 371-377.

[7.17] L. Paratte, H. Lorenz, R. Luthier and N.F. de Rooy, Miniature gear reduction unit driven by a silicon electrostatic wobble motor, J.Micromech. Microeng., 2 (1992), pp. 221-223.

[7.18] Ph. Lerch, B. Romanowiwicz, L. Paratte, N. F. de Rooij and Ph. Renaud, Numerical simulations of planar wobble motors, Sensors and Actuators, A 46-47, 1995, pp. 640-644.

[7.19] I.H. Shames and C.L. Dym, Energy and finite element methods in structural mechanics, McGraw-Hill, New York, 1985.

[7.20] Y. C. Tai and R. S. Muller, Frictional study of IC-processed micromotors, Sensors and Actuators, A21, 1990, pp. 180-183.

[7.21] S.F. Bart, M. Mehregany, L.S. Tavrow, J.H. Lang and S.D. Senturia, Electric micromotor dynamics, IEEE Trans. Electron Devices, ED-39, 1992, pp. 566-575.

[7.22] F.S. Sherman, Viscous Flow, McGraw-Hill, 1990.

[7.23] M.J. van der Reijden, Characterization of RF-sputtered silicon for application in micromechanics, Master's Thesis, University of Twente, 1995.

[7.24] R. Legtenberg, H. Jansen, M. de Boer and M. Elwenspoek, Anisotropic resctive ion etching of silicon using $SF_6/O_2/CHF_3$ gas mixtures, J. Electrochem. Soc., 142, 1995, pp. 2020-2028.

[7.25] V. R. Dhuler, M. Mehregany and S. M. Phillips, A comparative study of bearing designs and operational environments for harmonic side-drive micromotors, IEEE Trans. on El. Dev., Vol. 40, No. 11, 1993, pp. 1985-1989.

[7.26] M. Mehregany, S. M. Philips, E. T. Hsu and J. H. Lang, Operation of harmonic side-drive micromotors studied through gear ratio measurements, Proc. 6th Int. Conf. Solid-State Sensors and Actuators (Transducers '91), San Fransisco, CA, USA, June 24-27, pp. 59-62.

[7.27] S. M. Phillips and M. Mehregany, Effect of rotor slip on the gear ratio of harmonic side-drive micromotors, Sensors and Actuators, A36, 1993, pp. 249-254.

[7.28] V. R. Dhuler, M. Mehregany and S. M. Phillips, An experimental technique and a model for studying the operation of harmonic side-drive motors, IEEE Trans. on El. Dev., Vol. 40, No. 11, 1993, pp. 1977-1984.

[7.29] M. Mehregany, S.D. Senturia and J.H. Lang, Friction and wear in microfabricated harmonic side-drive motors, Proc. IEEE Solid-State Sensor and Actuator Workshop, Hilton Head Island, SC, U.S.A. June 4-7, 1990, pp. 17-22.

Chapter Eight

ELECTROSTATIC MICROACTUATORS WITH INTEGRATED GEAR LINKAGES FOR MECHANICAL POWER TRANSMISSION*

In this chapter a surface micromachining process is presented which has been used to fabricate electrostatic microactuators that are interconnected with eachother and linked to other movable microstructures by integrated gear linkages. The gear linkages consist of rotational and linear gear structures and the electrostatic microactuators include curved electrode actuators, comb drive actuators and axial gap wobble motors. The micromechanical structures are constructed from polysilicon. Silicon dioxide was used as a sacrificial layer and silicon nitride was used for electrical insulation. A cyclohexane freeze drying technique was used to prevent problems with stiction. The actuators, loaded with various mechanisms, were successfully driven by electrostatic actuation. The work is a first step towards mechanical power transmission in micromechanical systems.

8.0 INTRODUCTION

With improving performance and fabrication techniques, micromechanical actuators are merging into the field of mechanical power transmission for driving purposes. It has been previously shown that multi-level linkages can be fabricated by dissolved wafer, bond and assembly techniques [8.1]. Two silicon wafers are successively processed, aligned and bonded to a glass wafer, and then dissolved in EDP to free micromechanical mechanisms. Other examples of assembled devices that transfer mechanical power are magnetic micromotors where Permalloy and PMMA parts are fabricated with sacrificial LIGA techniques which are subsequently assembled with submicron tolerances [8.2]. Axial gap wobble motor have also been fabricated from electroplated nickel rotors that were coupled to miniature pinion and gear trains using assembling techniques [8.3].

Devices where mechanical linkages have been integrated with actuator

* presented at the IEEE Micro Electro Mechanical Systems Workshop, San Diego, CA, U.S.A., Feb. 12-15, 1996, pp. 204-209.

fabrication are vibromotors, where a slider is driven by oblique impact of resonant comb structures [8.4], and a comb-drive based microengine where the linear motion of comb structures is converted into a rotary motion of an output gear by connecting rods [8.5]. These latter processes have the advantage of batch fabrication without the need for assembly of multiple wafers requiring alignments, bonding etc., or the addition of other separately fabricated parts.

In this paper a fabrication process is presented where different types of surface micromachined electrostatic actuators are fabricated in one process. These are interconnected and linked to other microstructures using gear mechanisms without the need for assembling techniques. In our previous work several electrostatic actuators that can generate relatively large forces, torques and displacements have been developed and fabricated using surface micromachining techniques. Examples are bi-stable curved electrode actuators [8.6], linear comb drive actuators [8.7] and axial gap wobble motors [8.8]. Mechanisms include gear trains, linear gear racks, sliders and spring structures. First experimental results have shown operational actuators and functional micromechanisms. For example electrically powered micromotors drive gear trains and gear racks. In the latter case a transformation of rotational into linear motion is obtained.

The fabrication process can be used to study and optimise properties of micromechanical gear mechanisms and measure output force or torque of electrostatic actuators. Examples are devices for measurements on static and dynamic friction of gear linkages and measurement of micromotor output torque.

8.1 DESIGN ISSUES

8.1.1 General design issues

Since the fabrication of the comb drive actuators and curved electrode actuators is relatively simple and can be done in a one mask fabrication process, [8.6, 8.7] this process has been merged into the fabrication process of the axial gap wobble motor [8.8]. The micromechanical structures are constructed from polysilicon. Silicon dioxide has been used as a sacrificial layer and silicon nitride was used for electrical insulation. A cyclohexane freeze drying technique is used to prevent problems with stiction.

The operation principle of a lower stator axial gap wobble motor is based on

an inclined rotor that is supported at its center and rolling on its outer radius. Excitation of stator poles results in an axial rocking motion of the rotor. This rocking motion is transformed into a rotational motion because of a small difference in the radius of the rotor and its resultant contact point circle at the stator poles. In contrast to polysilicon side drive motors, where stator poles are surrounding the rotor, the stator poles of the axial gap wobble motor are located underneath the rotor. This results in a large torque generation because of a large rotor to stator overlap and a readily accessible rotor for mechanical power take off. For a more detailed description of the axial gap wobble motors reference is made to [8.8].

Because the rotor of the axial-gap wobble motor makes an axial rocking motion and is rolling on its outer radius, some adjustments are necessary when external gear teeth are added. By an additional etch step a circular reduction is created in the rotor structure. Now, the rotor will roll on this circular reduction and can have an arbitrary outline. The rotor and gears can rotate and rock in axial directions using a ball bearing while for linear movements a slider bearing was applied using slots that are etched into the silicon wafer. The motor rocking motion places a constraint on the thickness of the gears and therefore the gear thickness should be larger than two times the thickness of the sacrificial layer below it. In our fabrication process a sacrificial layer thickness of about 2 μm and a gear thickness of about 6 μm was used.

8.1.2 Tooth design

Gears are an efficient way to transmit mechanical power at almost any speed ratio desired. Parallel axis gears transmit power with greater efficiency than any other form of gearing. The most common type of gear is the spur gear which has teeth on the outside of a cylinder which are parallel to the cylinder axis. This type of gear can be fabricated relatively easy using anisotropic etching techniques.

A conjugate tooth shape is needed in order to transform motion with constant angular velocity. Involute and cycloidal tooth shapes are conjugate tooth profiles. However, cycloid gearing requires center distances to be maintained in order to obtain conjugate action, where involute profiles maintain conjugate action even with variations in gear center distances [8.9].

The gear ratio is a constant and can be found from the ratio of gear teeth numbers. It can be applied to all types of gears with conjugate and non-conjugate gear tooth surfaces and corresponds to the ratio between the gear

revolutions. Only in cases of conjugate tooth profiles is the velocity ratio equal to the gear ratio. If not, the gears transform rotation with a varying instantaneous velocity ratio.

In this first approach no optimisation has been done on gear design. Because of limitations in our present mask layout program and pattern generator, gear teeth with a trapezoidal shape have been used. This will negatively affect the performance of our gears. However, at this stage the main goal is the development of a fabrication process for integrated electrostatic actuators and gear linkages; and to demonstrate the feasibility of these micromechanical gear linkages in order to transfer mechanical power.

In our design two different gears have been used. The largest gear has 36 teeth and a base radius of 100 µm which also forms the rotor of electrostatic axial gap wobble motors. Smaller gears have 18 teeth and a base radius of 50 µm. The total depth of the gear teeth is 11 µm, the thickness is 6 µm and a pressure angle of 20 degrees has been used. In order to ensure proper patterning and etching a minimum clearance of 2 µm between engaged gear teeth and a bearing clearance of 1 µm has been used. As a result, gear backlash will be relatively large.

8.2 FRICTION AND WEAR

Although some work has been done on aspects like friction, wear and lubrication of micromechanisms [8.10-8.19], many issues with regard to tribological properties, design and operation of microsystems are unexplored and need to be investigated. Frictional effects should be minimised by a proper bearing design and a suitable gear tooth profile set resulting in a lateral, pure rolling motion between gear teeth. The use of low friction materials [8.15, 8.17, 8.18] and lubricants [8.20-8.23] seems to be promising applications. However, one should bear in mind that the operation of axial gap wobble motors is based upon friction between the rotor and stator surface.

The lifetime of gears and micromotors is limited by wear [8.8, 8.10, 8.11]. Friction and wear studies using specimen-on disc [8.15, 8.19] have been performed and indicate that diamond-like carbon is an attractive material with respect to friction and wear properties. The wear mechanism of brittle materials like DLC, SiO_2, Si_3N_4 and SCS was found to be dominated by asperity fracture, and wear of polysilicon is dominated by asperity deformation [8.19]. In general wear has been found to follow macroscopic theory, where

materials of highest hardness show the lowest wear rates, and wear rate is dependent on contact pressure.

A problem related to the axial gap wobble motor, is that the rocking motion of the rotor gives rise to axial motions between the rotor teeth and the teeth of the gear structure that is driven. This will induce additional frictional forces. The normal force at the tooth surfaces is roughly equal to the excess motor torque divided by the rotor radius. The torque of a motor with a radius of 100 µm can theoretically be in the range of nNm, at high electrostatic fields [8.8], leading to normal forces in the 10 µN range. The axial frictional force resulting from the rocking motion is a fraction of this normal force after multiplication by the frictional coefficient of the materials in contact (e.g. 0.3-0.5). This axial frictional force is small compared to the axial electrostatic forces of the motor which are in the range of mN. Therefore friction between gears as a result of the rocking motion is not expected to strongly affect motor torque and performance.

8.3 FABRICATION PROCESS

The fabrication of electrostatic axial gap micromotors, comb drive actuators and curved electrode actuators together with integrated gear mechanisms is based on a seven mask process using polysilicon surface micromachining techniques. The process steps are illustrated in fig. 8.1. Starting material is a (100) p-type 3" silicon wafer. First a 1 µm thick stress reduced silicon nitride layer is deposited by LPCVD. This is followed by the deposition of a 0.5 µm thick LPCVD polysilicon layer. This polysilicon layer is subsequently doped with boron by solid source indiffusion for one hour at 1100 ˚C. After boron indiffusion the BSG layer is stripped in a buffered HF-solution and the polysilicon is patterned to form the stator poles of the motor and ground planes of electrostatic actuators (mask #1, fig. 8.1a). Now a second stress reduced LPCVD silicon nitride layer with a thickness of 0.5 µm is deposited which serves as an insulation layer. In this Si_xN_y layer, contact windows are etched by RIE in a CHF_3/O_2 gas mixture in order to make electrical contact to the stator poles and ground planes (mask #2, fig. 8.1b). Next a SiO_2 layer is grown by PECVD with a thickness of 2 µm which defines the air gap spacing between the stator and the rotor of the micromotor and partly defines the sacrificial layer of the structures (fig. 8.1c). Local reductions are etched in this

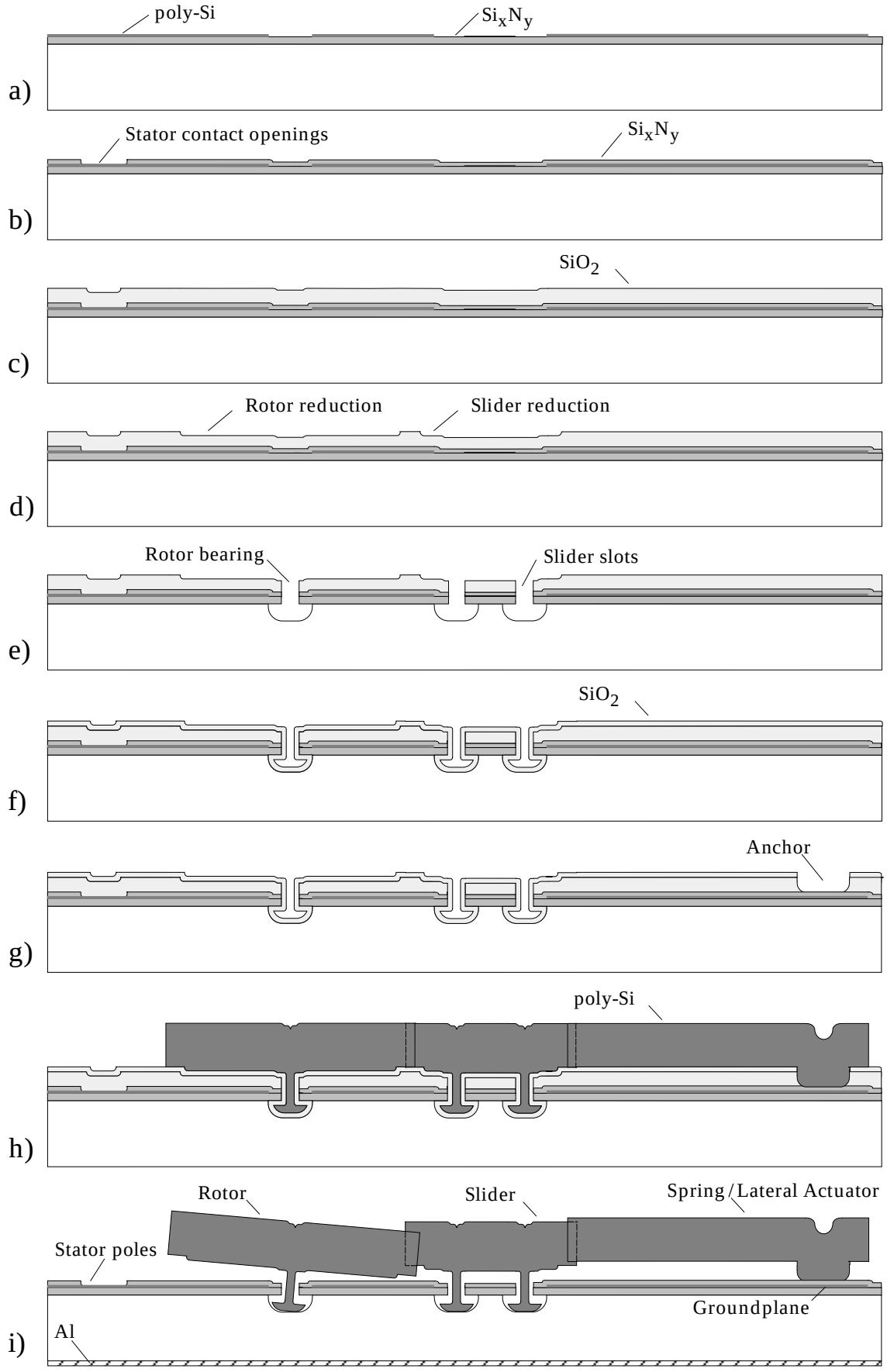

Fig. 8.1 (a), (b), (c), (d), (e), (f), (g), (h), (i) *Processing sequence for electrostatic actuators with integrated gear linkages.*

SiO_2 layer using a BHF solution to define the circular region on which the rotors will roll (mask #3, fig. 8.1d).

The ball bearings and slider slots are formed by RIE etching of the SiO_2 layer using a CHF_3 plasma, RIE etching of the Si_xN_y layers using a CHF_3/O_2 gas mixture and dry isotropic underetching of the silicon wafer in a SF_6/N_2 gas mixture (mask #4,fig. 8.1e). After this a SiO_2 layer with conformal step coverage is grown by LPCVD from TEOS to define the bearing spacing of the rotor structures (fig. 8.1f). In the silicon dioxide sacrificial layer anchors for the electrostatic actuators are patterned by etching in BHF (mask #5, fig. 8.1g). Now a 6 μm thick LPCVD polysilicon layer is deposited that is also doped by boron indiffusion as described before. The boron indiffusion also reduces the residual stress of the polysilicon layer. After stripping the BSG layer in BHF a resistivity of about 3 Ω square is obtained. A 1 μm thick PECVD silicon oxide layer is grown that serves as an etch mask for the polysilicon layer and prevents boron outdiffusion in the subsequent annealing step at 1100 ˚C for 3 hours in order to reduce stress gradients as a result of the one sided diffusion step. Backside layers are stripped by dry etching. The silicon oxide is patterned by RIE using CHF_3 gas and the polysilicon is anisotropically etched using a SF_6, O_2, CHF_3 gas mixture [8.16] (mask #6, fig. 8.1h). In order to remove the polysilicon from the slots in which the sliders have to move, an isotropic etch step in a SF_6/N_2 gas mixture is needed in addition to the anisotropic etch while other areas are protected by photoresist (mask #7). After a thorough cleaning procedure the sacrificial layers are etched in concentrated HF for 50 min. This is followed by dilution rinsing in DI water, rinsing in isopropanol and rinsing in cyclohexane while preventing the wafers from drying. Now freeze drying is used to remove the cyclohexane at a temperature of -10 ˚C under a high N_2 flow in order to prevent stiction problems [8.17]. The last step is evaporation of a 1 μm thick aluminum backside layer (fig. 8.1i). The final result is shown in fig. 8.2 to 8.10.

8.4 EXPERIMENTAL RESULTS

First experiments have shown that the micromotors can successfully drive gear trains and slider gear racks resulting in, respectively, torque leverage, and rotational to linear transformation. Up to now no integrated micromechanisms that are driven by electrostatic micromotors have been reported.

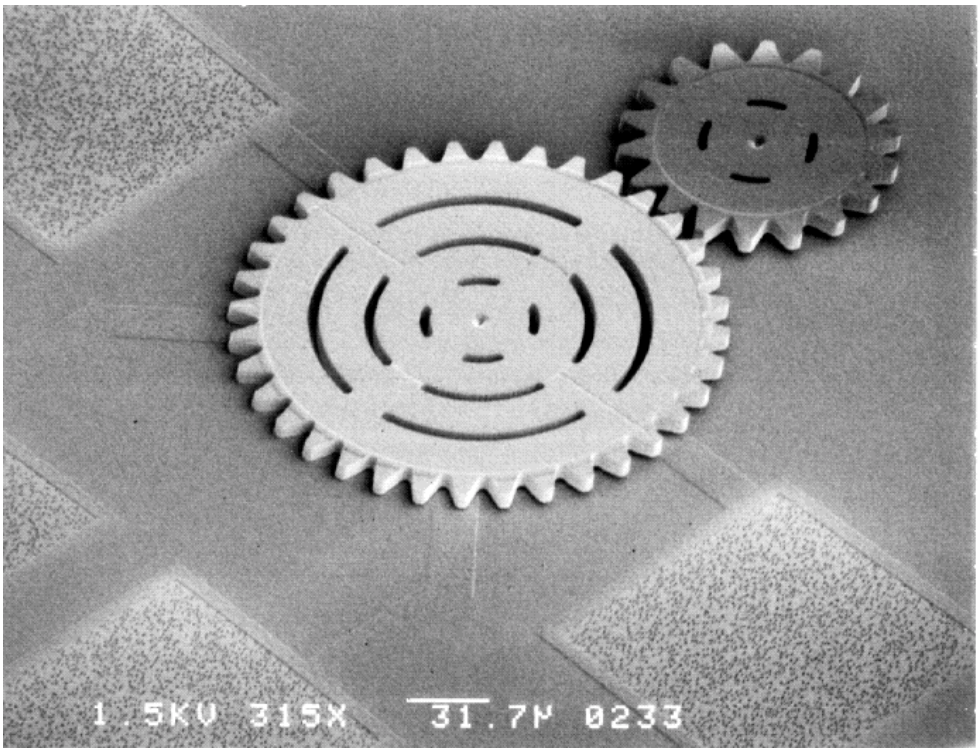

Fig. 8.2 *SEM photograph of an axial gap wobble motor with gear teeth driving a smaller gear wheel. The rotor and the smaller gear have a base radius of respectively 100 µm and 50 µm.*

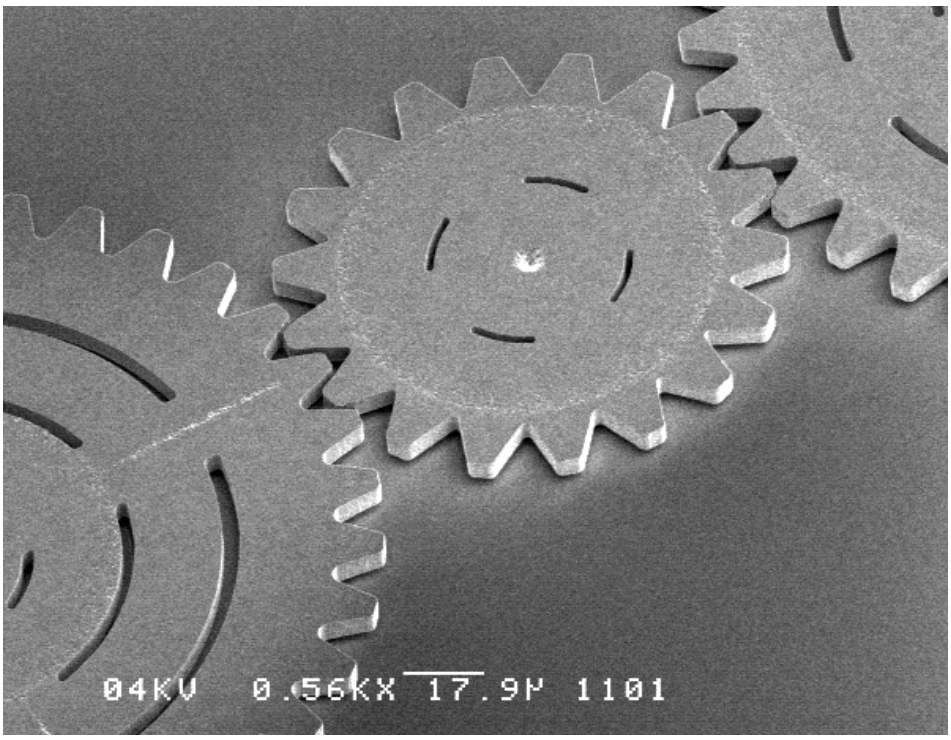

Fig. 8.3 *Close-up of the gear teeth. The gear teeth have a thickness of 6 µm, a depth of 11 µm and a diametrical pitch of 18.5 µm.*

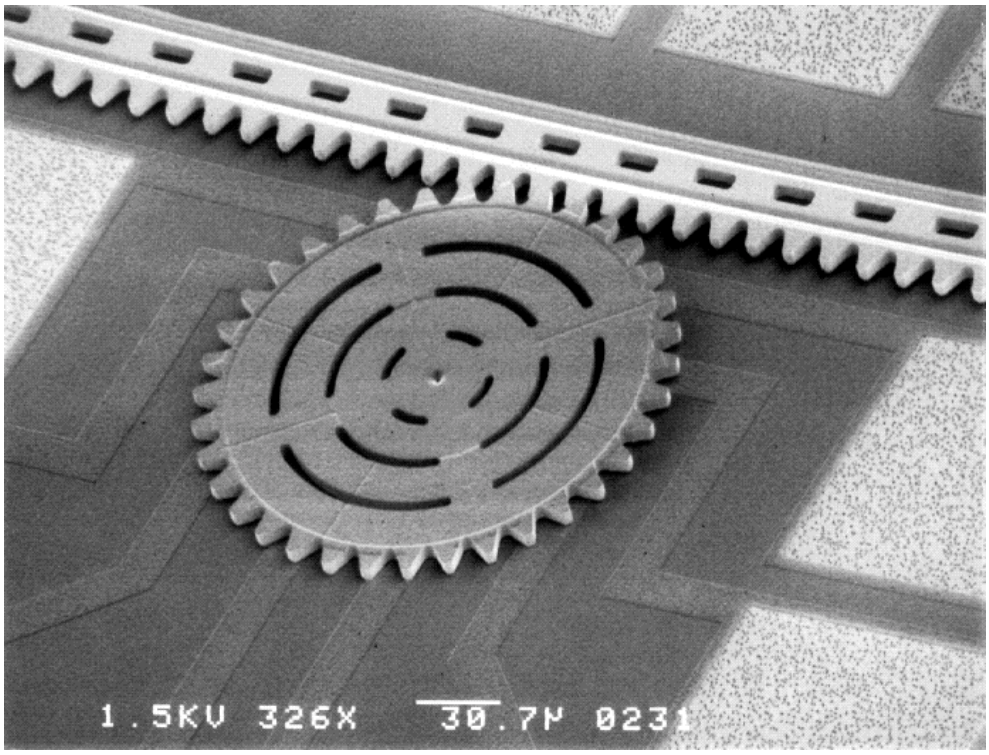

Fig. 8.4 *SEM photograph of an axial gap wobble motor connected to a gear rack resulting in transformation of the rotational into linear motion.*

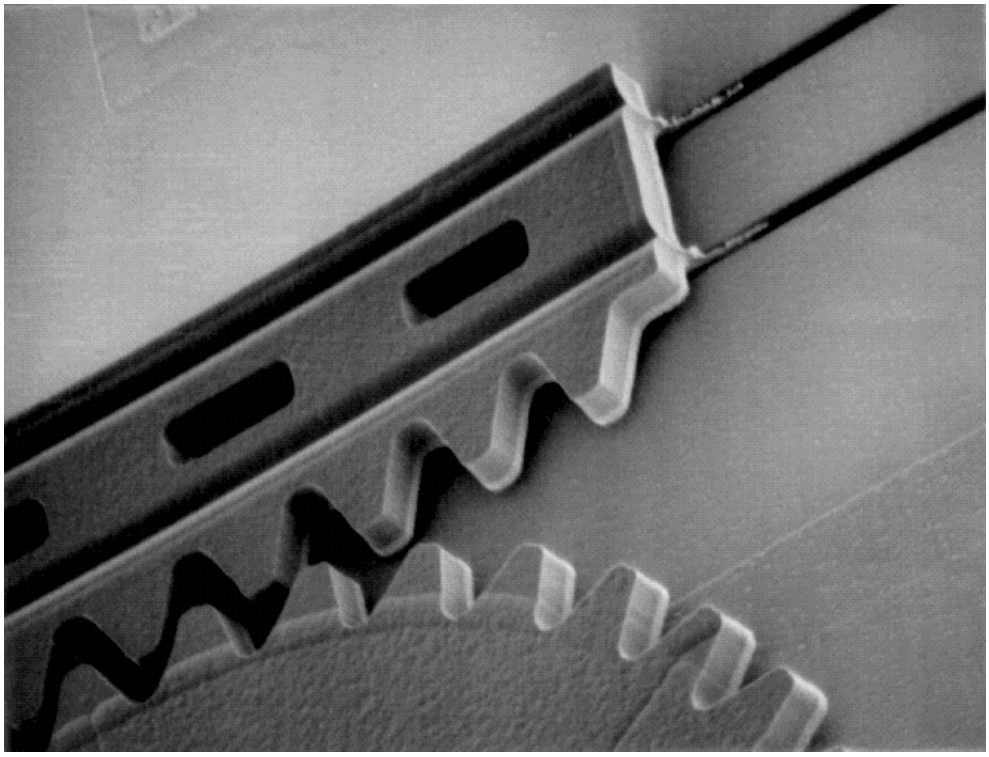

Fig. 8.5 *Close-up of the gear rack. The slider is able to move on its bearing along slots that are etched into the wafer.*

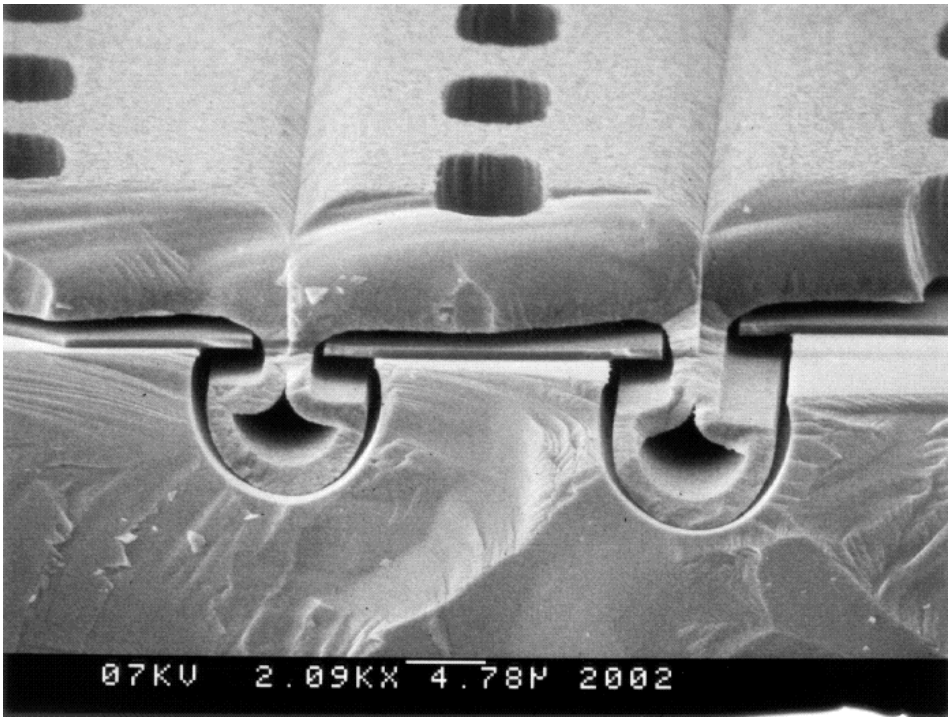

Fig. 8.6 *Cross section of a linear slider showing the slots and bearing that guide its motion.*

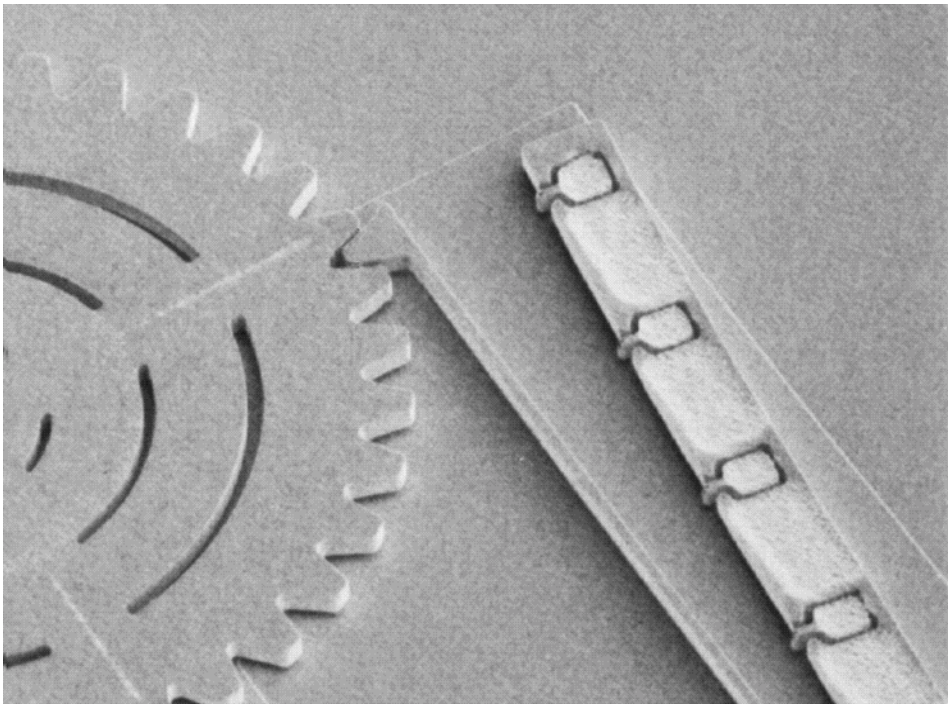

Fig. 8.7 *Curved electrode actuator for fixing gear position.*

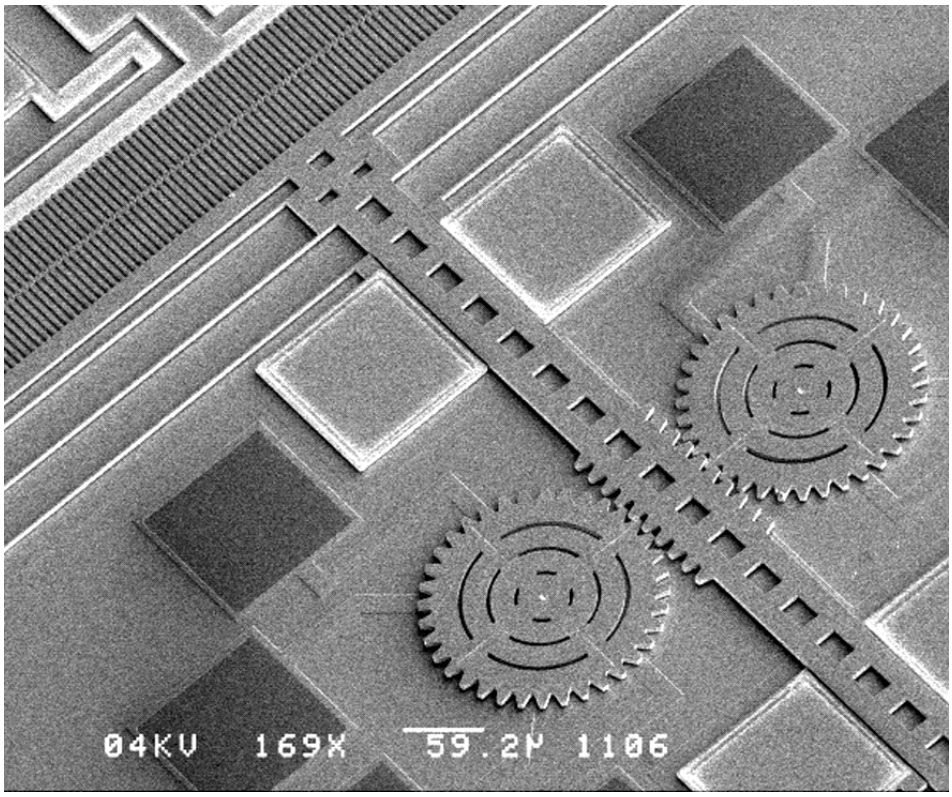

Fig. 8.8 *Motors linked to a gear rack suspended by folded flexures of comb drive actuators. Such structures could be used to measure output torque and motor dynamics.*

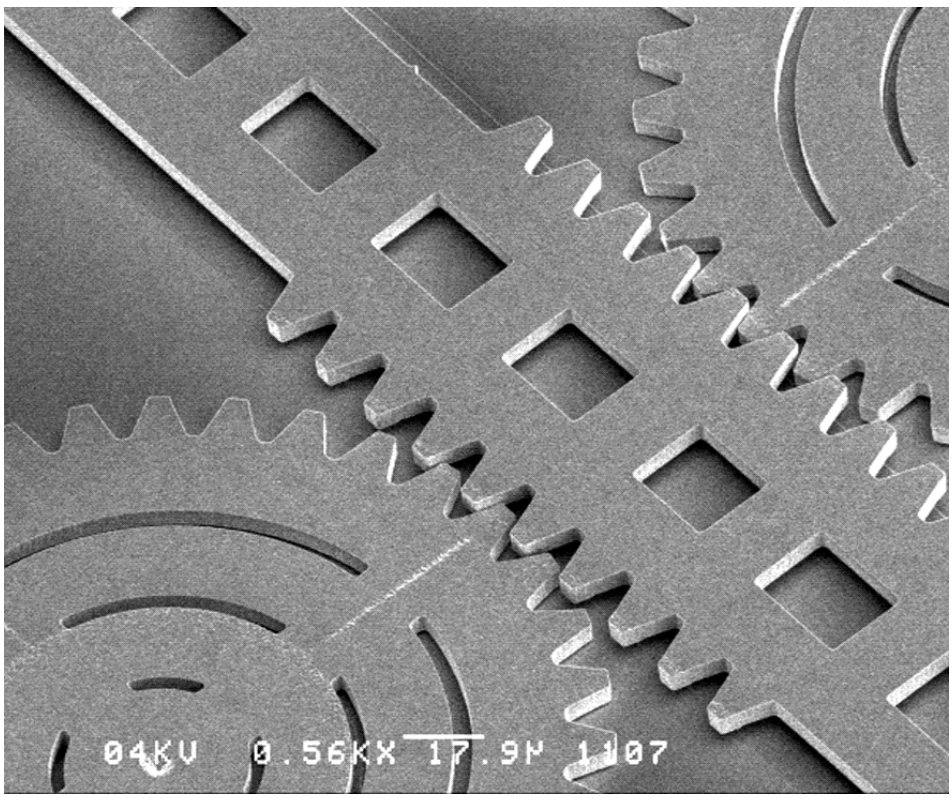

Fig. 8.9 *Close up view of comb drive structure connected to axial gap wobble motors from fig. 8.8.*

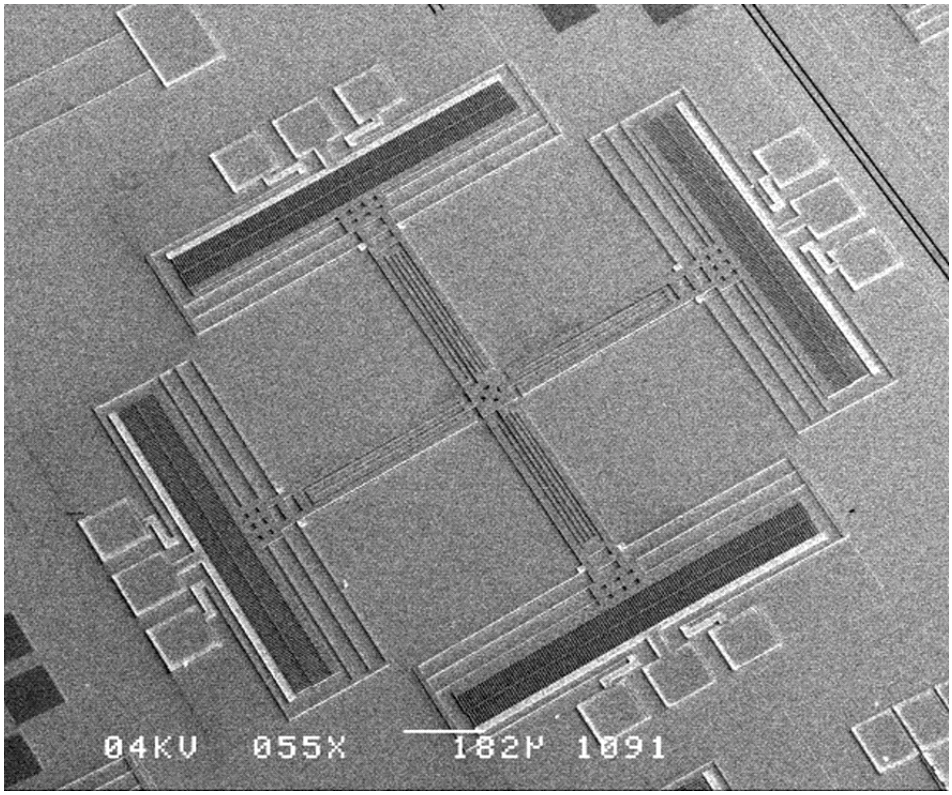

Fig. 8.10 *XY-stage fabricated in the same process run.*

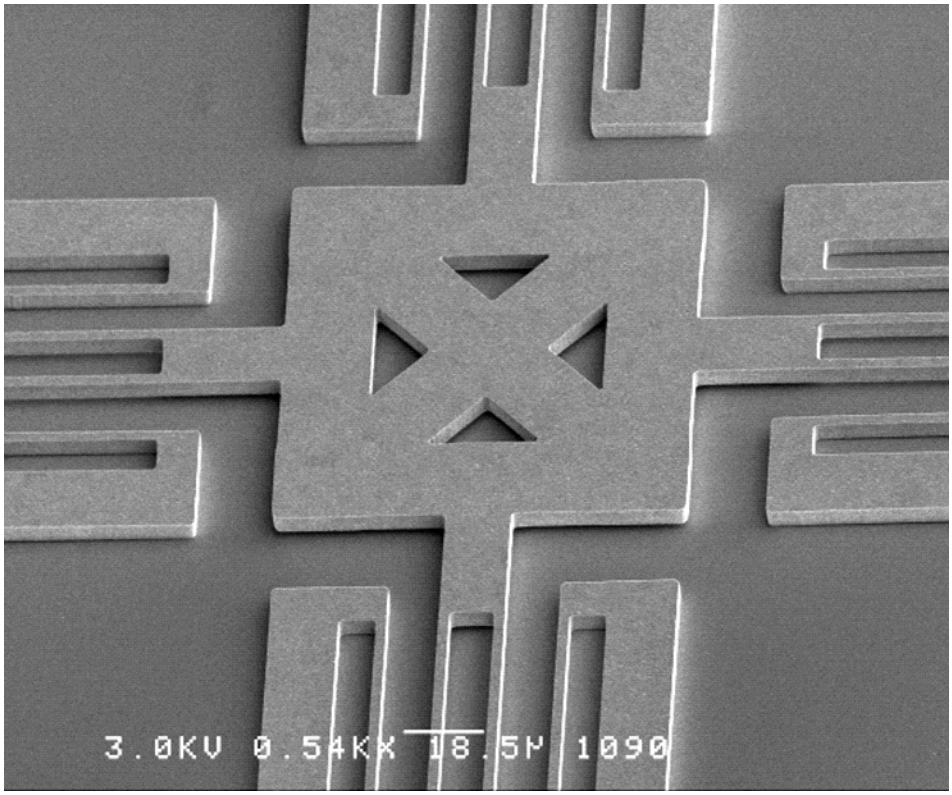

Fig. 8.11 *Close up of the center of the XY stage from fig. 8.10.*

Comb drive structures and curved electrode actuators in conjunction with micromechanical mechanisms have also been driven electrostatically.

Variations in operation characteristics of gears have been observed which are expected to result from the non-conjugate gear teeth profile that has been used. Problems such as gear backlash and impact were also noticed which were caused by etching- and bearing clearances. Furthermore frictional problems were encountered with large slider structures (up to 2 mm long). Long sliders could be moved manually by probe needles but did not slide by electrical powering micromotors. It is suggested that stress gradients clamp long slider structures in their bearing slots resulting in frictional forces which are larger than the output force of the motors. Further experimental work is needed to obtain more quantitative results.

8.5 APPLICATIONS

Specially designed devices with gear linkages can be used to investigate tribological properties and system design aspects of micromechanical gear systems. The fabricated devices will be used to explore essential features of these issues.

For instance, measurements on gear trains that are driven by comb drive structures using a gear rack can be used to obtain information on frictional properties of the gear teeth and bearing. In the same way the frictional properties of sliders can be investigated. Gear linkages can also be used to determine the torque output of electrostatic micromotors by, for example, loading the motor with a spring and measuring the deflection to voltage characteristic.

Future applications of integrated actuator systems can be found in areas like micropositioning, micromanipulation (i.e. pick and place), scanning probe microscopy, information storage and micro robotics.

8.6 CONCLUSIONS

A micromachining process for the fabrication of electrostatic microactuators which are linked with each other and connected to other movable microstructures by integrated gear linkages has been presented. The fabrication is based on polysilicon surface micromachining and sacrificial layer etching

techniques. First experimental results show that electrically powered actuators successfully drive various micromechanisms. The work is a first step towards mechanical power transmission in micromechanical systems. Mechanical power transmission of microactuators may strongly increase the number of useful applications and may lead to new possibilities for microelectromechanical systems.

REFERENCES

[8.1] Y. Gianchandani and K. Najafi, Batch fabrication and assembly of micromotor-driven mechanisms with multi-level linkages, Proc. IEEE MEMS, Proc. IEEE Micro Electro Mechanical Systems, Travemünde, Germany, Feb. 4-7, 1992, pp. 141-146.

[8.2] T.R. Christenson, J. Klein and H. Guckel, An electromagnetic micro dynamometer, Proc. IEEE Micro Electro Mechanical Systems, Amsterdam, The Netherlands, Jan. 29-Feb. 2, 1995, pp. 386-391.

[8.3] L. Paratte, H. Lorenz, R. Luthier and N.F. de Rooij, Miniature gear reduction unit driven by a silicon electrostatic wobble motor, J.Micromech. Microeng., 2 (1992), pp. 221-223.

[8.4] M.J. Daneman, N.C. Tien, O. Solgaard, A.P. Pisano, K.Y. Lau and R.S. Muller, Linear microvibromotor for positioning optical components, Proc. IEEE Micro Electro Mechanical Systems, Amsterdam, The Netherlands, Jan. 29-Feb. 2, 1995, pp. 55-60.

[8.5] E.J. Garcia and J.J. Sniegowski, Surface micromachined microengine as the driver for micromechanical gears, Proc. of the 8th Int. Conf. on Solid-State Sensors and Actuators (Transducers '95), Stockholm, Sweden, June 25-29, 1995, Vol. 1, pp. 365-368.

[8.6] R. Legtenberg, E. Berenschot, M. Elwenspoek and J. Fluitman, Proc. IEEE Micro Electro Mechanical Systems, Amsterdam, The Netherlands, Jan. 29-Feb. 2, 1995, pp. 37-42.

[8.7] R. Legtenberg, A.W. Groeneveld and M. Elwenspoek, Towards position control of electrostatic comb drives, Proc. 6th European workshop on micromachining, micromechanics and microsystems (MME '95), Copenhagen, Denmark, Sept. 3-5, 1995, pp. 124-127.

[8.8] R. Legtenberg E. Berenschot, J. van Baar, Th. Lammerink and M. Elwenspoek, An electrostatic lower stator axial gap wobble motor: Design and fabrication, Proc. of the 8th Int. Conf. on Solid-State Sensors and Actuators (Transducers '95), Stockholm, Sweden, June 25-29, 1995, Vol. 2, pp. 404-407.

[8.9] D.W. Dudley, Handbook of practical gear design, McGraw-Hill, New York, 1984.

[8.10] K.J. Gabriel, F. Behi and R. Mahadevan, In Situ friction and wear measurements in integrated polysilicon mechanisms, Sensors and Actuators, A21-A23, 1990, pp. 184-188.

[8.11] M. Mehregany, S.D. Senturia and J.H. Lang, Friction and wear in microfabricated harmonic side-drive motors, Proc. IEEE Solid-State Sensor and Actuator Workshop, Hilton Head Island, SC, U.S.A. June 4-7, 1990, pp. 17-22.

[8.12] M.G. Lim, J.C. Chang, D.P. Schultz, R.T. Howe and R.M. White, Polysilicon microstructures to characterize static friction, Proc. IEEE Micro Electro Mechanical Systems, Napa Valley, CA, U.S.A., Feb. 11-14, 1990, pp. 82-88.

[8.13] R. Kaneko, Microtribology related to MEMS, Proc. IEEE Micro Electro Mechanical Systems, Nara, Japan, Jan. 30-Feb. 2, 1991, pp. 1-8.

[8.14] K. Noguchi, H. Fujita, M. Suzuki and N. Yoshimura, The measurement of friction on micromechatronics elements, Proc. IEEE Micro Electro Mechanical Systems, Nara, Japan, Jan. 30-Feb. 2, 1991, pp. 148-153.

[8.15] S. Suzuki, T. Matsuura, M. Uchizawa, S. Yura and H. Shibata, Friction and wear studies on lubricants and materials applicable to MEMS, Proc. IEEE Micro Electro Mechanical Systems, Nara, Japan, Jan. 30-Feb. 2, 1991, pp. 143-147.

[8.16] A.P. Lee, A.P Pisano and L. Lin, Normal and tangential impact in micro electromechanical structures, Proc. IEEE Micro Electro Mechanical Systems, Nara, Japan, Jan. 30-Feb. 2, 1991, pp. 21-26.

[8.17] K. Deng and W.H. Ko, A study of static friction between silicon and silicon compounds, J. Micromech. Microeng., Vol. 2, 1992, pp. 14-20.

[8.18] U. Beerschwinger, S.J. Yang, R.L. Reuben, M.R. Taghizadeh and U. Wallrabe, Friction measurements on LIGA-processed microstructures, J. Micromech. Microeng., Vol. 4, 1994, pp. 14-22.

[8.19] U. Beerschwinger, D. Mathieson, R.L. Reuben and S.J. Yang, A study of wear on MEMS contact morphologies, J. Micromech. Microeng., Vol. 4, 1994, pp. 95-105.

[8.20] P. Cléchet, C. Martelet, M. Belin, H. Zarrad, N. Jaffrezic-Renault and S. Fayeulle, Lubrication of silicon micromechanisms by chemical grafting of long-chain molecules, Sensors and Actuators, A44, 1994, pp. 77-81.

[8.21] H. Zarrad, J.M. Chovelon, P. Cléchet, N. Jaffrezic-Renault, C. Martelet, M. Belin, H. Perez and Y. Chevalier, Optimization of lubricants for silica micromotors, Sensors and Actuators, A46-47, 1995, pp. 598-600.

[8.22] H. Zarrad, P. Cléchet, M. Belin, C. Martelet and N. Jaffrezic-Renault, The use of long-chain molecules for the lubrication of micromechanisms, J. Micromech. Microeng., Vol. 3, 1993, pp. 222-224.

[8.23] K. Deng, R.J. Collins, M. Mehregany and C.N. Sukenik, Performance impact of monolayer coating of polysilicon micromotors, Proc. IEEE Micro Electro Mechanical Systems, Amsterdam, The Netherlands, Jan. 29-Feb. 2, 1995, pp. 368-373.

Chapter Nine

ELECTROSTATICALLY DRIVEN VACUUM ENCAPSULATED POLYSILICON RESONATORS*

Basic design issues and a fabrication process based on surface micromachining techniques for electrostatically driven vacuum encapsulated polysilicon resonators are presented. A novel freeze drying method, that does not require vacuum equipment, is presented. Reactive sealing with LPCVD silicon nitride is used to create the evacuated cavity, resulting in cavity pressures close to the deposition pressure. Design issues regarding choice of materials, technology and lay-out are discussed. First experimental results, including an admittance plot of the one-port resonator and a plot indicating the dependence of the *Q*-factor on the resonator geometry and ambient pressure are presented.

9.0 INTRODUCTION

Resonant sensors are very attractive for the precise measurement of mechanical quantities such as pressure and force. They offer high sensitivity and resolution together with a semi-digital output, i.e., a frequency [9.1-9.4]. The central part of the sensor is a vibrating mechanical element called the resonator, which provides the frequency(shift) output.

Surface micromachined resonators, that are operated in a flexural mode of vibration, have been used by several research groups in the past [9.5-9.7]. Without taking special precautions, these resonators suffer from small signal responses as a result of a low mechanical quality factor. Lowering of the quality factor is a direct consequence of the introduction of a second surface in close proximity to the resonator surface. This leads to so-called "squeeze film" damping which can be observed for the normal vibrational motion of two closely spaced surfaces [9.5, 9.8]. Squeeze film damping becomes significant if the gap spacing is small compared to the lateral dimensions of the resonator. Evacuating the surroundings would eliminate the above effect. At the same time, unwanted environmental effects such as changes in the density of the

* published in Sensors and Actuators A, 45 (1994), pp. 57-66.

surrounding medium, humidity and dust are eliminated as well. Thus, the resonator must be placed inside a vacuum housing. This was realized in a very elegant way by Ikeda *et al* in 1988 [9.9, 9.10]. They fabricated single crystalline silicon resonators housed locally in on-chip vacuum shells using a self aligned selective epitaxial technology in combination with selective anisotropic etching and hydrogen evacuation techniques. The same concept, but based on a different fabrication technology, has been presented by Guckel *et al* in 1990 [9.11, 9.12]. They employed the polysilicon/silicon dioxide sacrificial layer etching technique to realize a similar structure.

This chapter deals with design and processing issues of electrostatically driven vacuum encapsulated polysilicon resonators. A discussion of the resonator performance, including a description of the theoretical model is given in [9.13]. The fabrication process is based upon the polysilicon/silicon dioxide sacrificial layer etch technique. A novel freeze drying procedure, which, as opposed to earlier reports, offers enhanced speed and does not require any vacuum equipment, is presented. For the excitation and detection of the vibration, the emphasis is on a single element or one-port approach [9.14].

9.1 DESIGN ISSUES

9.1.1 Basic Structure

The basic structure of the resonator is shown in fig. 9.1. The resonator consists of a prismatic beam with a rectangular cross section and is housed in an evacuated cavity. From an electric view point, the structure defines a four-terminal device. Both the one- [9.6, 9.14] and two-port approach [9.5, 9.7, 9.10] can be used for excitation and detection. Details of the electric driving scheme are presented in reference [13].

Electrostatic excitation and detection has been employed [9.3-9.7]. This is attractive because of its simplicity and compatibility with micromachining- and IC-technologies. The simple structure makes the mechanical properties, and in particular the residual stress, much easier to control. Also, the scheme does not suffer from disturbing frequency shifts due to thermally-induced axial loads. Moreover, no additional transducer materials are required that would be necessary for some other drive and detection schemes, such as piezo-electric transduction. Thus, the electrostatic scheme provides an excellent way

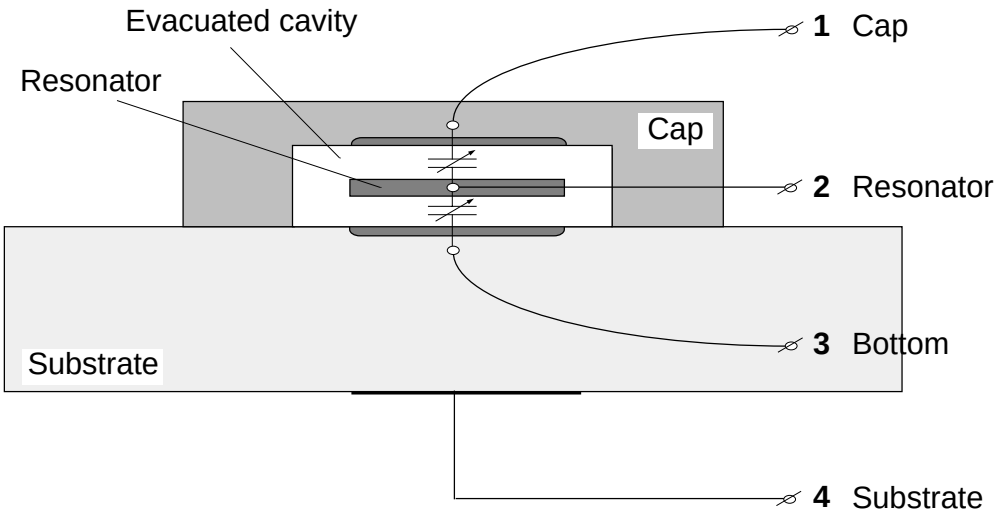

Fig. 9.1 *Schematic cross section of a vacuum encapsulated flexural beam resonator, depicted as a four-terminal device.*

to come to an "all-silicon device", which is attractive to minimize differential thermal expansion effects.

9.1.2 The Resonator

The static and dynamic characteristics of the resonator are determined by its in-plane geometry and by its characteristic dimensions perpendicular to the plane [9.4, 9.13]. Flexural beam resonators were designed with lengths of 210, 310, 410 and 510 µm and widths of 25, 50 and 100 µm. The beam thickness is approximately 1.5 µm. Furthermore, a beam-to-substrate gap spacing of approximately 1.2 µm and a beam-to-cap gap spacing of 1.5 µm were chosen. These dimensions lead to static capacitances (excluding any parasitics) in the range from 0.03-0.3 pF.

Parasitic loads, which are mainly capacitive, have to be kept very low or have to be compensated for in order to be able to detect the resonance [9.14]. The on-chip parasitic loads are mainly determined by the area of the bonding pads and the interconnecting wires. Thus, wire lengths were kept as short as possible and a relatively small bonding pad area of $150 \times 150\,\mu m^2$ was used.

Chips, measuring $6 \times 6\,mm^2$, including 12 different resonant structures were designed. As a minimum feature size, a rather conservative value of 5 µm was used. Figure 9.2 shows a typical layout of the resonator. A total number of ten masks is needed for the fabrication.

"Drop-in's" of electric and mechanical diagnostics were used for characterization. They include checks for alignment accuracy, structures to measure the sheet- and contact resistances and further, ring- and buckled beam structures to determine the residual strain [9.15].

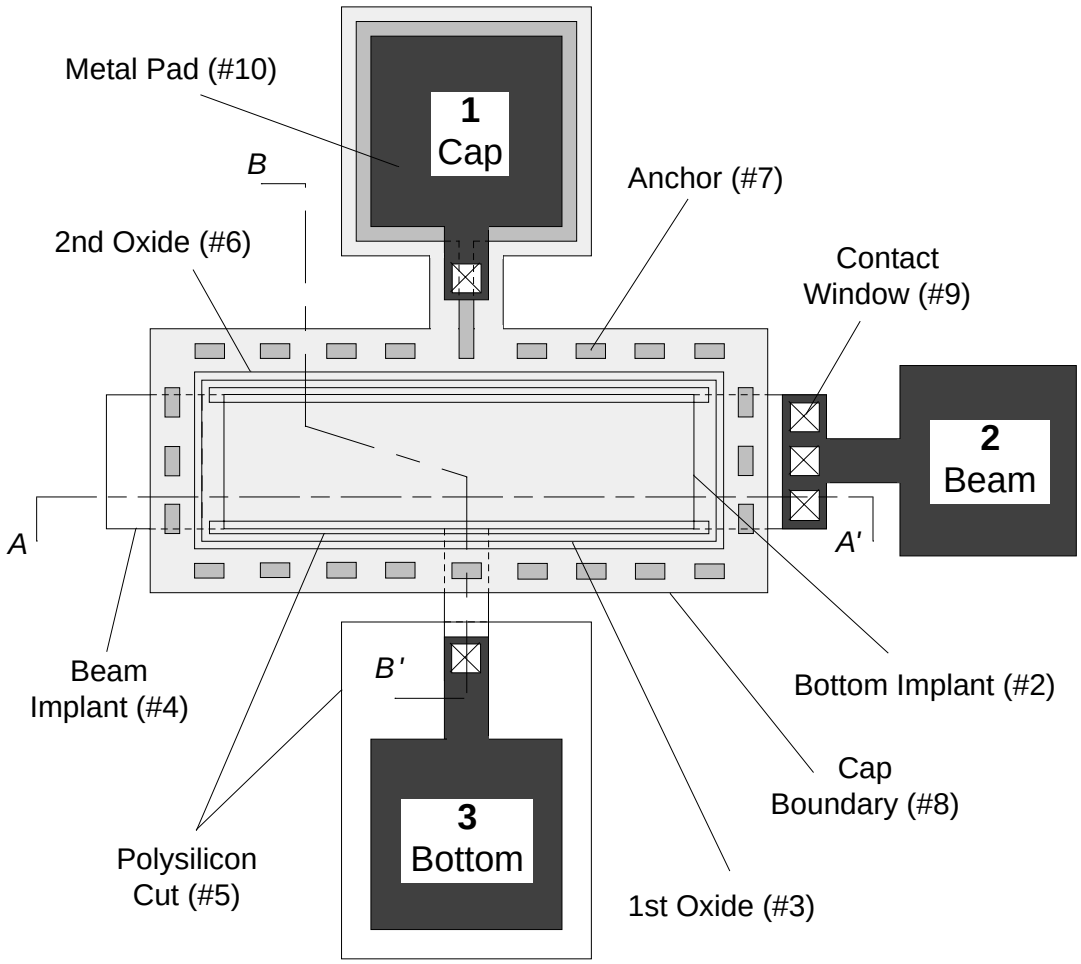

Fig. 9.2 *Typical resonator layout. The resonator consists of a doubly supported beam. The in-plane beam dimensions are 410 × 100 μm².*

9.1.3 The Sealing Cap

The mechanical stiffness of the sealing cap must be large enough to prevent excessively large deflections caused by the internal vacuum, which may lead to physical contact between the beam and the cap or the substrate. Thus, the upper limit for the cap width is determined by a given maximum deflection. The maximum deflection w_o of a clamped rectangular plate with lateral dimensions $b \times a$ can be approximated as [9.16]:

$$w_o \approx \frac{0.00260\,\Delta p\, a^4}{D} \qquad \text{for} \quad b > 2a \tag{9.1}$$

where Δp is the difference in pressure of the cavity interior and the ambient and D is the flexural rigidity of the plate. The coefficient 0.00260 depends on the length over width ratio b/a and is within two percent accuracy if this ratio is larger than 2. For a cap thickness of 2.5 μm this leads to an upper limit of the

width of approximately 150µm if the maximum cap deflection should not exceed 0.5µm. Finite element analyses of a more realistic cap structure have indicated an increase of the maximum deflection of 20-30% due to small corrugations that are a result of the fabrication process (e.g. see fig. 9.5h). This leads to a smaller value for the upper limit of the width. The cap thickness used is approximately 2.6 µm, which is sufficient to keep the inward deflection after sealing below 0.5µm for 100µm wide beams.

9.2 TECHNOLOGY AND MATERIALS

9.2.1 Surface Micro Machining

Surface micromachining is used to fabricate the polysilicon resonant structures. The technology relies on the construction of mechanical parts from a thin film material in combination with a sacrificial layer thin film which is used as a spacer between the structural parts [9.5, 9.17, 9.18]. After selective chemical removal of the sacrificial layer, freely movable members remain. Surface micromachining offers small dimensions and a good dimensional control, especially in the thickness direction. Furthermore, a very elegant way to fabricate evacuated cavities by means of surface micromachining techniques has recently been presented [9.17, 9.19].

9.3.2 Materials

Taking the planar silicon thin film technology as a starting point, the aim is to the develop an "all silicon device". This provides a good thermal match with the silicon substrate and further, IC compatible processing. Fabrication is based on the polysilicon/silicon dioxide sacrificial layer technique.

In order to obtain a high sensitivity of the frequency per unit applied strain, i.e., the gauge factor, slender beams are required with a low residual strain [9.4]. A tensile strain is desired to minimize the chance for buckling. A tensile strain in the range of 10-100 ppm is considered to be optimal. The residual stress of polysilicon can be well controlled provided that proper deposition conditions and anneal cycles are used [9.15, 9.19-9.21]. Polysilicon with a low tensile strain can be obtained by low pressure chemical vapour deposition (LPCVD) from silane (SiH_4) at processing temperatures close to the transition temperature from amorphous to (poly)crystalline layers (≈580 °C [9.21]). Thermal annealing in nitrogen converts the as-deposited built-in compressive strain into a controllable tensile strain depending on the annealing temperature [9.15].

The electrodes of the driving capacitor are defined by locally doping the silicon substrate, the polysilicon beam and the cap. In order to prevent doping of unwanted places, undoped oxides must be used as the sacrificial layer material. Undoped low frequency (50 kHz) plasma enhanced chemical vapour deposited (PECVD) oxides, provide an acceptable compromise between a good step coverage and a high sacrificial layer etch rate. Doping is done by ion implantation of boron. Boron results in lower sheet resistivities in polysilicon than phosphorous and shows less segregation at the grain boundaries [9.22]. Boron implantation may however affect the mechanical properties of the polysilicon layer. Electrical insulation of the cap, the resonator and the substrate, is achieved using an separating layer of LPCVD silicon nitride. The layer also serves as the anchor material for the different polysilicon layers as indicated in fig. 9.3. The capacitance and the conductivity between the different terminals provide a first indication about the integrity of the insulating layers and whether the beams are free standing or not.

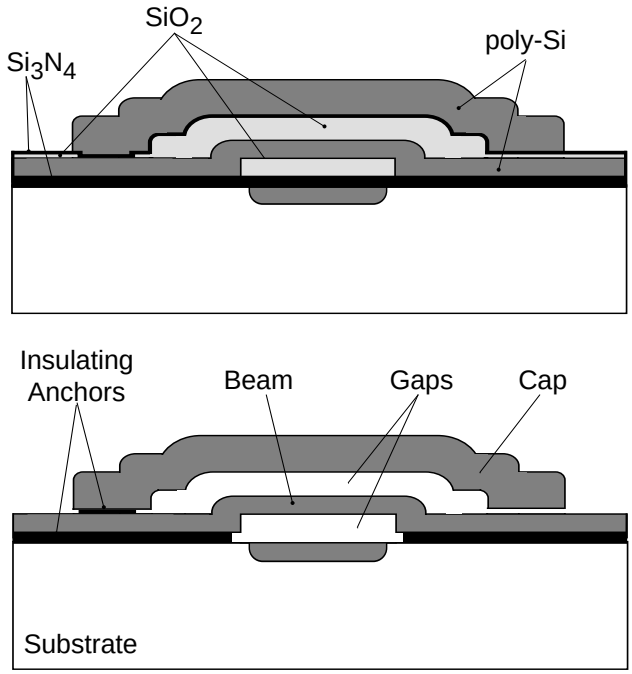

Fig. 9.3 *Schematic of the electrical insulation between the resonant beam, the substrate and the cap using silicon nitride anchors; (a) prior to and (b) following the sacrificial layer etch.*

9.2.3 Sticking and Freeze Drying

After etching the sacrificial layers in a undiluted (49 %) HF-solution, a specific drying procedure is required to prevent sticking of the free structural members to the substrate. Standard drying procedures such as dry spinning or air drying produce surface tension forces which cause “pull-down” of the thin

film structures. Once contact has been made, other forces like van der Waals forces, electrostatic forces, hydrogen bridging, and chemical reactions come into play resulting in permanent attachment of the structures to the substrate [9.23-9.25]. An elegant way to solve this so called sticking problem is "freeze drying". The freeze drying method has been developed as a drying method for biological specimens by Boyde and Wood in 1969 [9.26]. Guckel *et al.* [9.24] and later Takeshima *et al.* [9.27] implemented this technique for sacrificial layer etching of surface micromachined structures. They describe a process whereby a final rinse agent is frozen and subsequently sublimated in a few hours under vacuum conditions.

In this thesis a new and faster freeze drying technique is presented. It does not require any vacuum equipment but instead can be performed under atmospheric conditions. Cyclohexane which freezes at about 7˚C is used as the final rinse agent. Freezing and subsequent sublimation is readily accomplished by placing the substrate under a nitrogen flow on a regulated peltier element with a temperature below the freezing point. The total time for the freeze-sublimation process depends on the geometry of the sample and typically takes 5-15 minutes for the structures described in this chapter.

Details of the cyclohexane rinse-freeze-sublimation procedure are given in chapter 2.

9.2.4 Reactive Sealing

The reactive sealing technique as developed by Burns and Guckel [9.17, 9.19] is an elegant way to create vacuum-sealed cavities. It exploits the difference in geometry between the small etch channels and the larger cavities to close off the latter by growing a thin film in the channels. Good step coverage is favourable for good sealing properties but also results in the deposition of a thin layer inside the cavity before the etching channels are closed.

In the case of the electrostatic driving scheme, a material with good insulating properties must be chosen. The deposition of electrically conductive material inside the cavity creates a miniature Faraday cage around the beam prohibiting the build-up of an electric field. The field is essential for electrostatic excitation and detection. Furthermore, it is preferable to use a material with a tensile residual strain in order to minimize the chance for buckling of the resonator. LPCVD of silicon nitride was chosen as the reactive sealing process.

The residual pressure inside the cavity after sealing is important with respect to the attainable quality factors [9.3, 9.4, 9.28]. The cavity pressure after sealing is a function of the processing pressure and temperature, the gas flows, the reaction products and subsequent (out)diffusions. The overall chemical reaction for the deposition of silicon nitride from dichlorosilane (DCS) and a surplus of ammonia (NH_3) is [9.29]:

$$3\,Si_2Cl_2H_2 + (4 + x)\,NH_3 \rightarrow Si_3N_4\downarrow + 6\,HCl\uparrow + 6\,H_2\uparrow + x\,NH_3\uparrow \qquad (9.2)$$

The reaction above clearly indicates that the number of gaseous molecules increases. This means that the cavity pressure will be higher than the deposition pressure whence the etch channels are closed off. According to Boyle Gay-Lussac's law for an ideal gas, the final cavity pressure p_{cavity} can be expressed as:

$$p_{\text{cavity}} = p_{\text{process}} \frac{V_{\text{unsealed}}}{V_{\text{sealed}}} \frac{T_{\text{o}}}{T_{\text{process}}} \frac{n_{\text{right}}}{n_{\text{left}}} \qquad (9.3)$$

where T_{o} and T_{process} denote room temperature and the processing temperature, respectively, $V_{\text{unsealed}} / V_{\text{sealed}}$ denotes the ratio of the volume of the cavity prior to and after sealing, p_{process} denotes the processing pressure and $n_{\text{right}} / n_{\text{left}}$ denotes the mole ratio of gaseous products and reactants.

To get an idea of the final cavity pressures, a DCS to NH_3 flow ratio of 3:4 (i.e., x=0) and no subsequent reactions and diffusions after sealing are assumed. For the reaction given by eq. (9.2) the mole ratio equals 12/7. The ratio $V_{\text{unsealed}} / V_{\text{sealed}}$ results in a slight increase of the sealing pressure and is due to a volume reduction as a result of the inward deflection of the sealing cap. This deflection is generally undesirable and is therefore kept small, resulting in a volume ratio close to unity. For a processing pressure of 200 mTorr (0.26 mbar) and a deposition temperature of 800 °C, eq. (9.3) predicts a sealing pressure of about 100 mTorr (0.13 mbar). A more dedicated process performed at a pressure of 20 mTorr, a temperature of 850 °C and the same gas flow ratio as indicated above leads to a sealing pressure of approximately 10 mTorr, but exhibits a lower deposition rate. By using a flow ratio DCS:NH_3 = 1:3, a surplus of ammonia results (i.e., x=5) and the mole ratio is equal to 17/12. This leads to a lowering of the final cavity pressure from 100 mTorr to 83 mTorr. Extending the surplus to infinity, results in a final cavity pressure of 58 mTorr. These simple examples indicate that the mole ratio is not the determining

factor, but instead, the processing pressure and the processing temperature are the most important parameters that determine the final cavity pressure. Low final cavity pressures using a LPCVD silicon nitride sealing layer, are obtained at a high deposition temperature and a low deposition pressure.

9.3 FABRICATION SEQUENCE

A scheme of the fabrication process is shown in fig. 9.4. The substrates are (100) n-type silicon wafers. The fabrication sequence begins with a dry etching step to define the alignment marks into the silicon substrate (Mask#1). Next, boron is implanted (dose=$5x10^{15}$ cm^{-2} and energy=100 keV) through a photoresist mask (Mask#2) to define the bottom electrode (see fig. 9.4a). This is followed by a blanket phosphorous implant (dose=$1x10^{15}$ cm^{-2} and energy=150 keV) of the back-side of the wafer to obtain a good back side contact. After plasma ashing the photoresist, the wafer is cleaned and is given an HF-dip (1 min. in $HF:H_2O$=1:100) to remove the native oxide. A 200 nm thick, stoichiometric LPCVD silicon nitride layer is grown for the insulating (anchoring) layers (see also figs. 9.3a,b). The first sacrificial layer consists of a 1.18 µm thick PECVD oxide layer, grown from a 2% SiH_4 (in N_2) and N_2O mixture. This layer is densified for 30 minutes at 800 ˚C in a nitrogen ambient to improve the thermal stability. Patterning of the oxide layer (Mask#3) is done by wet chemical etching using buffered HF (BHF). After cleaning, the wafers are given an HF-dip to remove the native oxide and to ensure proper attachment of the next LPCVD polysilicon layer. This polysilicon layer is 1.50 µm thick and is grown by pyrolizing silane (50 sccm) at a temperature of 590 ˚C and a pressure of 250 mTorr, giving a deposition rate of approximately 6.3 nm/min. (see fig. 9.4b). The following step is the implantation of boron (dose=$1x10^{16}$ cm^{-2} and energy=150 keV) through a photoresist mask (Mask#4) to define the electrode of the resonant beam. After plasma ashing the photoresist and subsequent cleaning, the length and width of the beams are defined by reactive ion etching (RIE) in a SF_6 plasma (Mask#5). At the same time, the polysilicon is removed at the places for the substrate metallization contacts (see fig. 9.4c). This is followed by the deposition, densification and patterning (Mask#6) of the second PECVD sacrificial oxide layer (see fig. 9.4d). The thickness of the oxide layer is approximately 1.55 µm. Wet oxidation at 1000 ˚C for 8 minutes forms a 80 nm thick oxide layer in which the anchors (and etch channels) are defined using BHF (Mask#7). For electric insulation, a

50 nm LPCVD silicon nitride layer is grown which serves as the insulation layer between the beam- and cap electrodes (see fig. 9.4e and figs. 9.3a,b). The next step involves cleaning and removal of the native oxide, followed by LPCVD of a polysilicon layer for the cap with a thickness of approximately 2.64 µm. A blanket boron implantation (dose=$1x10^{16}$ cm^{-2} and energy=100 keV) forms the conductor for the cap electrode. Patterning of the doped polysilicon layer defines the cap structure (Mask #8, see fig. 9.4f). This is done using RIE in a SF_6/N_2 plasma, which gives an etch selectivity of 40:1 for polysilicon over silicon oxide.

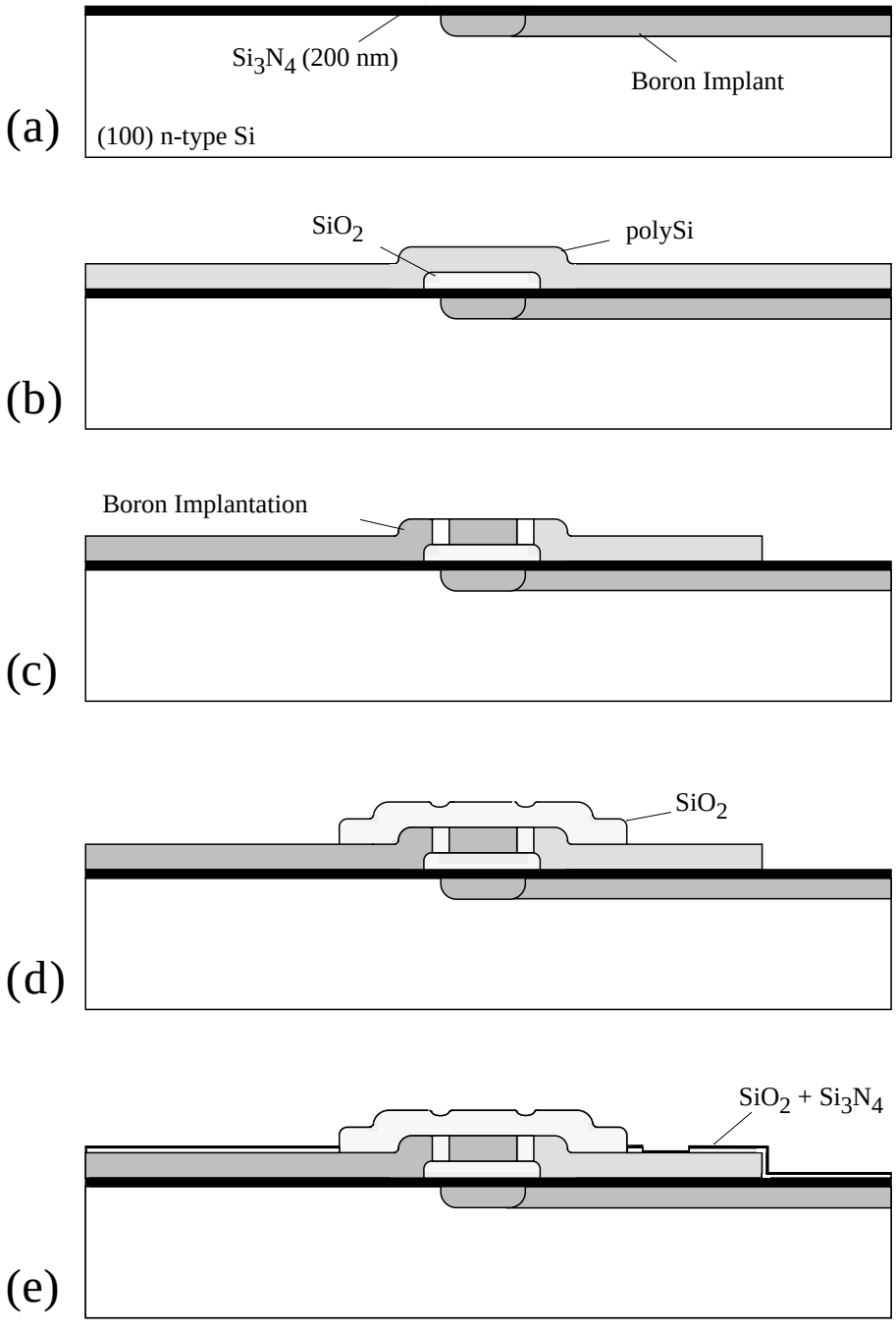

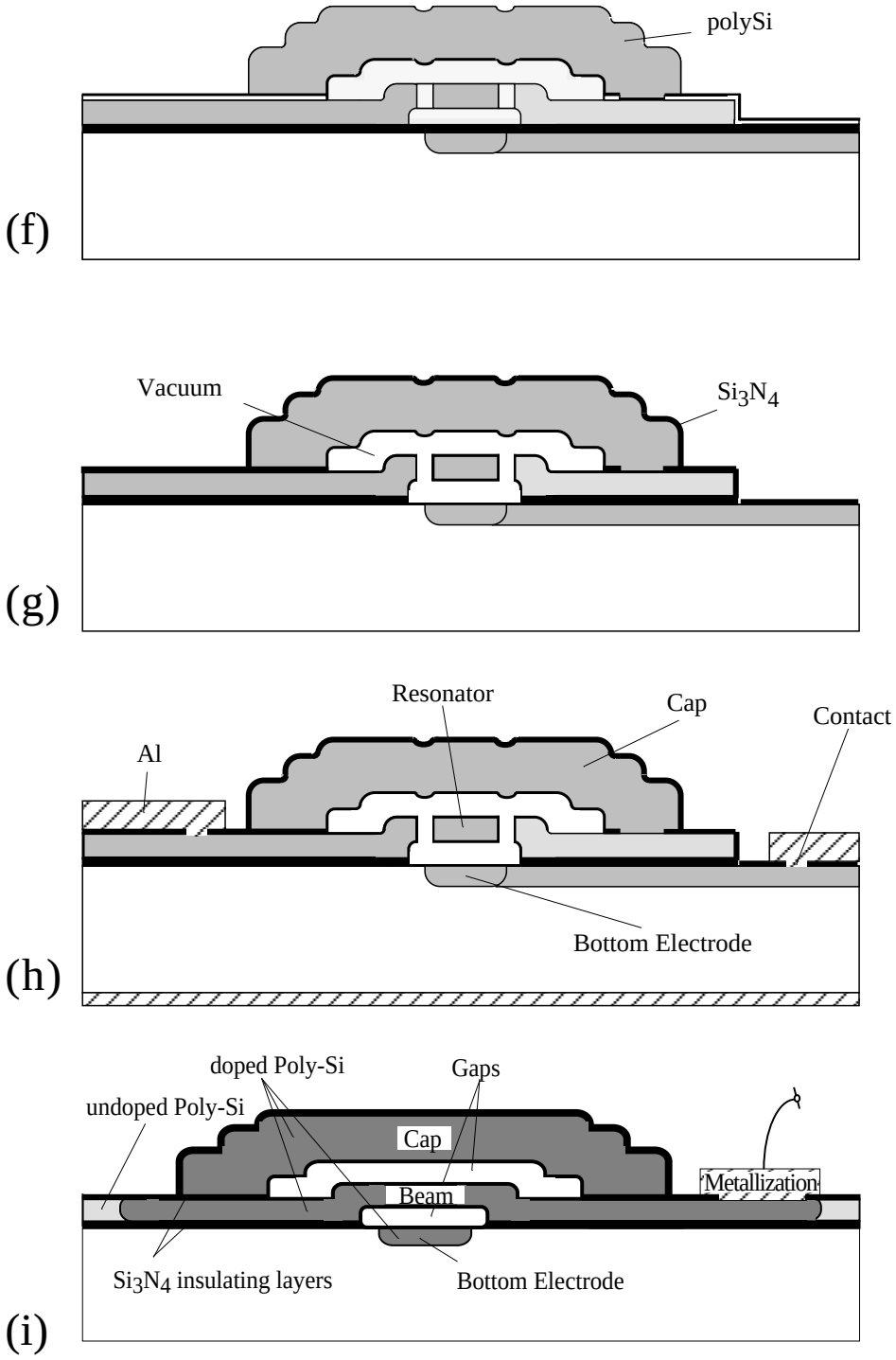

Fig. 9.4a-i *Processing sequence for sealed polysilicon resonators. The different stages of the process are explained in the text.* ***9.4a-h****: cross-sectional view B-B' and* ***9.4i****: cross-sectional view A-A' of fig. 9.2.*

The etching is stopped as soon as the underlying silicon nitride and silicon oxide double layer of the etch channels is exposed. From this point on, thick photoresist layers (3μm) have to be used to ensure sufficient step coverage. Annealing in a nitrogen ambient for 1 hour at a temperature of 1000˚C is necessary for the electric activation of the implanted boron and moreover, to obtain a low tensile strain in the polysilicon layers. Following a thorough cleaning step, the sacrificial layer etch and subsequent freeze drying procedure is performed. Sacrificial layer etching is done in an undiluted (49%) HF-solution and takes about two hours. Quenching in DI-water is done for 30 minutes and next IPA is added. The wafers are rinsed for 1 hour in an IPA solution, followed by a final rinse cycle in cyclohexane for 1 hour. Next, the freeze drying is carried out as described in the previous section (see fig. 9.4g). The mechanical test structures can now be examined to check whether the mechanical stress is in the region of interest and whether sacrificial layer etching and freeze drying have been successful. LPCVD of approximately 200 nm stoichiometric silicon nitride is used to close off the etch channels. The surface passivation of the pn-junction of the bottom electrodes in the substrate is important. Dry thermal oxidation is the best way to accomplish this, but experiments revealed buckled beams even after growing oxide layers as thin as 10 nm at a temperature of 800˚C. It was found that the leakage currents of the pn-junctions that are passivated with silicon nitride are on the order of $10\,\mu A/cm^2$, which is considered to be satisfactory. The contact windows for the substrate-, beam- and cap electrodes are defined using RIE in a CHF_3/O_2 plasma (Mask#9). Metallization consists of a 1 μm thick aluminum layer. Prior to the metallization, the thin films that have accumulated on the backside of the wafer are stripped by means of RIE in a SF_6 and CHF_3 plasmas. Metal patterning (Mask#10) is done by wet chemical etching. The final step is a 5 minutes anneal in a N_2/H_2O ambient at 450˚C to obtain good ohmic contacts. Final cross sections of the sealed resonator are shown in figs. 9.4h and 9.4i.

9.4 RESULTS

The SEM photograph of fig. 9.5a shows a top view of a sealed resonator. To inspect the inside of the cavity for residues, and check whether or not the beams are free standing, caps have been manually removed. This was done by peeling off a carefully attached tape. The cavity inside turned out to be clean and displayed free standing beams having smooth surfaces (see figs. 9.5b,c).

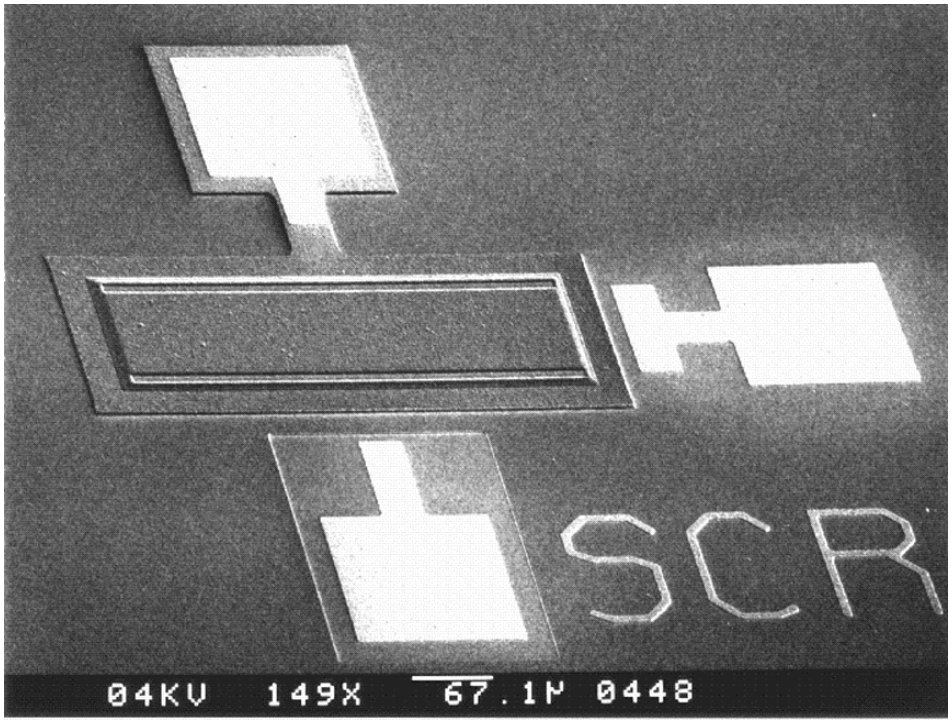

Fig. 9.5 *(a) SEM photograph of a sealed polysilicon resonator.*

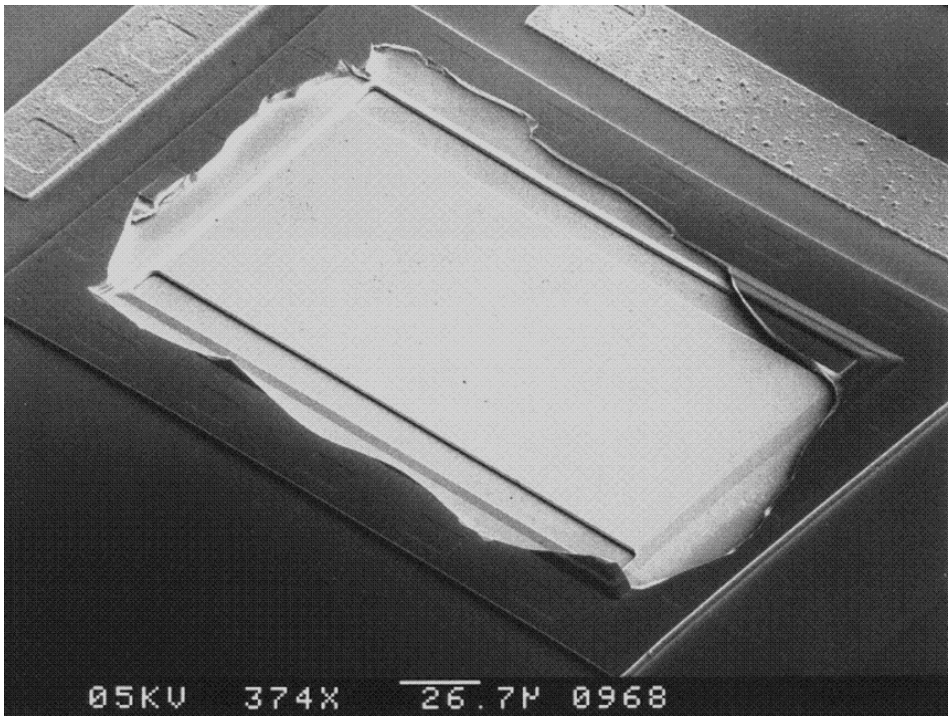

Fig. 9.5 *(b) Resonator with cap removed showing cavity interior.*

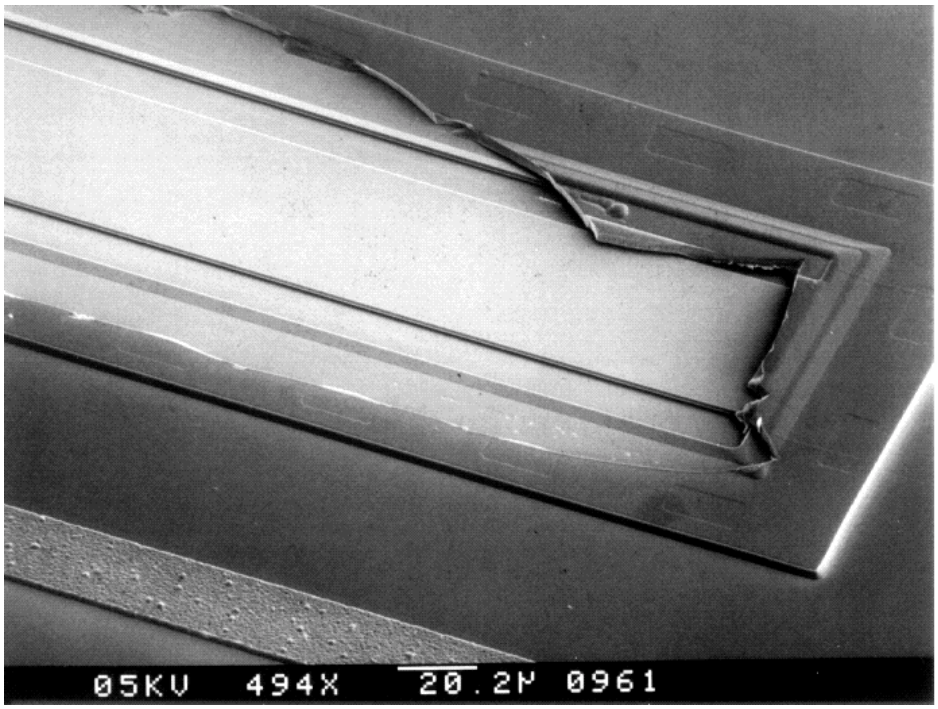

Fig. 9.5 *(c) Close up of cavity interior.*

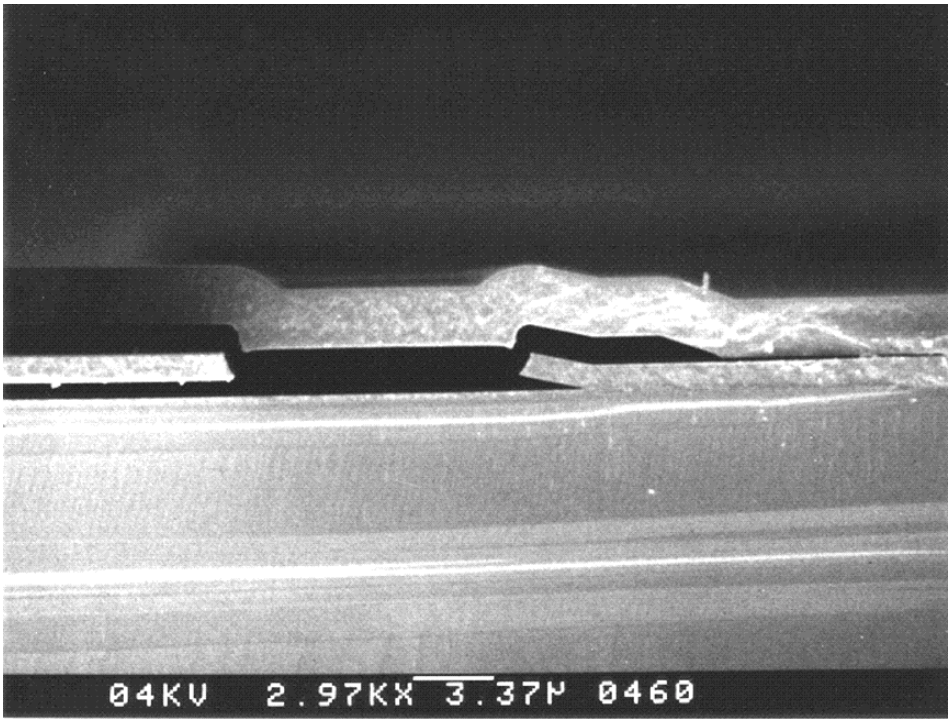

Fig. 9.5 *(d) Magnified view of part of the cross section.*

Cross-sectional views of the resonator are shown in fig. 9.5d. These SEM photograph clearly indicate (part of) the free standing beam and the shape of the cap (compare fig. 9.4h).

9.4.1 Electrical and Electromechanical Behaviour

Electrical measurements indicated sheet resistances of 24Ω/square, 30Ω/square and 22Ω/square for the bottom electrode, the resonator electrode and the cap electrode, respectively. The contact resistance turned out to be about 1Ω for a $20\times20\,\mu m^2$ contact for all three electrodes. Standard I-V measurements used to check the integrity of the nitride insulating anchors revealed high ohmic (GΩ's) anchors. The residual strain has been extracted from the polysilicon ring and buckled beam diagnostics and is within the range from -8×10^{-7} (compressive) to $+6\times10^{-5}$ (tensile).

First tests aimed at finding the resonance frequency have indicated that care must be taken with respect to probing the samples. Static charges induce electric forces that cause "pull-in" of the beams, resulting in permanent attachment of the latter to the cap or to the substrate. This phenomenon was observed while testing uncapped resonators.

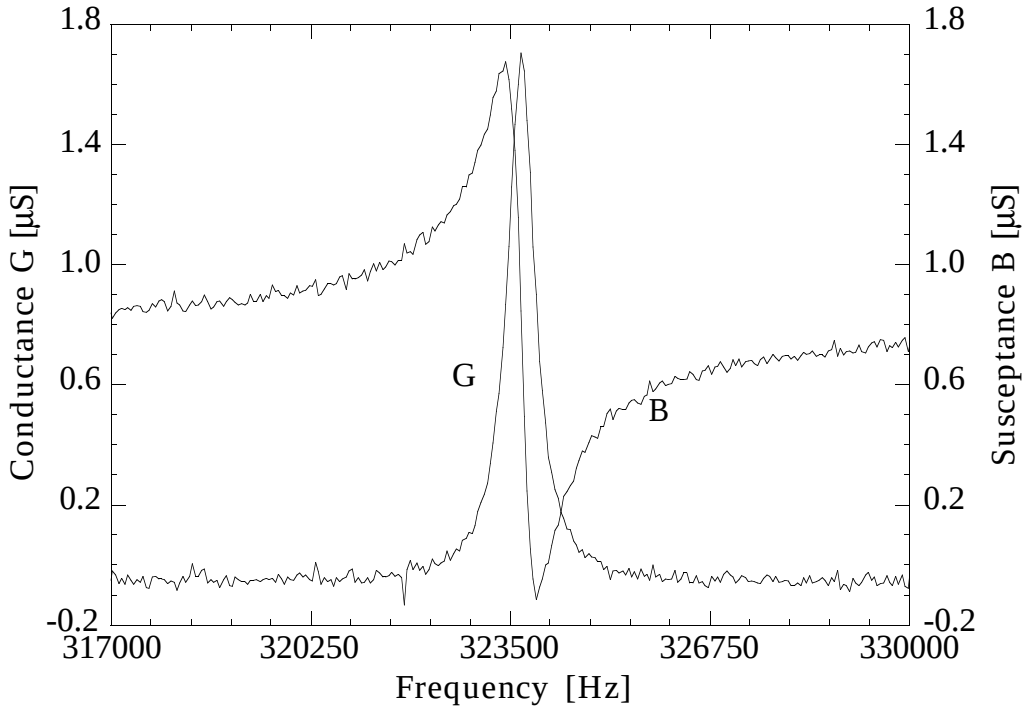

Fig. 9.6 *Admittance Bode plot of an electrostatically driven vacuum encapsulated polysilicon resonator in a one-port configuration [9.13]. Resonator dimensions are 210×100×1.5 µm. The observed resonant frequency is 323,682 Hz.*

Figure 9.6 shows a typical example of a measured Bode plot showing the conductance and the susceptance as a function of the driving frequency of a 210 μm long polysilicon beam resonator.

9.4.2 Quality factor and sealing pressure

Vacuum sealing provides pressures in the molecular regime, where the gas molecules are not interacting with each other. Energy losses due to viscous damping are negligible in this pressure regime. The damping mechanisms that remain, include losses due to individual collisions of the gas molecules with the resonating surfaces (momentum damping), losses into the mount and intrinsic (material) damping. If momentum damping is considered to be the dominant loss mechanism and if the resonator was operating in free space, the mechanical quality factor as a function of the ambient pressure p can be expressed as [9.28]:

$$Q_{\mathrm{n}} = \frac{3}{8\sqrt{6}} \frac{\alpha_{\mathrm{n}}^2}{p} \left[\frac{h}{l}\right]^2 \sqrt{\frac{\pi E \rho R T}{M}} \tag{9.4}$$

where α_{n} is a constant depending on the edge conditions and on the mode of vibration n ($\alpha_1 = 4.73$ for a clamped-clamped beam), h and l are the thickness and the length of the resonator, respectivley, E and ρ are the Young's modulus and the specific mass of the resonator material, respectively, R ($\approx 8.31\,\mathrm{JK^{-1}mol^{-1}}$) is the universal gas constant, T is the absolute temperature and M is the molecular mass of the gas. The mechanical quality factor of the one-port resonators can be extracted from the measured Bode-plot and turned out to be a function of the resonator length. It is noted that the quality factor varied across the wafer, probably as a result of variations of the sealing pressure.

In order to measure the quality factor as a function of pressure, a leak must be introduced to the cavity. Fracturing the cap is not considered to be the best solution, since this would remove the upper gap and thus would give misleading results if effects such as squeeze film damping are significant. Therefore, an especially designed "dual cavity structure" has been used to measure the quality factor as a function of the pressure inside the cavity. The structure consists of two cavities that are interconnected through a narrow channel. One cavity houses the resonator. By fracturing the other cavity and placing the structure in a vacuum chamber, the pressure of the cavity containing the resonator could be regulated by the external vacuum system. This way, the resonator is still sandwhiched between two air gaps, and thus

forms a realistic representation of the actual situation. The results are shown in fig. 9.7. The graph indicates that the quality factor is inversely proportional to the pressure (as predicted by eq. (9.4)) in the range from 0.01 to 1.0 mbar. This suggests that in this pressure regime, momentum damping is the dominating loss mechanism. However, measured Q-values are more than one order of magnitude smaller than predicted and some form of "enhanced momentum damping" exists. This discrepancy has also been observed by Zook *et al.* [9.30]. The primary cause for the discrepancy is the fact that the assumption of free space surrounding the resonator which is used to derive eq. (9.4) is not true. Squeeze film effects have to be taken into account [9.5, 9.8]. This is further strengthened by the distinct values for Q that are measured of a 310 µm long beam with (i.e., dual structure) and without a cap, or in other words, with two gaps and a single gap, respectively. The Q-factor for the structures with two gaps was approximately a factor 2 to 3 smaller than the Q-factor of the structures with a single gap. Details of the theory of squeeze film effects are beyond the scope of this chapter and reference is made to the literature, e.g., see reference [9.8] and references therein. The stationary value of the Q-factor at very low pressures is determined by intrinsic damping effects and by losses into the mount. Measurements have indicated stationary Q-factors close to 18,000 (see fig. 9.8).

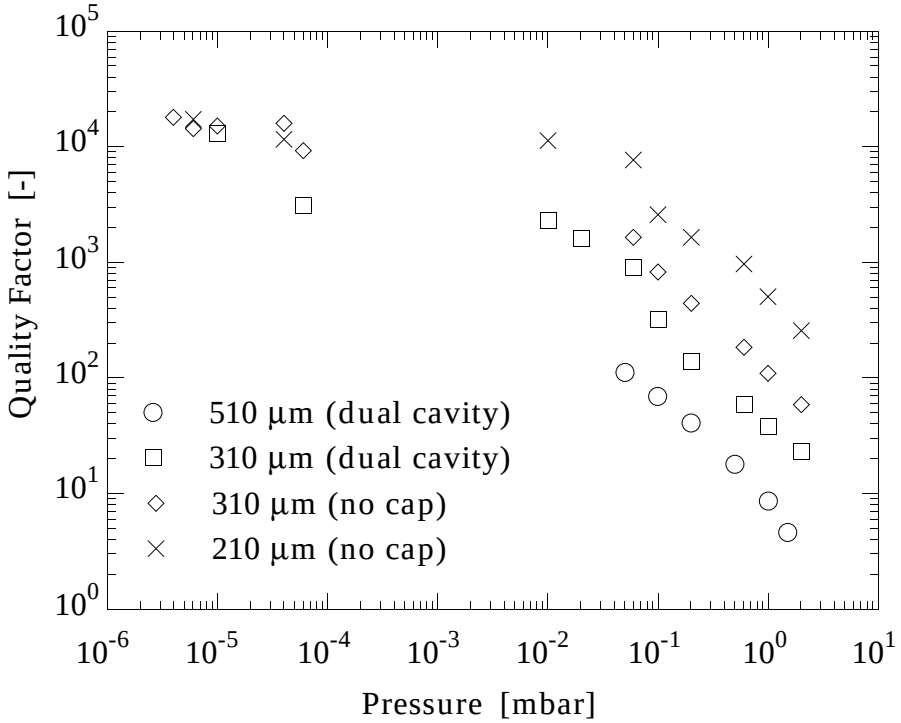

Fig. 9.7 *Measured quality factor as a function of ambient pressure for beams with and without cap and for different beam lengths. Beam thickness and width are 1.5 µm and 100 µm, respectively, lower and upper gap spacing are approximately 1.2 µm and 1-1.5 µm, respectively.*

The reactive sealing process with LPCVD silicon nitride was done at three different process pressures of respectively 200, 50 and 20 mTorr. Typical values of measured quality factors are given in table 9.1.

Sealing Pressure [mTorr]	Quality factor at beam length of			
	510 μm	410 μm	310 μm	210 μm
200	60	80	150	300
50	200	300	700	1300
20	300	400	700	2000

Table 9.1 *Measured average quality factors of sealed resonators with varying beam length after reactive sealing with silicon nitride at different process pressures. Standard deviation of measured quality factors is large, averaging about 50% of the given values.*

The dual cavity structure described above is also used to determine the final cavity pressure of sealed resonators. By matching the Bode plots of sealed resonators and dual cavity resonators, a first indication of the cavity pressure is obtained. This revealed sealing pressures in the range from 0.1-0.2, 0.03-0.05 and 0.02-0.04 mbar which is in fair agreement with predicted values of respectively 0.1, 0.03 and 0.01 mbar obtained from eq. (9.3) for the process pressures as given in table 1. More experimental data together with a theoretical model of the resonator behaviour are given in [9.13].

9.5 CONCLUSIONS

Resonators housed in evacuated cavities have been succesfully fabricated with surface micromachining using sacrificial layer spacers. Low strain fine-grained LPCVD polysilicon has been used for the structural parts and undoped PECVD silicon oxide as the sacrificial layer material. Electrostatic excitation and detection was used as the driving and sensing mechanism. Electrical insulation of the different electrodes is accomplished by means of LPCVD silicon nitride layers. A novel freeze drying method using cyclohexane has been developed to prevent sticking. The advantages of this procedure as compared to other known freeze-drying procedures are its enhanced speed and the fact that no vacuum equipment is required. Reactive sealing with LPCVD silicon nitride yields cavity pressures close to the processing pressure. First measurements have indicated the typical resonance characteristics that are expected for resonators operated in a one-port configuration. Quality factors are determined by enhanced momentum damping due to squeeze film

effects, and turn out to be inversely proportional to the ambient pressure for moderate sealing pressures (0.01-1.0 mbar). Measured sealing pressures are estimated to be in the range of 0.01-0.2 mbar depending on process pressure, resulting in quality factors up to 3000 (highest measured values) for the 210 μm long beams. A more dedicated sealing procedure at lower deposition pressures and/or higher temperatures is required to obtain cavity pressures in the regime, where the quality factor is independent of pressure and is solely determined by intrinsic losses and losses into the mount. Subsequent annealing at elevated temperatures may further reduce the sealing pressure due to outdiffusion of gaseous species. Measurements have indicated that quality factors close to 18,000 are feasible at pressures below 0.01 mbar.

REFERENCES

[9.1] R. M. Langdon, Resonator sensors - a review, J. Phys. E: Sci. Instrum, 18 (1985) 103-115.

[9.2] R. T. Howe, Resonant microsensors, Proc. 4th Int. Conf. Solid-State Sensors and Actuators (Transducers '87), Tokyo, Japan, June 2-5, 1987, pp. 843-848.

[9.3] G. Stemme, Resonant silicon sensors, J. Micromechanics and Microengineering, 1 (1991) 113-125.

[9.4] H. A. C. Tilmans, M. Elwenspoek and J. H. J. Fluitman, Micro resonant force gauges, Sensors and Actuators A, 30 (1992) 35-53.

[9.5] R. T. Howe and R. S. Muller, Resonant-microbridge vapor sensor, IEEE Trans. Electron Devices, ED-33 (1986) 499-506.

[9.6] M. W. Putty, S. C. Chang, R. T. Howe, A. L. Robinson and K. D. Wise, One-port active polysilicon resonant microstructures, Proc. IEEE Micro Electro Mechanical Systems, Salt Lake City, Utah, February 20-22, 1989, pp. 60-65.

[9.7] C. Linder, E. Zimmerman and N.F. de Rooy, Capacitive polysilicon resonator with MOS detection circuit, Sensors and Actuators A, 25-27 (1991) 591-595.

[9.8] M. Andrews, I. Harris and G. Turner, A comparison of squeeze-film theory with measurements on a microstructure, Sensors and Actuators A, 36 (1993) 79-87.

[9.9] K. Ikeda, H. Kuwayama, T. Kobayashi, T. Watanabe, T. Nishikawa and T. Yoshida, Three dimensional micromachining of silicon resonant strain gauge, Proc. of the 7th Sensor Symp., Tokyo, Japan, 1988, pp. 193-196.

[9.10] K. Ikeda, H. Kuwayama, T. Kobayashi, T. Watanabe, T. Nishikawa and T. Yoshida, Silicon pressure sensor with resonant strain gauge built into diaphragm, Proc. of the 7th Sensor Symp., Tokyo, Japan, 1988, pp. 55-58.

[9.11] H. Guckel, J. J. Sniegowski, T. R. Christenson and F. Raissi, The application of fine-grained, tensile polysilicon to mechanically resonant transducers, Sensors and Actuators, A21-A23 (1990) 346-351.

[9.12] J. J. Sniegowski, H. Guckel and T. R. Christenson, Performance characteristics of second generation polysilicon resonating beam force transducers, Proc. IEEE Solid-State Sensors and Actuators Workshop, Hilton Head Island, SC, U.S.A., June 4-7, 1990, pp. 9-12.

[9.13] H. A. C. Tilmans and R. Legtenberg, Electrostatically driven vacuum encapsulated polysilicon resonators; Part II - Theory and performance, Sensors and Actuators, A45, 1994, pp. 67-84.

[9.14] H. A. C. Tilmans, D. J. IJntema and J. H. J. Fluitman, Single element excitation and detection of (micro-) mechanical resonators, Proc. 6th Int. Conf. Solid-State Sensors and Actuators (Transducers '91), San Francisco, U.S.A., June 24-27, 1991, pp. 533-537.

[9.15] H. Guckel, D. W. Burns, H. A. C. Tilmans, D. W. DeRoo and C. R. Rutigliano, Mechanical properties of fine grained polysilicon; the repeatability issue, IEEE Solid-State Sensors Workshop, Hilton head Island, SC, USA, June 6-9, 1988, pp. 96-99.

[9.16] S. P. Timoshenko and S. Woinowsky-Krieger, Theory of plates and shells, Mc Graw-Hill, New York, 2nd ed., 1970, p. 202.

[9.17] H. Guckel and D.W. Burns, A technology for integrated transducers, Proc. 3rd Int Conf. Solid State Sensors and Actuators (Transducers '85), Philadelphia, PA, USA, June 11-14, 1985, pp. 90-92.

[9.18] R. T. Howe, Surface micromaching for microsensors and microactuators, J. Vac. Sci. Technol. B, 6(6), 1988, pp. 1809-1813.

[9.19] D. W. Burns, Micromechanics of integrated sensors and the planar processed pressure transducer, Ph.D. Thesis, Dept. of Materials Science, University of Wisconsin, Madison, WI, USA, 1988.

[9.20] R. T. Howe and R. S. Muller, Stress in polycrystalline and amorphous silicon thin films, J. Appl. Phys. 54 (8), August 1983, pp. 4674-4675.

[9.21] T. I. Kamins, Design properties of polycrystalline silicon, Sensors and Actuators, A21-23 , 1990, pp. 817-824.

[9.22] J. C. North, A. C. Adam and G. F. Richards, Ion implantation doping of polycrystalline silicon, Electrochem. Soc. Fall meeting, Pittsburgh, PA., Extended Abstr. 78-2, 1978, p. 542.

[9.23] P. Scheeper, J. A. Voorthuyzen and P. Bergveld, Surface forces in micromachined structures, Techn. Digest MME '90, 2nd Workshop on Micromachining, Micromechanics and Microsystems, Berlin, Germany, 26-27 November, 1990, pp. 47-52.

[9.24] H. Guckel, J. J. Sniegowski, T. R. Christenson, S. Mohney and T. F. Kelly, Fabrication of micromechanical devices from polysilicon films with smooth surfaces, Sensors and Actuators, 20, 1989, pp. 117-122.

[9.25] R. Legtenberg, J. Elders and M. Elwenspoek, Stiction of surface micromachined structures after rinsing and drying: model and investigation of adhesion mechanism, Proc. 7th Int Conf. Solid State Sensors and Actuators (Transducers '93), Yokohama, Japan, June 7-10, 1993, pp. 198-201.

[9.26] A. Boyde and C. Wood, Preparation of animal tissues for surface-scanning electron microscopy, J. Microsc., 90, 1969, pp. 221-249.

[9.27] N. Takeshima, K. J. Gabriel, M. Ozaki, J. Takahasji, H. Horiguchi and H. Fujita, Electrostatic parallelogram actuators, Proc. 6th Int. Conf. Solid-State Sensors and Actuators (Transducers '91), San Fransisco, CA, USA, June 24-27, 1991, pp. 63-66.

[9.28] F. R. Blom, S. Bouwstra, M. Elwenspoek and J. H. J. Fluitman, Dependence of the quality factor of micromachined silicon beam resonators on pressure and geometry, J. Vac. Sci. Techn. B, 10, 1992, pp. 19-26.

[9.29] K. F. Roenigk and K. F. Jensen, Low pressure CVD of silicon nitride, J. Electrochem. Soc., 134, 1987, pp. 1777-1885.

[9.30] J. D. Zook, D. W. Burns, H. Guckel, J. J. Sniegowski, R. L. Engelstad and Z. Feng, Characteristics of polysilicon resonant microbeams, Sensors and Actuators, A35, 1992, pp. 51-59.

Chapter Ten

CONCLUSIONS

10.1 GENERAL CONCLUSIONS

Chapter one:

There exists an increasing demand for new transducers based on IC fabrication and other thin film technologies. In this thesis the fabrication of different types of electrostatic microactuators based on polysilicon surface micromachining techniques is described. Electrostatic actuators are used for the transformation of electric input energy into mechanical output energy. They benefit from available microfabrication techniques and materials as developed in IC technology and exhibit good performance characteristics such as high energy density in micron sized gaps, high efficiency and fast response time.

Chapter two:

Surface micromachining can be used to fabricate deformable and mechanism type of microstructures with more than one degree of freedom. Polysilicon surface micromachining is based upon the selective removal of sacrificial layers from a multilayer sandwich of patterned thin films consisting of sacrificial silicon oxide layers and structural polysilicon thin films. The ability to control residual stress in polysilicon thin films, characterise polysilicon mechanical properties and model the silicon dioxide sacrificial layer etch process as well as the development of methods to prevent stiction, together with a variety of new fabrication processes and the possibility to integrate electronics make polysilicon surface micromachining a well developed and versatile technology. A notorious problem in surface micromachining is stiction of polysilicon structures after rinsing and drying. A novel freeze drying method using cyclohexane has been developed to prevent stiction problems and was used as a fabrication technique to realise the structures and devices presented in this thesis.

Chapter three:

The mechanisms that cause stiction of polysilicon structures, which are fabricated by surface micromachining techniques, have been investigated in order to obtain a more fundamental understanding of stiction.

It was found that during the drying process, attractive capillary forces are responsible for bringing micromechanical structures into contact with the substrate. A model for the surface tension forces during drying has been developed and applied to doubly clamped beams. For these beams a pull-in length exists beyond which the beams are forced into contact with the underlying substrate. Measurements of the pull-in length are in qualitative agreement with the theory. The measured values of the pull-in length are somewhat lower than predicted by theory. This is suggested to result from dynamical effects during the drying process.

After complete drying, structures remain stuck to the substrate. The measured adhesion energy of the resultant bond has been determined using the detachment length of the beams after complete drying. The resulting bonding strength's were independent of the used rinsing liquids, water and isopropanol. The measured adhesion energies ranged from 0.05 to 0.10 J/m^2 for hydrophobic silicon surfaces and from 0.24 to 0.26 J/m^2 for hydrophilic silicon surfaces. These energies indicate that van der Waals forces are responsible for stiction of hydrophobic surfaces and hydrogen bridging is the dominant bond mechanism in case of the hydrophilic surfaces. These results are in agreement with wafer bonding experiments.

Chapter four:

The fabrication of electrostatic actuators demands small gaps and compliant or high aspect ratio polysilicon microstructures. This requires anisotropic etching techniques of silicon. Reactive ion etching using SF_6, O_2, CHF_3 gas mixtures for the anisotropic etching of silicon has been investigated.

The etching behaviour was found to be affected by loading, the mask material and the cathode material. Reproducable and uniform results have been obtained by using a silicon cathode and a silicon dioxide mask. Surface response methodology was used to characterise etch rate, mask selectivity, bias voltage and anisotropy as a function of the RF power, the process pressure, the SF_6 flow, the O_2 flow and the CHF_3 flow in order to optimise anisotropic etching conditions.

The effect of several variables on the measured responses has been discussed.

The addition of CHF_3 can be used to produce smooth etch surfaces in the anisotropic regime and is useful for a fine tuning of the anisotropy. AES measurements indicate that anisotropic etching results from sidewall passivation by silicon oxide species. The anisotropic etch mechanism in SF_6, O_2, CHF_3 plasmas is based on ion-enhanced inhibitor etching. SF_6 provides the reactive neutral etching species, in the form of F atoms. O_2 supplies the inhibitor film forming species that passivate the surface with a SiO_xF_y layer. SF_6 and CHF_3 generate ion species, SF_x^+ and CF_x^+ respectively, that suppress the formation the inhibitor film at horizontal surfaces.

The fabrication of structures with aspect ratios of about 10 has been demonstrated. The process is applied to deep trench etching and fabrication of high aspect ratio structures used in micromachining.

Chapter five:

An electrostatic actuator design has been presented where a deformable mechanical structure is bent around a fixed curved electrode by means of electrostatic forces. Such a design is attractive because relatively large deflections and force generation can be obtained. For the shape of the curved electrode simple polynomials have been used.

A theory based upon energy methods is presented to describe the static behaviour of the actuator. Furthermore 3D coupled electromechanical simulations using CoSolve-EM have been performed. The results from both models are in qualitative agreement with each other. When the beam deflection is not constrained by the curved electrode geometry, instable behaviour occurs at a certain pull-in voltage and a hysteresis exists to release the structure after pull-in. For polynomial designs, with an order above two, it was found that the beam deflection becomes constrained by the curved electrode geometry before pull-in occurs. Our models predict completely stable behaviour in this situation.

Curved electrode actuators have been fabricated from polysilicon by surface micromachining techniques using a one-mask process. Electric insulation has been realised by stand off bumper structures between the movable beam and the fixed electrode or by a silicon nitride sidewall layer.

Measurements of non-constrained beam deflections show that the qualitative behaviour of the energy model is in agreement with theory but that the pull-in voltages are higher than theoretically predicted. This effect is a result of the presence of a groundplane as shown in 3D coupled electromechanical simulations. Constrained designs employing bumper

structures show a stepwise behaviour as a result of a number of stable positions at the bumper positions. The static behaviour of these designs has been modelled by CoSolve-EM and was found to be in fair agreement with experimental data. Experimental data of samples with a continuous sidewall insulator did not show stable behaviour up to maximal deflection in contrast to our theoretical results. It is suggested that this is caused by imperfections at the sidewall surfaces, as a result of the fabrication process, which prevent the movable beam from smoothly zipping along the curved electrode and act like small bumpers leading to local instabilities.

Curved electrode structures are therefore mainly suited for bi-stable actuator applications like for example microswitches, microgrippers, microvalves and micro pumps.

Chapter six:

The design, fabrication and experimental results of lateral comb-drive actuators for large displacements at low driving voltages is presented. A comparison of several suspension designs is given, and the lateral large deflection behaviour of clamped-clamped beams and a folded flexure design has been modelled. An expression for the axial spring constant of folded flexure designs including bending effects from lateral displacements, which reduce the axial stiffness, has also been derived. The maximum deflection that can be obtained by comb-drive actuators is bounded by electromechanical side-instability. Expressions for the side-instability voltage and the resulting displacement at side-instability are given. The electromechanical behaviour around the resonance frequency was described by an equivalent electric circuit.

Devices have been fabricated by polysilicon surface micromachining techniques using a one mask fabrication process. Static and dynamic properties have been determined experimentally and are compared with theory. Static properties are determined by displacement-to-voltage, capacitance-to-voltage and pull-in voltage measurements. The lateral Young's modulus of the polysilicon layer has been obtained from static displacement-to-voltage measurements and turned out to be approximately 170 GPa. The modelled lateral spring constant of the folded beam design was somewhat larger than experimentally determined values. This is likely to be a result of compliant trusses in our fabricated design in contrast to rigid trusses that have been assumed in our theoretical model, or by a non-rectangular cross section of the beams as a result of underetching. The theoretical axial spring constant of a folded beam which includes a reduction in spring constant with increasing

lateral deflection was found to be in good agreement with experimental results in contrast to theoretical spring constants simply determined from Hooke's law. The electromechanical behaviour can be adequately described by the presented equivalent circuit which was used to extract the resonance frequency and quality factor from admittance measurements.

Typical actuator characteristics are deflections of about 30 µm at driving voltages around 20 V, a resonance frequency around 1.6 kHz and a quality factor of approximately 3. An approach towards position control and feedback was briefly discussed.

Chapter seven:

The design and fabrication of an electrostatically driven lower-stator axial-gap wobble motor has been presented. In contrast to side drive motors, the stator poles are located underneath the rotor instead of surrounding the rotor sides. This results in a higher torque generation and easily accessible rotor structures that are suited for mechanical power transmission to other structures that can be fabricated on-chip.

Based on small tilt angles, a rigid disk rotor and simplified electrostatic fields, a theoretical model describing the static and dynamic behaviour of the motor has been given. For the realised micromotors, the torque generation can be in the range of nNm at high electrostatic fields. The torque coverage for different excitation schemes in case of both open-loop excitation and closed-loop excitation, which requires position feedback, is discussed. Because of large normal forces, generated by the axial electrostatic field, the motors can be easily operated in no-slip conditions. The kinetic behaviour is complex and related to a cycloid. A fixed point at the rotor even moves opposite to the rotational direction of the rotor during small time intervals of a wobble cycle. This may have consequences for certain applications. Based on side-driven micromotor results an equation of motion for the rotor has been derived that includes rotational rotor inertia, viscous drag and coulombic frictional terms. The rotational inertia of the rotor is mainly determined by its inertia about the rocking axes.

Fabrication is based on a four mask process using polysilicon surface micromachining techniques. Silicon nitride has been used for electrical insulation between the rotor and stator poles and silicon oxides were used as sacrificial layers that have been removed in an HF solution. The rotor and stator poles have been constructed from doped polysilicon. To increase the stiffness of the rotor it is made from polysilicon and a thick sputtered

amorphous silicon film. A new ball bearing design, which is not self-aligned, has been used for the rotor in order to avoid photoresist step coverage problems.

Motors have been successfully operated at driving voltages of a few Volts. Motor performance has been characterised by measuring the gear ratio and start and stop voltage measurements using single pole, open-loop excitations with square-wave voltage signals. Although some variation in gear data has been observed for different motors, the gear ratio seems to be independent of the driving frequency up to a maximum measured frequency of 10 kHz. The gear ratio was found to be strongly dependent on the driving voltage. It is suggested that this is caused by the mechanical deformation of the rotor that results from the axial electrostatic forces. The gear ratio was also found to be dependent on operation time showing an initial increase and decrease of the gear ratio after which it remained constant until motor failure. This behaviour is suggested to result from wear at the ball bearing and the surfaces at the contact point circle. Motor lifetimes varied between a few ten thousand wobble cycles to some millions of wobble cycles for two different process runs. This resembles operation times ranging from a few minutes to several hours at rotor speeds between a few and several hundred rpm. A theoretical prediction of the transient response of the motor has been given using measured and estimated calculated parameters for the equation of motion.

Chapter eight:

A surface micromachining process is presented which has been used to fabricate electrostatic microactuators that are interconnected with each other and linked to other movable microstructures by integrated gear linkages. The gear linkages consist of rotational and linear gear structures and the electrostatic microactuators include curved electrode actuators, comb drive actuators and axial gap wobble motors.

The micromechanical structures are constructed from polysilicon. Silicon dioxide has been used as a sacrificial layer and silicon nitride was used for electrical insulation. A cyclohexane freeze drying technique is used to prevent problems with stiction. First experimental results show that electrically powered actuators successfully drive various micromechanisms. The work is a first step towards mechanical power transmission in micromechanical systems. Mechanical power transmission of microactuators may strongly increase the number of useful applications and may lead to new possibilities for microelectromechanical systems.

Chapter nine:

Basic design issues and a fabrication process based on surface micromachining techniques for electrostatically driven vacuum encapsulated polysilicon resonators are presented.

Resonators housed in evacuated cavities have been succesfully fabricated with surface micromachining using sacrificial layer spacers. Low strain fine-grained LPCVD polysilicon has been used for the structural parts and undoped PECVD silicon oxide as the sacrificial layer material. Electrostatic excitation and detection was used as the driving and sensing mechanism. Electrical insulation of the different electrodes is accomplished by means of LPCVD silicon nitride layers. A novel freeze drying method using cyclohexane has been developed to prevent sticking. The advantages of this procedure as compared to other known freeze-drying procedures are its enhanced speed and the fact that no vacuum equipment is required. Reactive sealing with LPCVD silicon nitride yields cavity pressures close to the processing pressure.

First measurements have indicated the typical resonance characteristics that are expected for resonators operated in a one-port configuration. Quality factors are determined by enhanced momentum damping due to squeeze film effects, and turn out to be inversely proportional to the ambient pressure for moderate sealing pressures (0.01-1.0 mbar). Measured sealing pressures are estimated to be in the range of 0.01-0.2 mbar depending on process pressure, resulting in quality factors up to 2000 for 210 µm long beams. A more dedicated sealing procedure at lower deposition pressures and/or higher temperatures is required to obtain cavity pressures in the regime, where the quality factor is independent of pressure and is solely determined by intrinsic losses and losses into the mount. Subsequent annealing at elevated temperatures may further reduce the sealing pressure due to outdiffusion of gaseous species. Measurements have indicated that quality factors close to 18,000 are feasible at pressures below 0,01 mbar.

10. 2 CONCLUDING REMARKS

A fabrication technology based on polysilicon surface micromachining techniques and first actuator designs based on electrostatic actuation have been presented in this thesis. Emphasis has been given to the design of actuators which can generate relatively large forces and displacement. High output actuators are generally attractive in many (possible) applications.

The fabrication of microactuators based on polysilicon surface micromachining techniques is an emerging technology is search of applications. Further development of microactuators depends strongly on the development of useful applications. Polysilicon surfacemicromachining is most suited to fabricate small microsystems where all functions are integrated on-chip. Many applications require millimeter or larger workspaces and output forces of mN. Therefore an upscaling of submillimeter devices, which generally generate forces in the range of 1 to 10 μN, is necessary. This can be easily realised by increasing planar dimensions. However, in order to fabricate robust actuators and increase output forces, this also calls for an increase in the third dimension, i.e. structure thickness. Possible solutions to this problem are the deposition of very thick doped silicon layers or wafer bonding techniques with anisotropic etching techniques, or plating methods based on high aspect ratio UV or X-ray exposure. With these fabrication techniques and provided that micron sized air gaps still can be obtained, many of the advantages that are offered by electrostatic actuation, as described in Chapter 1, still hold.

Important aspects for microactuators are feedback and control, mechanical power transmission and microtribology. At this point these issues are in an infantile stage and are important subjects for further research.

APPENDIX A:

RESPONSE SURFACE METHODOLOGY

Response surface methodology (RSM) is a statistical technique by which experimental strategy and data analysis are combined efficiently to generate a parametric model that represents the process response. It can be applied to any process in which the response can be measured in a continuous fashion and where the settings can be manipulated independently. Once the response has been modelled, graphical representations of the response surfaces formed in the parameter space can be generated for use in process optimization. RSM is only applicable for responses that can be represented as continuous functions.

Response surface designs are fractional factorial designs requiring three or more levels of each process variable. The number of trials in a full factorial design is k^f where k is the number of levels and f is the number of factors. A fractional factorial design is a selected subset of such trials. The number of trials or experimental runs in the design must exceed the number of coefficients in the model. In general a design should be chosen that will support a full quadratic model which includes linear, two factor interactions and quadratic terms for curvature. The general form of the full quadratic model is:

$$Y = b_0 + \sum_{i=1}^{f} b_i X_i + \sum_{i=1}^{f} b_{ii} X_i^2 + \sum_{i=1}^{f-1} \sum_{j=2}^{f} b_{ij} X_i X_i \qquad \text{(A1)}$$

where the X_i represent the independant input variables (*i.e.*, process parameters), the b_i are the coefficients for the linear terms, the b_{ii} are the coefficients for the quadratic terms, and the b_{ij} are the coefficients for the cross terms. In order to estimate the regression coefficients in this model, each variable must take at least three levels. This suggests the use of factorials designs of the 3^k series. One disadvantage of these series is that with more than three variables the experiments become large. Furthermore, the coefficients b_{ii} of the squared terms are estimated with relatively low precision from a 3^k-factorial. Special designs for fitting second order response surfaces have been developed which are called central composite rotatable designs.

If there are more than 6 process variables under consideration, screening designs should be used as a first step to determine the most significant variables. The unknown coefficients in the model can be found by the method of least squares fitting from the experimental data. In matrix notation the n distinct sets of conditions can be written as:

$$\boldsymbol{\eta = X\,\beta} \tag{A2}$$

where η is the $nx1$ vector of expected values for the response, $\boldsymbol{X}$ is the nxp matrix of independent variables, and β is the $px1$ vector of parameters. Since $\boldsymbol{x_1,x_2,...,x_p}$ are the colums of $\boldsymbol{X}$, the normal equations can be written as:

$$\boldsymbol{X}'(\boldsymbol{y}-\hat{\boldsymbol{y}}) = 0 \tag{A3}$$

where the prime(') means transpose. Upon substitution of $\hat{\boldsymbol{y}} = \boldsymbol{X\,b}$:

$$\boldsymbol{X}'(\boldsymbol{y}-\boldsymbol{X\,b}) = 0 \tag{A4}$$

or

$$\boldsymbol{X}'\,\boldsymbol{X}\,\boldsymbol{b} = \boldsymbol{X}'\,\boldsymbol{y} \tag{A5}$$

Since it is supposed that the columns of $\boldsymbol{X}$ are linearly independent, $\boldsymbol{X}'\,\boldsymbol{X}$ has an inverse, and:

$$\boldsymbol{b} = \left[\boldsymbol{X}'\,\boldsymbol{X}\right]^{-1}\boldsymbol{X}'\,\boldsymbol{y} \tag{A6}$$

The full form of eq. (A6) is shown in table A1. The effect of experimental error on the validity of a parameter model can be adressed using statistical analysis. First the experimental error can be estimated by repeating experimental data and calculating the standard deviation of the replicate differences:

$$s^2 = \frac{\sum_i (y_i-\overline{y})^2_{obs}}{(n-p)} = \frac{S_R}{(n-p)} \tag{A7}$$

where $(y_i-\overline{y})^2_{obs}$ corresponds to the variation of an observation y_i from the mean $y$of the observations of the experiment, n is the number of observations and p is the number of variables in the model.

Also the lack-of-model-fit can be estimated by performing trials that are necessary to determine the number of coefficients and calculating the deviation between the model and the experimental data. An indication of the agreement between model and data is provided by the R^2 index:

$$R^2 = \frac{\sum_i (y_i-\overline{y})^2_{pred}}{\sum_i (y_i-\overline{y})^2_{obs}} \tag{A8}$$

in which $(y_i - \bar{y})^2_{pred}$ represents the variation of a predicted response y_i from the mean $\bar{y}$ of the predicted responses and $(y_i - \bar{y})^2_{obs}$ corresponds to the variation of an observation y_i from the mean $\bar{y}$ of the observations of the experiment.

b0		32	0	0	0	0	0	24	24	24	24	24	0	0	0	0	0	0	0	0	0	Σ X0 Y
b1		0	24	0	0	0	0	0	0	0	0	0	0	0	0	0	0	0	0	0	0	Σ X1 Y
b2		0	0	24	0	0	0	0	0	0	0	0	0	0	0	0	0	0	0	0	0	Σ X2 Y
b3		0	0	0	24	0	0	0	0	0	0	0	0	0	0	0	0	0	0	0	0	Σ X3 Y
b4		0	0	0	0	24	0	0	0	0	0	0	0	0	0	0	0	0	0	0	0	Σ X4 Y
b5		0	0	0	0	0	24	0	0	0	0	0	0	0	0	0	0	0	0	0	0	Σ X5 Y
b11		24	0	0	0	0	0	48	16	16	16	16	0	0	0	0	0	0	0	0	0	Σ X1 X1 Y
b22		24	0	0	0	0	0	16	48	16	16	16	0	0	0	0	0	0	0	0	0	Σ X2 X2 Y
b33		24	0	0	0	0	0	16	16	48	16	16	0	0	0	0	0	0	0	0	0	Σ X3 X3 Y
b44		24	0	0	0	0	0	16	16	16	48	16	0	0	0	0	0	0	0	0	0	Σ X4 X4 Y
b55	=	24	0	0	0	0	0	16	16	16	16	48	0	0	0	0	0	0	0	0	0	Σ X5 X5 Y
b12		0	0	0	0	0	0	0	0	0	0	0	16	0	0	0	0	0	0	0	0	Σ X1 X2 Y
b13		0	0	0	0	0	0	0	0	0	0	0	0	16	0	0	0	0	0	0	0	Σ X1 X3 Y
b14		0	0	0	0	0	0	0	0	0	0	0	0	0	16	0	0	0	0	0	0	Σ X1 X4 Y
b15		0	0	0	0	0	0	0	0	0	0	0	0	0	0	16	0	0	0	0	0	Σ X1 X5 Y
b23		0	0	0	0	0	0	0	0	0	0	0	0	0	0	0	16	0	0	0	0	Σ X2 X3 Y
b24		0	0	0	0	0	0	0	0	0	0	0	0	0	0	0	0	16	0	0	0	Σ X2 X4 Y
b25		0	0	0	0	0	0	0	0	0	0	0	0	0	0	0	0	0	16	0	0	Σ X2 X5 Y
b34		0	0	0	0	0	0	0	0	0	0	0	0	0	0	0	0	0	0	16	0	Σ X3 X4 Y
b35		0	0	0	0	0	0	0	0	0	0	0	0	0	0	0	0	0	0	0	16	Σ X3 X5 Y
b45		0	0	0	0	0	0	0	0	0	0	0	0	0	0	0	0	0	0	0	16	Σ X4 X5 Y

$$b_0 = \frac{7}{44}\sum X_0\, y - \frac{3}{88}\sum_{i=1}^{5} X_{ii}\, y$$

$$b_i = \frac{1}{24}\sum X_i\, y$$

$$b_{ii} = \frac{11}{352}\sum X_{ii}\, y + \frac{1}{352}\sum_{i=1}^{5} X_{ii}\, y - \frac{3}{88}\sum X_0\, y$$

$$b_{ij} = \frac{1}{16}\sum X_{ij}\, y$$

Table A1 *Full form of equation (A6) and calculation of the regression coefficients for a central composite rotatable second order design for five parameters.*

REFERENCES

[A1] W.G Cochran and G.M. Cox, Experimental designs, 2 nd ed., John Wiley & Sons, Inc. 1964.

[A2] G.E.P. Box, W.G. Hunter and J.S. Hunter, Statistics for experimentors, John Wiley & Sons, Inc.

APPENDIX B:

LARGE DEFLECTION BEHAVIOUR OF A BEAM FIXED AT BOTH ENDS

A bar with uniform *EI*, fixed at both ends and subject to a vertical load *P* at the centre is onefold statically indeterminate (see Fig. 1).

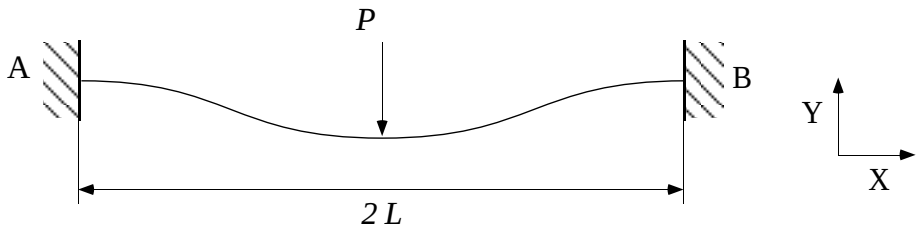

Fig. B1 *Flexible bar subjected to a vertical load at the center.*

The emphasis is not on the deflections being large due to the flexibility of the bar, but rather on the presence of longitudinal forces *N* that develop. For reasons of symmetry only the rigth-hand half will be analysed. The bending moment at a point *(x,y)* is:

$$M = EI\,\frac{d^2y}{dx^2} = N\,y + M_0 - \frac{P}{2}\left(L - x\right) \qquad \text{(B1)}$$

where M_0 is a bending moment at the centre to satisfy boundary conditions. The solution of this equation is:

$$y = \frac{P}{2\,N\,t}\left\{Sinh\,tx - Tanh\,\frac{tl}{2}\left(1 + Cosh\,tx\right)\right\} + \frac{P}{2\,N}\left(L - x\right) \qquad \text{(B2)}$$

where

$$t = \sqrt{N\ /\ EI} \qquad \text{(B3)}$$

at $x = 0$ (the centre) the deflection becomes:

$$\delta = \frac{P\,L^3}{8\,EI}\,\frac{u - Tanh\,u}{u^3} \qquad \text{(B4)}$$

where

$$u = \frac{t\,L}{2} \qquad \text{(B5)}$$

If $N=0$, then $t=0$ and $u=0$, and the expression becomes:

$$\delta = \frac{P\,L^3}{24\,EI} \tag{B6}$$

which is the deflection according to the conventional theory. Equation (B4) contains the unknown u which is a function of the equally unknown t. Therefore to find δ, a further relationship is necessary. This can be found from the longitudinal expansion of the bar during deflection. The change in length is:

$$\Delta l = \frac{1}{2}\int_0^L \left(\frac{dy}{dx}\right)^2 dx \tag{B7}$$

Since the slope is small the axial force can be considered constant along the bar. Hence:

$$N = A\,E\,\frac{\Delta l}{L} = \frac{A\,E}{2\,L}\int_0^L \left(\frac{dy}{dx}\right)^2 dx \tag{B8}$$

Taking the first derivative of eq. (B2) and squaring it, substitution in (B8) leads to:

$$N^3 = \frac{AE\,P^2}{8}\left[\frac{3}{2} - \frac{1}{2}\,Tanh^2\,u - \frac{3}{2}\,\frac{Tanh\,u}{u}\right] \tag{B9}$$

and since $N = EI/t^2$:

$$P = \frac{16\,EI\,\sqrt{2I/A}}{L^3}\,u^3\left(\frac{3}{2} - \frac{1}{2}\,Tanh^2 u - \frac{3}{2}\,\frac{Tanh\,u}{u}\right)^{-\frac{1}{2}} \tag{B10}$$

Combining this expression for P with equation (B4):

$$\delta = 2\,\sqrt{\frac{2I}{A}}\,\left(u - Tanh\,u\right)\left(\frac{3}{2} - \frac{1}{2}\,Tanh^2 u - \frac{3}{2}\,\frac{Tanh\,u}{u}\right)^{-\frac{1}{2}} \tag{B11}$$

The center deflection for a given P can be found by obtaining u from the implicit expression (B10) and solve equation (B11).

REFERENCES

[B1] R. Frisch-Fay, Flexible bars, Butterworths (London), 1962.

[B2] Timoshenko, Theory of Elasticity, 20 (1989), pp. 107-114.

APPENDIX C: LARGE DEFLECTION BEHAVIOUR OF A CLAMPED-GUIDED BEAM

In fig. C1 a beam with one end fixed and the other guided is shown.

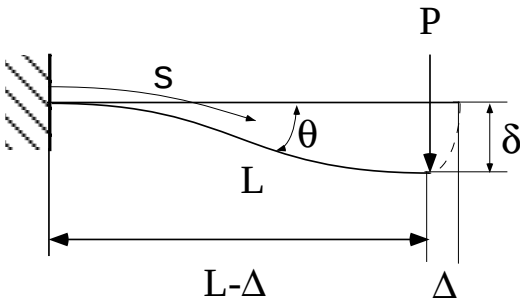

Fig. C1 *Sketch of clamped-guided beam including parameters.*

When one of the ends of the beam is not constrained in the *x*-direction axial forces will not develop. In this case large deflection theory has to be applied and the differential equation that has to be solved is:

$$M = EI\,\frac{d\theta}{ds} = P\left(L - x - \Delta\right) \tag{C1}$$

Differentiating with respect to *s* gives:

$$\frac{d^2\theta}{ds^2} = -\frac{P}{EI}\,\frac{dx}{ds} = -\frac{P}{EI}\,Cos\,\theta \tag{C2}$$

Integrating this equation results in:

$$\frac{1}{2}\left(\frac{d\theta}{ds}\right)^2 = -\frac{P}{EI}\,Sin\,\theta + C_i \tag{C3}$$

The integration constant C_i can be found from the boundary condition, which is, that the slope at the middle of the beam is maximal θ_0 from which follows:

$$C_i = \frac{P}{EI}\,Sin\,\theta_0 \tag{C4}$$

yielding:

$$\frac{d\theta}{ds} = \sqrt{\frac{2P}{EI}\left(Sin\,\theta_0 - Sin\,\theta\right)} \tag{C5}$$

The bar is assumed to be inextensible, in other words, it will not change its length during bending. Therefore:

$$\int_0^{\theta_0} ds = \frac{1}{2} L \tag{C6}$$

Combining equation (C5) and (C6) the following expression results:

$$\frac{1}{2} L \sqrt{\frac{2P}{EI}} = \int_0^{\theta_0} \frac{d\theta}{\sqrt{Sin\ \theta_0 - Sin\ \theta}} \tag{C7}$$

In order to bring the right side to the standard form of elliptic integrals a change in variables is introduced:

$$Sin\ \phi = \sqrt{\frac{1 + Sin\theta}{1 + Sin\theta_0}}$$
$$p = \sqrt{\left(1 + Sin\theta_0\right)/2} \tag{C8}$$

After some manipulation this gives:

$$\frac{1}{2} L \sqrt{\frac{P}{EI}} = \int_{\phi_1}^{\pi/2} \frac{d\phi}{\sqrt{1 - p^2\ Sin^2\ \phi}}$$
$$\phi_1 = ArcSin \sqrt[-\frac{1}{2}]{2\ p^2} \tag{C9}$$

This equation has one unknown, the modulus p. It can be found by trial and error and numerically solving the integral. Since $dy = 2\ ds\ Sin\theta$, the vertical deflection is given by:

$$\delta = 2 \sqrt{\frac{EI}{2\ P}} \int_0^{\theta_0} \frac{Sin\theta\ d\phi}{\sqrt{Sin\ \theta_0 - Sin\ \theta}} \tag{C10}$$

By using the same substition as before:

$$\delta = 2 \sqrt{\frac{EI}{P}} \int_{\phi_1}^{\pi/2} \frac{\left(2\ p^2\ Sin\phi - 1\right) d\phi}{\sqrt{1 - p^2\ Sin\ \phi}} \tag{C11}$$

The expression for the deflection of a cantilever beam loaded at the tip can be obtained in the same way and is given by:

$$\delta = \sqrt{\frac{EI}{P}} \int_{\phi_1}^{\pi/2} \frac{\left(2\ p^2\ Sin\phi - 1\right) d\phi}{\sqrt{1 - p^2\ Sin\ \phi}} \tag{C12}$$

where p can be found from:

$$\sqrt{\frac{PL^2}{EI}} = \int_{\phi_1}^{\pi/2} \frac{d\phi}{\sqrt{1 - p^2\, Sin^2\, \phi}} \qquad \text{(C13)}$$

REFERENCES

[C1] R. Frisch-Fay, Flexible bars, Butterworths (London), 1962.

[C2] S. Timoshenko and J.N. Goodier, Theory of Elasticity, 3rd ed., McGraw-Hill, New York, 1987.

APPENDIX D: DETAILED PROCESSING SEQUENCES

PROCESS SEQUENCE: CURVED ELECTRODE ACTUATORS
COMB DRIVE ACTUATORS

Wafers: p-type, 100-oriented, 3 ", 5-10 Ωcm.

O 1	St. cleaning:	- 5 min. fuming nitric acid (100%) I		
		- 5 min. fuming nitric acid (100%) II		
		- DI quick dump rinse		
		- 15 min. boiling nitric acid (70%)		
		- DI quick dump rinse		
		- spin drying		
O 2	Wet Thermal Oxidation, 2 µm SiO_2, 10 hrs at 1150 ˚C			
O 3	LPCVD polySi:			
		p	- 250 mTorr	
		T	- 590 ˚C	
		SiH_4	- 50 sccm	
		t	- 16 hrs (≈ 6 µm)	
O 4	Thick PR front side protection			
O 5	strip backside:			
		RIE polySi:	SF6	- 50 sccm
			p	- 50 mTorr
			P	- 75 Watt
			electrode styros	
			loading 3 wafers	
			t	- 12 min, 30 sec
O 6	Standard cleaning			
O 7	HF (1:100) dip			
O 8	Diffusion, solid source boron diffusion, 1100 ˚C, N_2, 3 hours			
O 9	Strip Boron Oxide, BHF, 60 min.			
O 10	Standard cleaning			
O 11	PECVD SiO_2:			
		T	- 300 ˚C	
		SiH_4	- 200 sccm	
		N_2O	- 710 sccm	
		p	- 650 mTorr	
		P	- 60 Watt LF	
		t	- 21 min.	d≈0.6 µm
O 12	Standard S1805 Lithography :			
	PR spinning	- spinning HMDS, 4000 rpm, 30 sec.		
		- spinning Shipley S1805, 4000 rpm, 30 sec.		
	Pre bake, 20 min., 90 °C, hot plate			
	Exposure, vacuum contact, 2.5 sec., integrated, 15 mW/cm^2, Development, 60 sec., Shipley 351 developer (1:1)			
	Post bake, 20 min., 135 °C, hot plate			

O 13	Clean RIE chamber, O_2 - 20 sccm p - 100 mTorr P - 200 Watt t - 10 min. styros electrode
O 14	RIE SiO_2 CHF_3 - 10 sccm p - 20 mTorr P - 50 Watt styros electrode T - 25 ˚C t - ≈ 21 min.
O 15	Plasma ash PR, 150 ˚C, 200 Watt, 50 sccm O_2, 15 min.
O 16	RIE polySi: SF_6 - 30 sccm O_2 - 11 sccm CHF_3 - 7 sccm p - 100 mTorr P - 100 Watt t - ≈ visual etch stop, ≈9 min, 30 sec. Use etch step 5 min. maximal Silicon electrode critical step, do not overetch, stop -> inspection small gaps exhibit RIE lag! additional etch as short as possible if necessary
O 17	Standard cleaning also add dummy wafers
O 18	Sacrificial layer etching, BHF, 1 µm / 13 min place dummy wafer opposite to front side process wafer
O 19	dilution rinsing , 15 min., use clean quartz / teflon ware in next steps
O 20	add IPA (carefull)
O 21	IPA rinse, 15 min.
O 22	Cyclohexane rinse, 15 min.
O 23	Freeze drying, -10 ˚C, N_2 flow
O 24	evaporation Al backside, 1 µm

PROCESS SEQUENCE: ELECTROSTATIC WOBBLE MOTORS

Wafers: p-type, 100-oriented, 3 ", 5-10 Ωcm.

O 1	St. cleaning:	- 5 min. fuming nitric acid (100%) I		
		- 5 min. fuming nitric acid (100%) II		
		- DI quick dump rinse		
		- 15 min. boiling nitric acid (70%)		
		- DI quick dump rinse		
		- spin drying		
O 2	LPCVD Si_xN_y:			
		p	- 200 mTorr	
		T	- 850 ˚C	
		DCS	- 70 sccm	
		NH_3	- 18 sccm	
		t	- 120 min.	d≈ 1 μm
O 3	LPCVD polySi:			
		p	- 250 mTorr	
		T	- 590 ˚C	
		SiH_4	- 50 sccm	
		t	- 90 min.	d≈0.5 μm
O 4	Standard cleaning			
O 5	HF (1:100) dip			
O 6	Diffusion, solid source boron diffusion, 1100 ˚C, N_2, 60 min.			
O 7	Strip Boron Oxide, BHF, 60 min.			
	Rsq = 67.5 Ω			
O 8	Standard S1813 Lithography **MASK STATOR**:			
	PR spinning	- spinning HMDS, 4000 rpm, 30 sec.		
		- spinning Shipley S1813, 4000 rpm, 30 sec.		
	Pre bake, 20 min., 90 °C, hot plate			
	Exposure, 6 sec., integrated, 15 mW/cm^2,			
	Development, 60 sec., Shipley MF 312 developer (1:1)			
	Post bake, 20 min., 135 °C, hot plate			
O 9	RIE polySi:			
		SF_6	- 30 sccm	
		O_2	- 10 sccm	
		CHF_3	- 7 sccm	
		p	- 100 mTorr	
		P	- 100 Watt	
		t	- ≈ 2 min.	
		Silicon electrode		
O 10	Standard cleaning			
O 11	LPCVD Si_xN_y:			
		p	- 200 mTorr	
		T	- 850 ˚C	
		DCS	- 70 sccm	
		NH_3	- 18 sccm	

t - 60 min. d≈ 0.5 µm

O 12 Standard S1813 Lithography **MASK CONTACT**

O 13 RIE Si_xN_y

CHF_3 - 25 sccm
O2 - 5 sccm
p - 10 mTorr
P - 75 Watt
t - ≈ 7 min.

O 14 Standard cleaning

O 15 PECVD SiO_2:

T - 300 ˚C
SiH_4 - 200 sccm
N_2O - 710 sccm
p - 650 mTorr
P - 60 Watt LF
t - 70 min. d≈2 µm

O 16 Standard S1828 Lithography **MASK BEARING**:

PR spinning - spinning HMDS, 4000 rpm, 30 sec.
- spinning Shipley S1828, 4000 rpm, 30 sec.

Pre bake, 30 min., 90 °C, hot plate

Exposure, 12 sec., integrated, 15 mW/cm^2,

Development, 60 sec., Shipley MF 312 developer (1:1)

Post bake, 30 min., 120 °C, hot plate

O 17 RIE SiO_2

CHF_3 - 10 sccm
p - 20 mTorr
P - 50 Watt
styros electrode
T - 10 ˚C
t - ≈ 58 min.

O 18 RIE Si_xN_y

CHF_3 - 25 sccm
O_2 - 5 sccm
p - 10 mTorr
P - 75 Watt
t - ≈ 21 min.

O 19 O_2 plasma ashing:

P - 150 Watt
T - 150 °C
O_2 - 50 sccm
p - 2.00 mbar
t - 20 min.

O 20 RIE Si:

SF_6 - 12 sccm
N_2 - 100 sccm
p - 100 mTorr
P - 50 Watt
aluminium electrode

		T	- 10 ˚C	
		t	- ≈ 10 min.	
O 21	Standard cleaning			
O 22	LPCVD TEOS:			
		p	- 400 mTorr	
		T	- 700 ˚C	
			- 50 sccm	
		t	- 130 min.	d ≈ 1 µm
O 23	LPCVD polySi :			
		p	- 250 mTorr	
		T	- 590 ˚C	
		SiH_4	- 50 sccm	
		t	- 360 min.	d ≈ 2.0 µm
O 24	Standard cleaning			
O 25	HF (1:100) dip			
O 26	Diffusion, solid source boron diffusion, 1100 ˚C, N_2, 60 min.			
O 27	Strip Boron Oxide, BHF, 60 min.			
	Rsq = 7.7 Ω			
O 28	Standard cleaning			
O 29	HF (1:100) dip			
O 30	Sputtering Si:			
		p	- 3.0 10^{-2} mbar	
		P	- 500 Watt	
		Ar	- stand 121	
		t	- 6 hours	d ≈ 6.0 µm
O 31	Standard cleaning			
O 32	Annealing, 450 ˚C, N_2, 1 hour			
O 33	PECVD SiO_2:			
		T	- 300 ˚C	
		SiH_4	- 200 sccm	
		N_2O	- 710 sccm	
		p	- 650 mTorr	
		P	- 60 Watt LF	
		t	- 40 min.	d≈1.2 µm
O 34	Standard S1813 lithography **MASK ROTOR**			
O 35	RIE SiO_2			
		CHF_3	- 10 sccm	
		p	- 20 mTorr	
		P	- 50 Watt	
		t	- ≈ 25 min.	
O 36	O_2 plasma ashing			
O 37	RIE Si:			
		silicon electrode		
		SF_6	- 30 sccm	
		O_2	- 10 sccm	
		CHF_3	- 7 sccm	
		p	- 100 mTorr	
		P	- 100 Watt	
		t	- ≈ 10 min.	

O 38	Wet etching in BHF, ≈ 40 min.
O 39	Standard cleaning
O 40	Thick PR spinning and pre bake
O 41	RIE backside strip poly: SF_6-30 sccm / p-50 mTorr / P-100 Watt / t-2'.40" strip TEOS / Si_xN_y: CHF_3,O_2-25:5,p-10 mTorr / P-75 Watt / t-16 min. strip poly: SF_6-30 sccm / p-50 mTorr / P-100 Watt / t-40' strip Si_xN_y: CHF_3,O_2-25:5,p-10 mTorr / P-75 Watt / t-13'
O 42	Standard cleaning
O 43	Sacrificial layer etching, undiluted HF (50%), 15 min.
O 44	QDR rinsing + spin drying (slow)
O 45	evaporation Al backside, 1 µm

PROCESS SEQUENCE: ELECTROSTATIC ACTUATORS WITH INTEGRATED GEAR LINKAGES

Wafers: p-type, 100-oriented, 3 ", 5-10 Ωcm.

O 1	St. cleaning:	- 5 min. fuming nitric acid (100%) I		
		- 5 min. fuming nitric acid (100%) II		
		- DI quick dump rinse		
		- 15 min. boiling nitric acid (70%)		
		- DI quick dump rinse		
		- spin drying		
O 2	HF dip			
O 3	LPCVD Si_xN_y:			
		p	- 200 mTorr	
		T	- 850 ˚C	
		DCS	- 70 sccm	
		NH_3	- 18 sccm	
		t	- 120 min.	d≈ 1 μm
O 4	HF dip			
O 5	LPCVD polySi:			
		p	- 250 mTorr	
		T	- 590 ˚C	
		SiH_4	- 50 sccm	
		t	- 90 min.	d≈0.5 μm
O 6	Standard cleaning			
O 7	HF (1:100) dip			
O 8	Diffusion, solid source boron diffusion, 1100 ˚C, N2, 60 min.			
O 9	Strip Boron Oxide, BHF, 60 min.			
	Rsq = 67.5 Ω			
O 10	Standard S1813 Lithography **MASK STATOR**:			
	PR spinning	- spinning HMDS, 4000 rpm, 30 sec.		
		- spinning Shipley S1813, 4000 rpm, 30 sec.		
	Pre bake, 20 min., 90 °C, hot plate			
	Exposure, 6 sec., integrated, 15 mW/cm^2,			
	Development, 60 sec., Shipley MF 312 developer (1:1)			
	Post bake, 20 min., 135 °C, hot plate			
O 11	RIE polySi:			
		SF_6	- 30 sccm	
		O_2	- 10 sccm	
		CHF_3	- 7 sccm	
		p	- 100 mTorr	
		P	- 100 Watt	
		t	- ≈ 2 min.	
		Silicon electrode		
O 12	Standard cleaning			
O 13	HF dip			
O 14	LPCVD Si_xN_y:			

		p	- 200 mTorr	
		T	- 850 ˚C	
		DCS	- 70 sccm	
		NH_3	- 18 sccm	
		t	- 60 min.	d≈ 0.5 µm
O 15	Standard S1813 Lithography **MASK CONTACT**:			
O 16	RIE Si_xN_y			
		CHF_3	- 25 sccm	
		O_2	- 5 sccm	
		p	- 10 mTorr	
		P	- 75 Watt	
		t	- ≈ 7 min.	
O 17	Standard cleaning			
O 18	PECVD SiO_2:			
		T	- 300 ˚C	
		SiH_4	- 200 sccm	
		N_2O	- 710 sccm	
		p	- 650 mTorr	
		P	- 60 Watt LF	
		t	- 70 min.	d≈2 µm
O 19	Standard S1813 Lithography **MASK REDUCTION**:			
O 20	Wet etch SiO_2 BHF, 3 min., 45 sec.			
O 21	Standard cleaning			
O 22	Standard S1828 Lithography **MASK BEARING**:			
	PR spinning	- spinning HMDS, 4000 rpm, 30 sec.		
		- spinning Shipley S1828, 4000 rpm, 30 sec.		
	Pre bake, 30 min., 90 °C, hot plate			
	Exposure, 12 sec., integrated, 15 mW/cm^2,			
	Development, 60 sec., Shipley MF 312 developer (1:1)			
	Post bake, 30 min., 120 °C, hot plate			
O 23	RIE SiO_2			
		CHF_3	- 10 sccm	
		p	- 20 mTorr	
		P	- 50 Watt	
		styros electrode		
		T	- 10 ˚C	
		t	- ≈ 58 min.	
O 24	RIE Si_xN_y			
		CHF_3	- 25 sccm	
		O_2	- 5 sccm	
		p	- 10 mTorr	
		P	- 75 Watt	
		t	- ≈ 21 min. (1 µm -> 14 min.)	
O 25	O_2 plasma ashing:			
		P	- 150 Watt	
		T	- 150 °C	
		O_2	- 50 sccm	
		p	- 2.00 mbar	

t - 20 min.

O 26 RIE Si:
SF_6 - 12 sccm
N_2 - 100 sccm
p - 100 mTorr
P - 50 Watt
aluminium electrode
T - 10 ˚C
t - ≈ 10 min.

O 27 Standard cleaning

O 28 LPCVD TEOS:
p - 400 mTorr
T - 700 ˚C
- 50 sccm
t - 130 min. d ≈ 1 μm

O 29 Standard S1828 Lithography **MASK ANCHORS**:

O 30 Wet etch SiO_2 BHF, 30 min.

O 31 Standard cleaning

O 32 HF (1:100) dip

O 33 LPCVD polySi :
p - 250 mTorr
T - 590 ˚C
SiH_4 - 50 sccm
t - 16 hours d ≈ 6 μm

O 34 Standard cleaning

O 35 HF (1:100) dip

O 36 Diffusion, solid source boron diffusion, 1100 ˚C, N_2, 60 min.

O 37 Strip Boron Oxide, BHF, 60 min.
Rsq = 2.2 Ω

O 38 PECVD SiO_2:
T - 300 ˚C
SiH_4 - 200 sccm
N_2O - 710 sccm
p - 650 mTorr
P - 60 Watt LF
t - 40 min. d≈1.2 μm

O 39 Annealing, 3 hours, 1100 ˚C, N_2, 180 min.

O 40 Standard S1813 lithography **MASK ROTOR**

O 41 RIE SiO_2
CHF_3 - 10 sccm
p - 20 mTorr
P - 50 Watt
t - ≈ 25 min.

O 42 O_2 plasma ashing

O 43 Thick PR spinning and pre bake

O 44 RIE backside
strip poly / TEOS / Si_xN_y / poly: SF_6-30 sccm / p-50 mTorr / P-100 Watt / t-15'
strip Si_xN_y: CHF_3,O_2-25:5,p-10 mTorr / P-75 Watt / t-12'

O 45 O_2 plasma ashing

O 46 RIE Si:

silicon electrode
SF_6 - 30 sccm
O_2 - 10 sccm
CHF_3 - 7 sccm
p - 100 mTorr
P - 100 Watt
t - ≈ 19.5 min.

O 47 Lithography step coverage 6 µm **MASK OPEN RAILS**

1 PR spinning - spinning HMDS, 4000 rpm, 30 sec.
- spinning Shipley S1828, 4000 rpm, 30 sec.

Pre bake, 20 min., 90 °C, hot plate

2 PR spinning - spinning HMDS, 4000 rpm, 30 sec.
- spinning Shipley S1828, 4000 rpm, 30 sec.

Pre bake, 20 min., 90 °C, hot plate
Exposure, 90 sec., integrated, 15 mW/cm^2,
Development, 120 sec., Shipley 351 developer (1:1)

Post bake, 10 min., 120 °C, hot plate (large reflow)

O 48 RIE Si:

SF_6 - 12 sccm
N_2 - 100 sccm
p - 100 mTorr
P - 50 Watt
aluminium electrode
T - 10 ˚C
t - ≈ 10 min.

O 49 Standard cleaning

O 50 Sacrificial layer etching, undiluted HF (50%), 50 min.

O 51 Freeze drying procedure

O 52 evaporation Al backside, 1 µm

PROCESS SEQUENCE: SEALED CAPACITIVE RESONATORS

Wafers: n-type, 100-oriented, 3 ", 5-10 Ωcm.

O 1	St. cleaning:	- 5 min. fuming nitric acid (100%) I		
		- 5 min. fuming nitric acid (100%) II		
		- DI quick dump rinse		
		- 15 min. boiling nitric acid (70%)		
		- DI quick dump rinse		
		- spin drying		
O 2	Standard 31 Lithography MASK ALN:			
	PR spinning	- spinning HMDS, 4000 rpm, 30 sec.		
		- spinning Shipley 1400-31, 4000 rpm, 30 sec.		
	Pre bake, 20 min., 90 °C, hot plate			
	Exposure, 8 sec., integrated, 15 mW/cm^2,			
	Development, 60 sec., Shipley MF 312 developer (1:1)			
	Post bake, 20 min., 135 °C, hot plate			
O 3	RIE Si:	SF_6	- 12 sccm	
		P	- 40 Watt	
		p	- 20 mTorr	
		t	- 2 min.	
O 4	Standard cleaning			
O 5	Standard 31 Lithography MASK BOT			
O 6	Ion Implantation ICE Lab.			
		front side: B, $5*10^{15}$ cm^{-2}, 100 keV		
		back side: P, $1.5*10^{15}$ cm^{-2}, 150 keV		
O 7	O_2 plasma ashing:			
		P	- 150 Watt	
		T	- 150 °C	
		O_2	- 50 sccm	
		p	- 2.00 mbar	
		t	- 30 min.	
O 8	Standard cleaning			
O 9	LPCVD Si_3N_4:			
		p	- 200 mTorr	
		T	- 800 ˚C	
		DCS	- 22 sccm	
		NH_3	- 66 sccm	
		t	- 36 min.	d≈ 2000 Å
O 10	PECVD SiO_2:			
		T	- 300 ˚C	
		SiH_4	- 200 sccm	
		N_2O	- 710 sccm	
		p	- 650 mTorr	
		P	- 60 Watt LF	
		t	- 35 min.	d≈1 µm
O 11	Annealing 30 min. at 800 ˚C in N_2			

O 12 Standard 31 Lithography MASK GAP
O 13 Wet etching in BHF, ≈ 13 min.
O 14 Standard cleaning
O 15 HF-dip (1:50), 1 min.
O 16 LPCVD polySi (beam):
p - 250 mTorr
T - 590 ˚C
SiH_4 - 50 sccm
t - 240 min. d≈1.5 µm
O 17 Standard 31 lithography MASK TOP
O 18 Ion implantation ICE Lab.
front side: B, $1*10^{16}$ cm^{-2}, 100 keV
O 19 O_2 plasma ashing, 30 min.
O 20 Standard 31 lithography MASK POLYCUT
O 21 RIE polySi:
SF_6 - 12 sccm
N_2 - 100 sccm
p - 100 mTorr
P - 20 Watt
t - ≈7 min.
O 22 Standard cleaning
O 23 PECVD SiO_2:
T - 300 ˚C
SiH_4 - 200 sccm
N_2O - 710 sccm
p - 650 mTorr
P - 60 Watt LF
t - 52 min. d≈1.5 µm
O 24 Annealing 30 min. at 800 ˚C in N_2
O 25 Standard lithography MASK PSG
O 26 Wet etching in BHF, ≈ 20 min.
O 27 Standard cleaning
O 28 Wet thermal oxidation (channel oxide):
1000 ˚C, 12 min. without ramp, N_2- 1 slm
d≈ 800Å
O 29 Standard 31 lithography MASK ANCHOR
O 30 Wet etching in BHF, ≈ 2.5 min.
O 31 Standard cleaning
O 32 HF-dip (1:50), 1 min.
O 33 Optional: LPCVD Si_3N_4:
p - 200 mTorr
T - 800 ˚C
DCS - 22 sccm
NH_3 - 66sccm
t - 9 min. d≈ 500 Å
O 34 Standard cleaning
O 35 HF-dip (1:50), 1 min.
O 36 LPCVD polySi (Cap):
p - 250 mTorr

T - 590 ˚C
SiH_4 - 50 sccm
t - 420 min. d≈2.7 μm

O 37 Optional: Blanket ion implantation ICE Lab.
front side: B, $1*10^{16}$ cm^{-2}, 100 keV

O 38 St. cleaning

O 39 Mechanical anneal, 60 min., 900/1000 ˚C in N_2

O 40 Standard 37 Lithography MASK CAP:
PR spinning - spinning HMDS, 3500 rpm, 30 sec.
- spinning Shipley 1400-37, 3500 rpm, 30 sec.
Pre bake, 30 min., 90 °C, hot plate
Exposure, 8 sec., integrated, 15 mW/cm^2,
Development, 60 sec., Shipley MF 312 developer (1:1)
Post bake, 30 min., 135 °C, hot plate

O 41 RIE polySi:

SF_6 - 5 sccm
N_2 - 50 sccm
p - 20 mTorr
P - 40 Watt
t - ≈15 min.

SF_6 - 12 sccm
N_2 - 100 sccm
p - 100 mTorr
P - 20 Watt
t - ≈18 min.

O 42 O_2 plasma ashing

O 43 Standard cleaning

O 44 Sacrificial layer etch, HF (50%), 120 min.

O 45 Dilution rinse in DI water, 60 min.

O 46 IPA rinse, 60 min.

O 47 Cyclohexane rinse, 60 min.

O 48 Freeze drying, 15 min. in N_2

O 49 (a) Optional: Dry thermal oxidation, 800 ˚C, O_2- 1 slm, 5-10 min.
(b) LPCVD Si_3N_4:

p - 200 mTorr
T - 800 ˚C
DCS - 66 sccm
NH_3 - 22 sccm
t - 36 min. d≈ 2000 Å

O 50 Standard 37 lithography MASK CONTACT

O 51 RIE Si_3N_4

CHF_3 - 25 sccm
O_2 - 5 sccm
p - 10 mTorr
P - 75 Watt
t - 2.5 min.

O 52 Standard cleaning

O 53	HF-dip (1:50), 1 min.
O 54	Evaporation of Al, front side, d≈ 1 µm
O 55	Standard 37 lithography, no mask
O 56	RIE backside strip Si_3N_4, 2000 Å strip poly, 2.7 µm strip Si_3N_4, 500 Å strip poly, 1.5 µm strip Si_3N_4, 2000 Å
O 57	Standard 37 lithography MASK METAL
O 58	PAN etch, 40 ˚C, 5 min.
O 59	Resist strip in fuming nitric acid, 10 min.
O 60	Evaporation of Al, back side, d≈ 1 µm
O 61	Annealing, 10 min. in N_2 / H_2O at 450 ˚C

APPENDIX E: ELECTROSTATICS

Electrostatics in free space

An electrostatic field due to stationary electric charges in free space will be considered. The fundamental postulates of electrostatics in free space are:

$$\nabla \cdot \vec{E} = \frac{\rho}{\varepsilon_0} \tag{E1}$$

$$\nabla \times \vec{E} = 0 \tag{E2}$$

where $\vec{E}$ is the electric field intensity which is defined as the force per unit charge that a very small stationary test charge experiences when it is placed in a region where an electric field exists, ρ is the volume charge density of free charges and ε_0 is the permittivity of free space (ε_0 = 8.85 10^{-12}). The first equation implies that a static electric field is not solenoidal unless ρ=0. The second equation asserts that static electric fields are irrotational.

In practical applications one is ussually interested in the total field of an aggregate or a distribution of charges. This can be more conveniently obtained by the integral forms of eq. (E1) and (E2):

$$\oint_S \vec{E}\, ds = \frac{Q}{\varepsilon_0} \tag{E3}$$

where Q is the total charge contained in the volume V bounded by the surface S. This equation is a form of Gauss's law which asserts that the total outward flux of the E-field over any closed surface in free space is equal to the total charge enclosed in the surface divided by ε_0. By integration of the curl relation over an open surface and invoking Stokes's theorem one has:

$$\oint_C \vec{E}\, dl = 0 \tag{E4}$$

where the line integral is performed over a closed contour C bounding an arbitrary surface.

Electric Potential

Because scalar quantities are easier to handle than vector quantities the curl-free electrostatic vector field is expressed as the gradient of a scalar field which is called the electric potential:

$$\vec{E} = -\nabla V \tag{E5}$$

The electric potential has physical significance as it is related to the work in carrying a charge from one point to another. The work must be done against the field explaining the negative sign. The potential difference between two points P_2 and P_1 is defined by:

$$V_2 - V_1 = \int_{P_1}^{P_2} \vec{E}\, dl \tag{E6}$$

Conductors in static electric fields

In this section the electric field and charge distribution inside the bulk and on the surface of a conductor will be examined. If an electric field is set up in a conductor the exerting electric force will redistribute introduced charges in such a way that both the charge and the field inside vanish. When there is no charge in the interior of a conductor, $\vec{E}$ will be zero. Since $\vec{E}=0$ inside a conductor it has the same electric potential everywhere. The surface of a conductor is an equipotential surface. Under static conditions the $\vec{E}$-field on a conductor surface is everywhere normal to the surface. The tangential component of the $\vec{E}$-field on a conductor surface is zero. The normal component of the $\vec{E}$-field at a conductor/free-space boundary is equal to the surface charge density divided by the permittivity of free space.

Dielectric in static electric fields

Ideal dielectrics do not contain free charges but contain bound charges. A dielectric material can be polarised in the presence of an external electric field. Because a polarised dielectric gives rise to an equivalent volume charge density ρ_p eq. (E1) must be modified to include the effect of ρ_p:

$$\nabla\cdot\vec{E} = \frac{\rho + \rho_p}{\varepsilon_0} \tag{E7}$$

Defining a polarisation vector $\vec{P}$ as:

$$-\nabla\cdot\vec{P} = \rho_p \tag{E8}$$

equation (E7) can be written as:

$$-\nabla\cdot\left(\varepsilon_0 \vec{E} + \vec{P}\right) = \rho \qquad \text{(E9)}$$

Now a new fundamental field quatity, the electric flux density $\vec{D}$, is defined such that:

$$\vec{D} = \varepsilon_0 \vec{E} + \vec{P} \qquad \text{(E10)}$$

The use of vector $\vec{D}$ enables one to write a divergence relation between the electric field and the distribution of free charges in any medium without dealing with the polarization vector $\vec{P}$ or the polarization charge density ρ_p. Combining eqs. (E9) and (E10) gives:

$$-\nabla\cdot\vec{D} = \rho \qquad \text{(E11)}$$

or in integral form:

$$\oint_s \vec{D}\, ds = Q \qquad \text{(E12)}$$

Equation (E12) is another form of Gauss's law stating that the total outward electric flux over any closed surface is equal to the total free charge enclosed in the surface. When the dielectric properties of the medium are linear and isotropic the polarization is directly proportional to the electric field intensity and:

$$\vec{D} = \varepsilon_0 \varepsilon_r \vec{E} \qquad \text{(E13)}$$

where ε_r is a dimensionless constant known as the relative permittivity or dielectric constant of the medium.

If the electric field is very strong bound electrons can be accelerated under the influence of the electric field and avalanche effects of ionization due to collisions may occur. This phenomenon is called dielectric breakdown. The maximum electric field intensity that a dielectric material can withstand without dielectric breakdown is called the dielectric strength of the material.

Capacitance

The potential of an isolated conductor is directly proportional to the total charge on it. One can write:

$$Q = C\,V \tag{E14}$$

where the constant C is called the capacitance of the isolated conducting body. The capacitance is the electric charge that must be added to the body per unit increase in its electrical potential. A capacitor consists of two conductors separated by free space or a dielectric medium. Of considerable importance are parallel plate capacitors which consists of two parallel conducting plates of area A separated by a uniform distance d. A cross section is shown in fig. E1. The plates have a uniformly distributed charges $+Q$ and $-Q$ with surface densities $+\rho_S$ and $-\rho_S$.

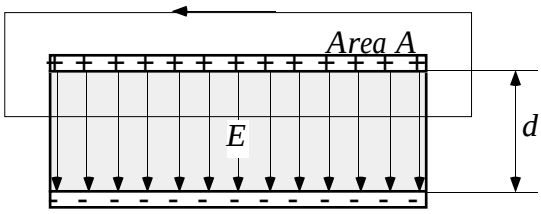

Fig. E1 *Cross section of a parallel-plate capacitor.*

The electrical flux density can be found from eq. (E12). The total outward electric flux over a rectangular box enclosing one of the capacitor plates as shown in fig. E1 only has a contribution from the lower face which is equal to $\vec{D}$.A when fringing fields at the edges are neglected. This total outward electric flux is equal to the total free charge Q enclosed. Using expression (E13) the expression for the electrostatic field becomes:

$$\vec{E} = \frac{Q}{\varepsilon_r\,\varepsilon_r\,A} \tag{15}$$

The potential difference can be found from eq. (E6):

$$V_{21} = V_2 - V_1 = \int_0^d \frac{Q}{\varepsilon_r\,\varepsilon_r\,A}\,dl = \frac{Q\,d}{\varepsilon_r\,\varepsilon_r\,A} \tag{E16}$$

and finally the capacitance for the parallel plate capacitor can be found from eq. (E14) yielding:

$$C = \frac{Q}{V_{21}} = \frac{\varepsilon_r \varepsilon_r A}{d} \qquad \text{(E17)}$$

Capacitors are often combined in various ways in electric circuits. The two basic versions are series and parallel connections. The equivalent capacitance C_{ser} of several capacitances in series is given by:

$$\frac{1}{C_{par}} = \frac{1}{C_1} + \frac{1}{C_2} + \frac{1}{C_3} + \cdots + \frac{1}{C_n} \qquad \text{(E18)}$$

and the equivalent capacitance C_{par} of several parallel conected capacitances is given by:

$$C_{par} = C_1 + C_2 + C_3 + \cdots + C_n \qquad \text{(E19)}$$

Electrostatic Energy and Forces

As already stated before the electric potential is related to the work in carrying a charge from one point to another. The electrical energy in the form of several quantities can be found from:

$$W_e = \frac{1}{2} Q\, V = \frac{1}{2} \int_V \vec{D}.\vec{E}\, dv = \frac{1}{2} C\, V^2 \qquad \text{(E20)}$$

The electrostatic co-energy is defined by:

$$W'_e = W_e - Q\, V = -\frac{1}{2} Q\, V = -\frac{1}{2} \int_V \vec{D}.\vec{E}\, dv = -\frac{1}{2} C\, V^2 \qquad \text{(E21)}$$

When an isolated system of charged bodies is considered, the mechanical work done by the system is:

$$dW = \vec{F}_Q.dl \qquad \text{(E22)}$$

where F_Q is the total eletrostatic force acting on the body under the condition of constant charges. Since the system is isolated with no external supply of energy the mechanical work must be done at the expense of the stored electrostatic energy that is:

$$dW = -dW_e = \vec{F}_Q.dl \qquad \text{(E23)}$$

Since *dl* is arbitrary this leads to:

$$\vec{F}_Q = -\nabla W_e \qquad \text{(E24)}$$

In cartesian coordinates the component forces are:

$$\left(F_Q\right)_x = -\frac{\partial W_e}{\partial x}$$
$$\left(F_Q\right)_y = -\frac{\partial W_e}{\partial y}$$
$$\left(F_Q\right)_z = -\frac{\partial W_e}{\partial z} \qquad \text{(E25 a,b,c)}$$

or in case the system can rotate about an axis the torque T_Q can be found from its derivative to the angle of rotation ϕ:

$$\left(T_Q\right) = -\frac{\partial W_e}{\partial \phi} \qquad \text{(E26)}$$

When the conducting bodies are held at a fixed potential through connections to external sources a displacement by a conducting body would result in a change in total electrostatic energy and requires the sources to transfer charges to the conductors in order to keep them at their fixed potentials. The total energy supplied by the sources to the system is:

$$dW_{source} = V\, dQ \qquad \text{(E27)}$$

The mechanical work done by the system is:

$$dW = \vec{F}_V.dl \qquad \text{(E28)}$$

where F_V is the electric force on the conducting body under the condition of constant potential. The charge transfer also changes the the electrostatic energy of the system by an amount:

$$dW_e = \frac{1}{2}\, V\, dQ \qquad \text{(E29)}$$

Conservation of energy demands that:

$$dW + dW_e = dW_{source} \qquad \text{(E30)}$$

The electrostatic force under the condition of constant potential now becomes:

$$\vec{F}_V = \nabla W_e \qquad \text{(E31)}$$

which only differs by a sign change from the electrostatic force at constant charge.

Static or Dynamic eletrostatic fields?

A final question that has to be answerred is when electrostatic fields can be considered as quasi-static fields or have to be considered as dynamic fields. For the time-harmonic varying electrostatic field, with angular frequency ω, of a parallel plate condensator with circular plates that have a radius R that is large compared to the plate distance d the following expression can be derived:

$$E = E_0 \left[1 - \frac{\omega^2 \varepsilon_0 \varepsilon_r \mu_0 r^2}{4} \right] \qquad \text{(E32)}$$

This electric field is can be approximated by a time dependent quasi-static electrostatic field when:

$$\frac{\omega R}{2 c} << 1 \qquad \text{(E33)}$$

where c is the speed of light in vacuum (3.10^8 m/s). For example for a radius of 1mm a quasi static approach can be used up to frequencies of about 100 Ghz.

BIBLIOGRAPHY

S. Bouwstra, P. Kemna, R. Legtenberg, Thermally excited resonating membrane mass flow sensor, Technical Digest Eurosensors '87, Cambridge, UK, September, 1987, pp. 20-21.

S. Bouwstra, R. Legtenberg and Th. J.A. Popma, Silicon-rich LPCVD silicon nitride films for micromechnical structures, Technical Digest Eurosensors II and 4th Sensors and Actuators symposium, Enschede, The Netherlands, November 1988, p. 167.

S. Bouwstra, R. Legtenberg, H. A. C. Tilmans and M. Elwenspoek, Resonating microbridge mass flow sensor, Technical Digest Transducers '89 and Eurosensors III, Montreux, Switzerland, June 1989, pp. 140-141.

S. Bouwstra, P. Kemna and R. Legtenberg, Thermally excited resonating membrane mass flow sensor, Sensors and Actuators, A20, 1989, pp. 213-223.

S. Bouwstra, R. Legtenberg, H. A. C. Tilmans and M. Elwenspoek, Resonating microbridge mass flow sensor, Sensors and Actuators, A21- A23, 1990, pp. 332-335.

R. Legtenberg, S. Bouwstra and M. Elwenspoek, Low-temperature glass bonding for sensor applications using boron oxide thin films, Proc. 2nd Workshop on micromaching, micromechanics and microsystems (MME '90), Berlin, Germany, November 26-27, 1990, pp. 94-99.

R. Legtenberg, S. Bouwstra and J.H.J. Fluitman, Resonating mass flow sensor with low-temperature bonded cap wafer, Sensors and Actuators , A25-A27, 1991, pp. 723-727.

R. Legtenberg, S. Bouwstra and M. Elwenspoek, Low-temperature glass bonding for sensor applications using boron oxide thin films, J. Micromech. Microeng., 1, 1991, pp. 157-160.

H. A. C. Tilmans and R. Legtenberg, Electrostatically driven vacuum encapsulated polysilicon resonators, poster presentation Eurosensors VI (Book of Abstracts, p. 353), San Sebastian, Spain, 5-7 October, 1992. p. 353.

H. A. C. Tilmans, R. Legtenberg, H. Schurer, D. J. IJntema, M. Elwenspoek and J. H. J. Fluitman, (Electro)mechanical characteristics of electrostatically driven vacuum encapsulated polysilicon resonators, IEEE Trans. Ultrasonics, Ferroelectrics and Frequency Control, Vol. 41, No. 1, January 1994. pp. 4-6.

R. Legtenberg and H. A. C. Tilmans, Electrostatically driven vacuum encapsulated polysilicon resonators, Part I: Design and fabrication, Sensors and Actuators, A45, 1994, pp. 57-66.

H. A. C. Tilmans and R. Legtenberg, Electrostatically driven vacuum encapsulated polysilicon resonators, Part II: Theory and performance, Sensors and Actuators, A45, 1994, pp. 67-84.

R. Legtenberg, H. Tilmans, J. Elders and M. Elwenspoek, Stiction of surface micromachined structures after rinsing and drying: Model and investigation of adhesion mechanisms, Proc. 7th Int. Conf. Solid State Sensors and Actuators (Transducers '93), Yokohama, Japan, June 7 - 10, 1993, pp. 198-201.

R. Legtenberg, H. Jansen, M. Elwenspoek and J. Fluitman, Micro Joints, Book of abstracts, 13-th Benelux Meeting on Systems and Control, Veldhoven, The Netherlands, March 2-4, 1994, p. 26.

R. Legtenberg, H. Tilmans, J. Elders and M. Elwenspoek, Stiction of surface micromachined structures after rinsing and drying: Model and investigation of adhesion mechanisms, Sensors and Actuators, A43, 1994, pp. 230-238.

R. Legtenberg, E. Berenschot, M. Elwenspoek and J. Fluitman, Electrostatic curved electrode actuators, Proc. IEEE Micro Electro Mechanical Systems, Amsterdam, The Netherlands, Jan. 29-Feb. 2, 1995, pp. 37-42.

J.R. Gilbert, R. Legtenberg and S.D. Senturia, 3D coupled electromechanics for MEMS: Applications of CoSolve-EM, Proc. IEEE Micro Electro Mechanical Systems, Amsterdam, the Netherlands, Jan. 29-Feb. 2, 1995, pp. 122-127.

H. Jansen, M. de Boer, R. Legtenberg and M. Elwenspoek, The black silicon method: a universal method for determining the parameter setting of a fluorine-based reactive ion etcher in deep silicon trench etching with profile control, J. Micromechanics and Microengineering, Vol. 5, 1995, pp. 115-120.

H. Jansen, M. de Boer, J. Burger, R. Legtenberg and M. Elwenspoek, The black silicon method II:The effect of mask material and loading on the reactive ion etching of deep silicon structures, Microelectronic Engineering, Vol. 27, 1995, pp. 475-480.

C. Gui, R. Legtenberg, M. Elwenspoek and J. Fluitman, Q-factor dependance of one-port encapsulated polysilicon resonators on reactive sealing pressure, J. Micromechanics and Microengineering, Vol. 5, 1995, pp. 183-185.

C. Gui, R. Legtenberg, H. Tilmans, J. Fluitman and M. Elwenspoek, Nonlinearity and hysteresis of resonant strain gauges, Proc. IEEE Micro Electro Mechanical Systems, Amsterdam, The Netherlands, Jan. 29-Feb. 2, 1995, pp. 157-162.

R. Legtenberg, H. Jansen, M. de Boer and M. Elwenspoek, Anisotropic reactive ion etching of silicon using SF6/O2/CHF3 gas mixtures, J. Electrochem. Soc., Vol. 142, No. 6, June, 1995, pp. 2020-2027.

European Patent No. 94202519.8: Process for producing micromechanical structures by means of reactive ion etching.

R. Legtenberg, E. Berenschot, J. van Baar, Th. Lammerink and M. Elwenspoek, An electrostatic lower stator axial gap wobble motor: design and fabrication, Proc. 8th Int. Conf. Solid State Sensors and Actuators (Transducers '95), Stockholm, Sweden, June 25 - 29, 1995, pp. 404-407.

R. Legtenberg, A.W. Groeneveld and Miko Elwenspoek, Towards position control of electrostatic comb drives, Proc. Micro Mechanics Europe Workshop, Copenhagen, Denmark, September 3-5, 1995, pp. 124-127.

R. Legtenberg, E. Berenschot, M. Elwenspoek and J.H.J. Fluitman, Electrostatic actuators with integrated gear linkages for mechanical power transmission, Proc. IEEE Micro Electro Mechanical Systems, San Diego, CA, U.S.A., Feb. 11-15, 1996.

R. Legtenberg, E. Berenschot, J. van Baar and M. Elwenspoek, An electrostatic axial gap wobble motor, submitted to the Journal of Micro Electro Mechanical Systems.

R. Legtenberg, A.W. Groeneveld and M. Elwenspoek, Comb drive actuators for large displacements, J. Micromech. Microeng., 6, 1996, pp. 320-329.

DANKWOORD (Acknowledgements)

De resultaten zoals beschreven in dit proefschrift zouden niet mogelijk zijn geweest zonder de inbreng van vele personen van zowel binnen als buiten Universiteit Twente.

Allereerst wil ik mijn promotoren Jan Fluitman en Theo Popma en assistent promotor Miko Elwenspoek bedanken voor het geven van de mogelijkheid om als HTS'er te promoveren, alsmede voor het in mij gestelde vertrouwen om dit succesvol af te ronden. Het was destijds een moeilijke beslissing om mijn vaste aanstelling als technicus aan de universiteit op te geven en de sprong te wagen. Miko wil ik verder bedanken voor de vele discussies die een belangrijke bijdrage hebben geleverd aan hoe te opereren als zelfstandig wetenschapper. Voorts wil ik Siebe Bouwstra en Harrie Tilmans bedanken voor het overdragen van hun expertise op het gebied van micromechanica en vele andere zaken, gedurende mijn aanstelling als technicus. Samenwerken met jullie was een fijne tijd en heeft een grote rol gespeeld in de ontwikkeling van mijn kennis en ervaring.

De stichting FOM/STW wordt bedankt voor de financiele ondersteuning van het project en het aanbieden van diverse cursussen en de sponsoring van diverse reizen en verblijven in zowel binnen- en buitenland. Naast conferentie bezoeken ben ik ook in de mogelijkheid gesteld om een aantal maanden aan het Massachusetts Institure of Technology te werken. My stay, during the summer of 1994, at the MEMCAD group of the Microsystem Technology Laboratories at the Massachusetts Institute of Technology in Boston, supervised by Steve Senturia, was a very stimulating and pleasant experience which I will never forget. Steve, thank you for giving me the opportunity to work in your group and arranging the visit to the Hilton Head 1994 conference. I also wish to thank John Gilbert, Peter Osterberg and Dan Sobek for their help and sharing their time with me. It was fun.

De bijdragen van verschillende studenten, in chronologische volgorde: Hans Schurer, Geert Langereis, Nico van Dellen, Marc van der Reijden, Remmert Wittebrood, John van Baar en Aart-Wichert Groeneveld dienen ook vermeld te worden. Bedankt voor jullie inspanning en inzet.

Vanwege het technologische karakter van het onderzoek heeft de staf van de MESA cleanroom een belangrijke bijdrage aan het werk gehad. Allemaal hartelijk dank voor jullie hulp en ondersteuning. Met name wil ik Arie Kooy bedanken voor zijn hulp en inzet bij het ontwerpen en het flitsen van vele maskers. Altijd wist hij maskers met moelijke flitspatronen en dimensies die

op de grenzen van de mogelijkheden van de patroon generator lagen te voorschijn te toveren. Verder wil ik Bert Otter in het bijzonder danken voor zijn hulp bij het maken van de AFM scans en de vele SEM foto's.

Veel dank ben ik ook verschuldigd aan Erwin Berenschot. Zijn ondersteuning en technologische vaardigheden hebben een belangrijke bijdrage geleverd aan de realisatie van vele devices in dit proefschrift. Verder wil ik Meint de Boer bedanken voor zijn hulp bij het anisotroop ets onderzoek en samen met Henri Jansen voor de vele discussies op het gebied van anisotroop etsen.

Voorts wil ik alle MicMec'ers bedanken voor de samenwerking en de plezierige werksfeer. De vele koffie, taart en bier hebben hier zeker aan bijgedragen. Met name mijn voormalige en huidige kamergenoten; Han Gardeniers, Job Elders, Thijs van Toor, Jan-Kees te Riet Scholten, Gui Chenqun en Joost van Kuijk wil ik hierbij noemen.

Ook Dick Ekkelkamp, Judith Beld en Jose Nijhuis-Effing wil ik danken voor hun hulp op administratief en financieel gebied.

Veel dank ben ik verder verschuldigd aan Jan van Schoot en Gerlo Hesselink. In het PC imperium binnen vakgroep TDM heb ik een onmisbare hulp gehad van hen op het gebied van software ondersteuning op mijn MacIntosh.

Han Gardeniers en Marina Maund wil ik hierbij bedanken voor het aandachtig doorlezen van mijn concept proefschrift en de respectievelijke inhoudelijke correcties en verbeteringen van de Engelse taal.

Verder dank ik mijn familie en vrienden voor hun interesse, steun en momenten van ontspanning.

Als laatste maar zeker niet in de minste plaats wil ik Manuela bedanken voor haar geduld, liefde, zorg en vertrouwen in mij tijdens de afgelopen vier jaren.

BIOGRAPHY

Rob Legtenberg was born on June 21, 1964, in Hengelo, The Netherlands. He received a B.Sc. degree in Applied Physics from the Hogere Technische School, Enschede, The Netherlands, in 1985. His graduate project at the University of Twente, Enschede, The Netherlands, dealt with the fabrication of passive and active planar optical waveguides by spin- and dip coating.

After fulfilling his military service, he joined the Micromechanical Research Group at the University of Twente as a process engineer in 1986. His work included the development of micromachining techniques and fabrication and characterisation of micromechanical devices. The main subjects were resonating microbridge mass flow sensors and vacuum encapsulated electrostatically driven polysilicon resonators. Cooperative work on the realisation of resonating force sensors, micropumps, flow sensors and liquid dosing systems was also performed.

In 1992 he started the research on electrostatic actuators fabricated by surface micromachining techniques, as described in this thesis, in the same group at the MESA Research Institute at the University of Twente. During the summer of 1994 he visited the MEMCAD group at the Massachusetts Institute of Technology (MIT), supervised by Prof. S. D. Senturia, to work on coupled electromechanical simulations of curved electrode actuators using the CoSolve-EM system.

Besides his work he enjoys music and piano playing, reading, billiards, fitness, as well as jogging and outdoor activities. Growing bonsai trees, home improvement and spending time with friends are also amongst his favourite activities.

LEVENSLOOP

Rob Legtenberg werd geboren op 21 Juni, 1964, in Hengelo. Na de middelbare school begon hij in 1981 met de studie Technische Natuurkunde aan de Hogere Technische School te Enschede waar hij in 1985 afstudeerde. Zijn afstudeeropdracht had betrekking op de fabricage van passieve en actieve planaire golfgeleiders door middel van spin- en dip coating.

Na het doorlopen van de militaire diensplicht trad hij in 1986 in dienst van Universiteit Twente als proces technoloog binnen de onderzoeksgroep Micromechanische Systemen. Hier werkte hij aan de ontwikkeling van "micromachining" technieken en de fabricage en karakterisatie van micromechanische sensoren en actuatoren. Belangrijke onderwerpen waren resonerende mass-flow sensoren en vacuum ingekapselde, electrostatisch aangedreven, resonatoren van polykristallijn silicium. Voorts heeft hij bijdragen geleverd aan de realisatie van resonerende kracht sensoren, micro pompen, flow sensoren en micro doseer systemen.

In 1992 trad hij als promovendus in dienst van het MESA Research Institute van de Universiteit Twente en startte het onderzoek naar electrostatische actuatoren die door middel van "surface micromachining" technieken worden gefabriceerd, zoals beschreven in dit proefschrift. Van juni 1994 tot en met augustus 1994 werkte hij aan het Massachusetts Institute of Technology (MIT), onder leiding van Prof. S. D. Senturia, aan gekoppelde electromechanische simulaties van kromme electrode actuatoren met behulp van het CoSolve-EM systeem.

Naast zijn werk houd hij van muziek, piano spelen, lezen en biljarten. Hij slooft zich regelmatig uit in het fitness centrum, doet wat aan joggen en houd van kamperen. Verder zijn het kweken van bonsai, klussen in huis en uitgaan met vrienden favoriete bezigheden van hem.